JAYAPALAN, ANITHA. Ph.D. Core-Shell - Cobalt Oxide @ Carbon Nanodot Hybrid Nanoparticles – Evaluation for Photocatalytic and Cancer Theranostic Applications. (2023) Directed by Dr. Jianjun Wei. 184 pp.

Metal oxide carbon-based nanocomposites have gained tremendous consideration in recent years due to the porous metal oxides with carbon structural and morphological tunability for their use in wide areas of research, such as catalysis, energy storage, and theranostic applications. These types of hybrid nanocomposites are advantageous as the metal oxides have a high storage capacity for catalytic applications, and their toxicity could be considerably reduced by carbon shell architectures to improve bioavailability. Cobalt oxide nanoparticles (Co_3O_4 NPs) and carbon nanodots (CNDs) were chosen for this research to construct a hybrid core-shell structure to achieve multifunctionalities by synergizing the spinel nature of the Co_3O_4 NPs with its mixed valence state and the porous CNDs. Specifically, this dissertation work is focused on the evaluation of the synergistic properties of Co_3O_4@CND hybrid NPs, for the photocatalytic activity in the photodegradation of dye molecules (Chapter two), energy storage as supercapacitor materials (Chapter three), and the delivery of small drugs to cancer cells for theranostic study (Chapter four). In chapter one, a comprehensive review of the multifunctional hybrid core-shell NPs with Co_3O_4 NPs and CNDs with a brief literature knowledge on their physicochemical, optoelectronic, and biological properties and their various applications was provided. In Chapter two, the photocatalytic activity of the Co_3O_4@CND hybrid NPs was investigated by evaluating the photodegradation of organic dye upon visible and UV lights, respectively. The results indicated that the Co_3O_4@CND hybrid NPs had higher efficiency and kinetics in dye degradation than Co_3O_4 NPs or CNDs. This high efficiency and kinetics were explained by the heterojunction interfacial surface between the core Co_3O_4 NPs and shell CNDs, which improved the electron-hole pair separation and migration for the photocatalytic reactions.

In chapter three, the Co_3O_4@CND hybrid NPs used in a supercapacitor electrode and evaluated the energy storage by electrochemical means and compared to Co_3O_4 NPs or CNDs. The cyclic voltammetry experiments were performed to evaluate the capacitance performance of the Co_3O_4@CNDs hybrid NPs as a supercapacitor with different binder solvents, including nafion, polyvinyl difluoridine (PVDF), and polytetrafluoroethylene and activated carbons. The findings of this thrust are that the capacitance with the PVDF binders and activated carbons of the Co_3O_4@CNDs hybrid NPs showed better energy storage than other binders used. In chapter 4, the use of Co_3O_4@CND hybrid NPs for imaging and specific targeting of cancer cells was investigated. The multifunctional biological applications of the hybrid NPs in cellular imaging, antioxidant effect in cells, and anticancer activity with or without conjugating small drug molecules, including polymers (polyethylene glycol) and ligands (folic acid, heparin, and transferrin) were evaluated, and proven. Improved anticancer efficacy and bioavailability of Co_3O_4@CNDs were achieved through a receptor-ligand activation mechanism for specific cancer cell targeting. Co_3O_4@CND hybrid NPs-transferrin-DOX ligand complex demonstrated specific anticancer activity of almost 50% for lung cancer cells without harming normal human endothelial cells. The overall findings of this dissertation work presented advanced knowledge associated with the structural properties of core-shell Co_3O_4@CND hybrid NPs, superior performance in photocatalysis, energy storage, and cancer theranostic effects, and a fundamental understanding of their reactions.

CORE-SHELL - COBALT OXIDE @ CARBON NANODOT HYBRID NANOPARTICLES – EVALUATION FOR PHOTOCATALYTIC AND CANCER THERANOSTIC APPLICATIONS

by

Anitha Jayapalan

A Dissertation
Submitted to
the Faculty of The Graduate School at
The University of North Carolina at Greensboro
in Partial Fulfillment
of the Requirements for the Degree
Doctor of Philosophy

Greensboro

2023

Approved by

Dr. Jianjun Wei
Committee-Chair

DEDICATION

I want to heartfully dedicate the research to my mother in heaven. With her blessings and strong willpower, I strived hard to make her aim of me succeeding with a doctorate. She took the initiative and encouraged me to join the Ph.D., but unfortunately, I lost her suddenly after starting my Ph.D. journey during my second year. I believed that her blessings were always with me and that helped me to fulfill my aim by pushing forward through this journey for her. I also wanted to dedicate this to my father who is my real superhero and role model, and he constantly motivated me to push through and succeed in this Ph.D. with perseverance. Finally, the support of my family, my father, and my sister were great support for me, and without their love and motivation, I would really not have made it this far. I want to heartfully thank and dedicate this Ph.D. research to my family for being everything for whom I am today and for succeeding in this Ph.D. with perseverance.

APPROVAL PAGE

This dissertation written by Anitha Jayapalan has been approved by the following committee of the Faculty of The Graduate School at The University of North Carolina at Greensboro.

Committee Chair

Dr. Jianjun Wei

Committee Members

Dr. Dennis Lajeunesse

Dr. Tetyana Ignatova

Dr. Zhenquan Jia

March 15, 2023

Date of Acceptance by Committee

March 15, 2023

Date of Final Oral Examination

ACKNOWLEDGEMENTS

Firstly, I would like to express my sincere gratitude to Dr. Jianjun Wei for his constant support and guidance throughout this research. His research knowledge, organizational skills, and insights into problem-solving always inspired me in many ways to expand my knowledge and think critically.

Next, I would like to thank my committee members, Dr. Tetyana Ignatova, Dr. Dennis Lajeunesse, and Dr. Zhenquan Jia for their insightful comments, guidance, and encouragement to support my project over the years. In addition, I also want to extend my sincere thanks to Dr. Kyle Nowlin, Dr. Steven Crawford, and Dr. Olubunmi Ayodele for their extensive support in handling the instruments with proper training and troubleshooting support inside the laboratory.

I also want to thank all my senior group members and labmates, Dr. Alex Sheardy, Dr. Durgamanjari Arvapalli, Dr. Chevva Harish, Dr. Wendi Zhang, Dr. Bhawna Bagra, Dr. Zuowei Ji, Dr. Kokougan Allado, Dr. Ziyu Yin, Dr. Gayani Pathiraja and my current group members Mengxin Liu, Frank Tukur, Mahsa Azami, Anu Anele, Nagmeh Aboualigaledari, Bukola Adesanmi, Raphael Ayivi, Panesun Tukur, and Lane Webster for their insightful thoughts and support during my research. Also, I would like to thank my friend Dr. Lakshmi Gayitri Chivukula for her extensive support and constant encouragement for years.

Finally, I would express my eternal gratitude to my family, my parents, Jayapalan and Mala (in heaven), and to my sister Shobana Jayapalan for constantly motivating me and lifting me whenever I was down. My dad was my role model in overcoming any difficulties in my life and his confidence and boldness motivated me to go further during my hurdles in this Ph.D. journey. My mother’s blessings and wishes for me to get a doctorate made me stubborn to

continue my Ph.D. despite all the hurdles I faced. My sister helped me in all possible ways and constantly supported me during this research.

TABLE OF CONTENTS

LIST OF TABLES

LIST OF FIGURES

CHAPTER I: INTRODUCTION

The tenability of using hybrid nanoparticles (NPs) using a single component have significantly grown in recent decades with copious inquisitiveness for a variety of multifunctional applications and understand their mechanism, interfacial properties, and activities [1], [2]. Hybrid NPs are a mixture of two or more NPs with different properties combined for a variety of functions, such as to increase the efficiency of one over the other or combine significant advantageous properties in various materials to obtain a synergistic effect or to decrease the adverse effects of one material and make it more compatible for multifunctional applications [3]–[5]. Hybrid nanomaterials comprised of organic and/or inorganic nanostructures with an interfacial region between core and shell for imparting more stability, are extensively employed for numerous applications, such as catalysis, energy storage, and biomedicine for cancer diagnosis and therapy [2], [6]–[8].

The intriguing heterogeneous chemistry behind the formation of these hybrid NPs with physical interactions associated with van der waals and hydrogen bonding electrostatics or non-covalent functionalization with electrostatics or π-π stacking chemistry at the interface of two or more different materials leading to fascinating properties have made researchers inquisitively approach for understanding their mechanism and applications in various fields [9], [10]. By contemplating all these factors, innovating new nanomaterials for multifunctional applications with a deeper understanding of their science would satisfy the necessity of expanding irrepressible requirements in the world [11].

Diverse structures of hybrid nanoparticles, such as core-shell, heterodimer, dot-in-nanotube, nano branches, etc., have been researched for multifunctional applications, such as targeted drug delivery, development of delivery vehicles, environmental, and catalytic

applications [4], [12]. Amongst these different structures, core-shell hybrid NPs are more advantageous with inner core and outer shell materials for exhibiting a surprisingly new property not found in either the core or the shell components with a desirable morphology and tunable pore size [8], [12]. Core-shell NPs possess immensely attractive imputable to their properties, such as being vastly functional with modified properties, by coating with the shell materials to improve biocompatibility, surface functionalization, reduce toxicity, enhance photoluminescence, and increase the functionality, core stability, and dispersibility [13].

A vital factor to be considered while synthesizing these core-shell NPs for catalysis, energy storage, and biomedical applications involves controlling the core size and shell thickness with an efficient strategy in tailoring their properties [14]. Different synthesis techniques, such as physical fabrication strategies, chemical polymerization, self-assembly, sol-gel methods, and biosynthetic techniques, have been researched with a motivation to synthesize core-shell hybrid nanomaterials with no aggregation in a simple manner and without using any organic solvents for their use in biomedical applications [8], [12]. Considering these necessities in mind, a modest new microwave-synthetic approach has been reported in various recent studies with several advantages in synthesizing hybrid NPs rapidly with better control over their morphology, without the organic capping agents to control the aggregation and only water-based in an energy-efficient manner [15]–[17].

Selecting the core and shell materials primarily depends on the corresponding applications of the NPs with a miscellany of chemical and biological attributes [12]. Carbon-based materials, such as carbon nanodots that could be used as shell materials, are safer organic materials with more advantageous biocompatible and easy-to-surface functionalize properties [18]. Transition metal oxides are inexpensive, abundantly available, and reported for their

extensively high catalytic activity, energy storage, and environmental applications with few biomedical uses for using them mainly as core materials [2], [15], [19], [20]. Carbon-based metal oxide core-shell hybrid NPs include the coating of carbon layers on the metal oxide NPs to improve the catalytic properties, biocompatibility, and nontoxicity [13], [21] in the field of optoelectronics, sensing, catalysis, and electrochemical applications [22]–[25].

Cobalt oxide NPs (Co_3O_4 NPs) are a p-type transition metal oxide with two mixed valence states, Co^{2+} and Co^{3+}, due to the tetra- and octahedral sites present in its crystalline structure [26]. Literature has been reported extensively for their use in combination with carbon structures in the applications, such as energy storage, capacitors, rechargeable lithium-ion batteries, and photocatalysts for the degradation of dyes and organic pollutants,[27]–[30] and as biosensor, antimicrobial, antioxidant, and anticancer applications [26], [31]–[34]. CNDs are new, quasi-spherical NPs, rich in functional groups, such as hydroxyl, carboxylate, and epoxy groups, with excellent solubility and significant optical and quantum properties and are being extensively studied as a photocatalytic material for dye degradation studies, biomedical applications, and electrochemistry [18], [35], [36]. Because of their size of less than 10 nm (very small), they serve as an excellent drug delivery vehicle with high fluorescence, biocompatibility, antioxidant, and solubility and are safely used in many cancer diagnoses and therapy (theranostics) applications [37]–[40]. With this extensive literature knowledge, the state-of-the-art advances of cobalt oxide-carbon hybrid nanomaterials and their applications in different areas are discussed further in detail in this introduction.

As a photocatalyst

Water pollution with organic synthetic dyes has been a serious global threat in recent years due to the widespread industrialization to meet the demands of the rapidly expanding

population. Many attempts, such as physical, chemical, and biological methods, are being researched and currently in use to degrade these organic dyes and organic pollutants, which are highly toxic and cancerous to all the living species on the earth, including plants, aquatic species, and animals [41]–[43]. Photocatalytic dye degradation reactions are one of the chemical techniques which are significantly advantageous among the practically available methods as the byproducts released yield non-toxic substances, such as carbon dioxide and water mostly, whereas other processes, such as ozonation and fenton reactions, might not degrade the dye properly and lead to hazardous byproducts [44], [45]. However, the efficiency of photocatalysts primarily relies on prominent attributes, such as suitable band edge position, optimal band gap energy, reduced charge recombination, enhanced charge separation, transfer, and surface-active sites [46]. The unique physicochemical properties of nanomaterials, such as the high surface area to volume ratio, high adsorption capacity, fast kinetics, and porosity, have led to extensive research with increasing interest to solve the challenges with the current techniques, such as cost, recyclability with efficient degradation kinetics, and efficiency [46]–[48].

Particularly, the metal oxide NPs are advantageous with high chemical stability, continuous absorption bands with narrow and emissive spectra, and optimal bandgap for a high generation of electron-hole pairs, which slow down their recombination rate and improve the degradation kinetic rate and efficiency [49]. However, due to their narrow band gap, some metal oxide NPs, such as titania, degrades only in the UV, which might be disadvantageous because UV light are not abundantly available and needs a costly set-up for degrading dyes on a large scale [50]. Amongst the metal oxide NPs, extensive research has been reported on copper oxide, titanium dioxide, and zinc oxides as photocatalysts [49], [51], [52], whereas Co_3O_4 NPs are not widely studied for dye degradation, although they were reported as fascinating catalysts in other

photocatalytic reactions and electrochemistry studies [30], [53]–[56]. Co_3O_4 NPs are one of the metal-oxide semiconductors with direct optical band gap values reported at 1.48 and 2.19 eV, and some nanostructured Co_3O_4 NPs with carbon combinations are reported in the applications, such as photocatalytic reactions, including hydrogen production, wastewater splitting, water oxidation, and gas sensors [27], [29], [53], [54], [57], [58] and dye, pharmaceuticals, and organic pollutants degradations [28], [59]–[62]. CNDs are small-sized (<10 nm) semiconductors with quantum confinement properties and a widened energy gap of up to 3.5 eV with an excellent light-trapping ability for degrading dyes in the visible light region [35], [36], [63]. But carbon-based NPs have some disadvantages, such as cost, commercialization, widened band gap, high efficiency, and could not significantly degrade multiple pollutants at the same time [48]. Current research works have gained much curiosity in achieving a widened absorption of dyes for the photocatalytic degradation reactions from the UV to the visible region using hybrid NPs with novel peculiar properties that are not present in their counterparts [49]. With this concept in mind, the wide band gap of CNDs could be reduced by combining them with metal oxide NPs possessing a narrow band gap in the form of hybrid NPs to increase the photocatalytic degradation efficiency in UV as well as the visible region. Few literature studies were reported using Co_3O_4 and carbon nanomaterial hybrids as photocatalysts, such as EDTA-capped Co_3O_4 NPs [64], Co_3O_4@mesoporous carbon spheres [29], and Co_3O_4 NPs assembled coatings [65]. The study reported with Co_3O_4 NPs assembled coatings possessed some drawbacks, such as there was inefficient control of the size with low absorption in the visible region [65], and the EDTA-capped Co_3O_4 NPs did not possess uniform morphology, and their synthesis was complicated [64], whereas the study with Co_3O_4@mesoporous carbon spheres produced a more efficient catalyst for degrading dyes with simpler biological microwave method [29]. Although

some literature studies reported combinations of Co_3O_4 with carbon nanomaterials, a core-shell design of hybrid NPs with Co_3O_4 NPs and CNDs was not studied till now as a photocatalyst for dye degradation reactions. A core-shell design with a porous matrix for NPs could be advantageous because of their small size, high surface area to volume ratio, high porosity, and adsorbent nature very essential for photocatalytic dye degradations [66]. Hence, based on the efficient photocatalytic dye degradation results by Singh et al. [64] and Akshatha et al. [29], I used Co_3O_4 NPs and CNDs and synthesized a novel core-shell synthesis in chapter II and evaluated their photocatalytic degradation efficiency, kinetics, and mechanism studies. While studying photocatalytic dye degradation studies, some important factors affecting the dye degradation reactions needed to be considered in mind, such as dye concentration, catalysts dosage, irradiation light source used, and charge of the dyes [67], [68].

Electrochemical applications, such as Supercapacitors

With the well-defined literature studies about the Co_3O_4 NPs and CNDs, the Co_3O_4 NPs were primarily used in combination with certain carbon-based materials in many electrochemical applications as a supercapacitor. The spinel nature and mixed oxidation valence states of Co_3O_4 NPs (Co(II) and Co(III)) due to the tetrahedral and octahedral sites in their crystalline structure contributed majorly for the electrochemical studies. Carbon nanomaterials, such as CNDs and graphene quantum dots were also extensively researched owing to their high inter-particle conductivity, chemical stability, enhanced mass-transport efficiencies, and being earth-abundant non-metal and have been reported as excellent conducting catalysts compared to the existing platinum catalyst [69]–[71]. Carbon nano/quantum dots have also been reported as excellent electron acceptors or donors due to quantum confinement properties due to a size of less than 10 nm[18]. The favorable charged sites created by the nitrogen functionalization on the carbon

surface could break the electro-neutrality present on the graphitic carbon framework, resulting in increased catalytic activity compared to the GQDs without nitrogen [72]. Many reported literature studies used Co_3O_4 NPs in combination with carbon-based materials such as nanotubes, nanofibers, etc., with excellent electrochemical properties such as supercapacitors [73]–[75]. These literature findings suggested a clearer idea that Co_3O_4@CNDs hybrid NPs with core-shell structure could be tested as supercapacitors. Hence, the objectives of this chapter III include relating the catalytic properties of Co_3O_4@CNDs hybrid NPs for their applications as a supercapacitor. Cyclic voltammetry was the primary tool used for conducting these electrochemical studies for capacitance calculations. The findings in chapter III provided a clearer understanding of the Co_3O_4@CNDs hybrid NPs for their use in electrochemistry for energy storage applications.

As a biological agent as an antioxidant, bioimaging, and effective specific anticancer material

The Co_3O_4@CNDs were synthesized in consideration that they could be used for biological applications and hence their core-shell size was well controlled using the microwave technique so that their diameter was less than 50 nm, as discussed in Chapter II. The maximum average size of the Co_3O_4@CNDs was only 20 nm, and the synthesis was also easier with a microwave technique, without using any organic solvents such that there were not much toxic for using them in the biological study and that they could easily cross the biological barriers and reach the internal human tissues easily. The morphology was precise with carbon shells, with excellent fluorescence, and hence could be easily functionalized to obtain a better targeting for treating the cancer cells. However, there existed a question behind the optical properties of these core-shell Co_3O_4@CNDs hybrid NPs as it was better than the CNDs and Co_3O_4 NPs while

studying their properties in Chapter IV. Also, how it could be linked to the biological mechanism of action in human normal and cancer cells needs to be understood for their use as a biological agent. Hence, a detailed investigation of their optical and biological properties was studied and explained in Chapter IV, with their biocompatibility and anticancer activity improvement with ligands and drug loading. Core-shell Co_3O_4@CNDs were widely studied in general for their multifunctional biological properties, such as antioxidant, anticancer, and bioimaging agents in cells and are more advantageous due to their multiple significant properties, such as better optical properties including absorbance and fluorescence, faster pharmacokinetics, better efficacy, and improved accumulation of drugs with their porous structure[14], [76]–[79]. Albanelly Soto-Quintero et al. used curcumin to promote the synthesis of silver NPs and their self-Assembly with a thermo-responsive polymer in core-shell nanohybrids and proved their synergistic antioxidant, and antimicrobial in one bioavailable hybrid system. Another study by Mehdi Abedi et al. reported a core-shell imidazoline–functionalized mesoporous silica superparamagnetic hybrid NPs as a potential theranostic agent for controlled delivery of platinum (II) compound and demonstrated its combined cancer chemotherapy and imaging.

With this extensive knowledge from the state of the art of the core-shell NPs for biological applications, the increased fluorescence and better optical properties obtained while studying the synthesized Co_3O_4@CNDs properties in chapter II aroused a curiosity to explore their use in biological applications. The better optical properties, such as enhanced absorbance and fluorescence, and excitation-dependent emission of the Co_3O_4@CNDs, were expected due to the oxygen and nitrogen defect states formed in the core-shell matrix and heterogeneous interfacial layer according to our characterization results, which were not present in their counterparts, CNDs, and Co_3O_4 NPs. The biological properties of Co_3O_4@CNDs were studied in

chapter III, and their role as an antioxidant, bioimaging agent, a specific anticancer drug with excellent targeting efficiency, and an effective vehicle for drug delivery was proved. CNDs are widely researched and demonstrated for their biological properties, such as antioxidant, bioimaging, and anticancer activities, due to their excellent fluorescent properties, in our group by Ji et al. [39], [80], Zhang et al. [38], [81], and Arvapalli et al. [37], [82]. Co_3O_4 NPs are also reported for antioxidant and anticancer properties [26], [32], [83] but are not widely studied because of their inadequate optical properties and metal-oxide toxicity. Hence, by using this ideal core-shell Co_3O_4@CNDs hybrid NPs, the toxicity of Co_3O_4 NPs to normal human cells could be significantly reduced because of the biocompatible carbon shell layers when used for biological studies. Also, the anticancer activity of the Co_3O_4 NPs was expected to combine with that of the CNDs and produce a more significant efficiency in human cancer cells. But still, there might be some toxicity due to the Co_3O_4 NPs in these hybrid NPs towards the human cells, which might be an adverse effect while using this conjugate.

The cancer cells in humans consist of overexpressed receptors, such as growth factors, folate, and transferrin binding proteins on their surface, which could be combined with a specific ligand [84]. This strategy used for anticancer therapy are called active targeting, such that the NPs or drugs could be combined with ligands to specifically attack the overexpressed cancer receptor surfaces and initiate a reaction leading to endocytosis or pinocytosis and then to cancer cell death[85], [86]. An active targeting strategy for killing human cancer cells more effectively and precisely using a ligand-receptor mechanism was reported to be a more efficient treatment technique [87]. The idea of using ligands was proposed in this chapter to increase biocompatibility to reduce the adverse side-effect, the toxicity due to the Co_3O_4 NPs in the Co_3O_4@CNDs and improve the anticancer specificity for lung cancer cells by active cancer

targeting mechanism. Also, these Co_3O_4@CNDs were loaded with an anticancer drug, doxorubicin (DOX), to enhance their anticancer efficiency, and their characteristics as a drug delivery vehicle were also proved. These compelling findings may pave a way for a clearer understanding of the ligand-receptor mechanism and active targeting and provide an idea for better biological properties using core-shell NPs.

In summary, this dissertation study involves synthesizing Co_3O_4@CNDs hybrid NPs with a modest approach and exploring their physicochemical, optoelectronic, and biological properties for multifunctional applications, such as photocatalyst, supercapacitors for energy storage, and biological studies, such as antioxidant, bioimaging, and anti-cancer therapy. The overall goal of this dissertation research was to provide a clearer understanding of the properties of the core-shell Co_3O_4@CNDs hybrid NPs and study their mechanisms involved in the multiple application studies, such as catalysis, energy storage, and biomedical areas. The photocatalytic and biomedical applications investigatory analysis in this dissertation provided a deeper knowledge about the use of these Co_3O_4@CNDs hybrid NPs to the thriving need of society with a vision to serve as an essential tool in satisfying the critical water pollution crisis and specific, safer, and targeted anticancer medicament, thereby catering to the expanding needs of the world.

CHAPTER II: EVALUATION OF UV AND VISIBLE LIGHT RESPONSIVE COBALT OXIDE CARBON Co_3O_4@CND HYBRID NANOPARTICLES AS A PHOTOCATALYST FOR DYE DEGRADATION

Introduction

Rapid industrialization in the evolving lives has become a reason for continuous effluence due to the immediate release of synthetic dyes leading to arduous torments for human health and changes in the ecosystems and the biosphere with a menace to the aquatic biota [88] [89] [90]. Dyes are classified as cationic, for example, methylene blue (MB), and anionic, for example, indigo carmine (IC), based on their chemical structure [91], [92]. Dyes are copiously used in numerous applications, such as textiles, papers, pharmaceuticals, and cosmetics [91]. These dye substances are a significant reason for extensive environmental pollution because of their widespread effluents. Many attempts, such as bio, chemical, and physical means of treatment, have been accomplished to eliminate these dyes in the polluted water [90]. However, these methods cause secondary hazardous pollutants as byproducts, which need to be purified by degrading them further again [91]. Photocatalytic degradation as a chemical method involving a heterogenous catalysis approach is advantageous over other methods. It has many benefits, such as fast degradation at ambient temperatures with non-carcinogenic byproducts, including carbon dioxide and water [91].

First-generation nanoparticle (NP) catalysts, such as TiO_2 NPs, have a wide band gap capable of working with ultraviolet (UV) light sources [93]. The solar light can also be used, which consists of a 4% UV and 43% visible light range [93]. Transition metal oxide (TMO) nanomaterials fall under the semiconductor nanomaterials, which possess significant photo-

activity and are widely studied as photocatalysts [94]. The spinel oxide materials with narrow bandgap, cost-effective NPs promise to overcome some challenges, such as difficulty in charge separation and wider bandgap [93]. Metal oxide-mediated photocatalysis under UV and/or visible light have shown to possess better stability and efficiency than metal-free photocatalysts [94].

Hybrid nanocomposite photocatalysts play a significant role in pollutant removal with improved efficacies by facilitating charge separation, reducing the photogenerated electron-hole recombination pairing, and improving the overall photocatalytic activity [95]. The architectures of hybrid nanocomposites can be designed as core-shell to achieve optimal photocatalytic activity by tuning the heterojunction interfaces, which inhibits electron-hole recombination [89], [94]. Among the reported hybrid nanocomposites, carbon nanocomposites have been recently explored as one of the components to improve photocatalytic reactions by forming heterojunction interfaces [94]. Interacting carbon with other semiconductors causes a change in the intrinsic properties of semiconductor particles, such as band gap, charge carrier density, the lifetime of charge separation, non-radiative paths, and surface properties [96]. Some examples of carbon-based nanocomposites include graphene oxide (GO) or its reduced form (rGO), carbon nanodots (CNDs), carbon quantum dots (CQDs), and carbon spheres that possess favorable optoelectronic properties such as band structures, photosensitizing and inhibiting charge recombination [94]. The use of carbon materials in the shell region is expected to facilitate charge separation by lowering the electron-hole recombination rate during the catalytic process [97]. This is because carbon-based materials could serve as electron donors and/or acceptors to prolong the life of photogenerated electron-hole pairs [95], [96]. Here listed a few carbon-based hybrid nanocomposites recently reported for dye degradation, including core-shell

Fe_3O_4@carbon sphere tailored Co_3O_4 nano chains, $CuFe_2O_4$@g-C_3N_4 core-shell photocatalyst, 3D core-shell-CQDs-Ag_3PO_4-benzoxazine tetrapod's composite system[94], zinc oxide@ GO [98]. Moreover, porous structural layers on the surface of NPs offer excellent adsorption of dye molecules [99].

Cobalt oxide (Co_3O_4) NPs are p-type semiconductor nanomaterials with Co^{3+} and Co^{2+} vacancies. The Co_3O_4 NPs synthesized by the sol-gel process have a narrow optical band gap value of around 2.0 eV, providing an advantage in using visible light for photoactivation [62]. To improve the photocatalytic activity of using Co_3O_4 NPs, several synthetic techniques, such as sol-gel, electron beam decomposition, pulsed laser deposition, and electroless deposition, have been reported for designing Co_3O_4 NPs and core-shell hybrid NPs, [65]. Nevertheless, there is a need to develop methods for synthesizing uniform Co_3O_4 NPs and their core-shell hybrid NPs for highly efficient photocatalysts. The microwave synthesis method was reported as a green process for NP synthesis [100].

In this work, a nanocomposite is designed with a core-shell structure of cobalt oxide and CNDs (Co_3O_4@CNDs). A simple, microwave-assisted synthesis was carried out to obtain the hybrid Co_3O_4@CNDs core-shell NPs, Co_3O_4 NPs, and CNDs. This research aims to explore the physicochemical properties of these NPs as a photocatalyst for a comparison study in dye degradation with visible and UV light sources. Two representative dye molecules, cationic methylene blue (MB) and anionic Indigo Carmine (IC) were tested at different concentrations by measuring the degradation efficiency. Methylene blue (MB) is a photochemically active azo dye that has been reported as a significant hazard to human health with several detrimental environmental effects as it is carcinogenic by its form and non-biodegradable [88]. Indigo Carmine (IC), a vat dye, is considered significantly toxic among the indigoid classification of

dyes. Severe toxicity and carcinogenicity with these dyes have also been reported [101]. We found the hybrid Co_3O_4@CNDs core-shell NPs perform superior to either using the Co_3O_4 or CNDs NPs in the two-dye degradation. The kinetics and reaction mechanism for photocatalytic degradation of the dyes based on experimental results are examined and reported in this research.

Materials and methods

Materials

Chemicals and reagents, including cobalt acetate tetrahydrate (Sigma Aldrich), pure anhydrous ethanol (Sigma Aldrich), 25- 28% ammonium hydroxide solution (Sigma Aldrich), citric acid (ACROS Organics), ethylenediamine (EDA, Fisher Scientific), MB (Fisher Scientific) and IC (Chemsavers), ethylenediamine tetraacetic acid (EDTA, Sigma Aldrich), silver nitrate ($AgNO_3$, Sigma Aldrich), isopropanol (IPA, Fisher Scientific), and hydroquinone (HQ, Fisher Sci) were purchased and used without further purification and are of analytical grade.

Synthesis of Co_3O_4 and Co_3O_4@CNDs hybrid NPs

Figure S2.1 a showed the protocol of a modest microwave approach used for Co_3O_4 NPs synthesis. The reaction is similar to the previously reported method [102]. Briefly, 0.5 g of cobalt acetate tetrahydrate was dissolved in 25 mL of pure anhydrous ethanol and homogeneously mixed for 15 minutes. Then, 2.5 mL of 25-28% ammonia was added slowly and mixed for another 10 minutes to achieve a thorough mixture. The mixture was carefully transferred into a 100 mL round-bottomed (RB) flask and placed in a microwave synthesizer (CEM Corp 908005 Microwave Reactor Discovery System). The reaction was kept in a closed, sealed, pressure-controlled microwave reactor with 300 W, 100 psi, and 150˚C for 30 minutes. The microwave synthesizer was rapidly air-cooled, and a black precipitate solution was collected. The precipitates were purified by centrifugation (using Solvall Legend XFR Floor Model Centrifuge)

at 10000 rpm for 10 minutes, washed, and dried at 80˚C in a muffle furnace. The black-colored particles were collected after drying and labeled as Co_3O_4 NPs for the following characterization and usage.

The procedure of synthesizing CNDs shell to Co_3O_4 NPs followed our previous reports [103] to synthesize Co_3O_4@CNDs hybrid NPs, as shown in the schematic in **Figure S2.1b**. Firstly, 50 mg of Co_3O_4 NPs were weighed in an RB flask, and 1 mL of deionized (DI) water was added. The NPs were dispersed completely using sonication for stirring. Next, 960 mg of citric acid was added to this solution and mixed thoroughly. Then, 1 mL of EDA was slowly added with continuous stirring. All the contents were stirred thoroughly to acquire a uniform homogeneous dispersion. These contents were then transferred into a microwave reactor, and parameters were set at 300 W, 150˚C for 18 minutes, followed by continuous air-cooling and reflux in open conditions. After the reaction, the content was air-cooled immediately. The content after the microwave reaction was dispersed in water and dialyzed using a 1 kDa MWCO membrane for 72 hours. The final NPs product was dried using a freeze drier (Labconco FreeZone 6 Freeze Dryer). The dried product was collected, labeled as Co_3O_4@CNDs hybrid NPs, and stored in the refrigerator for further characterization and usage. The CNDs were obtained using the same synthesis procedure without adding Co_3O_4 NPs, as described in previously reported work [103].

Characterization of the synthesized particles

The Co_3O_4, CNDs, and Co_3O_4@CNDs hybrid NPs were imaged using Transmission electron microscopy (TEM, Carl Zeiss Libra 120 Plus and 2100 Plus, Jeol) to study their morphology along with the Selected Area Electron diffraction (SAED). X-ray powder diffraction (XRD, Agilent Technologies Oxford Gemini) with a copper source, Raman spectroscopy

(Horiba XploRA One Raman Confocal Microscope System), Fourier transform infrared spectroscopy (FTIR, Varian 670 and Shimadzu IR Affinity-1), and X-ray photoelectron spectroscopy (XPS, Thermo Fisher ESCALAB 250 Xi), Malvern zeta sizer (DLS, Malvern Instruments ZEN3600) were used to characterize the crystallinity, elemental, structural morphology and surface charge of the NPs, respectively. UV-Visible (Agilent) and Photoluminescence (PL) spectroscopy (Horiba Spectrophotometer) were used to determine the optical properties of the NPs and for the dye degradation study. The differences in optical, structural, elemental, crystalline, and surface charge properties were identified and compared between Co_3O_4, CNDs, and Co_3O_4@CNDs hybrid NPs.

Procedure for Photocatalytic activity

The photocatalytic activity of the Co_3O_4@CNDs was examined by MB and IC dye degradation studies under irradiation with visible and UV light sources. Before adding the NPs, the absorbance of the dye solution was measured using UV-visible spectroscopy and labeled as "MB only" and "IC only". The Co_3O_4@CNDs (1 mg/mL) were mixed with 10 mL of MB or IC (20 mg L^{-1}) in a DI water solution in a beaker. The dye solution was equilibrated for 20 minutes with the NPs at 1200 rpm in the dark, and the samples collected were labeled as "Eqb time," and an absorption spectrum was measured. Then the dye solution with NPs was treated with visible light (Power: 500mW, wavelength 447 nm, 5 mm diameter, Big Laser Co.,) and a UV light source (Power: 500mW, wavelength 365 nm). The same procedure was repeated with MB or IC dye concentration at 50 mg L^{-1}. The dye solution with NPs at time intervals after the irradiation with the light source was collected (100 µL), filtered, diluted to 1 mL, and analyzed by reading their absorbances at the maximum absorption wavelength of 664 for MB and 610 nm for IC using UV-Visible spectroscopy [104], [105]. All the collected dye with NPs solution was

centrifuged at 10000 rpm for 10 minutes before taking the measurements. Control experiments were performed using CNDs and Co_3O_4 NPs alone for comparison. Also, the same experiments were performed in the dark (without light) to compare their photodegradation and without any NPs to see if the dye solution degrades by itself. Every experiment was repeated three times, and the standard error was calculated. The extent of dye degradation or decolorization was calculated using the following **Eq. 1**.,

$$\text{Degradation efficiency}(\%) = 100\times \frac{A_0 - A_t}{A_0} = 100\times \frac{C_0 - C_t}{C_0} \qquad (1)$$

where A_t and A_0 are the absorbance of the dye with catalysts, and C_t and C_0 are the concentrations of dye solution with catalysts at time t and 0 minutes, respectively [104].

The reactive species scavenging experiment was carried out by degradation of MB dye under visible and UV light irradiation with active radicals' scavengers, such as 1 mM of HQ, EDTA, and $AgNO_3$, and 5 mL of IPA, which were added to 20 mg L^{-1} MB dye solution along with NPs [36], [105].

Results and Discussion

Materials characterization

Different color NPs, such as black, brown, and blackish-brown representing Co_3O_4, CNDs, and Co_3O_4@CNDs hybrid NPs, were obtained from the synthesis (see **Figure S2.2**). A summary of different reported syntheses, parameters used, and the respective size of Co_3O_4 NPs is listed in **table S2.1**.

The morphology (size and shape) of the NPs was analyzed from the TEM images, **Figures 1a** and **b** showing Co_3O_4 NPs and Co_3O_4@CNDs. In **Figure 1b,** the darker shades are surrounded by lighter regions (carbon) in every NP, indicating the core-shell morphology of the hybrid NPs. The morphology of CNDs is shown in **Figure S2.3**.

Figure 1. TEM images of a. Co_3O_4 NPs, b. Co_3O_4@CNDs; HRTEM images of c. Co_3O_4 and d. Co_3O_4@CNDs

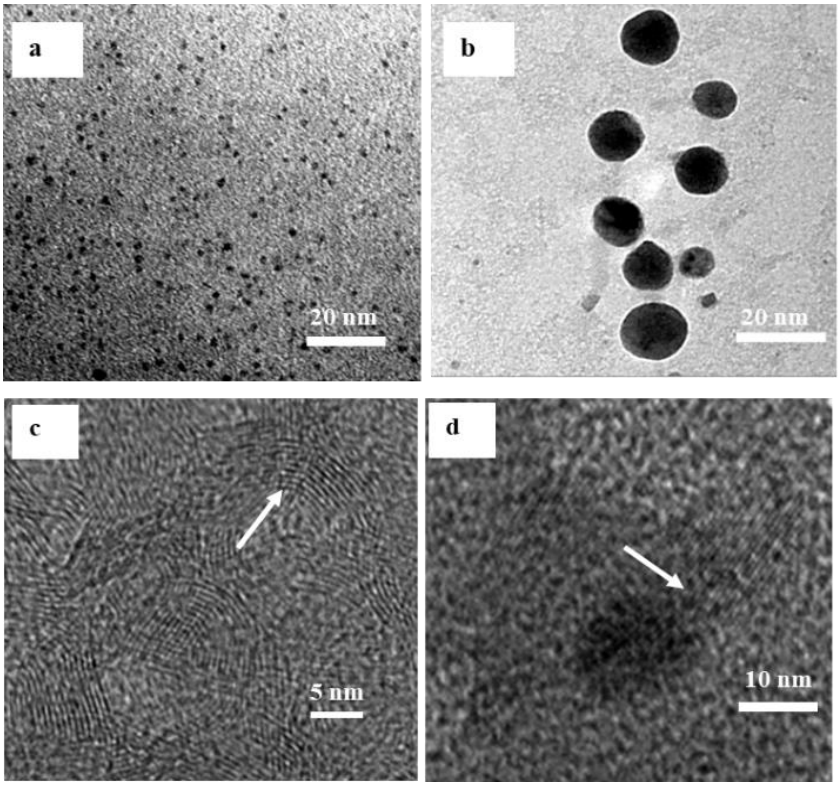

The morphology of CNDs was consistent with the previously reported work in our group (with a size of 5.5±2.5 nm) [103]. All these synthesized NPs were spherical and uniform, with no aggregation. The average size for Co_3O_4 NPs are 3±1 nm, whereas 16.65±3.7 nm for Co_3O_4@CNDs (**Figure S2.4a and c)**. The SAED patterns of Co_3O_4 NPs **(Figure S2.4b)** showed alternative dark and bright rings, confirming their high crystallinity. The diffraction patterns of the Co_3O_4@CNDs **(Figure S2.4d)** showed some planes of Co_3O_4, including (111), (220), (311), and (422), with very few spots, and have a low level of crystallinity. The high-resolution TEM (HRTEM) image of Co_3O_4 **(Figure 1c)** and Co_3O_4@CNDs hybrid NP **(Figure 1d)** possessed lattice fringes supporting their respective crystallinity as in the SAED patterns, with an

interplanar distance of 3.9 and 2.5 Å, respectively. **Figure 1d** displays a core-shell morphology of the Co_3O_4@CNDs hybrid NP in an enlarged view at a scale of 10 nm.

The XRD patterns of Co_3O_4, CNDs, and Co_3O_4@CNDs hybrid NPs are shown in **Figure 2**. For the pure Co_3O_4 NPs, the XRD profile displayed high crystallinity, suggesting their cubic spinel structure [53], [73], corroborating with the JCPDS 42-1467. Diffraction angles at the 2Θ of 17°, 29°, 33°, 37°, 43.6°, 51°, 55°, 59°, and 68° representing the crystalline planes (111), (002) (220), (311), (400), (422), (511), (333), and (440), respectively of the Co_3O_4 NPs [57], [65]. The XRD spectrum of the CNDs showed a strong peak (002) at 21.8°, corresponding to the graphitic planes, implying that they are amorphous in nature [106], [107]. The XRD profiling at (111), (311), (222), and (440), owing to the presence of trace amounts of Co_3O_4, and the carbon at 21.8° with the plane (002) [56], [107], [108]. The Co_3O_4@CNDs hybrid NPs are mostly amorphous as they resemble CNDs spectra, due to the carbon shells. **Table S2.2** represented the XRD comparison for 2Θ and planes of Co_3O_4 NPs, CNDs, and Co_3O_4@CNDs.

Figure 2. XRD of Co_3O_4@CNDs, CNDs, and Co_3O_4 NPs

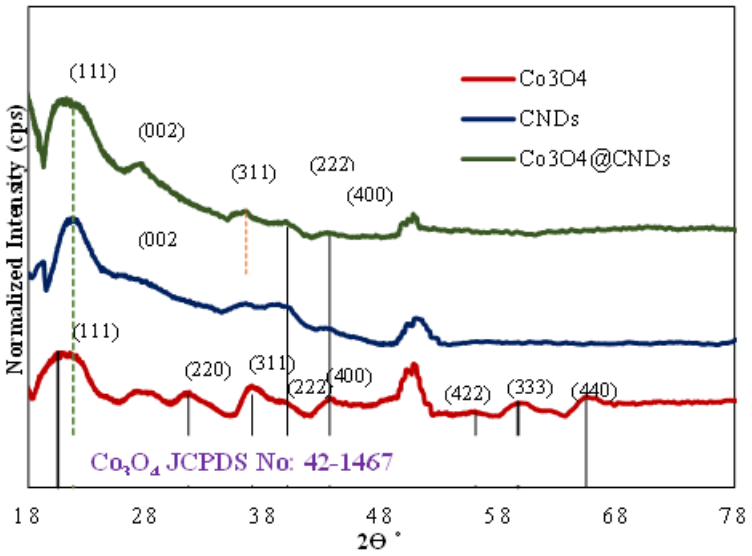

Figure S2.5 showed the FTIR spectra of Co_3O_4, CNDs, and Co_3O_4@CNDs hybrid NPs. FTIR spectra of Co_3O_4 NPs showed stretching vibrational peaks observed at 570 and 660 cm^{-1}, specific to strong absorptions of Co-O, precisely the octal Co-(III)-O and tetrahedral coordinated Co-(II)-O, of the Co_3O_4 NPs [109], [110]. The peaks observed at 1461 and 1590 cm^{-1} were characteristic of the aliphatic alkyl and amine groups, which was expected due to the ethanol groups or unreacted ammonia residues from the synthesis of Co_3O_4 NPs [100], [111]. FTIR spectra of Co_3O_4@CNDs hybrid NPs r revealed broad peaks of 3100–3400 and 2900–3050 cm^{-1}, attributing to the -O-H and the -C-H, respectively, which contributes to their stability [112], [113]. The double bond region peaks observed at 1542 and 1635 cm^{-1} were ascribed to the -C=C- and -C=O- in Co_3O_4@CNDs hybrid NPs [112], [113]. The Co_3O_4@CNDs contain Co_3O_4 peaks at 570 and 660 cm^{-1}, confirming their presence [109], [110].

Raman spectra **(Figure S2.6)** displayed peaks at 465, 517, and 670 cm^{-1} attributing to the E_g, F_{2g}, and A_{1g} modes of Co_3O_4 NPs [62], [65], [110]. Additionally, the Raman spectra contained peaks at 1341 and 1565 cm^{-1}, characteristic of the D and G bands of the CNDs [53]. The D bands' intensity ratio to G-bands (I_D/I_G) was 0.99 for the Co_3O_4@CNDs hybrid NPs, characteristic of the graphitic layers in the carbon nanomaterials [108]. This ratio was 0.97 for pure CNDs. The increased intensity ratio in the hybrid NPs infers that the graphitic carbon structure is distorted [53], [113] because of Co_3O_4 and defect states created in the structure of the Co_3O_4@CNDs.

The XPS spectra of Co_3O_4, CNDs, and Co_3O_4@CNDs hybrid NPs are shown in **Figure S2.7**. XPS spectra of Co_3O_4@CNDs showed the presence of C (284.6 eV), N (399.1 eV), O (531.1 eV), and Co (780.7 eV), in the Co_3O_4@CNDs hybrid NPs, whereas that of CNDs showed C, N, and O, and the Co_3O_4 NPs showed the presence of Co, C, and O. The deconvolution

spectra of the Co_3O_4 NPs are shown in **Figure S2.8a-c**. and that of Co_3O_4@CNDs hybrid NPs are shown in **Figure 3a-d**. The HR C1s core spectra of Co_3O_4 NPs **(Figure S2.8a)** and

Figure 3. HRXPS of a. C 1s, b. O 1s, c. N1s, and d. Co 2p in Co_3O_4@CNDs hybrid NPs

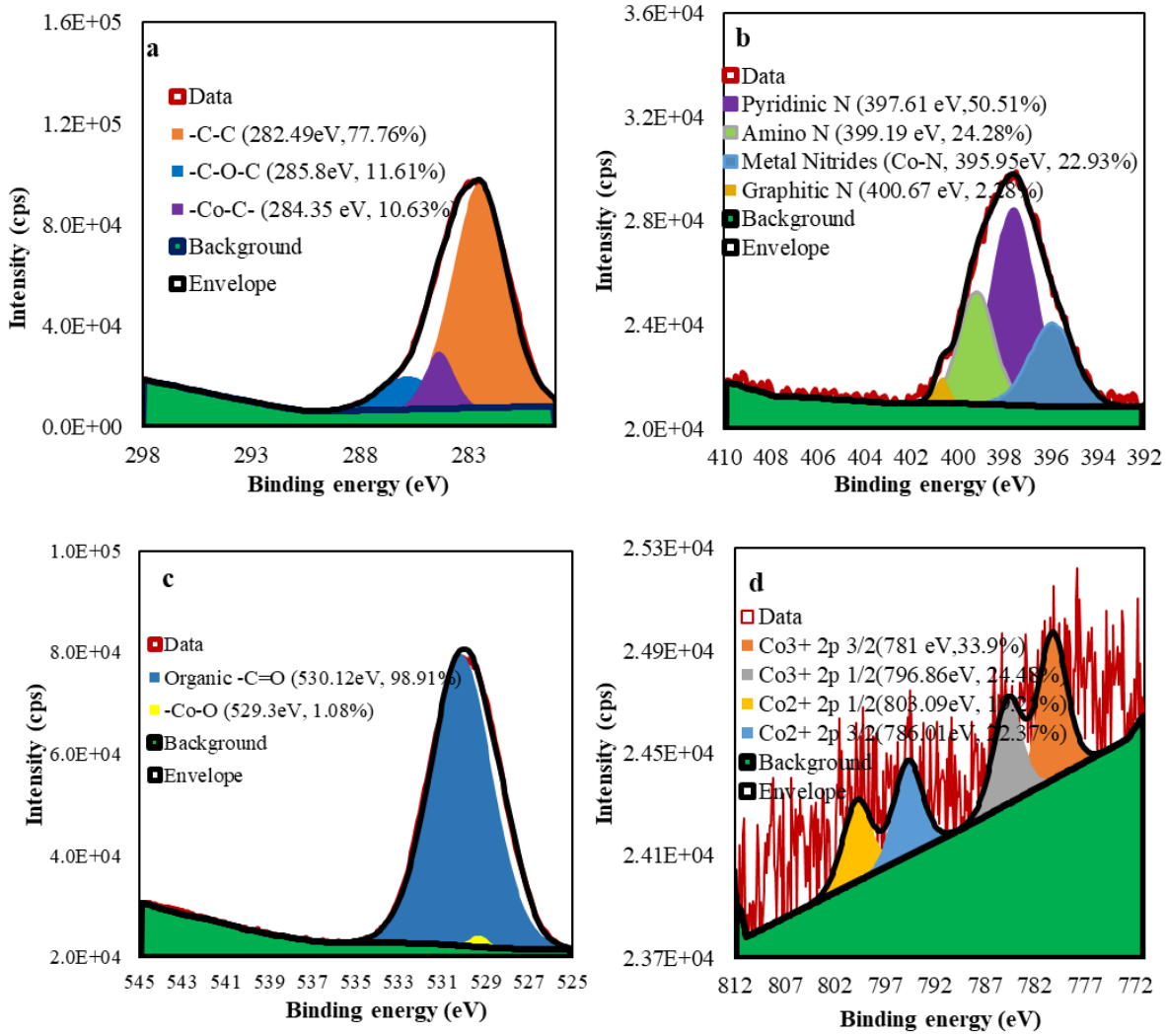

Co_3O_4@CNDs hybrid NPs **(Figure 3a)** included peaks at 283, 285, and 287 eV attributed to the -Co-C, sp^2 and sp^3 hybridized -C-C, and the -C-O-C groups due to oxidation on carbon surfaces, respectively [108], [114], [115]. The graphitic -C-C represented the basal carbon surface [108]. The N1s spectra **(Figure 3b)** revealed the prominent pyrrolic-N at 399 eV, and the pyridinic and graphitic-N formed at 398 and 401 eV, respectively [53], [116], which was due to -C-N bonding

formed from precursors, and the metal nitrides at 396 eV, formed because of the hybridization [114]. The HR O1s spectra **(Figure S2.8b and Figure 3c)** showed peaks at 529.9 and 531.3 eV due to the -Co-O and -C=O bonding in the Co_3O_4 NPs [53], [65]. The deconvoluted Co2p spectra **(Figure S2.8c and Figure 3d)** comprised peaks corresponding to the $Co2p_{3/2}$ (781.0 eV) and $Co2p_{1/2}$ (796.9 eV) with their respective satellite peaks at 786.0 and 803.1 eV confirmed that they possessed both Co^{2+} and Co^{3+} vacancies in the Co_3O_4 [65], [109]. The HRXPS of O1s **(Figure 3c)** and Co2p spectra **(Figure 3d)** also confirmed that the synthesized NPs contain Co_3O_4 as they resembled the deconvoluted peaks in Co_3O_4 NPs **(Figure S2.8b and c)** were observed. The Co-C- and Co-O- peak intensities are significantly reduced in the Co_3O_4@CNDs because the Co_3O_4 NPs are covered by carbon shells with hybridization. The Co atoms were expected to be present in the inner core of the hybrid NPs as they were detected only in trace amounts (0.93%). The more detailed XPS interpretation data comparison of the constituents of the NPs are shown in **Table S2.3**.

Optical absorption and Bandgap investigation analysis

The optical properties of Co_3O_4, CNDs, and Co_3O_4@CNDs hybrid NPs were carried out by UV-Visible, and PL spectra and are presented in **Figures 4a and b**. The absorbance and PL properties of the core-shell materials are responsible for the changes in the impurity levels, energy band structure, localized crystalline defects, exciton relaxations, lattice vibrations, and specific magnetic excitations [91]. UV-Visible comparison of Co_3O_4@CNDs, CNDs, and Co_3O_4 NPs in **Figure 4a** showed that Co_3O_4@CNDs hybrid NPs and CNDs had two peaks at 260 and 350 nm ascribed to the π–π^* transition of the -C=C- bond in the carbon core and n–π^* transition of the -C=O- corresponding to the molecular state transitions, respectively [103], [117]. No significant broad absorption peaks were observed in the Co_3O_4 NPs owing to the quantum

confinement effects [57]. In **Figure 4b**, the observed PL effect in the Co_3O_4@CNDs hybrid NPs was higher than the CNDs. An emission peak at 450 nm was observed when excited at 360 nm wavelength in Co_3O_4@CNDs and CNDs [103]. The slight PL emission for Co_3O_4 NPs at these wavelengths was attributed to intrinsic and extrinsic surface defect states, which might be expected from the impurities and deficiency levels created during the synthesis [57]. The absorbance and PL enhancement were observed for the core-shell Co_3O_4@CNDs than the CNDs which might be expected due to the synergistic effect obtained from the hybridization. The stronger PL intensity of the Co_3O_4@CNDs might be due to larger oxygen defects or vacancies in their core-shell structures, and this can enhance photocatalytic activity [118].

The optical band gap energy (E_g) of the synthesized NPs was determined by using Tauc's relation with the following **Eq. 2**.

$$(\alpha h\upsilon)^n = A\times(h\upsilon - E_g) \quad (2)$$

Where A, α, hυ, and E_g are the proportionality constant, the absorption coefficient, the photon energy, and the band gap of the synthesized nanomaterials, whereas n denotes the electronic transition (or) optical transition values [112]. By linear extrapolating the plots of $(\alpha h\upsilon)^2$ vs. hυ **(Figure 4c)**, the band gap was found to be 1.55 and 1.77, 2.9 and 2.51 eV for the Co_3O_4 NPs, CNDs, and Co_3O_4@CNDs hybrid NPs, respectively. The band gap of Co_3O_4 NPs values calculated as 1.55 and 1.77 eV was ascribed due to Co^{3+} and Co^{2+} vacancies in their structure on the lower and higher energy side regions [65]. The reduction in the band gap of Co_3O_4@CNDs hybrid NPs than the pure CNDs was due to the heterojunction formation, which might contribute to improved photoactivity [119]. The obtained ideal band gap of Co_3O_4@CNDs NPs could slow down the recombination of photogenerated electron-hole pairs by the synergistic effect and overlap of emission bands in the PL spectra of CNDs and Co_3O_4, which can excite the

NPs faster during photocatalytic reactions [109]. This band gap of Co_3O_4@CND NPs, lesser than CNDs and more than Co_3O_4 NPs, making it a robust photocatalyst to be effective in both visible and UV regions.

Figure 4. a. UV-Visible and b. PL spectroscopic data, and c. Tauc's plot of Co_3O_4@CNDs, CNDs, and Co_3O_4 NPs

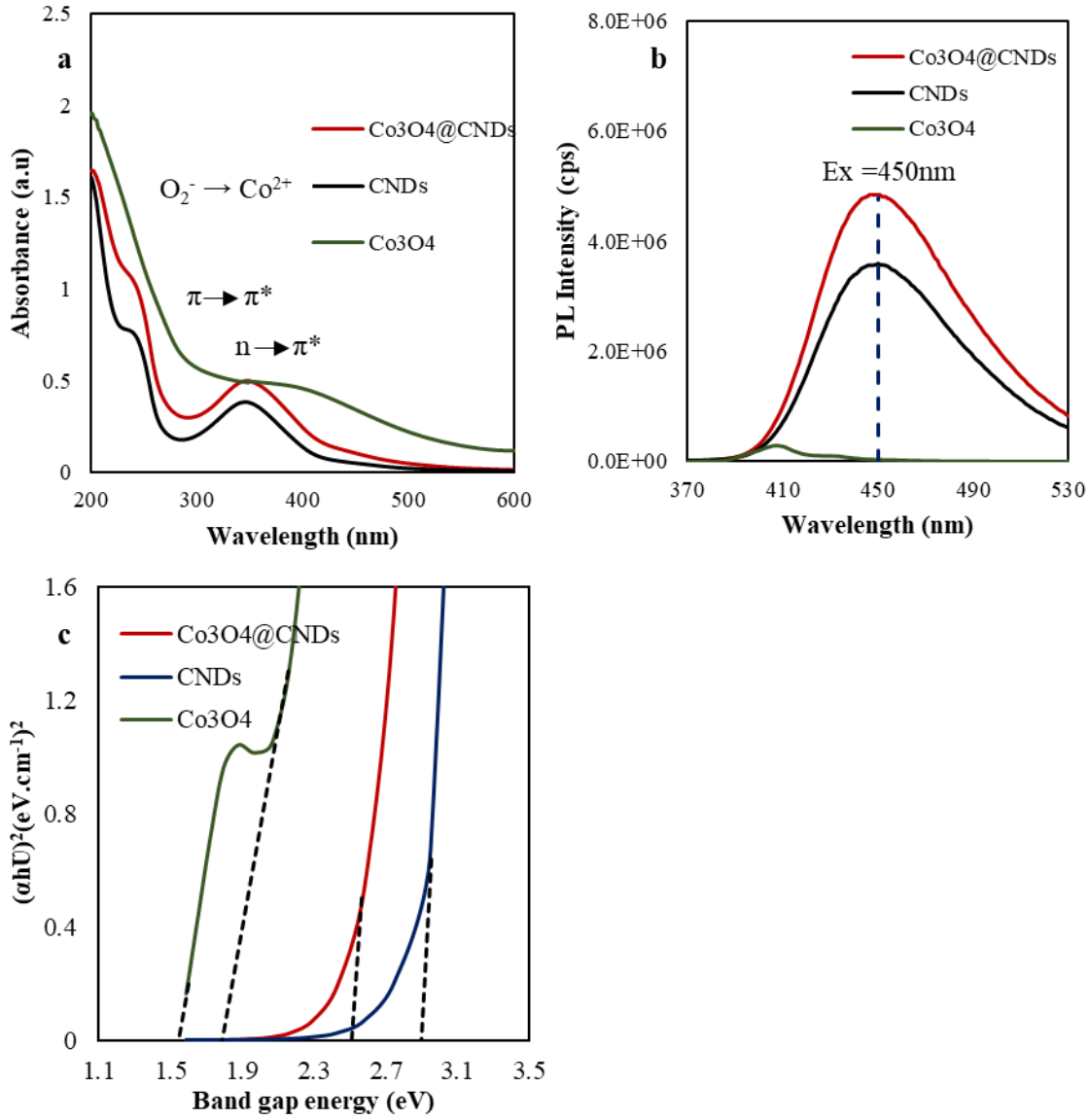

Figure S2.9, with particle size and zeta potential of Co_3O_4@CNDs, provided an understanding of the surface charge determination of NPs. The zeta potential of Co_3O_4@CNDs,

CNDs, and Co_3O_4 NPs are -5.6, -12.1, and +17.6 mV, respectively. The zeta potential of the Co_3O_4@CNDs hybrid NPs is close to zero and aggregates faster, a common attribute of their hybridized morphology. Also, they possessed a negative charge due to the CND shell layer on them, which was more negative in their pure form.

Dye degradation studies

Parameter optimizations are an essential investigation to get an overall concluding idea about the effective degradation of dye over the catalyst surface [120]. The UV-visible spectrophotometer studied the dye degradation activity, and time-dependent absorption spectra were obtained from the measurements of MB and IC with λ_{max}, 664, and 610 nm, respectively. Experiments were carried out three times, and the average and standard errors were calculated. The absorbance spectra of MB and IC solution from 200 to 800 nm in both visible and UV light irradiation are shown in **Figures S2.10 to S2.17a, b, and c** for all the NPs at all the time points and different dye concentrations. The intensity of absorption plots gradually decreased with increasing the irradiation time in all the dye degradation studies for Co_3O_4@CNDs, CNDs, and Co_3O_4 NPs.

Effect of the wavelength of light

The wavelength of the irradiation source is one of the critical parameters that affect dye degradation in aqueous solutions [44]. The artificial UV irradiation source is commonly more reproducible than sunlight or visible light and brings higher efficiency in degrading organic dyes [120]. Due to the hybridization and optimal band gap obtained, our work studied dye degradation for Co_3O_4@CNDs hybrid NPs in both the visible and UV light regions (with two different light source wavelengths).

Effect of different photocatalysts

Photocatalytic activity of various catalysts changes with the variations in the lattice mismatch, and their surface that contains impurities on them impacts the adsorption behavior of a dye [120]. It also influences the lifetime and recombination rate of electron-hole pairs [120]. The higher surface area is also a defining factor in some photodegradation reactions [121]. Many adsorbed organic molecules with high surface area favor the reaction rate [91], [122]. The electron-hole recombination also varies depending on the particle size, influencing the reaction rate [120], [123]. We compared the dye degradation activities of the photocatalysts, such as Co_3O_4@CNDs, CNDs, and Co_3O_4 NPs. The difference in their photocatalytic activity observed was also due to the particle size and surface charge variation in these three NPs, as confirmed by the TEM and zeta potential characterizations.

Effect of dye concentration

The optimization of dye concentration is another vital factor while studying photocatalytic degradation. The rate of dye degradation primarily alters with the dye concentration [91], [120]. The effect of the dye degradation study for Co_3O_4@CNDs, CNDs, and Co_3O_4 at two different concentrations (20 and 50 mg L^{-1}) of MB and IC dyes are described in the following **Figures 5 and S2.18,** respectively. With an increase in dye concentration, the photocatalytic degradation efficiency decreased, as expected from the literature [91].

The degradation rate is determined by the possibility of OH^- radicals' generation on the catalyst's surface and OH^- radicals reacting with dye molecules [124]. When the dye concentration increases, many dye molecules exist for energy transfer leading to a reduction in the efficiency of the catalyst and its reaction rate [120], [125]. Also, the necessity of the catalyst surface required for the degradation increases simultaneously as the active sites are covered

faster by increasing the degradation time during the process [125]. The decrease in degradation rate with the increase in dye concentration was expected to occur for various reasons, such as: 1. As the dye's concentration increases, dye molecules are adsorbed on the catalyst's surface, with a substantial quantity of UV rather than Co_3O_4@CNDs hybrid NPs. Hence, the light penetration to the catalyst's surface decreases [88], [91], [120]. 2. The hydroxyl radical's generation decreases since dyes occupy the active sites [120], [126]. 3. The adsorbed dye on the catalyst surface inhibits the effect of adsorbed molecules with the photoinduced positive holes since there is no direct contact with the semiconductor [44], [120], [127].

Visible light-induced dye degradation study. The MB and IC dye degradation of Co_3O_4@CNDs, CNDs, and Co_3O_4 NPs under visible and UV light sources are shown in **Figure 5 and S2.18** at two different dye concentrations, respectively. The absorbance plots of the visible light-based dye degradation performances of the nanomaterials (i.e., Co_3O_4@CNDs, CNDs, and Co_3O_4) with MB and IC dyes are shown in **Figures S2.10 and 11, and 14 and 15a, b, and c** respectively with two different dye concentrations (20 and 50 mg L^{-1}). The decrease in the degradation of MB and IC dye with the Co_3O_4@CNDs, CNDs, and Co_3O_4 NPs under visible light was calculated by measuring their absorbances at regular time intervals. The C_t/C_0 vs. time plots showed a gradual reduction in absorbance with an increase in irradiation time until 75 minutes, and then the decrease was not observed from 75 to 120 minutes **(Figures 5a and b)**. The plots showed the dependence of C_t/C_0 versus the irradiation time from 0 to 120 minutes with 20 mg L^{-1} a. MB and b. IC dye degradation in visible light. The 71% MB dye degradation of Co_3O_4@CNDs nanocomposite was observed after 75 mins of degradation reaction, but at the same time, the Co_3O_4 NPs showed only 56% of dye degradation. The dye degradation percentage vs. reaction time graph demonstrated less catalytic activity of Co_3O_4 NPs and CNDs

against the MB and IC dye degradation compared with Co_3O_4@CNDs nanocomposite. The same trend was obtained in the case of IC dye degradation also. The 62.9% IC dye degradation of Co_3O_4@CNDs nanocomposite after 75 mins of reaction was observed, but at the same time, the Co_3O_4 NPs showed only 45.2% of degradation **(Figure 5b)**. The same trend was obtained in the case of 50 mg L^{-1} MB and IC dye degradation also, as shown in **Figures S2.18a and b**. An increase in the efficiency to 67% in the MB dye degradation with Co_3O_4@CNDs was observed compared to the Co_3O_4 NPs at the same time **(Figure S2.18a)**, and 61.5% of IC dye was degraded within 75 minutes with Co_3O_4@CNDs was observed compared to CNDs and Co_3O_4 NPs, 59.3% and 51.9%, respectively **(Figure S2.18b)**. But comparatively, 20 mg L^{-1} MB and IC dyes were degraded to the maximum extent than the 50 mg L^{-1} dyes with all the NPs.

UV light-induced dye degradation study. The UV irradiation source's energy (~3.39 eV) is higher than the band gap energy of the NPs used. Hence, the drawback of electron-hole recombination is avoided when a UV source is used [120]. The wavelength of the light source can influence the effectiveness of photodegradation [44]. If the irradiation wavelength is shorter, it can encourage the electron-hole formation and increase the catalyst's efficiency [120]. The UV light-based dye degradation performances of the nanomaterials (i.e., Co_3O_4@CNDs, CNDs, and Co_3O_4) were evaluated with the photodegradation of MB and IC dye as indicated in **Figures S2.11 and S2.12, and S2.15 and S2.16a, b, and c** respectively with two different dye concentrations (20 and 50 mg L^{-1}). The results showed a gradual reduction in absorbance with an increase in irradiation time until 40 minutes, and then the decrease was not observed after 40 to 60 minutes **(Figures 5c and d)**. When the UV light source was irradiated, about 62% of MB dye was degraded at 40 minutes with Co_3O_4@CNDs hybrid NPs, whereas, for CNDs and Co_3O_4 NPs, the degradation was 52% and 42%, respectively **(Figure 5c)**. The same trend was obtained

in the case of IC dye degradation. About 59.2% of IC dye was degraded within 40 minutes with Co_3O_4@CNDs hybrid NPs, whereas, for CNDs and Co_3O_4 NPs, the degradation was 50.3% and

Figure 5. C_t/C_0 vs. time plots of 1mg/mL of Co_3O_4@CNDs, CNDs, and Co_3O_4 NPs with 20 mgL^{-1} a. MB and b. IC dye degradation in visible light, c. MB and d. IC in the presence of UV light

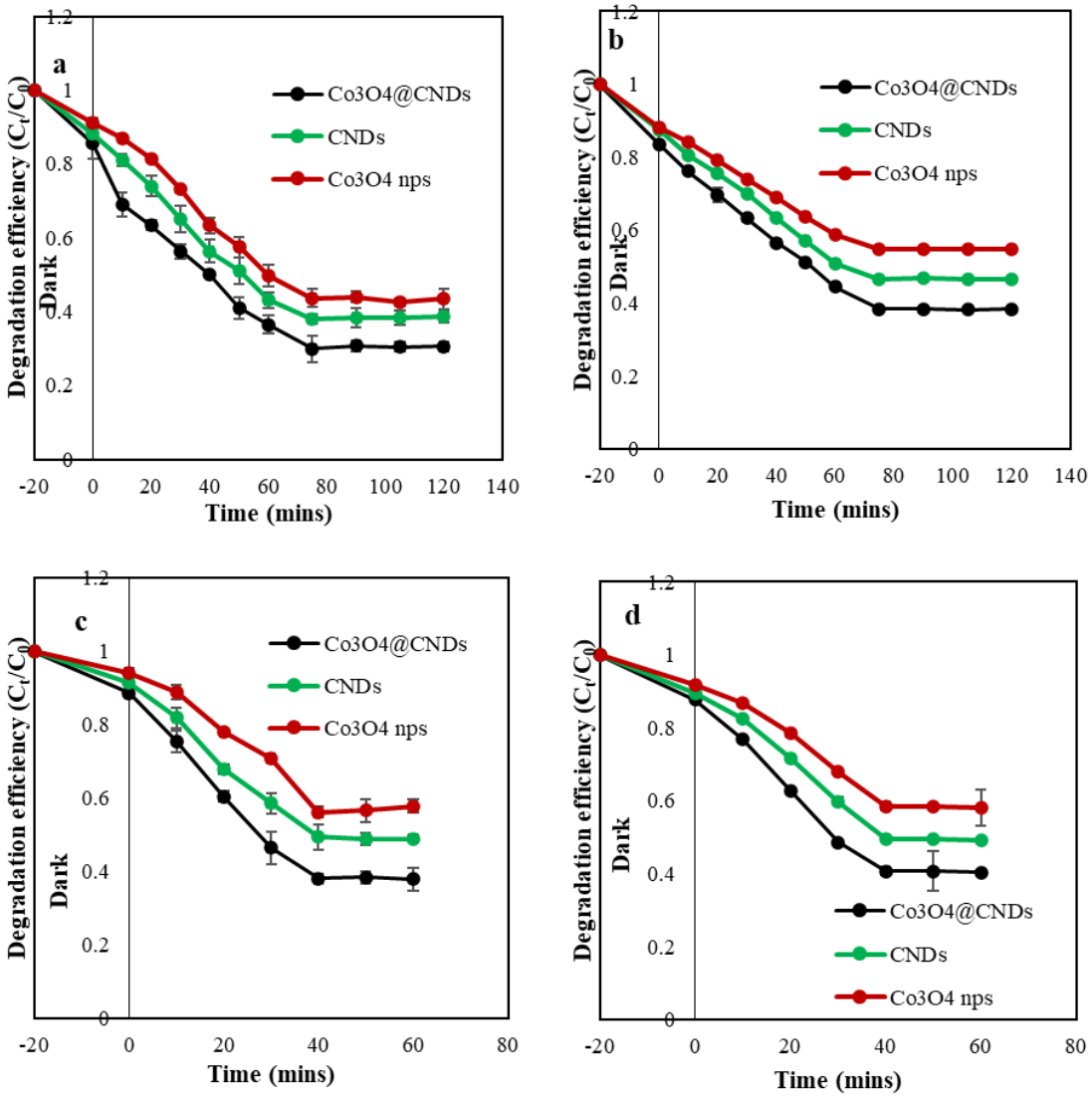

43.5% at 40 minutes, respectively **(Figure 5d)**. When the UV light source was irradiated with 50 mg L^{-1} MB dye, about 59% of MB dye was degraded within 40 minutes with Co_3O_4@CNDs

hybrid NPs, whereas, for CNDs and Co_3O_4 NPs, it was 50% and 40%, respectively **(Figure S2.18c)**. About 54.5% of IC dye was degraded within 40 minutes with Co_3O_4@CNDs hybrid NPs, whereas CNDs and Co_3O_4 NPs were 45.3% and 40.4% at 40 minutes, respectively **(Figure S2.18d)**. UV light shields the high dye concentration, thereby reducing the photons' path length entering the solution [91]. Also, photocatalytic activity for CND-containing hybrid NPs is much higher than pure Co_3O_4, confirming the synergetic effect of CNDs and Co_3O_4.

Tang et al. mentioned that the enhancement in photocatalytic activity of the carbon nanomaterial decorated composites enhances the separation of electron-hole pairs in Co_3O_4 due to the electrons with high mobility in carbon [128]. Our results revealed that a high dye concentration can inhibit the reactions between dye molecules and reactive radicals due to the NPs. The high dye concentration also impedes light penetration, and only some photons can reach the photocatalyst surface [91]. Hence, the release of charge carriers and reactive radicals in the dye molecules are reduced simultaneously, thereby decreasing the photodegradation efficiency [91].

Under dark

In the dark conditions, the degradation of the Co_3O_4@CNDs, CNDs, and Co_3O_4 NPs was studied for up to 120 mins using two different dye concentrations, 20 and 50 mg L^{-1}, for both the MB and IC dyes. All the control plots and their respective comparison plots are shown in appendix, **Figures S2.20- S2.25**. The absorbance plots, along with their respective degradation percentage plots versus time, in the dark, are shown along with the comparison of the light-based values for the Co_3O_4@CNDs, CNDs, and Co_3O_4 NPs, for both the MB and IC dyes in two different concentrations, 20 and 50 mg L^{-1}. During dark conditions, only physical adsorption occurs between the dye and NPs, and no degradation was observed with the increase in time.

From the plots (**Figures S2.20 to S2.23**), we observed that after attaining 20 minutes (the "Eqb time"), the degradation efficiency did not change, and the absorbance remained almost the same. These plots give a clear idea that only adsorption occurs in the dark condition, and the degradations were based on the light only, suggesting that the NPs undergo excitation in the presence of light and go through photocatalytic reactions for degrading the dyes. Without any NPs, there was no decrease in the concentration of MB, and IC was detected under UV/Visible irradiation (**Figure S2.24- 25**). At the same time points of UV/Visible based degradations, the blank test in the dark showed that there is not any degradation of MB and IC under UV and visible light radiation when the photocatalyst is not present.

Influence of time and the release of byproducts

The irradiation time is another crucial influencing factor in photocatalytic degradation processes [68]. The MB and IC dye absorbance was degraded to a maximum at 75 and 40 minutes, with visible and UV lights, respectively, after which no absorbance decrease was observed in both light illumination cases. The time points were extended to 120 and 60 in visible, and UV radiation and absorbance changes were observed. A rapid increase in degradation was observed in the first 75 and 40 minutes of reaction time in visible and UV light, as seen in **Figures 5 and S2.17**. After which, the degradation rate did not change until 120 and 60 min in visible and UV light, as no further degradation was observed. Since the absorption peak does not shift, MB can be metabolized into a single aromatic molecule with no more benzene rings, or it means that MB is degraded to maximum using these catalysts at 75 minutes, and hence there is no more degradation.

During the extended time points, there were no changes for the absorbance values at the absorbance maximum, 664 nm of MB in Co_3O_4@CNDs, CNDs, and Co_3O_4 NPs. Until 75

minutes in the visible light degradation and until 40 minutes in the UV light degradation, abundant hydroxyl radicals were available, so there was an increased rate of degradation.

Figure 6. FTIR of Co_3O_4@CNDs in the a. and b. MB and c. and d. IC dye degradation at the maximum degradation time of 120 minutes in the presence of visible light

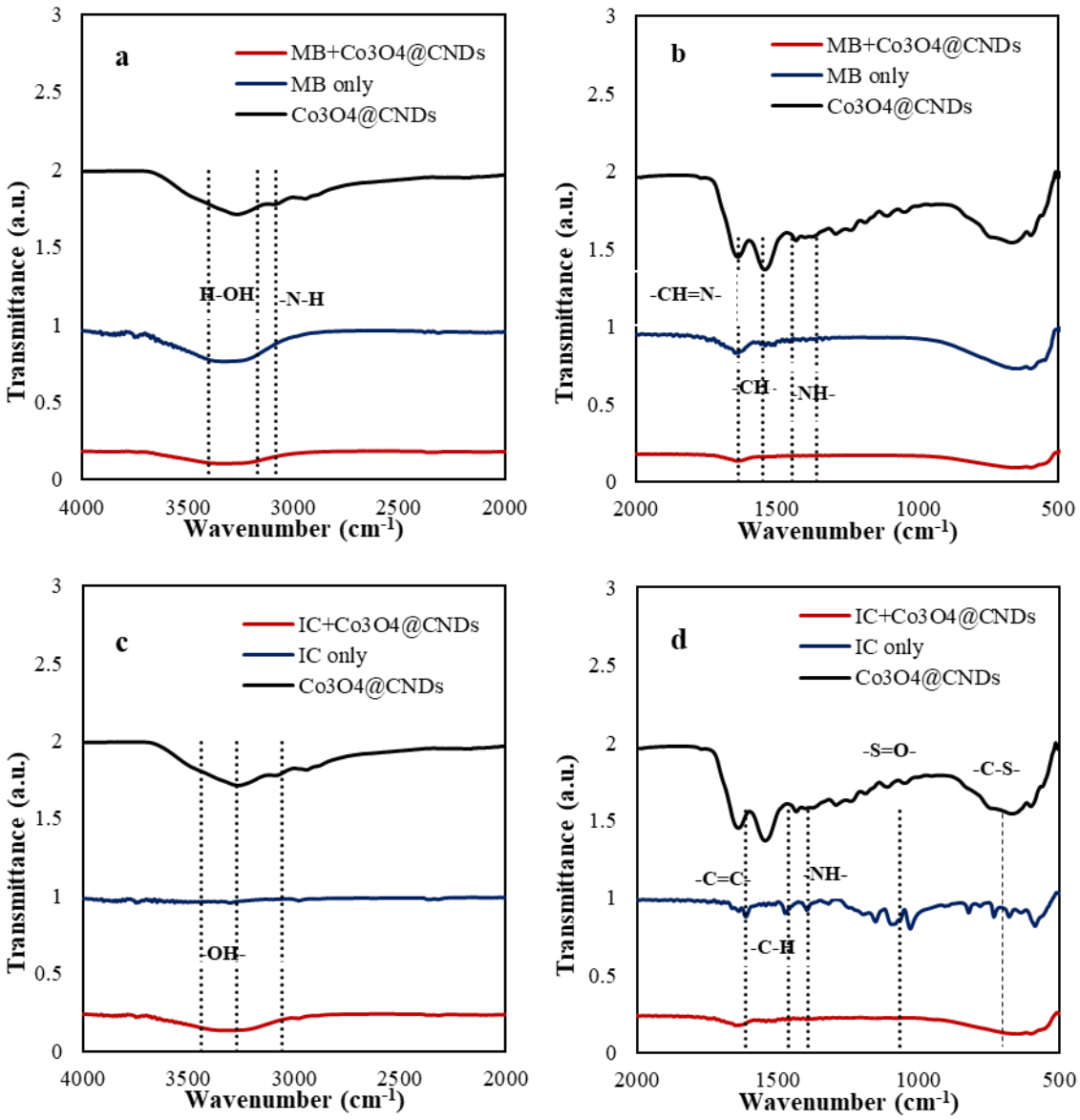

With the increase in time, all the hydroxyl radicals generated from the dyes are consumed, thereby decreasing the reaction rate of the catalyst. The extent of dye degradation was confirmed by observing the changes in the structure of the MB dye through FTIR spectroscopy

(Figure 6). The graphs were divided into two segments from 500 to 2000 cm^{-1} and from 2000 to 4000 cm^{-1} to show maximum clarity in the functional group changes in the MB and IC dyes **(Figures 6a, b, c, and d)**. Comparing the MB and IC structures before and after degradation at 75 minutes with visible light showed some significant observable changes in their structures, indicating the degradation extent.

The FTIR spectroscopy of MB after degradation compared with that of unreacted MB was measured from 500 to 4000 cm^{-1} **(Figures 6a and b)**. The FTIR data showed highly complicated vibrational modes due to its chemical structure, with the characteristic peaks at wavenumbers 1365 cm^{-1} due to its prominent aromatic amino group and aliphatic alkyl chains, –CH_2 or –CH_3 (1400–1300 cm^{-1}). Moreover, the main heterocycle skeleton of MB exhibited the band at 952 (due to –N–O) and 1490 cm^{-1}. The peak at almost 1635 cm^{-1} is attributed to the -CH = N, -C = N central ring and H–OH stretching (3428 cm^{-1}), -N–H (3183 cm^{-1}), and the aliphatic amine groups, -CH_3 bonds at 1539 cm^{-1}, which are the main chromophores in MB dye [129]–[131]. However, some of the influential characteristic bands mentioned above with the heterocycle skeleton structures, such as through H–OH (3400 and 1635 cm^{-1}) and –N–O (952 cm^{-1}), disappeared in treated MB solution indicating the maximum destruction of MB molecule by breaking of central and side aromatic rings and demethylation, clearly implying the successful degradation of MB by the Co_3O_4@CNDs under visible light irradiation.

The FTIR spectroscopy of the IC after degradation **(Figure 6c and d)** compared with that of the MB dye, which possesses highly complicated vibrational modes due to its chemical structure, with the characteristic peaks at wavenumbers, 1392 cm^{-1} due to its noticeable deformation vibrations of N–H and aliphatic alkyl chains, -C–H, –CH_2 or –CH_3 at 1461 cm^{-1}. The FTIR spectra of untreated IC showed the specific peaks in the fingerprint region (2000 - 500

cm^{-1}) for the ortho-para-disubstituted benzene rings, which is next to the peak at 1613 cm^{-1} for the C = C stretching of the benzene ring [132]. A characteristic peak in the region 1100 - 1000 cm^{-1}, related to the S = O stretch band with the most significant peak at 1068 cm^{-1} and another in the range 751 cm^{-1} for the C-S stretching vibrations due to sulfur-containing functional groups [132]. The observed bands in the 3300 - 3500 cm^{-1} are due to the O-H stretching attributed to water remains [132]. The band assigned to the carbonyl bond can also be observed at ~1660 cm^{-1} and N–H (3183 cm^{-1}), which are the main chromophores in IC dye [133]. Some above-mentioned characteristic bands with the heterocycle skeleton structure, such as through H–OH (3400 and 1628 cm^{-1}), disappeared in the treated IC solution indicating the maximum degradation of IC molecule by breaking of central and side aromatic rings and demethylation, implying degradation of IC by the Co_3O_4@CNDs under visible light irradiation.

The treated MB and IC solution exhibited characterization spectra of water and aliphatic amine groups with no traces of aromatic rings, which revealed that some degradation intermediates or byproducts of MB and IC were absorbed by the catalyst, indicating the dye decomposition to the maximum extent. The Co_3O_4@CNDs FTIR showed Co_3O_4 peaks at 578 and 667 cm^{-1} and the other remaining peaks with CNDs structure in the comparison plots. These peaks were observed in MB+Co_3O_4@CNDs and IC+Co_3O_4@CNDs after 75 minutes (at 120 minutes), confirming their presence and showing their catalytic ability and phase stability. After 75 minutes, the characteristic peaks of MB and IC are degraded to a maximum extent, and the structural changes are shown using these compared FTIR data. Thus, the FTIR data confirmed that the harmful aromatic structure of the dye is decomposed after the maximum degradation time. The photodegradation of the MB and IC mainly might have undergone the *n*-dealkylation of the aliphatic tertiary amine [88], [91], [133].

Effect of charge of dye (Anionic and Cationic)

In this study, we also compared the MB dye degradation (71%) with IC (62%), which exhibited a better photocatalytic activity. This higher degradation was due to the dyes' distinctive chemical structures and charge, as MB is cationic, and IC is anionic. The negative charge on the catalyst's surface facilitated the faster degradation of cationic dyes (MB) due to the increased electrostatic attraction forces [134]. In the case of anionic dyes (IC), a strong repulsion was observed between the dye molecule and catalyst surface, decreasing the degradation compared to cationic dyes (MB) [59].

Photocatalytic kinetics - Rate constant studies

The degradation extent was further analyzed by first-order kinetics reaction using the Langmuir-Hinshelwood (L-H) model. The reaction kinetics of the photocatalytic degradation rate of MB and IC were determined by fitting using the L–H kinetics model. From the fitting, the rate constants (k) can be calculated from **Eq. 3**.

$$\ln \frac{C_0}{C_t} = k \times t \quad (3)$$

where C_o/C_t is the MB degradation rate, and 'k' is the pseudo-first order reaction rate constant. The correlation coefficient (R^2) and the reaction rate constants, 'k,' were calculated from these plots. **Figures 7 and S2.19a-d** are the plots with $\ln(C_0/C_t)$ vs. irradiation time up to 120 and 60 minutes for the visible and UV light source-based degradations at 20 and 50 mg L^{-1} dye concentrations, respectively. The R^2 value of Co_3O_4@CNDs, CNDs, and Co_3O_4 NPs was closer to 1(above 0.9) for all dye degradations. A high k value means better photocatalytic activity. The graph from **Figures 7a and c** illustrated a straight line with a positive slope and the rate constant of 1.39 and 1.95×10^{-2} min^{-1} for Co_3O_4@CNDs hybrid NPs with 20 mg L^{-1} MB dye

degradation in the presence of visible and UV light, respectively. The photodegradation rate is decreased with increasing dye concentration in Co_3O_4@CNDs, CNDs, and Co_3O_4 NPs.

Figure 7. Ln(C_0/C_t) vs. time plots of 1mg/mL of Co_3O_4@CNDs, CNDs, and Co_3O_4 NPs with 20 mgL^{-1} a. MB and b. IC dye degradation in visible light, c. MB and d. IC in the presence of UV light

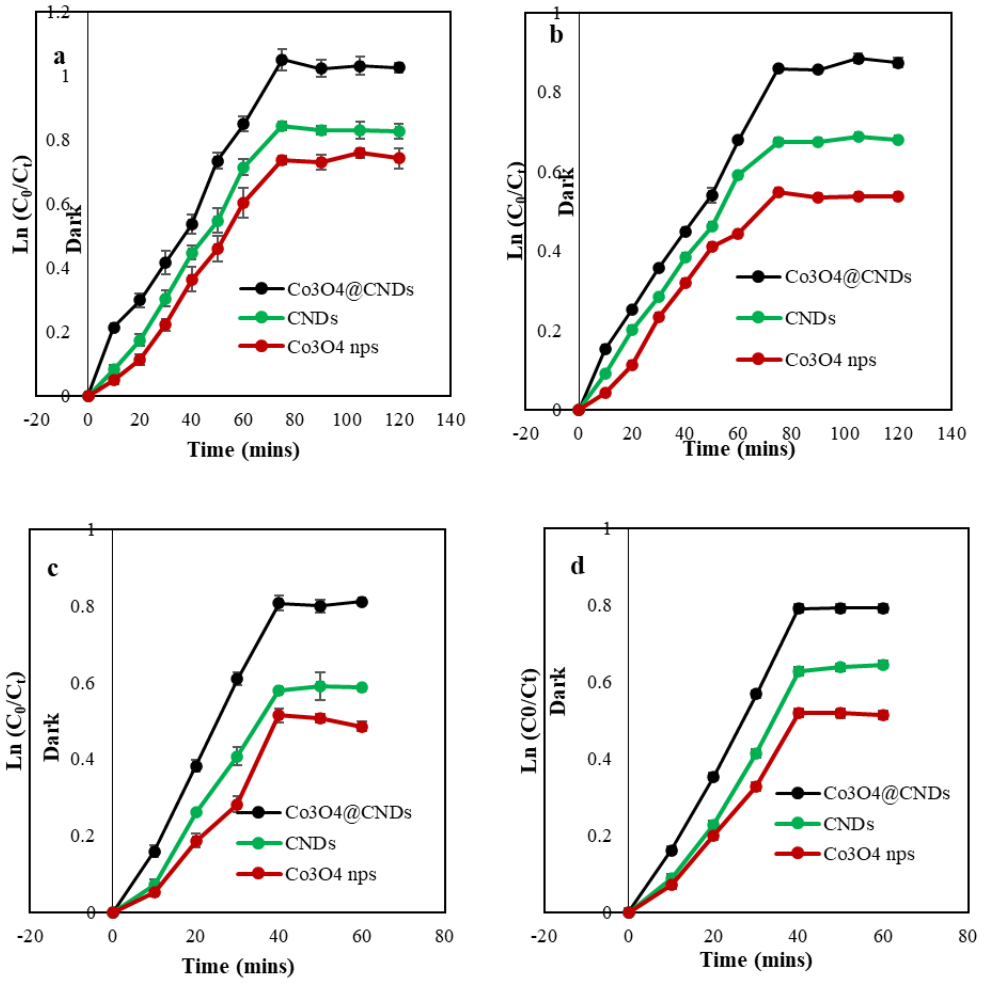

The R^2 value of Co_3O_4@CNDs had a higher value in the 20 mg L^{-1} MB dye degradation and showed a faster degradation rate than CNDs and Co_3O_4 NPs. The photocatalytic decomposition of MB and IC agreed with pseudo-first-order kinetics. The reaction rate constant, k, of the Co_3O_4@CNDs, CNDs, and Co_3O_4 NPs under visible and UV light were calculated as

shown in **Table S2.4 and S2.5** for both the MB and IC, respectively. The graph from **Figures 7b and d** illustrated a straight line with positive slope and k value of 1.15±0.01 and 1.92±0.04×10^{-2} min^{-1} for Co_3O_4@CNDs hybrid NPs with 20 mg L^{-1} IC dye degradation in the presence of visible and UV light, respectively. It can be observed that from the results, MB and IC photolysis is higher for UV light than that visible, as the degradation was achieved faster in the presence of UV light. The same trend was observed with the 50 mg L^{-1} dyes (**Figure S2.19a-d**). This superior photocatalytic activity of the Co_3O_4@CNDs hybrid composite might be due to the Co_3O_4 core and the surface of the nitrogen-doped as well as hydroxyl-containing carbon layers, as mentioned by Atchudan *et al*. [114]. These results revealed that the Co_3O_4@CNDs hybrid composite are a potential candidate for photocatalytic degradation of MB and IC under UV and visible light irradiation.

This study compared with the reported literature of MB and IC degradation by Co_3O_4 and carbon-based composites to justify the superior activity of the Co_3O_4@CNDs hybrid composite, shown in **Table S2.6.** Also, by considering previous works, the supported photocatalysts (Co_3O_4@CNDs hybrid NPs in this work), such as graphene-based nanocomposites, have a high tendency for trapping or absorbance of reactants and facilitate the transfer of reactants to active sites [36]. **Figure S2.26** comparison plots with $\ln(C_0/C_t)$ versus time implied that the degradation rate of MB with the UV (0.02/min) was higher and faster than that of the visible light (0.014/min).

Reaction mechanism and active species determination

Active species determination

The degradation reactions of the Co_3O_4@CNDs were performed in the presence of different scavengers, such as IPA, EDTA, HQ, and $AgNO_3$ of 1 mM concentration **(Figure**

S2.26a and b in the presence of visible light, whereas c and d with UV light). IPA, HQ, EDTA, and $AgNO_3$ were utilized for quenching the reactive species, such as $^{\bullet}OH$, O_2^-, h^+, and e^-, respectively [36], [68]. Adding these scavengers suppressed the photocatalytic reaction efficiency by decreasing the peak intensity considerably compared to no scavengers.

The observed efficiency of 22% for IPA-containing reaction suggests the significant contribution of $^{\bullet}OH$ from the photocatalyst for the degradation reactions. The degradation efficiency in HQ-aided reaction was 29%, indicating that the O_2^- radicals are majorly linked with the catalysts, leading to degradation. Besides, the 10% and 13% efficiency received from EDTA and $AgNO_3$-containing reactions indicate the poor quantity of h^+ and e^- reactive species formation from the Co_3O_4@CNDs catalysts with visible light. A similar trend was observed in the scavenging for the Co_3O_4@CNDs in the presence of UV light-based dye degradation. From the scavenging study that we performed in visible light, intermediate species that were expected to contribute to the degradation mechanism are $O_2^- > OH^- > e^- > h^+$ **(Figures S2.26a and b)**. Whereas, in the UV-light-based degradation, the charges that contribute are in the order of $O_2^- > e^- > OH^- > h^+$ **(Figures S2.26c and d)**.

For an improved photocatalytic process, the electron mobility must be low enough to impede the recombination process and accelerate the electrons to reach their active sites [104]. This low electron-hole pair recombination might be the reason for the high degradation percentage observed in visible than UV-based photocatalysis. But the UV-based degradation rate is higher than the visible as more electrons contribute to the degradation with UV light, as observed through this scavenging study. The band gap of Co_3O_4@CNDs is near 2.51, which might also be the reason for UV's high degradation rate of the photocatalytic activity than the visible source.

Mechanism of photocatalytic activity

A possible mechanism of photocatalytic dye degradations over the Co_3O_4@CNDs hybrid composite has been proposed based on the photocatalytic studies, as shown in **Figure 8**. The high photocatalytic performance in the Co_3O_4@CNDs might be expected due to their efficient interfacial charge migration and separation. The literature reported that carbon nanostructures encapsulating any nanomaterials could have an enhancing effect on photocatalytic activity [68], [128], [135]. The charge carriers could migrate to the surface of the particles to decompose organic dyes via this proposed mechanistic pathway **(Figure 8)**. With UV/Visible light irradiation, firstly, the electrons in the valence band (VB) get excited into the conduction band (CB), leaving behind holes in the VB of the Co_3O_4@CNDs. Generation of the O_2^- and OH^- radicals lead to dye degradation over the Co_3O_4@CNDs hybrid composite under UV/ visible light irradiation. The carbon shell layers on the Co_3O_4@CNDs hybrid NPs prevent the electron-hole pair recombination due to their core-shell morphology with heterojunction interfaces [104], [135], [136] over the CNDs and Co_3O_4 NPs. Hence, the improvement in photocatalytic performance was attributed to the synergistic effect between the Co_3O_4 NPs and CNDs.

While the photon energy is not high enough to excite the photocatalyst to release reactive charge carrier species, dye degradation occurs through the photosensitization process [91]. When visible/ UV light is illuminated, the dye molecule gets excited to its excited state (Low Unoccupied Molecular orbital - LUMO level), generating excess excited electrons there. Because the LUMO of the dyes is more negative than the CB of the photocatalysts, the photoexcited electrons move to the photocatalysts from the dye molecules, which might lead to the generation of reactive charge carrier species to initiate the photodegradation process [91], [136].

Figure 8. a. Charge transfer and b. Proposed Mechanism of Photocatalytic process in the Co_3O_4@CNDs

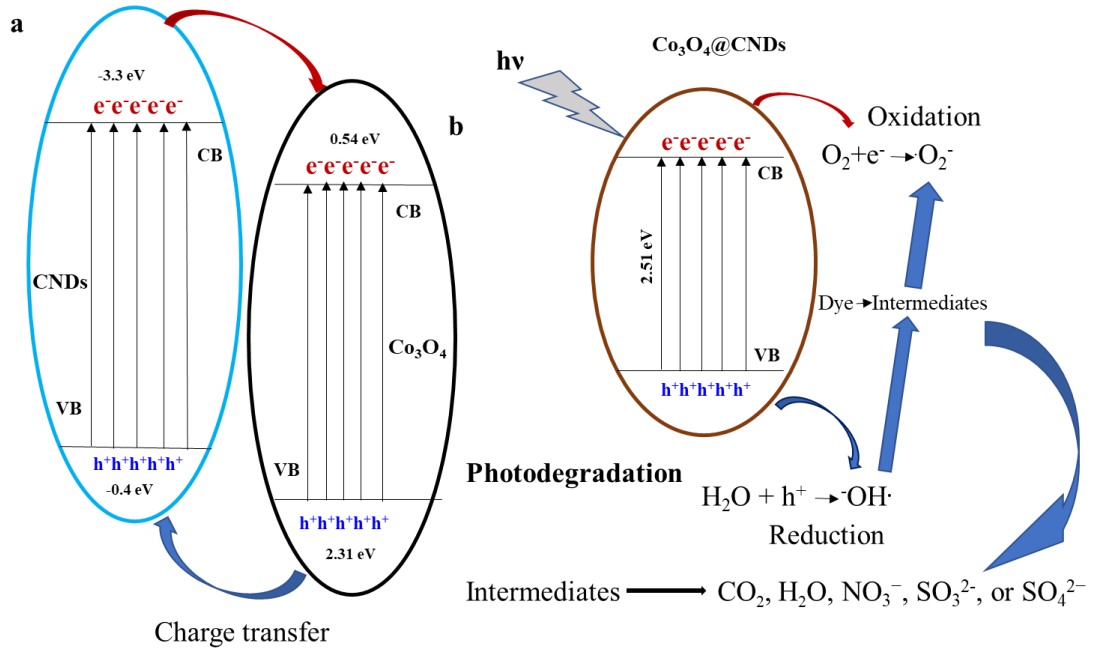

The VB and CB edge at the point of zero charges of the semiconductor can be calculated by the Mulliken electronegativity approach according to the following **Eq. 4. and 5.** [28]:

$$E_{VB} = X - E_e + 0.5E_g \quad (4)$$

$$E_{CB} = E_{VB} - E_g \quad (5)$$

where X is the electronegativity, which is the geometrical means of the electronegativity of the constituent atoms in the semiconductor, E_e is the free energy of a free electron on the hydrogen scale (NHE~4.5 eV), and E_g is the calculated optical band gap energy of the semiconductor [28]. The value of [X] is 5.927 eV for Co_3O_4 NPs, which is calculated from the reported electronegativity values of the atoms present in the NPs (calculations explained in detail in the SI). Based on the above **Eq. 4. and 5.**, the CB edge +0.542 and -3.3 eV, and VB edge +2.312 and -0.4 eV vs. NHE for Co_3O_4 and CNDs NPs are calculated respectively from **Eq. 4**

and 5. These edge gap results reveal the possibility of electron transfer from CB of CNDs to CB of Co_3O_4 NPs, which is accompanied by narrowing band gap energy and preventing the recombination of the charge carriers.

Co_3O_4@CNDs + hU → $h^+ + e^-$ (6)

$H_2O + h^+ + e^- \rightarrow H^+ + OH\cdot$ (7)

$O_2 + e^- \rightarrow \cdot O_2^-$ (8)

Organic dyes (OD) + ($OH^{\cdot -}$ / $\cdot O_2^-$) → Degraded products (9)

OD + hU → OD^* (10)

$OD^* + Co_3O_4$@CNDs → Co_3O_4@CNDs (e^-) (11)

Co_3O_4@CNDs (e^-) + $O_2 \rightarrow \cdot O_2^- + {}^*Co_3O_4$@CNDs (12)

In the dye degradation process, the oxygen in the air acts as a potent oxidizing agent that catalyzes the process as an alternative to the existing oxygen donors. Co_3O_4@CNDs hybrid composite upon irradiation with visible/UV light sources with hU based reactive species, such as super hydroxy and oxy radicals ($OH^{\cdot -}$ and $\cdot O_2^-$), are responsible for effective light-based dye degradation **(Eq. 6. – 12.)**, which corresponds with that of the scavenging study **(Figure S2.27)**. Upon photonic illumination from visible and UV light sources, the dye-reacted species reacts with the electrons in the lattice plane of Co_3O_4@CNDs to form the super oxy ($\cdot O_2^-$) radicals in the presence of oxygen in the system that further enhance the dye degradation process into smaller intermediates and then to final byproducts such as CO_2 and H_2O [47], [51], [137].

Reusability test

The reusability and recovery of a catalyst after the light-based dye degradation catalytic experiment are vital for their use in industries and on a large scale [138]. The Co_3O_4@CNDs catalyst was readily separated from the reaction mixture by centrifuging for 20 minutes at 10,000

rpm and washing with DI water twice. This recovery confirms that the Co_3O_4@CNDs catalyst can be effectively reused. In this study, the reusability was checked for 3 cycles, and fresh MB and IC dye solution was used for every process for the photodegradation measurements. **Figures S2.28a and c** showed that Co_3O_4@CNDs hybrid NPs maintained their catalytic activity in the dye degradation study, which suggested good reusability around 72% of MB and 63% of the Co_3O_4@CNDs catalyst after 3 cycles. The data shown in **Figures S2.28b, and d** indicate no significant changes in the visible light-based dye degradation with Co_3O_4@CNDs hybrid NPs after 3 cycles compared with that before the recycling experiment at 75 minutes. The efficiencies are nearly identical in all the runs without any remarkable deviations in the effective percentage. The variation (1.8%) is only less than 2%, even in the 3rd run.

Moreover, the Co_3O_4@CNDs catalyst recovered from the reaction mixture at the end of three cycles of visible light-based MB and IC dye degradation was collected and characterized by XPS, as shown in **Figures S2.29a and b**, respectively. In the Figures, the catalyst with the dyes collected after three runs of the light-based experiment is compared with that of the MB and IC dyes before the recycling experiment and catalyst individually. The results showed that there is not much variation in the dye structure before and after degradation, which indicated good stability [139] of the Co_3O_4@CNDs catalyst. Hence, high stability and facile reusability of the Co_3O_4@CNDs are observed under visible radiation, confirming that they can significantly assist the industrial pollutant clear-out on a large scale, making these catalysts promising for their use in environmental remediation [129].

Discussion

From the photodegradation results, the following observations are revealed: (i) No degradation takes place without catalyst and light, (ii) under dark conditions, the observed

degradation may be due to physical adsorption or chemisorption of MB and IC dyes with Co_3O_4@CNDs, CNDs, and Co_3O_4 NPs, (iii) Co_3O_4@CNDs exposed to visible light has excellent photocatalytic degradation efficiency, which degraded 20 mg L^{-1} MB (72%) and IC (63%) dyes in 75 mins because the band gap of Co_3O_4@CNDs lies in the ideal visible region, (iv) Co_3O_4@CNDs exposed to UV light has excellent photocatalytic degradation rate compared to the visible light due to the wavelength of the light source, which degraded 20 mg L^{-1} MB at a rate of $(2.01\pm0.05)\times10^{-2}$ min^{-1} and IC at $(1.92\pm0.04)\times10^{-2}$ min^{-1} at 40 minutes itself. (v) The superoxide reactive oxygen species played an essential role in the visible and UV light-based photocatalytic dye degradation activity of Co_3O_4@CNDs hybrid NPs, which was inferred through a proposed mechanism. Thus, we speculate that the difference in degradation rate and the percentage is mainly due to the type of light wavelength.

Conclusion

In summary, the Co_3O_4@CNDs nanocomposite was synthesized by a simple microwave method. The synthesized NPs were analyzed through XRD, HRTEM, UV, PL, FTIR, Raman, and XPS spectroscopies. The structural, elemental, and morphological studies with the comparison analyses confirmed that Co_3O_4 is present in the core-shell structure of the Co_3O_4@CNDs hybrid NPs with CNDs in the shell. The photocatalytic degradation of MB and IC dye solution of these NPs was carried out under visible and UV light. The Co_3O_4@CNDs hybrid nanocomposite showed the highest dye degradation efficiency compared with pure Co_3O_4 and CNDs under both light irradiations. The heterojunction between pure Co_3O_4 and CNDs reduced the electron-hole recombination ability and improved the visible and UV light absorption of the nanocomposite. The scavenging experiment demonstrated OH* and O_2^- are the active species for the degradation of MB and IC dyes. Based on the scavenging results, a

mechanism for photodegradation was proposed with edge gap calculations. Therefore, the Co_3O_4@CNDs composite is a promising reusable photocatalyst for dye degradation under both UV and visible light. In conclusion, the Co_3O_4@CNDs hybrid NPs with a band gap of 2.51 eV is an appropriate candidate for photocatalytic application, especially in the visible and UV region. In addition, it finds attractive features like a simple operation, low cost, ambient conditions, high dye degradation efficiency with both UV and visible sources, and reusable.

CHAPTER III: ELECTROCHEMICAL CHARACTERIZATION ON Co_3O_4@CNDS FOR EVALUATING THEIR USE IN SUPERCAPACITOR APPLICATIONS

Introduction

With the fast-growing technological era and global warming, energy depletion occurs much faster, leading to exploring for greater capacity storage devices [140]. The need for energy storage devices, such as supercapacitors, has been gaining immense attention in recent years for renewable energy [141]. Nanomaterials offer many advantages over traditional bulk materials, including higher energy storage capacity due to their greater surface to volume ratio [140], power density [140], and greater cycle life [142]. Nanostructured materials (NSM), such as carbon-metal oxide composite electrodes, have shown promise toward achieving improved charge/ discharge capacity and cycling stability for supercapacitor energy storage [143].

An electrical double-layer capacitor (EDLC) involves physically storing energy to establish an electrical double-layer at the electrode-electrolyte interface for charge storage [144]. To create this electrical layer, a high specific surface area and chemically stable material is required, which is typically porous carbon[145], such as graphene, activated charcoal (AC), carbon black (CB), and carbon nanotubes (CNTs) [144]. A pseudo-capacitor stores electrical energy through rapid and continuous redox reactions between the electrodes and the electrolyte. Metal oxides and conducting polymers are commonly used as electrode materials in pseudo-capacitors, which also can generate high capacitance [145], [146]. The combination of faradaic and non-faradaic materials as core-shell 0D nanostructures provides significant merits including improved electrical conductivity, no agglomeration, and better chemical and mechanical stability

[147]. Therefore, composite electrodes exhibit such advantages as double-layer capacitance and pseudo-capacitance [147], [148].

Co_3O_4 NPs are one of the most reported metal oxides as they are economical and possess better conductivity and extremely high theoretical capacitance [145]. However, they still have some common drawbacks of the metal oxides, such as aggregation causing the low power density and capacitance to fade [145]. Porous carbon is usually chosen as the electrode material in commercial products because of the high cost of metal oxides and the poor stability of the conducting polymers [148]. Carbon nanomaterials such as CNDs, graphene, fullerenes, and carbon quantum dots (CQDs) were similarly studied for the supercapacitor applications, owing to their high surface area, inter-particle electrical conductivity, chemical stability, enhanced mass-transport efficiencies, and earth-abundant non-metal [149]–[152]. These properties can make them excellent supercapacitors as they can store more energy per unit mass and provide faster power delivery or conducting catalysts compared to the existing platinum catalyst [153], [154]. But the CNDs or CQDs could not be used as separate electrode materials due to their poor electron conductivity and low surface area [155]. Hence, although some promising studies were performed by using the CNDs in advanced supercapacitors, the applications are still in their infant stages and are better used with composite materials [155].

In a study by Aboagye et al., the specific capacitance of pure electrospun carbon nanofibers (E-CNFs) was only 4.6 F/g [156]. The Cyclic voltammetry (CV) curve of the pristine ECNFs at 5 mV s^{-1}, scan rate exhibited a long and narrow nonrectangular shape [156]. It enclosed a minimal area of the loop, suggesting minimal electrochemical double-layer capacitive behavior, and no significant redox peaks were observed [156]. In advanced research, the favorable charged sites created by the nitrogen functionalization on the carbon surface can break

the electro-neutrality present on the graphitic carbon framework, resulting in better electrochemical activities [157]. These were also expected precisely due to pyridinic and graphitic nitrogen on the carbon nanolayer surface, exposing the facet planes favoring the electrochemical properties [158]. By using nanocomposites or zero-dimensional (0D) nanomaterials alone, supercapacitors can have increased energy storage capacity, improved power delivery, and better thermal stability [147], [151].

Carbon materials, such as activated carbon, and carbon nanospheres, and transition metal oxides were combined and formed as hybrid NPs for electrode materials for their use as micro-supercapacitors [147]. Zhao et al. evaluated core-shell NPs with carbon core and MnO_2 shell with an optimized MnO_2 content (64 wt%), for the capacitance study and found a maximum specific capacitance of 190 F g^{-1} at 0.1 A g^{-1} higher than the carbon core (95 F g^{-1}) [147], [159]. Although much research was being carried out with these core-shell hybrid NPs, these materials might still need an insulating polymer binder to prepare the working electrode, which hinders its performance [147].

Cobalt oxide-based carbon hybrid materials have been reported with extensive applications in sluggish electrocatalytic reactions, and energy storage, such as supercapacitors, [160], [161] and cancer therapy, drug delivery, sensing, and bioimaging [149], [162]–[164]. However, the emerging and challenging need to develop a cost-effective and highly stable electrocatalyst for energy storage applications has led to extensive research exploring novel hybrid functional next-generation catalysts [165], [166]. Subsequently, hybrid NPs must be investigated for their use in energy storage, as supercapacitors are essential to improve the performance of the devices. Hence, we considered using novel, core-shell hybrid NPs as Co_3O_4@CNDs as an efficient supercapacitor in this work. This research mainly involves

understanding and investigating a novel, the Co_3O_4@CNDs core-shell hybrid NPs comprising Co_3O_4 deposited on a CNDs matrix for their supercapacitor energy storage applications with different polymer binders. CV was a basic, quick, and reliable electrochemical technique for providing valuable information about the electrochemical reactions for supercapacitor applications and measuring their energy storage as capacitors [75], [167].

Materials and Methods

Materials

Chemicals and reagents, such as cobalt acetate tetrahydrate (Sigma Aldrich), pure anhydrous ethanol (Sigma Aldrich), 25- 28% ammonium hydroxide solution (Sigma Aldrich), citric acid (ACROS Organics), ethylenediamine (EDA, Fisher Scientific), and electrodes, such as silver/ silver chloride (Ag/AgCl) reference, platinum counter, and glassy carbon working electrode (GCE, Fisher Scientific), and electrolyte, potassium hydroxide (KOH, Sigma Aldrich) were used. Nafion (Aldrich) and dimethyl formamide (DMF, Sigma), are binders for attaching any solution to the electrode. Different binders, such as polyvinylidene fluoride (PVDF, Sigma Aldrich) and polytetrafluoroethylene (PTFE, Aldrich), activated carbons such as activated charcoal (AC, Aldrich) and carbon black (CB, Fisher Scientific) and N-methyl pyrrolidone (NMP, Aldrich) were used. All the materials mentioned above were used in this research work without further purification and analytical grade.

Methods

Synthesis and characterization of Co_3O_4@CNDs hybrid NPs

The synthesis of the EDA-based N-rich CNDs procedure, reported by our group [168], [169], was modified to form a hybrid NPs with Co_3O_4 as a core in the carbon shell matrix. Since the reported hydrothermal methods have been time-consuming [170], a facile and reliable

microwave approach was done to obtain better control over the morphology. Hence, in this research, Co_3O_4 NPs were synthesized by a simple technique modified [102] using cobalt acetate tetrahydrate, ethanol, and ammonia. The Co_3O_4@CNDs hybrid NPs synthesis was performed to obtain an easy and convenient approach for obtaining core-shell NPs or a matrix containing Co_3O_4 and CNDs. After the microwave synthesis, the material was well characterized using the X-ray diffractometer (XRD), X-ray photoelectron spectroscopy (XPS), Raman spectroscopy, and Transmission electron microscope (TEM), as discussed in the previous chapters.

Electrochemical workstation

A VMP3 electrochemical workstation was used to perform the electrochemical study of the Co_3O_4@CNDs core-shell hybrid NPs. The electrochemical study was done using a three-electrode setup system with Co_3O_4@CNDs core-shell hybrid NPs as the working electrode, a platinum wire and an Ag/AgCl as the counter and reference electrode, respectively, in 6 molars (M) KOH solution.

Electrode Modification. Co_3O_4@CNDs core-shell hybrid NPs were used at 10 mg/mL concentration and mixed with a binder. The particles were mixed thoroughly and then ultrasonicated at room temperature for complete mixing and then drop-casted on the top of the GCE and dried before use. Different binders, such as PVDF and PTFE, were also used and compared. Conducting materials such as AC and CB were also used in combination and compared. According to the literature, PVDF and PTFE binders were used to improve the conductivity of the Co_3O_4@CNDs core-shell hybrid NPs to that of the Nafion and DMF binder. Optimization was done to find out the best concentration of Co_3O_4@CNDs core-shell hybrid NPs and binders. Co_3O_4@CNDs core-shell hybrid NPs, PVDF binder, and AC were mixed in a ratio of 6:1:3 and dissolved in 1 mL of N-MP. The mixture was ultrasonicated at room temperature

and thoroughly mixed. Then the slurry was drop-casted on the top of the GCE and dried at 80˚C. Co_3O_4@CNDs core-shell hybrid NPs, PTFE binder, and AC were mixed in a ratio of 6:1:3 and dissolved in 1 mL of N-MP. CB was also tried by replacing AC in the above slurry preparation to find which conducting material combination is best with Co_3O_4@CNDs core-shell hybrid NPs for better capacitance. Also, different ratios of these slurry materials were tried, such as 6:1:3, 7:1.5:1.5, and 8:1:1 were also attempted, optimized, and compared. The capacitance was calculated according to the formula as shown below:

$$C = \frac{1}{v * \Delta V} * \int_{v-}^{v+} I \, dV$$

Where C, v, ΔV, v^-, v^+, and I are capacitance, scan rate, voltage interval (e.g., -1 to +1), lower voltage (e.g., -1), lower voltage (e.g., +1), current value from the data [171].

Results and Discussion

Electrochemical measurements using Cyclic voltammetry

The electrochemical studies of the different electrodes prepared were conducted using the CV. Figure 1 displays the capacitance plot results from the CV obtained using the Co_3O_4@CNDs core-shell hybrid NPs with Nafion (a) and DMF (b). The CV curves of the Co_3O_4@CNDs core-shell hybrid NPs with Nafion (**Figure 1a**) and DMF (**Figure 1b**) within the scan range -1 to +1 V, corresponding to redox activities of Co_3O_4 and CNDs in 6M KOH solution by a characteristic, but a weak quasi-rectangular shape with redox reversibility.

Figure 9a had better redox reversibility than **Figure 9b** suggesting that the CV of the Co_3O_4@CNDs core-shell hybrid NPs with Nafion solvent was better than that with the DMF. It was obvious from these measurements that the binders played an important role in determining the capacitance properties of the Co_3O_4@CNDs core-shell hybrid NPs. Although DMF being a good solvent to improve ionic conductivity, some literature reports that the DMF affected the

capacitance properties compared to nafion, as they narrowed their electrochemical stability [172]. **Figure 9c** showed the CV plots of Co_3O_4 NPs only for comparison. The CV of Co_3O_4 NPs shows a characteristic plot with more oxidation current, which is basically due to the reaction of the oxides on the surface of the particles with the electrolyte, and the quasi-rectangular shape is not proper. The improper redox reactions might be expected due to the general characteristic attribute of these Co_3O_4 NPs where their capacitance usually begins to fade with their low power density due to their strong oxidizing ability, as reported in the literature [145].

Figure 9. CV plot for the capacitance of Co_3O_4@CNDs core-shell hybrid NPs with Nafion (a) and (b) DMF electrolytes and (c) CV plot for the capacitance of Co_3O_4 NPs

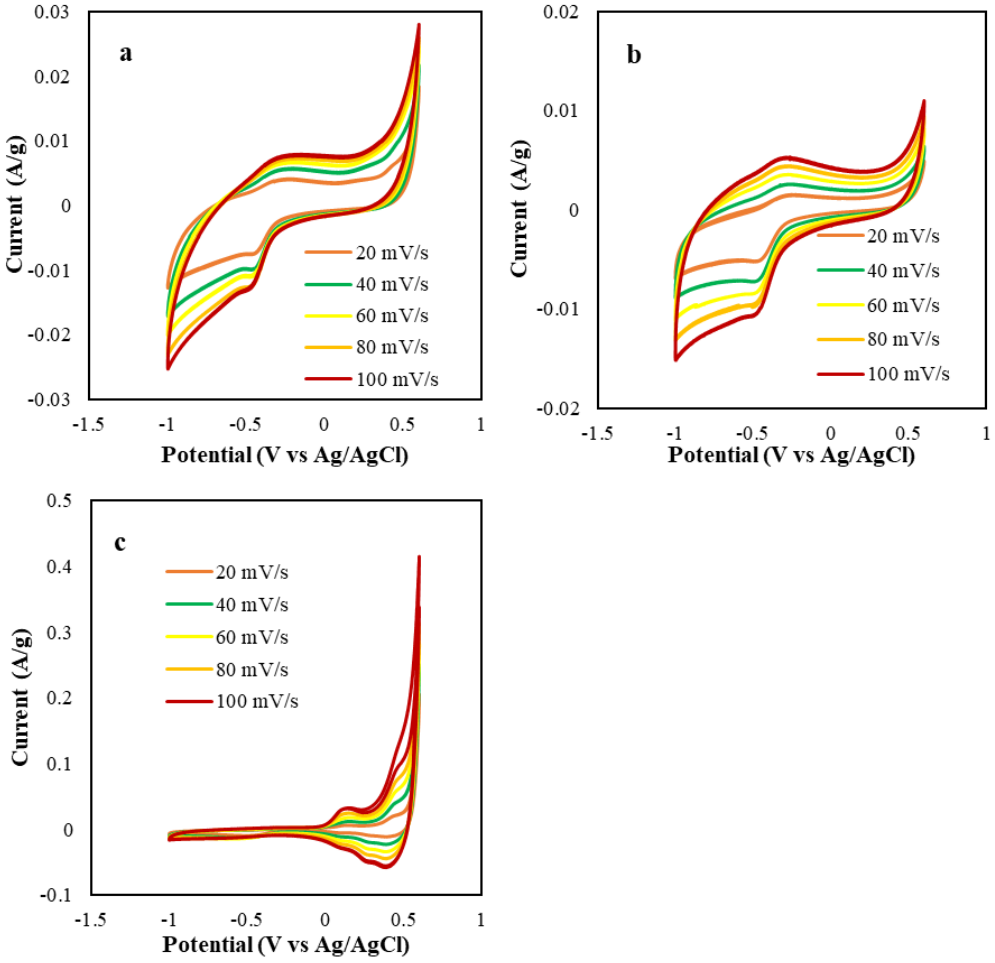

Figure 10. CV plots for capacitance determination of Co_3O_4@CNDs hybrid NPs with PVDF and CB at a. 6:1:3, b. 8:1:1, and 7:1.5:1.5

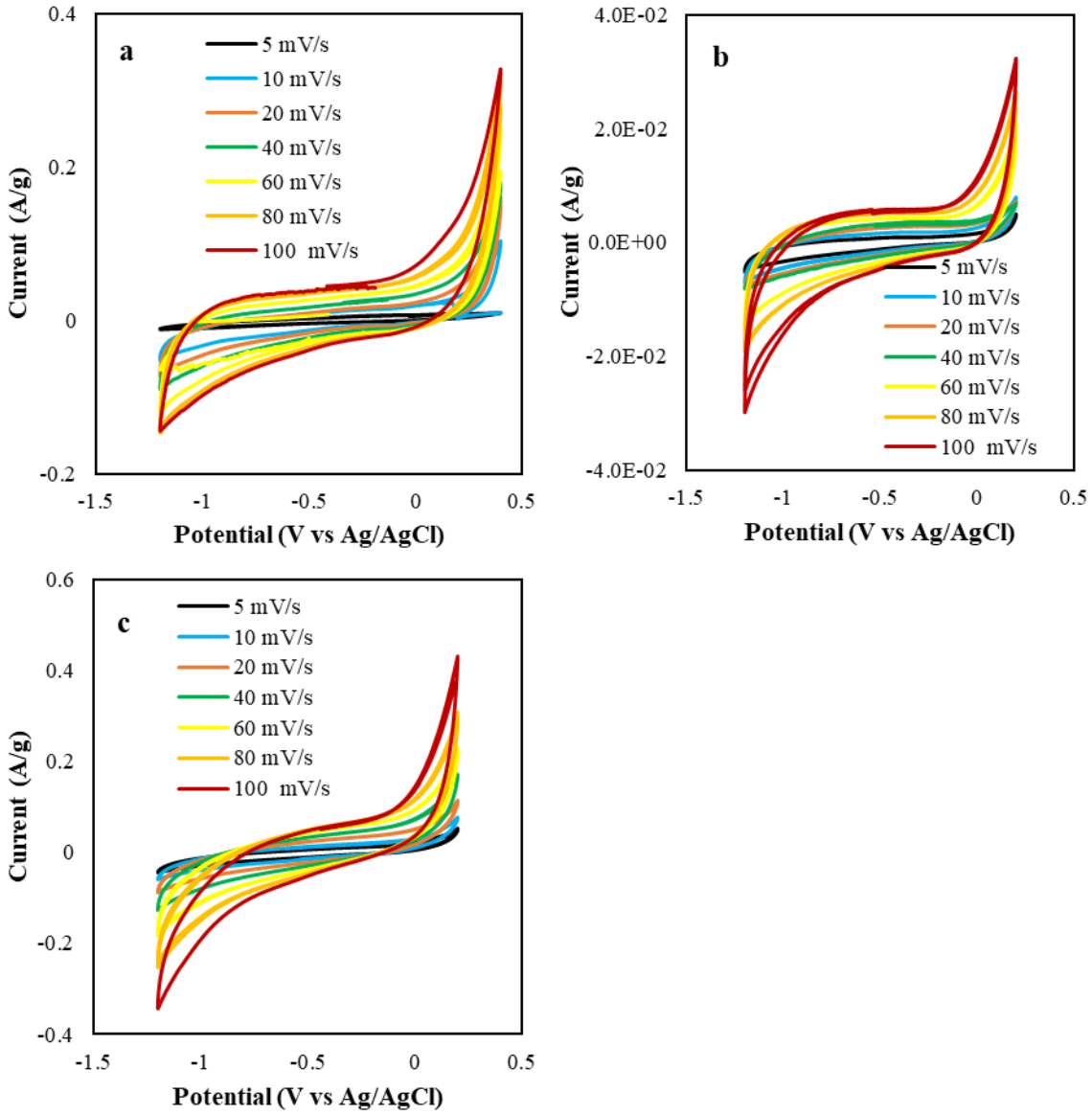

Figure 10 a-c represented the CV plots for capacitance determination of Co_3O_4@CNDs hybrid NPs with PVDF and CB at a. 6:1:3, b. 8:1:1, and 7:1.5:1.5. To get the better electrochemical performance of the Co_3O_4@CNDs hybrid NPs, PVDF and carbon black with the Co_3O_4@CNDs hybrid NPs were evaluated at different ratio combinations to optimize the better performance. Although the shapes were different in all the 3 CV graphs, the results suggested a

clear idea that the PVDF binder at a 7:1.5:1.5 ratio showed better performance than the other ratios used. The better electrochemical properties of the PVDF binder and CB combined with the Co_3O_4@CNDs hybrid NPs significantly improved the capacitance value than the one obtained by using just Nafion. From the literature evidence, the Nafion had a negative impact by reducing the energy storage capacity because the working electrodes prepared with Nafion are less mechanically stable, and aggregates as large micelles with the hydrophobic surface with their higher internal resistance, which can further inhibit the capacitance [173], [174]. These reasons might be the reason for the negligible capacitance value obtained from **Figure 9a**, and thus combining Co_3O_4@CNDs hybrid NPs with other polymer binders had been proved better.

Figure 11 a-c represents the CV plots for capacitance determination of Co_3O_4@CNDs hybrid NPs with PTFE and CB at a. 6:1:3, b. 8:1:1, and 7:1.5:1.5. To get the better electrochemical performance of the Co_3O_4@CNDs hybrid NPs, PTFE and CB with the Co_3O_4@CNDs hybrid NPs were evaluated at different ratio combinations to optimize the better performance. Although the shapes were different in all the 3 CV graphs, the results suggested a clear idea that the PTFE binder at a 6:1:3 ratio showed better performance than the other ratios used. The better electrochemical properties of the PTFE binder and CB combined with the Co_3O_4@CNDs hybrid NPs significantly improved the capacitance value than the one obtained by using just Nafion. But the PTFE mixture showed comparatively less performance than the PVDF one. Faradaic peaks were more prominent for electrodes prepared with the PVDF binder, followed by PTFE and Nafion. These properties are due to the decreased resistance for the ions desorption which reduces the capacitance, energy storage capacity, and the higher Fardaic contribution [174].

As a result, fewer ions might get adsorbed at the porous interface of the Co_3O_4@CNDs hybrid NPs. Hence, the capacitance values also declined for PTFE and Nafion as the electrolyte ions penetrate deep inside the pores in the PVDF binder mixture. Thereby, the PVDF with CB mixture improves the electron transfer at the electrode/electrolyte interface and facilitates pseudocapacitive charging of the Co_3O_4@CNDs hybrid NPs [174].

Figure 11. CV plots for capacitance determination of Co_3O_4@CNDs hybrid NPs with PTFE and CB at a. 6:1:3, b. 8:1:1, and 7:1.5:1.5

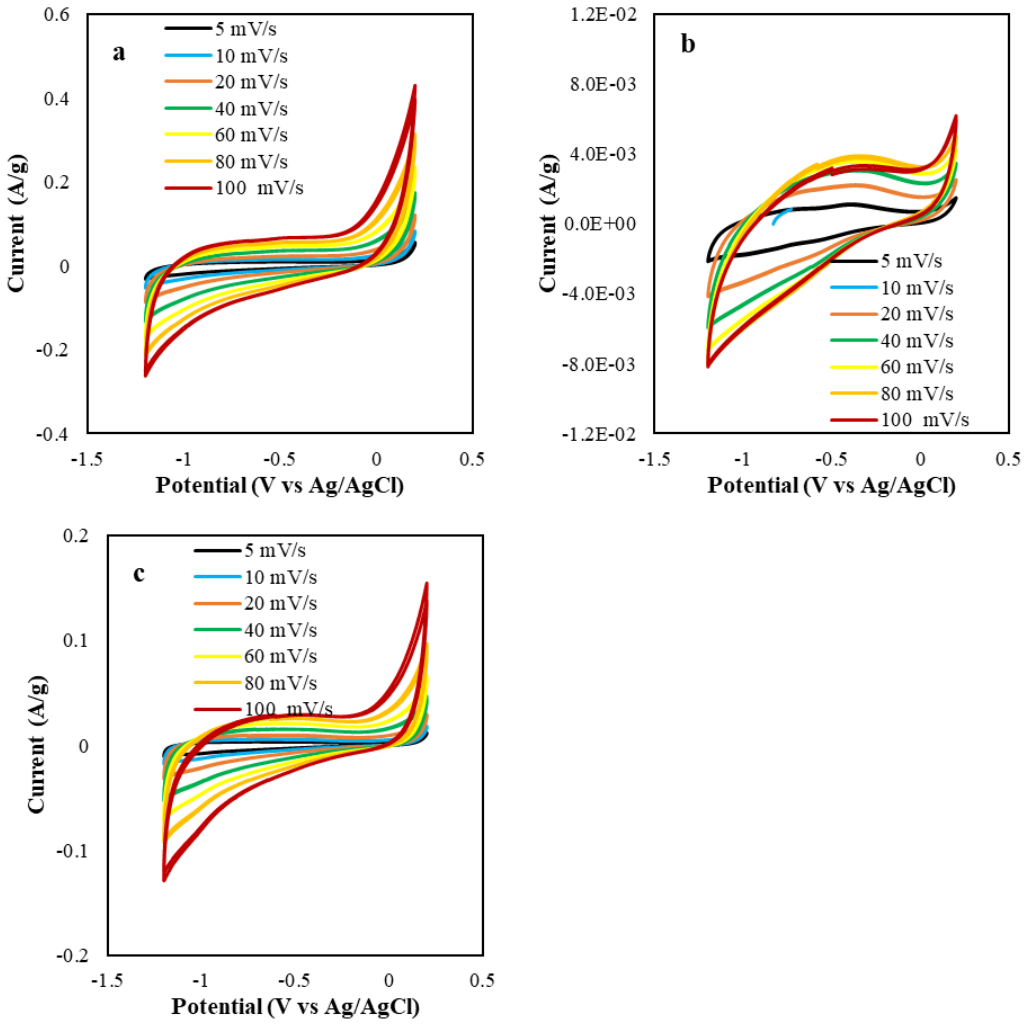

Figures 12 a and b represent the CV plots for capacitance determination of Co_3O_4@CNDs hybrid NPs with AC mixtures using PVDF and PTFE as binders. Replacing the CB with AC yielded comparatively better capacitance values for the Co_3O_4@CNDs hybrid NPs. The capacitance calculated for the Co_3O_4@CNDs hybrid NPs, PVDF, and AC mixture at the 6:1:3 ratio was 7.6 F/g, better than all the other binder mixtures. AC possesses superior specific surface area and porosity [175] than the CB which caused the capacitance of the Co_3O_4@CNDs hybrid NPs mixture to increase tremendously.

Figure 12. CV plots for capacitance determination of Co_3O_4@CNDs hybrid NPs with AC mixtures at a 6:1:3 ratio using PVDF and PTFE as binders

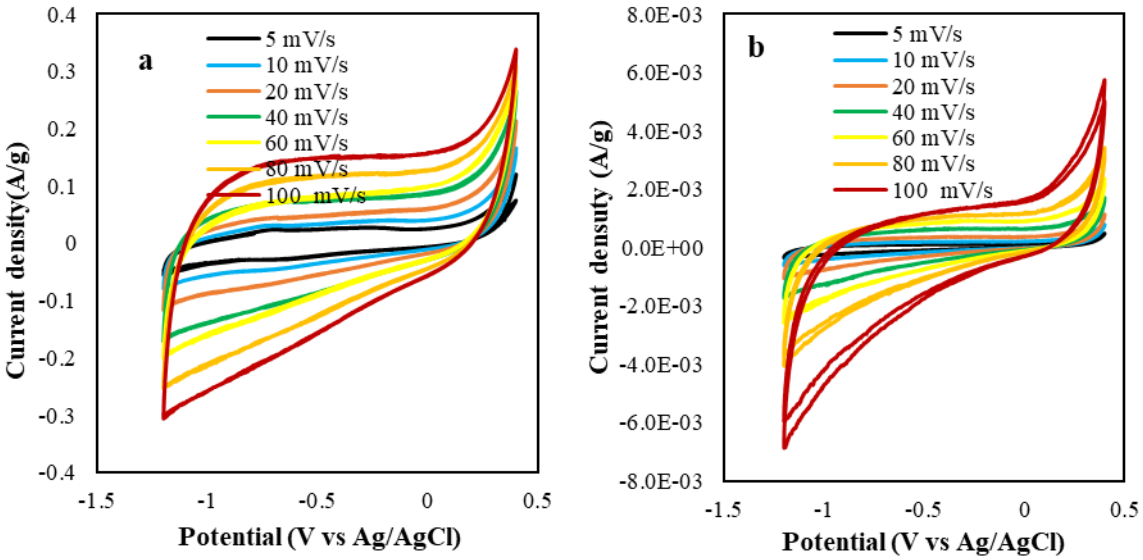

Discussion

The specific capacitance obtained from the CV curves followed the following trend: PVDF > PTFE > Nafion (Table 1). Maximum specific capacitances obtained for PVDF, PTFE, and Nafion binders were 7.6686, 0.3903, and 0.0225 F/g. The CV results showed that Co_3O_4@CND core-shell hybrid NPs, PVDF binder, and AC used in a 6:1:3 ratio had a better capacitance of 7.6686 F/g than all other nanocomposites. The 6:1:3 ratio was the best

combination of slurries that can be used for this capacitance study. Slurry preparation optimization studies were carried out, and the results have shown that the Co_3O_4@CNDs core-shell hybrid NPs, PVDF binder, and AC are the better combination that can be used. The specific capacitance values were calculated and analyzed with this combination. The results showed that the capacitance was 7.6686, 6.9649, and 7.0920F/g in 3 repeated trials. Hence, our results also confirm that most carbon shells are reactive in the Co_3O_4@CND core-shell hybrid NPs.

Table 1. Comparison of the CV plots of the capacitance values with the respective ratios of binders and activated carbons

S.No	Ratio used	Binder used	Conducting material used		Capacitance of Co_3O_4@CNDs (F/g)
			AC	CB	
1.		Nafion			0.0225
2.		DMF			0.016
3.	7:1.5:1.5	PVDF		CB	1.1456
4.	8:1:1	PVDF		CB	0.3337
5.	6:1:3	PVDF		CB	2.7822
6.	6:1:3	PTFE		CB	2.7081
7.	8:1:1	PTFE		CB	0.6418
8.	7:1.5:1.5	PTFE		CB	0.84
9.	**6:1:3**	**PVDF**	**AC**		**7.6686**
10.	6:1:3	PTFE	AC		0.3903

Table 1 showed the calculated comparison values with different binders and activated carbons. The CV plots of Co_3O_4@CNDs core-shell hybrid NPs, prepared with PVDF binder and AC slurry in a 6:1:3 ratio, were found to be in a quasi-rectangular shape which might be expected because of the shell containing the CNDs inferring that mostly the electrochemical double layer capacitance [151], [176], [177] was observed in the CV plots. The Co_3O_4 NPs inside the core might not be very reactive or not contribute enough to the electrochemical properties because of the carbon shell around them while present in the core-shell matrix. The size of Co_3O_4@CNDs core-shell hybrid NPs measured by TEM was 16.6±3.7 nm with core size ranging from 7-10 nm and shell size ranging from 5-10 nm., as reported in the previous chapter. The size of the core formation is expected to be based on the combination of two or three Co_3O_4 NPs inside the core, and that of the shell is based on each particle's core. Also, the size of the core of the Co_3O_4 NPs used for the synthesis was 3.0±1.0 nm, and the reported size of E-CNDs was ±5 nm.

The literature studies have shown that 3D nanostructured materials electrodes have a higher surface area, larger surface-to-volume ratio, and better structural stability over 0D, 1D, and 2D NSMs [178]. So, the less value of specific capacitance might be due to the 0D nature of the core-shell hybrid NPs with less surface area and porosity. Literature has suggested that the porous layers of carbon nanomaterials are often poorly porous or not easily accessible to electrolytes, and the mesoporous nature might contribute to the electrical double-layer capacitor [151]. The significant factors contributing to the carbon nanomaterials reported were high surface area, electrical properties, and porosity [147], [151]. The Co_3O_4@CNDs core-shell hybrid NPs might not have enough surface area, electrical properties, and porosity to contribute to the conductivity to use them for energy storage applications with their properties. Hence, our

results also confirm that most carbon shells are reactive in the Co_3O_4@CNDs core-shell hybrid NPs. These capacitance values were mainly attributed due to their morphological arrangement and as the Co_3O_4 NPs were entirely enclosed inside the carbon shell, which might have made them less or not reactive. So, it can be mainly attributed to the carbon shell region, PVDF binder, and AC used in the slurry preparation, and a minimal contribution from the Co_3O_4 NPs in the core.

In correlation with the literature studies reported, very low specific capacitance is one of the significant disadvantages of these core-shell 0D NPs [150]. The Co_3O_4@CNDs core-shell hybrid NPs possessed fewer electrochemical properties for energy storage applications, which might be ascribed due to their 0D nature. 1D, 2D, or 3D nanomaterials generally have a better electrochemical, electrical, high surface area, and porosity than core-shell NPs, usually 0D. In contrast, the 0-D materials possess high electrical resistance due to the grain surface and the boundaries [179]. They can be combined with 1D, 2D, or 3D nanomaterials or platinum NPs to make them be used as an efficient material for energy storage applications such as supercapacitors, ORR, etc., they can be simply combined with either silver nanowires, platinum NPs, or CNFs, or CNTs and can be evaluated for their electrochemical performance. Adding 0D nanomaterials to 1D or more dimensional materials increases the surface area of the material, allowing for more efficient energy storage. The increased surface area also reduces the internal resistance of the supercapacitor, leading to improved power delivery. Furthermore, combining different components improves thermal stability, which is beneficial for cyclic charging and discharging. Then these materials exhibit a higher specific capacitance, significant rate capability, and high cyclic stability due to the surface interactions, electrical properties, porosity,

chemical and mechanical stability, and ionic conductivity as reported in the literature [179].

Table 2 showed the capacitance comparison values from different literature studies.

Table 2. Comparison table for the capacitance of core-shell hybrid NPs reported

S.No.	Material	Type	Dimensionality	Capacitance	Reference
1.	E-CNFs	Nanofibers	3D	4.6	[156]
2.	CNTs/PANI	Composite fiber	3D	38mF/cm^2	[151]
3.	Se@Ag_2Se	Core-shell NPs		1.6pF	[177]
4.	Se@ZnSe	Core-shell NPs		40.1pF	[177]
5.	Se@CdSe	Core-shell NPs		44.2pF	[177]
6.	SiO2@BSA	Core-shell NPs		5.4 pF	[180]
7.	Co_3O_4@CNDs	Core-shell NPs		7.6	This work

Further works

Galvanostatic charge/discharge experiments can be carried out, and their specific capacitance can be calculated and compared with the CV results. EIS can be done to study the charge-transfer resistance that can contribute to the capacitance. The porosity of the Co_3O_4@CND core-shell hybrid NPs can be determined through the BET surface area analyzer gas adsorption, gas expansion, scanning electron microscopy (SEM), or TEM [181]. TEM has to be done for the Co_3O_4@CNDs core-shell hybrid NPs, prepared with PVDF binder and AC slurry in a 6:1:3 ratio to understand their extent of porosity.

Conclusion

This study evaluated the Co_3O_4@CNDs with different binders and ratios with different activated carbon mixtures for the capacitance performance. The capacitance for the Co_3O_4@CNDs core-shell hybrid NPs was calculated as 7.6 F/g. Although this value is less, it is better among the literature studies reported for the core-shell NPs. As there was not much stated on using the small NPs for the capacitance studies, these NPs could be used as an additive mixture to support any 1D, 2D, or 3D materials and increase their respective capacitance due to the hybridization. These preliminary study results were concluded with the hope that these Co_3O_4@CNDs core-shell hybrid NPs might work better with some support materials. Further future studies with these Co_3O_4@CNDs core-shell hybrid NPs with support materials answer the existing gaps in this study.

CHAPTER IV: MULTIFUNCTIONAL CORE-SHELL COBALT OXIDE @ CARBON NANODOT HYBRID CONJUGATES FOR IMAGING AND TARGETING A549 CELLS

Introduction

Carbon nanodots (CNDs) are amorphous, quasi-spherical luminescent carbon NPs with various surface functional groups, which provide excellent water solubility and could be easily functionalized for numerous applications [182]. Their remarkable optical properties, such as enhanced optical fluorescence, photostability, and excitation-dependent emission, combined with their other striking features, including low toxicity, made them a potential candidate for biological applications [183], [184]. The carbon core and surface functional groups are attributed to their improved biocompatibility and renal clearance [182], wherein their high photoluminescence and resistance to photobleaching and rapid penetrability to the nucleus of the cells make them a remarkable diagnostic tool for cellular bioimaging [185], [186]. CNDs are widely tested as a bioimaging probe [185], [186], antioxidant [80], [81], [187], anticancer agent [188], and nanodrug carriers as drug delivery vehicles to increase anticancer drug efficacy for effective targeting in current research studies, including our lab work [189]–[191]. Nevertheless, the delivery research using multifunctional CNDs as a bioimaging agent and vehicle for active targeting of anticancer drugs is expected to serve the booming thrust in theranostic research.

Semiconductor cobalt oxide NPs (Co_3O_4 NPs) are of high stability and multifunctionalities in a variety of applications, such as in sensing, magnetic resonance imaging, and biomedicine, e.g., antioxidant, anticancer, and drug delivery [192]–[194]. The optoelectronic properties of Co_3O_4 NPs have made them inquisitively significant for biological applications [195] including antibacterial [194], antioxidant [196], and anticancer activities [197]. Albeit

these applications, Co_3O_4 NPs possess significant toxicity in their ionic form, and their synthesis approaches are challenging as they generally require more energy and time-consuming techniques [31], [195] These notable toxicities of metal oxide nanomaterials are commonly tackled by combining them with carbon materials through some surface functionalization techniques [4], [198]. The Co_3O_4 NPs have also been researched for use as diagnostic agents and targeted drug delivery by surface functionalization with ligands or other small molecules, or conjugated anticancer drugs [31], [195], [199].

Nanomaterials can be designed and tuned flexibly, an immensely beneficial feature in developing multiple nano-bio interactions with a single composite system [87]. Core-shell NPs have been researched as theranostic tools for detection, imaging agents, and cancer-specific targeting [200]. They show various advantages by introducing multifunctionalities, such as fast pharmacokinetics, improved accumulation at the target sites, and enhanced efficacy [201]. Compared with conventional anticancer drugs, the specific targeting nanomaterial-based systems could reduce the toxicity to healthy tissues by increasing their bioavailability and efficiency to cancer cells passively or actively [87], [200]. To date, there is a critical need for designing and synthesizing multifunctional NPs for greatly improved cancer diagnosis, imaging, and treatment strategically.

Lung cancer spreads more rapidly in humans than in any other cancer, leading to early death within 5 years of diagnosis in 85% of patients, thus being the leading cause of cancer deaths [202]. Histologically lung cancer (LC) cells are classified as non-small cell LCs (NSCLCs) and small cell (SCLCs), amongst which NSCLCs account for 85% of the total LC patients. A549 cancer cells are lung adenocarcinoma cell lines, falling under the significant class

of NSCLC, so developing a theranostic drug against them is essential via passive and/or active targeting multifunctional nanomaterials-based drug delivery [84], [203].

The passive targeting process attempts to augment the nanomaterials accumulation through enhanced penetration and retention (EPR) in the tumor tissues, and the active targeting process necessitates conjugating specific ligands on nanomaterials for tumor receptors [85]. However, passive targeting is ineffective in many cases, as the tumor cells usually have a leaky vasculature, where the nanomaterials could leak through. As a result, the EPR effect might not be achieved effectively. Active targeting process may address this issue by loading anticancer drugs and binding ligands to nanomaterials to provide strong affinity and specificity to tumor cells more precisely [87], [204]. Generally, tumor cells have specific target molecules called receptors attached to the cell surface, while normal cells don't. These receptors possess a high affinity to certain specific molecules called ligands. The tumor microenvironment may contain overly expressed receptors such as EGFR (Epidermal growth factor receptor), FR (Folate receptor), CD44 receptors (Cluster of Differentiation), CD71 (Transferrin), luteinizing hormone release hormone (LHRH), adenosine triphosphatases (ATPases), and chemokine receptor type 4 (CXCR4) [84]. Ligands are substances that can target these receptors with high affinity, once the targeting materials containing the ligands reach the specific tumor sites [205]. The active targeting strategy using the ligands conjugated nanomaterials to bind overexpressed receptors on the cancer cell surfaces renders site-specific delivery drugs for tumor treatment [84], [87], [205], in general, by facilitating endocytosis and inhibiting the multi-drug resistance (MDR) effect of tumor cells [23], [28], [31]. Specific ligands that can be used for targeting lung cancer receptors include some small molecules such as folic acid (FA), transferrin (Trf), polymers (Polyethylene glycol-PEG, polyvinyl pyrrolidone – PVP, and silica NPs), and heparin (Hep) [84], [203], [205].

These molecules can be conjugated with nanomaterials or anticancer drugs effectively. Heparin, and PEGylated silica-based NPs, coupled with fluorescent dyes, are also used as ligands to increase the bioavailability, and target the A549 cells through energy-dependent endocytosis reactions [188], [206]–[208]. Successful use of these ligands to combine with the nanomaterials and anticancer drugs such as doxorubicin, curcumin, paclitaxel, and cisplatin was reported to have better targeting to the cancer cells and improved bioavailability [190], [203], [205]. Cross-linking chemistry is a common strategy for coupling ligands with NPs via covalent conjugation of amidation reactions and increasing their water solubility and conjugation efficiency [209]–[213].

In this work, we synthesized core-shell cobalt oxide @ CNDs (Co_3O_4@CNDs) hybrid NPs using a simple microwave-assisted synthetic method [169]. The hybrid NPs are advantageous for biological studies by offering photoluminescence (PL), high biocompatibility, small size, and controlled morphology. These advantages render them multifunctionalities as effective bioimaging and delivery agent. In this research, the hybrid NPs were conjugated with an anticancer drug, DOX, to increase their therapeutic effect, and various ligands, i.e., folic acid, heparin, transferrin, or other molecules specific to A549 cancer cells for a comparison study of their biocompatibility, targeting specificity and cytotoxicity.

Materials and Methods

Materials

Chemicals, including cobalt acetate tetrahydrate (Sigma Aldrich), pure anhydrous ethanol (Sigma Aldrich), 25- 28% ammonium hydroxide solution (Sigma Aldrich), citric acid (ACROS Organics), ethylenediamine (EDA, Fisher Scientific) and deionized (DI) water, dyes, such as Alamar blue (Thermo-fisher), Mitotracker red CMXRos (Thermo-fisher) and DCFH-DA (Sigma

Aldrich) were used in this work. Solvents, such as paraformaldehyde (FisherSci), Phosphate buffered saline (PBS) (Thermo-fisher), triethanolamine (Fisher Scientific), formamide (Sigma Aldrich), anhydrous dimethyl sulfoxide (Thermofisher), and ligand molecules and agents, including Folic Acid (FA) (Alfa Aesar), Bovine Serum Albumin (BSA, Sigma Aldrich), Doxorubicin (DOX, Fisher Sci), Heparin (Sigma Aldrich), Rhodamine (Sigma Aldrich), Polyvinyl pyrrolidone (PVP, Sigma Aldrich), Polyethylene glycol (PEG, Alfa Aesar), Tetra ethyl ortho silicate (TEOS, Sigma Aldrich), Transferrin (Trf, Sigma Aldrich) were used without further purification. EAhy926 and A549 cells were purchased from ATCC. Cell culture media, Dulbecco's Modified Eagle Medium (DMEM), and Ham's F-12 Nutrient Mixture (F-12K medium) were purchased from ATCC, whereas fetal bovine serum (FBS, Fisher Sci), penicillin-streptomycin, Pen-Strep (Thermo-fisher), and TrypLE buffer (Thermo-fisher) were used for the cell studies. All the materials mentioned above were used in this work without further purification and are of analytical grade.

Material Synthesis

Synthesis of Co_3O_4@CND hybrid NPs

Co_3O_4 NPs were synthesized first. Briefly, cobalt acetate tetrahydrate and absolute ethanol were used as precursors to synthesize Co_3O_4 NPs and then mixed and stirred with ammonia by following a reported procedure [102]. Then the content was transferred to a microwave synthesizer (CEM Corp 908005 Microwave Reactor Discovery System). under a pressure-controlled, sealed environment with 300 W power, 100 psi pressure, and 150°C temperature for 30 minutes. These particles were collected, purified at 10,000 rpm for 10 minutes, dried under the furnace at 80°C, and labeled as Co_3O_4 NPs. These Co_3O_4 NPs were used to synthesize core-shell hybrid NPs by following our established CNDs synthesis procedure

[169]. This simple microwave method without using any organic solvents produced core-shell Co_3O_4@CNDs hybrid NPs. CNDs alone were also synthesized for comparison of the characterization and cell studies.

Co_3O_4@CND hybrid NPs conjugation with FA-BSA-DOX

FA-BSA conjugation was carried out for effective attachment of FA to the Co_3O_4@CND hybrid NPs by EDC-NHS-based cross-linking reactions using a reported procedure [214]. Afterward, the product with FA and BSA was stirred for 24 hours. Then the FA-BSA complex was collected and dialyzed with 1 kDa membrane for three days to obtain purified particles and freeze-dried. Co_3O_4@CND hybrid NPs (5 mg in DI water mixed by sonication) and the FA-BSA complex dispersed in PBS solution (pH = 7.4) were added and stirred for 24 hours again. The final brown product was collected and dialyzed in a 1 kDa membrane for three days. The residues were then dried using a freeze-dryer (Labconco Free Zone 6 Freeze-Dryer) and labeled as FA-BSA-Co_3O_4@CNDs.

The DOX was loaded onto the FA-BSA-Co_3O_4@CND hybrid NPs by mixing [214], [215]. Firstly, 2 mg of the FA-BSA-Co_3O_4@CND hybrid NPs were dispersed in 10 mL of PBS solution by sonicating for 1 h to disperse thoroughly. Then 1 mg of DOX was added and stirred for 24 h in a dark condition. The excess of uncombined DOX was removed through centrifugation at a speed of 10,000 rpm. The precipitate was washed several times dialyzed with a 1 kDa membrane for 24 hours and freeze-dried. The dried products were labeled as FA-BSA-Co_3O_4@CNDs-DOX. The DOX drug loading capacity was calculated using **Eq. 1**:

$$\text{Dox loading ratio} = \frac{\text{Weight of the drug,DOX in Co3O4@CNDs NPs}}{\text{Weight of Co3O4@CNDs NPs}} \times 100\% \qquad (1)$$

Co_3O_4@CND hybrid NPs conjugation with Hep-DOX

Co_3O_4@CNDs-Hep was prepared using a method of self-assembly and graft copolymerization technique using a reported procedure where heparin was grafted on the surface of the Co_3O_4@CNDs by the amide bond formation between them [188]. Firstly, Hep (0.5 g) was first dispersed in 10 mL formamide, then 205 mg EDC and 115 mg NHS were added and stirred for 12 h in a dark place. Then, the obtained colorless solution was filtered by a 0.22 μm syringe filter to remove any residues, and the solution was precipitated by acetone. After drying the precipitates at 60 °C for 24 h, a light white sticky solid was obtained, labeled as Hep-NHS.

The Hep-NHS (0.3 g) was dispersed in 5 mL formamide and 5 mL anhydrous dimethyl sulfoxide and then mixed with 50 mg Co_3O_4@CNDs and 1% triethanolamine. All these contents were stirred for 12 h in the dark. Then the solution was precipitated with acetone and the residues were collected. The collected residues, Co_3O_4@CNDs-Hep, were washed with ethanol to remove unbound Hep. Finally, the Co_3O_4@CNDs-Hep solution was dried by freeze-dryer and stored at -20 °C before use.

DOX was loaded onto the Co_3O_4@CNDs-Hep by dialysis method [188]. Co_3O_4@CNDs-Hep (0.2 mM) was dispersed in DI water by ultrasonication at RT. DOX (0.1 mg/mL) was added into the yellow Co_3O_4@CNDs-Hep solution and stirred for 12 h in a dark place. After thorough mixing, the solution was dialyzed (1 kDa) against DI water for 48 h. DOX drug loading capacity on Hep-Co_3O_4@CNDs was calculated by using **Eq. 1**.

Co_3O_4@CND hybrid NPs conjugation with PVP, PEGylated silica, and Rhod

Co_3O_4@CND hybrid NPs conjugation with PVP-SiO_2-PEG-Rhod was done by modifying a reported procedure [208], [216]. Accordingly, a 10% aqueous ethanolic solution of PVP (50 mg PVP in 10 ml of ethanol) was added firstly to the Co_3O_4@CND hybrid NPs for

improving the chemical stability. The PVP-stabilized Co_3O_4@CND hybrid NPs were then separated by centrifugation at 10,000 rpm for 30 minutes by washing with acetone, and re-dispersing with ethanol. Then, 3-aminopropyltriethoxysilane (APS) and rhodamine B (Rhod) were mixed in the dark to yield trimethoxy silane (TMS) with Rhod. A solution of TEOS and Rhod-modified TMS with a molar ratio of 0.3/0.04 was added dropwise into the ethanol solution of PVP-stabilized Co_3O_4@CNDs NPs. Ammonia solution (0.86 mL; 30 wt% by NH3) was injected as a catalyst in the reaction to yield PVP-Co_3O_4@CNDs–SiO_2-PEG NPs with Rhod dye. These particles were washed and precipitated with ethanol by centrifugation at 10000 rpm for 50 mins. The separated hybrid NPs (45 mg) were again dispersed in 10 mL of absolute ethanol and mixed with 125 mg of 2- [methoxy (polyethylene oxy) propyl] trimethoxy silane (PEG-Si $(OMe)_3$; 0.02 mmol) at pH12 (adjusted with ammonia) for improving their biocompatibility. The final product, PVP-Co_3O_4@CNDs-SiO_2-PEG-Rhod simply labeled as Co_3O_4@CNDs-Rhod, was collected by washing and centrifuging with ethanol at 10,000 rpm for up to 60 minutes.

Co_3O_4@CND hybrid NPs conjugation with Trf-DOX

This conjugate was synthesized by linking the Co_3O_4@CNDs with EDC and NHS cross-linking reactions by covalently coupling carboxyl groups to primary amines [209]. The stepwise procedure was described below.

Firstly, Co_3O_4@CNDs (3 mg) dispersed in 2 mL of PBS, pH 7.4, were added with EDC (6.7 mg) stirred at room temperature. After 30 minutes, a 1 mL PBS solution of 4 mg mL^{-1} NHS was added to the above solution, and the mixture was stirred for another 30 minutes. Then 1 mL of 8 mg mL^{-1} PBS Trf solution was added dropwise and stirred the mixture for 2 hours at room temperature. The reaction mixture was then collected and purified using a 1 kDa dialysis membrane. The conjugated Co_3O_4@CNDs–Trf NPs were collected. One half was dried using

freeze-drier, and the other half was used for the DOX conjugation without further treatment [217].

Then, in the Co_3O_4@CNDs–Trf conjugate solution, EDC (6.7 mg) was added and stirred for 30 minutes at ambient temperature. Then, NHS (4 mg) was added and stirred again for another 30 minutes. Then, a solution of DOX (2 mg) in DMSO (0.1 mL) and DI water (1.0 mL) was added and stirred for two more hours. The final product was then purified by dialyzing using a 1 kDa membrane for three days. Co_3O_4@CNDs–Trf–DOX conjugates were then freeze-dried and stored at -20˚C for further characterization and cell viability studies [209]. DOX drug loading capacity was calculated for the Co_3O_4@CNDs–Trf–DOX by using Eq. 1.

Characterization

The morphology of the Co_3O_4@CNDs hybrid NPs and all other synthesized NPs, such as FA-BSA-Co_3O_4@CNDs-DOX, Hep-Co_3O_4@CND-DOX, Co_3O_4@CND-Rhod, and Co_3O_4@CND-Trf-DOX hybrids were characterized and compared using transmission electron microscopy (TEM, Carl Zeiss Libra 120 Plus). The ligand-attached synthesized NPs were also studied to understand their changes in the structures and optoelectronic properties after conjugation, by comparing them with their counterparts, including FA, FA-BSA, FA-BSA-Co_3O_4@CNDs, Hep-NHS, Hep- Co_3O_4@CNDs, Trf, Trf-Co_3O_4@CNDs, DOX, and Co_3O_4@CNDs. The characterization studies, such as Ultraviolet (UV) - Visible absorbance (Agilent), photoluminescent, PL (Horiba Spectrophotometer), Fourier Transform Infra-Red (FTIR) spectroscopies (Varian 670), and Malvern Zeta sizer – dynamic light scattering (DLS, Malvern Instruments ZEN3600) were performed for each of the synthesized NPs and their respective individual counterpart elements for evaluating their optical, structural, and surface charge properties for using them as an effective anticancer agent.

Cellular studies

Cell-culture

EAhy926 endothelial and A549 adeno-carcinomic lung epithelial cell lines were cultured in a DMEM and F-12K medium-containing 10% Fetal Bovine Serum (FBS) and 1% Pen-Strep and are grown in a CO_2 incubator (5%) at 37°C. After cultured and grown, these cells are passaged with Tryp LE/EDTA and cultured for further measurements.

Cellular uptake and Subcellular Localization analysis of Co_3O_4@CNDs hybrid NPs

Cellular uptake and sub-cellular localization of the Co_3O_4@CNDs hybrid NPs and CNDs were studied and compared through confocal microscopy. Firstly, 1×10^5 cells were seeded on coverslips and placed in 12-well plates. EAhy926 and A549 cells were treated with Co_3O_4@CNDs hybrid NPs and CNDs at concentrations of 0, 0.4, and 0.8 mg/mL in designated wells, respectively. After 20-24 hours of treatment, the cells were fixed with paraformaldehyde and then stained with Mitotracker red CMXRos dye (0.2 µM for EAhy926 and 0.1 µM for A549 cells, 10 mins, 37 °C, Molecular Probes, $\lambda_{ex}/\lambda_{em}$ at 579/599 nm) to stain the actin filaments in the mitochondria. Cells were washed with PBS twice before imaging. Co_3O_4@CNDs hybrid NPs and CNDs with concentrations of 0, 0.4, and 0.8 mg/mL were imaged at oil immersion 63X using a confocal microscope to verify the viability and uptake in EAhy926 and A549 cells. The sub-cellular localization of the dye and the NPs was observed by simultaneously imaging the cells on the coverslips for the Co_3O_4@CNDs hybrid NPs (with 0.4 mg/mL concentration). Imaging was performed under Zeiss Z1 Spinning Disk confocal microscope with Rhod channel for the mitochondrial layers in the cells and DAPI channels for the hybrid NPs using a higher magnification, 100X oil immersion objective lens for a deeper understanding of the sub-cellular localization. The concentrations of the NPs and Mitotracker Red were optimized to exclude

interference. Co_3O_4 NPs do not have much fluorescence in cells, and they were not used for comparison in this study.

Intracellular antioxidant measurement

The dichloro fluorescein diacetate (DCFH-DA) assay monitors the intracellular reactive oxygen species (ROS) levels in EAhy 926 and A549 cells, where the DCFH-DA acts as an oxidative stress and hydroperoxide probe [218]. Firstly, 1×10^4 cells were seeded in a 96-well plate and cultured for 24 hours. Then the cells were treated with different concentrations of Co_3O_4@CNDs hybrid NPs, Co_3O_4 NPs, and CNDs for 24 hours, such as 0 - 0.8 mg/mL. The cells were washed twice with 1X PBS, and 10 and 20 μM of DCFH-DA probe in FBS-free media was added to the treated EAhy926 and A549 cells, respectively. After incubating for 30 minutes at 37 °C, the cells were washed twice with 1X PBS to remove the dye interference and then replaced with 1X PBS for the measurement in the plate reader. The cells with PBS were incubated at 37 °C for 5 minutes, and the fluorescence intensity was measured at λ of excitation 485 and emission 530 nm. These measurements measure the oxidation of DCFH-DA to DCF due to intracellular ROS generation. As controls, the cells without NPs treatment and the NPs treated cells with no DCFH-DA are used. Cells treated with ascorbic acid (AA), a powerful antioxidant, were compared as a negative control. The normalized fluorescence intensity from the plate reader measurements was calculated by subtracting with the blank (no dye-treated cells).

Biocompatibility and Cytotoxicity studies

A viability assay was performed using the Alamar blue test. Percentage viability was carried out for the Co_3O_4@CNDs hybrid NPs and compared with their counterparts, Co_3O_4 NPs, and CNDs in both the EAhy926 and A549 cells. Briefly, 1×10^4 cells were seeded in every well in a 96-well plate with the DMEM and F12K complete media and incubated for 24 hours. Then

the cells were treated with different concentrations ranging from 0 - 0.8 mg/mL of Co_3O_4@CNDs hybrid NPs, Co_3O_4 NPs, and CNDs for 24 hours. As a control, the cells without NPs and the respective concentrations of NPs without cells were used for studying the extent of cytotoxicity in the cells. The Alamar blue assay quantitatively determines cell viability, assessed by their metabolic reactions. When Alamar blue was added to the cells, its oxidized form penetrates through the cytosol, thereby reducing the mitochondrial activity by accepting electrons from enzymes such as NADPH, FADH, FMNH, and NADH, as well as from the cytochromes [219]. The measurements were read on a plate reader at wavelengths of excitation at 560 and emission of 590 nm, representing the number of living cells. The percentage of viable cells was calculated using **Eq. 2**,

$$\text{Viability}(\%) = \frac{\text{Fl(treatment)} - \text{Fl(blank)}}{\text{Fl(control)} - \text{Fl(blank)}} \qquad (2)$$

where Fl is the fluorescence intensity. The percentage viability of all the synthesized NPs of Co_3O_4@CNDs hybrids with ligand and DOX conjugation was determined using the same AB assay protocol by comparing with the respective ligands, DOX, and Co_3O_4@CNDs hybrid NPs without conjugation to compare their biocompatibility and cytotoxicity in EAhy926 and A549 cells, respectively. Also, the counterparts, such as FA, FA-BSA, FA-BSA-Co_3O_4@CNDs, Hep-NHS, Hep-Co_3O_4@CNDs, Trf, Trf-Co_3O_4@CNDs, DOX, and Co_3O_4@CNDs were compared in the viability studies in EAhy926 and A549 cells to understand the anticancer activity of the ligands better. The effective drug dosage, IC_{50}, was 4 mg/mL in a reference stated, and a maximum concentration of 0.4 mg/mL (1/10th of IC_{50}) was chosen in their cell studies [206]. Similarly, in our study, we used higher concentrations of Co_3O_4@CND hybrid NPs conjugated with the ligands, such as 0, 0.1, 0.2, and 0.4 mg/mL, to measure their extent of biocompatibility and cancer-targeting effect safely.

Data Analysis

Each assay was carried out with three independent experiments. The confocal microscopic images were analyzed using Axiovision 4.8 and ImageJ software. The mean and standard error (SE) were calculated, and the data and their respective significant difference were analyzed using Microsoft Excel. An asterisk was indicated for significance at probability, $P < 0.05$ compared to the 0 mg/mL from a one-tailed t-test analysis. The fluorescence intensities in the quantified histograms in each plate reader measurement were subtracted from the background (blank) fluorescence.

Results and Discussions

Physicochemical properties and Characterization of synthesized NPs

After synthesizing Co_3O_4 NPs, CNDs, and Co_3O_4@CNDs hybrid NPs, they were dispersed in DI water to make the same concentration and checked to see if they possessed any fluorescence under UV light. **Fig. S4.1** showed a photograph with bluish fluorescence from CNDs and Co_3O_4@CNDs under the UV chamber. The DOX loading capacity using the FA-BSA-Co_3O_4@CNDs, Hep-Co_3O_4@CNDs, and Co_3O_4@CNDs–Trf was calculated as 96.25%, 93.75%, and 99.7% (wt), respectively, using **Eq. 1**. The successful conjugated NPs in this study were characterized using microscopy and spectroscopy means for morphology, structural and property analysis.

The TEM of the synthesized, dried Co_3O_4@CNDs before and after conjugations with the conjugated NPs were shown in **Figure. 13 a-e**, respectively. The TEM image of the Co_3O_4@CNDs (**Figure. 13a**) showed that the synthesized NPs were spherical and uniform. The average size obtained from the ImageJ analysis of the TEM image showed the core-shell

structures possessed an average size of 14.7±3.7 nm, with a core diameter of 11.9±2.9 nm and shell size of 2.8±0.4 nm covered on the core structure. All the NPs after conjugation with the

Figure 13. a. TEM image of a. Co_3O_4@CNDs, b. FA-BSA-Co_3O_4@CND-DOX, c. Hep-Co_3O_4@CND-DOX, d. Co_3O_4@CND-Rhod, and e. Co_3O_4@CND-Trf-DOX hybrids

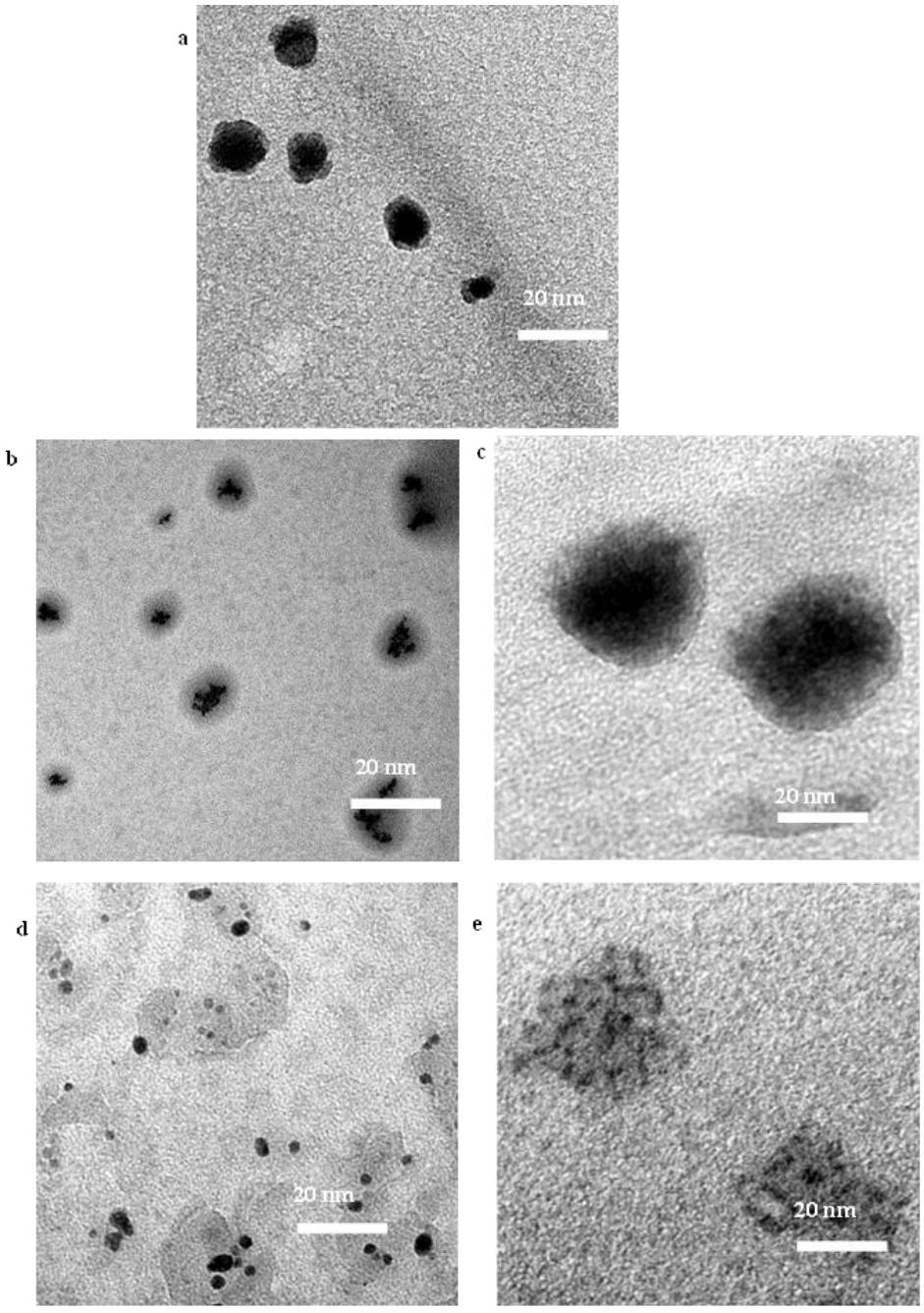

respective ligands were uniform and spherical in shape. The smaller size and modification with ligands are advantageous to selectively deliver Co_3O_4@CNDs and DOX into A549 cells with FA receptors, further reducing the hazard to normal human cells [84], [203]. TEM images of the ligand-conjugated NPs, FA-BSA-Co_3O_4@CNDs-DOX, Hep-NHS-Co_3O_4@CNDs-DOX, Co_3O_4@CNDs-Rhod and Co_3O_4@CNDs-Trf-DOX (**Figure. 13b-e**) suggested that their average sizes were in the range of 19.0±3.0, 29.5±2.5, 34.0±2.0, 30.0±6.0 nm, respectively. The TEM images of Co_3O_4@CNDs-Rhod (**Figure. 13d)**, and Co_3O_4@CNDs-Trf-DOX (**Figure. 13e)** containing some shell layers, which might be expected due to the silica covering and the PEG-ylation and the conjugation of Trf with DOX, which had increased the size of Co_3O_4@CNDs.

Figure 14. Comparison FTIR spectra of Co_3O_4@CNDs hybrid NPs, FA-BSA-Co_3O_4@CND-DOX, Hep-Co_3O_4@CND-DOX, Co_3O_4@CND-Rhod, Co_3O_4@CND-Trf-DOX hybrids, and DOX

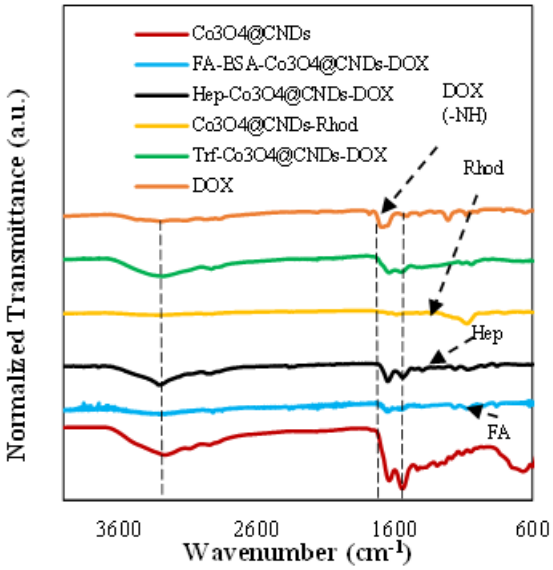

Figure. 14 showed the FTIR spectra of the four different synthesized NPs before and after conjugation and also compared them respectively with DOX. The FTIR spectra in **Figure. 14** demonstrated that the synthesized NPs with FA-BSA-Co_3O_4@CND-DOX, Hep-

Co_3O_4@CND-DOX, Co_3O_4@CND-Rhod, Co_3O_4@CND-Trf-DOX hybrids possessed the characteristic ligand peaks such FA, Hep, Rhod, Trf, and peaks representing DOX in their structure confirming the attachment of the ligands. The FTIR of the conjugates were individually compared with their counterparts such as FA, FA-BSA, and FA-BSA-Co_3O_4@CNDs for the FA-BSA-Co_3O_4@CNDs-DOX conjugates in **Figure. S4.2a**, Hep, and Hep-Co_3O_4@CNDs in **Figure. S4.2b**, and Sulfo-Rhod in **Figure. S4.2c** and Trf-Co_3O_4@CNDs and DOX in the **Figure. S4.2d**. FTIR spectra of Co_3O_4@CNDs hybrid NPs showed the peaks corresponding to Co (II) and Co (III) at 578 and 665 cm^{-1}, the valence states of Co_3O_4, and -C-C- (1542 cm^{-1}), -C=N (1635 cm^{-1}), -CH (2900-3050 cm^{-1}), and -OH (3100-3400 cm^{-1}) bonds, characteristic of CNDs [18], [29], [220]. Whereas, after conjugation, the FTIR (**Figure. S4.2a**) of the FA-BSA-Co_3O_4@CNDs and FA-BSA-Co_3O_4@CNDs-DOX showed the typical stretching vibration peaks, 937 cm^{-1}, attributed to FA [221]. Additional peaks with C–N double bonds (1640 cm^{-1}) and -N-H (1564 cm^{-1}) and amide bond (1700 cm^{-1}), and partial benzene ring vibration (1351 cm^{-1}), characteristic of DOX [222] were observed in the FA-BSA-Co_3O_4@CNDs-DOX, thereby confirming the attachment of DOX. The FTIR (**Figure. S4.2b**) comparison of the Hep-NHS-Co_3O_4@CNDs with its respective DOX modification demonstrated the presence of functional groups, such as Hep (-COO- group at 1612 cm^{-1}), NHS (ester group at 1693 cm^{-1}, which was formed during the conjugation of Hep and NHS), and peaks corresponding to the DOX structure (1643 cm^{-1}) [188], [207]. The FTIR (**Figure. S4.2c**) comparison of Co_3O_4@CNDs-Rhod, Sulfo-Rhod with Co_3O_4@CNDs inferred that many new peaks corresponding to the PEG, Rhod, and silica functionalization were observed. The symmetric and asymmetric stretching vibrations peaks of C–O–C were located at 1034 and 1234 cm^{-1}, respectively, indicating that the PEG-Co_3O_4@CNDs functionalization possesses hydroxyl, carbonyl, and carboxylic groups. The

strong peak at 1542 cm^{-1} is due to the stretching of -N-O bonds, and the peaks in the region 1600 -1300 cm^{-1} and at 2942 cm^{-1} represent graphitic bonds and -CH_2 from PEG [223], [224]. The smaller peaks at 1042 and 732 cm^{-1} are due to the silica functionalization (-Si-O-C and -Si-O-Si- symmetrical stretching vibration shift) present on their surface due to the condensation of TEOS with carbon in the conjugates [225]. The FTIR (**Figure. S4.2d**) comparison of the Co_3O_4@CNDs-Trf, inferred the modification as the stretching vibration peaks, such as -C═O in the amido (II) bond (1634 cm^{-1}), formed from the EDC-NHS chemistry, and benzene ring (1410 cm^{-1}) in the DOX structure was observed in the Co_3O_4@CNDs-Trf-DOX [210].

The optical photoelectronic properties of the NPs, such as absorbance and fluorescence, play a significant role in bioimaging in the cells, viability measurements, and other biological studies [57], [58]. The UV-Visible and PL spectroscopies (**Figure. 15a and b**) measured the absorbance and fluorescence of the Co_3O_4@CND hybrid NPs and the four mentioned conjugates compared with DOX. The absorbance band of the Co_3O_4@CND hybrid NPs, at 254 nm in the UV-Visible spectrum was attributed to the π–π^* transition of C=C bonds in the sp^2 domains [40], [59], and the band at 360 nm of the Co_3O_4@CND hybrid NPs characteristic to n-π intramolecular transitions of -C=O surface states [60], [61]. PL spectroscopy data showed that when the Co_3O_4@CND hybrid NPs are excited at 360 nm, they emit strongly at 450 nm wavelength with maximum fluorescence in correlation with the CNDs [61]. The UV-Visible and PL spectroscopy characterization of the synthesized NPs with ligand and DOX conjugations in **Figure. 15a and b** showed a noticeable change with some shifts in their absorbance and PL maximum intensities, thereby confirming the conjugation with their respective ligands had been successful. The absorbance and fluorescence were measured with different concentrations of Co_3O_4@CND hybrid NPs by UV-Visible and PL spectroscopies to calculate the quantum yield. The quantum yield (QY)

of the NPs was calculated based on the above characterization results using the normalized absorbance and fluorescence with **Eq. 3** [207], [224]:

$$\Phi_C = \Phi_{QS} \times [\frac{I_C}{I_{QS}}]^2 \times [\frac{\eta_C}{\eta_{QS}}]^2 \qquad (3)$$

where ϕ_C, ϕ_{QS}, I_C, I_{QS}, η_c, η_{QS} are quantum yield, intensities, and refractive index of water: 1.33 with the subscripts, C and QS representing the Co_3O_4@CND hybrid NPs and quinine sulfate. Also, the integrated fluorescence intensity was calculated using the cumulative absorbance and fluorescence intensities, where ϕ_{QS}=0.54 and (η_c^2/η_{QS}^2) = 1. The QY calculated using this formula for the Co_3O_4@CND hybrid NPs was 49.63±1.3%, slightly less than the CNDs (53.2±0.6%). The QY of the Co_3O_4@CND hybrid NPs was attributed to the hybridization with Co_3O_4 NPs, which might have decreased the extent of the QY, ascribing to the chemical nature and abundant surface energy of the NPs [207].

Figure 15. a. Comparison (a) UV-Visible absorbance and (b) PL spectra of Co_3O_4@CNDs hybrid NPs, FA-BSA-Co_3O_4@CND-DOX, Hep-Co_3O_4@CND-DOX, Co_3O_4@CND-Rhod, Co_3O_4@CND-Trf-DOX hybrids, and DOX

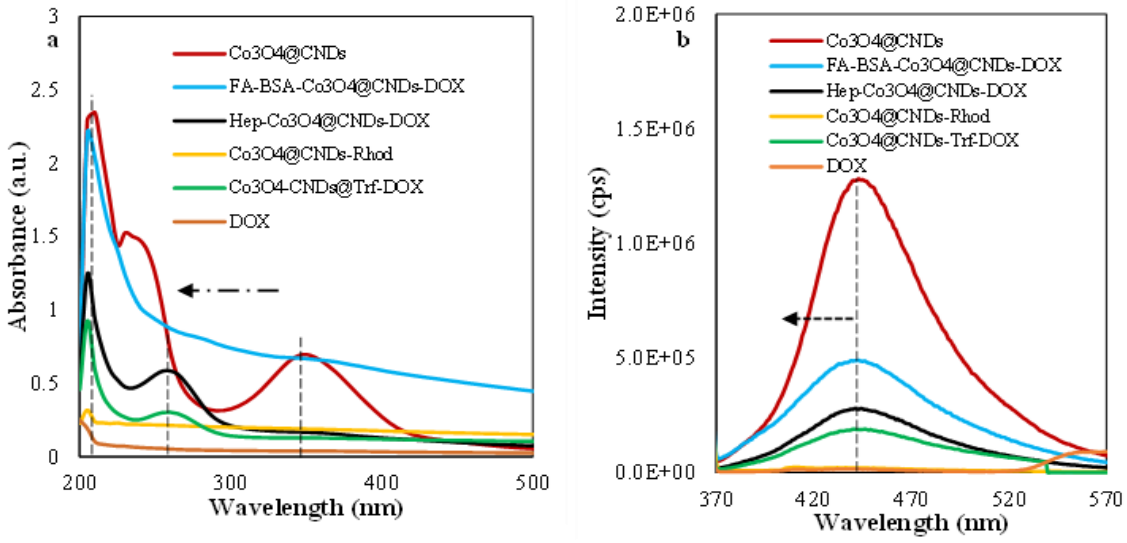

The UV-Visible absorbance spectra of the conjugates were individually compared with their counterparts such as FA, FA-BSA, and FA-BSA-Co_3O_4@CNDs for the FA-BSA-Co_3O_4@CNDs-DOX conjugates in **Figure. S4.3a**, Hep, and Hep-Co_3O_4@CNDs in **Figure. S4.3b**, and Sulfo-Rhod in **Figure. S4.3c** and Trf-Co_3O_4@CNDs and DOX in the **Figure. S4.3d**. In the UV-Visible absorption spectra of FA-BSA-Co_3O_4@CNDs compared with DOX (**Figure. S4.3a**), the main absorbance peak of the Co_3O_4@CNDs at 350 nm was slightly shifted after attaching FA-BSA and DOX. The absorbance peak of FA-BSA-Co_3O_4@CNDs with DOX was tailing around 229 nm. There was an increase in the absorbance intensity in the same tailing absorbance peak as in the FA-BSA-Co_3O_4@CNDs, thereby confirming the effective loading of the drug, DOX. The increase in the absorbance intensities after DOX conjugation was due to the strong hydrogen bonds and π-π interactions between them [214], [226]. In **Figure. S4.3b**, after conjugating the Co_3O_4@CNDs with the Hep-NHS, the absorbance peak shifted from 350 to 260 nm, characteristic of Hep-NHS [188], and the absorbance intensity at 260 nm increased compared to Hep-NHS. The UV-Visible absorption spectra (**Figure. S4.3c**) and PL spectroscopy (**Figure. S4.4c**) confirmed that the conjugation with the Rhod happened as the intensity was dropped for the Co_3O_4@CNDs-Rhod completely when compared with the Co_3O_4@CNDs. No absorbance and fluorescence intensity were observed in the conjugates, which might have been expected due to the PEGylation effect, which might have covered the Co_3O_4@CNDs-Rhod NPs completely. Photobleaching might also be a reason, with this complex, from the Rhod dye, and so their absorbance intensities might have been diminished [208]. In **Figure. S4.3d**, the absorbance maximum peak of Trf at 279 nm shifted slightly after conjugation with the Co_3O_4@CNDs. In the Co_3O_4@CNDs–Trf–DOX, the absorbance maximum hypsochromically shifted from 279 nm to 260 nm, which was expected mainly due to the DOX conjugation. [227].

An increase in the absorbance intensity was observed after modification with DOX in the Co_3O_4@CNDs–Trf–DOX compared with Co_3O_4@CNDs–Trf.

Similarly, the PL spectra with their counterparts are shown in **Figure. S4.4 a-d**. PL spectroscopy of the FA-BSA-Co_3O_4@CNDs (**Figure. S4.4a**) showed that the Co_3O_4@CNDs intensity decreased after modification with FA-BSA to a greater extent at 440 nm, whereas after modification with the DOX, the intensity dropped significantly. This significant drop in the fluorescence intensity of conjugates was expected due to the DOX which caused π-π stacking of molecules to a greater extent [226]. **Figure. S4.4b** showed that the PL intensity of Co_3O_4@CNDs was quenched after modification with Hep-NHS to a greater extent, and the emission was shifted slightly from 453 nm to 443 nm. The intensity for Hep-NHS at 440 nm was negligible. **Figure. S4.4d** showed that the Co_3O_4@CNDs intensity decreased after modification with Trf to a greater extent. After modification with the Trf and DOX, the intensity quenched still with a hypsochromic shifting of the emission spectrum from 448 nm → 442 nm to 420 nm, thereby confirming the effective conjugation.

The excitation dependencies (ED) of the NPs from the PL spectra were shown in **Figure. S4.5 a-e**. The ED plots of CNDs (**Figure. S4.5a**) and Co_3O_4@CND hybrid NPs (**Figure. S4.5b**) at different wavelengths were analyzed. These ED plots of the PL emission spectra were significant attributes for contributing to bioimaging and biotherapeutic applications [224]. CNDs and Co_3O_4@CND hybrid NPs were excitation-dependent at the wavelength 360 nm. Also, CNDs and Co_3O_4@CND hybrid NPs showed similar excitation wavelength dependencies until the 380 nm wavelength. But, after an excitation wavelength of 400 nm, they shifted significantly with lower emission intensities at different wavelengths in both spectra. From the PL spectroscopic data, we observed that the conjugated ligands possess different emission maximum wavelengths,

the ED plot of the FA-BSA-Co_3O_4@CNDs-DOX (**Figure. S4.5c**) at different wavelengths showed different emissions, ascribing that they were excitation-independent. The ED plot (**Figure. S4.5d**) of the Hep-NHS-Co_3O_4@CNDs-DOX excited at different wavelengths until 360 nm, showed emissions at the same wavelength with excitation-dependent fluorescent behavior, whereas when excited after 380 nm, the emission maximum shifted to the red region. At each excitation wavelength, two characteristic emission peaks were observed at 442 representatives of Hep-NHS and a split peak at 536 and 593 nm, characteristic of DOX [188] interactions with many proteins, such as growth factors and chemokines. The PL plot of the Co_3O_4@CNDs-Trf-DOX (**Figure. S4.5e**), excited at different wavelengths, showed that these NPs were excitation-independent. These excitation-dependent and independent emission spectra are essential for fluorescent properties in biological applications [225], [227].

The zeta (ʒ) potential of the NPs, ligands, and DOX are shown in **Figure. S4.6 a-e,** and the data were compared in **Table. S4.1**. The ʒ potential provided information about the surface charge and the dispersion stability of the NPs, which is also an essential factor for cell studies to reach them effectively [207]. The ʒ potential of the Co_3O_4@CND hybrid NPs was measured as -4.3 mV, which might be due to the hybridization of the Co_3O_4 NPs and CNDs. After modification with the FA-BSA, the negative charge of the ʒ potential values (**Figure. S4.6a**) of the FA-BSA-Co_3O_4@CNDs increased making the structure more stable with monodispersibility and stability. However, after DOX conjugation, the negative charge Co_3O_4@CNDs increased significantly from -19.1 to -11.8 mV, inferring their conjugation. FA possessed only a few functional groups for bioconjugation and hence modification with BSA increased the solubility of the NP conjugates. These FA-BSA conjugates are generally used as carriers to conjugate drugs (DOX), advantageous for selective and sensitive attachment to cancer cells, and also

increase the biological applicability of the entire complex [221]. In Hep-NHS conjugated Co_3O_4@CNDs, the negative charge of the ʒ potential (**Figure. S4.6b**) values of the Hep-NHS-Co_3O_4@CNDs was increased, making the structure more stable due to the sulfate and carboxylate groups in -NHS groups. The high negative charge of Hep mediates their electrostatic interactions with many proteins, such as growth factors and chemokines. But, after DOX conjugation, the negative charge decreased, inferring their conjugation with the Hep-NHS-Co_3O_4@CNDs by electrostatic interactions [188]. Co_3O_4@CNDs-Rhod showed an increase in the negative charge of the ʒ potential (**Figure. S4.6c**) values, as the structure became more stable with PEG and silica (SiO_2) linkages. After Co_3O_4@CNDs modification with the Trf, an increase in the negative charge of the ʒ potential (**Figure. S4.6d**) values of the Co_3O_4@CNDs-Trf-DOX was observed as the structure was more stable because of the Trf isoelectric point, 5.6 and negative charge in neutral conditions [228]. DOX is positively charged due to their electrostatic interactions and due to the π-π stacking and electrostatic interactions between the Co_3O_4@CNDs–Trf and DOX, the negative charge of the Co_3O_4@CNDs-Trf-DOX increased confirming the loading of DOX [210].

Cellular studies

Bioimaging studies of Co_3O_4@CND hybrid NPs

The cellular uptake of the Co_3O_4@CND hybrid NPs (**Figure. S4.7, S4.8**) at different concentrations, such as 0, 0.4, and 0.8 mg/mL, was imaged using confocal microscopy at 63X in both cell types for better understanding. The red-stained cells represent the mitochondrial layer of the cells stained with the Mitotracker red dyes, the blue fluorescence was observed from that of the NPs, and the merged images at the exact location in the cells showed the uptake of the NPs in the mitochondrial and nuclear regions. Co_3O_4 NPs were not used here for comparison because they

were not fluorescent in cells for imaging using confocal microscopy. Cells without any NPs (0 mg/mL) were used as a control for comparison while imaging the cellular uptake at different increasing concentrations, and hence no fluorescence was observed in the DAPI channel. At 0.4 mg/mL concentration of the Co_3O_4@CND hybrid NPs, the imaged cells showed significantly more viability than at 0.8 mg/mL in both the cell types. A significant viability reduction was clearly observed in the A549 than in the EAhy926 cells at 0.8 mg/mL of the Co_3O_4@CND hybrid NPs. These cellular uptakes of Co_3O_4@CND hybrid NPs provided a clear understanding of their viability and uptake inside the cells. We also see that with the increase in the concentration of Co_3O_4@CND hybrid NPs, an increase in fluorescence intensity inside the cells was observed. The brighter blue fluorescence of Co_3O_4@CND hybrid NPs was due to their high absorption and high QY, 50%, generating fluorescence that considerably exceeds small organic fluorophores and CNDs [229], [230]. Also, at a higher concentration, 0.8 mg/mL, there was an increase in the sub-cellular localization by the Co_3O_4@CND hybrid NPs. Hence, we confirmed that the Co_3O_4@CND hybrid NPs were uptaken by both cell types and could be used as bioimaging studies.

The sub-cellular localization studies of the Co_3O_4@CND hybrid NPs (**Figure. 16**) and CNDs (**Figure. S4.9**) were performed using confocal microscopy and imaged at 100X in both cell types for comparison. **Figure. 16** compares the Co_3O_4@CND hybrid NPs at a concentration of 0.4 mg/mL in the EAhy926 and A549 cells at 100X magnification. The results indicated that these NPs could be used as bioimaging agents in normal and cancer cells. **Figure. S4.9** shows the comparison of the CNDs with both cell types. The results inferred that the mitochondrial and nuclear uptake was observed by both Co_3O_4@CND hybrid NPs and CNDs in both EAhy926 and A549 cell types. In comparison with **Figure. S4.9**, showing CNDs uptake in the cells, the Co_3O_4@CND hybrid NPs (**Figure. 16**) showed better fluorescence (bright solid blue) because of

their increased absorption [229]. This bioimaging result inferred that an excellent sub-cellular localization of the Co_3O_4@CND hybrid NPs was observed in both cells.

Figure 16. Sub-cellular localization of Co_3O_4@CND hybrid NPs in EAhy926 and A549 cells at 100X magnification

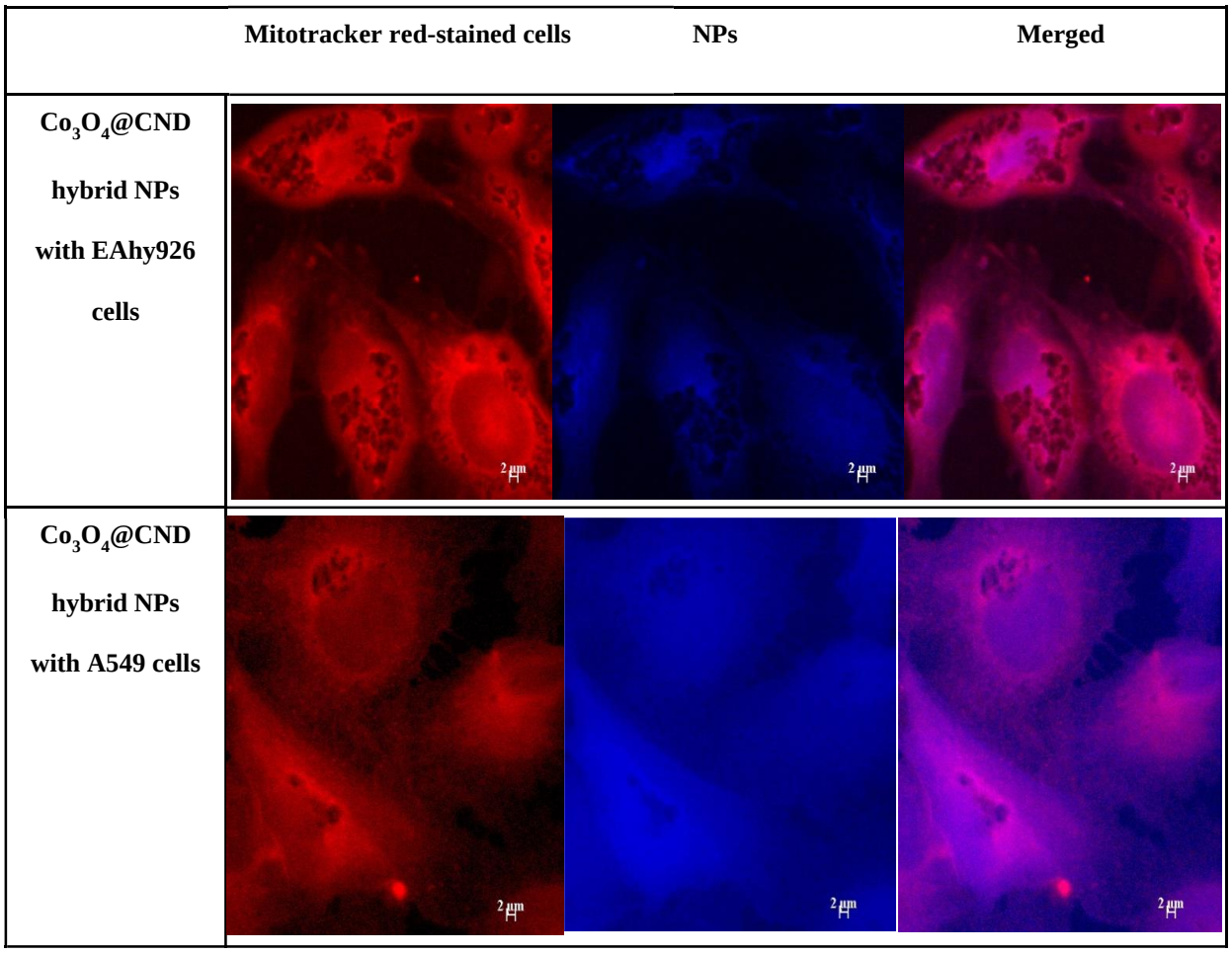

Antioxidation studies of Co_3O_4@CND hybrid NPs

Intracellular enzymes in the cells cleave the ester bonds of DCFH-DA dye into non-fluorescent intermediates, which oxidize further to a highly fluorescent product, DCF. The release of fluorescent DCF in the cells can be measured at 528 nm by exciting at 485 nm. The detected fluorescence intensity represented the intracellular ROS levels [231]. **Figure. 17a,b** illustrated the

changes in ROS levels of cell EAhy926 and A549 cells treated with the Co_3O_4@CND hybrid NPs, CNDs, and Co_3O_4 NPs, vs. AA. A decrease in the fluorescence intensity was observed in the Co_3O_4@CND hybrid NPs, Co_3O_4 NPs, CNDs, and AA-treated EAhy926 and A549 cells in a concentration-dependent pattern. AA, a powerful antioxidant, and an inhibitor of ROS were used as a control in this study for comparison. Both cells treated with AA exhibited similar results to the CNDs with increasing concentrations with less ROS in the A549 cells. Compared with CNDs and Co_3O_4 NPs, the ROS levels reduced rapidly in both cells with Co_3O_4@CND hybrid NPs. Co_3O_4 NPs exhibited relatively higher fluorescence than AA due to their rich vacancies in oxidation states. The Co_3O_4 NPs did not cause a profound decrease in ROS in EAhy926 and A549 cells, whereas CNDs treated cells showed a decrease similar to that of the Co_3O_4@CND hybrid NPs.

Figure 17. DCFH-DA assay results of Co_3O_4@CND hybrid NPs, CNDs, Co_3O_4 NPs, and ascorbic acid in a. EAhy926 and b. A549 cells

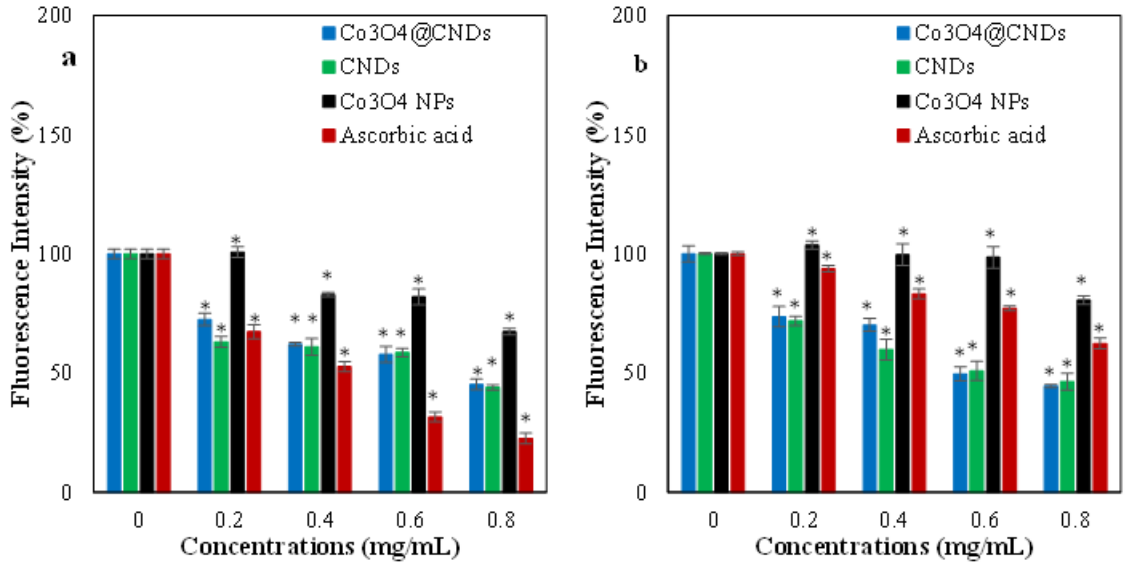

Figure. S4.10 compared the antioxidant activity of Co_3O_4@CND hybrid NPs only in both cells. Co_3O_4@CND hybrid NPs in EAhy926 cells with the concentration increment, the

fluorescence initially decreased, and then the rate gradually slowed down. Interestingly, in the A549 cells treated with Co_3O_4@CND hybrid NPs and Co_3O_4 NPs, the decrease in ROS was slightly higher compared to the EAhy926 with the concentration increment. Moreover, in A549 cells, the fluorescence intensity decreased rapidly, confirming that these Co_3O_4@CND hybrid NPs depicted a more significant antioxidant effect in A549 than in the EAhy926 cells, suggesting that they could be more advantageous as an anticancer agent. The results suggested that ROS was greatly reduced with high concentrations of the Co_3O_4@CND hybrid NPs in both cell types, thereby proving their role in the intracellular antioxidant effect associated with cell death. Also, the data indicated that the antioxidant effect of the Co_3O_4@CND hybrid NPs and CNDs was more than AA, with a more profound effect in Co_3O_4@CND hybrid NPs.

Cell viability of Co_3O_4@CND hybrid NPs

Figure 18. Percentage viability of the Co_3O_4@CND hybrid NPs, CNDs, and Co_3O_4 NPs in a. EAhy926 and b. A549 cells

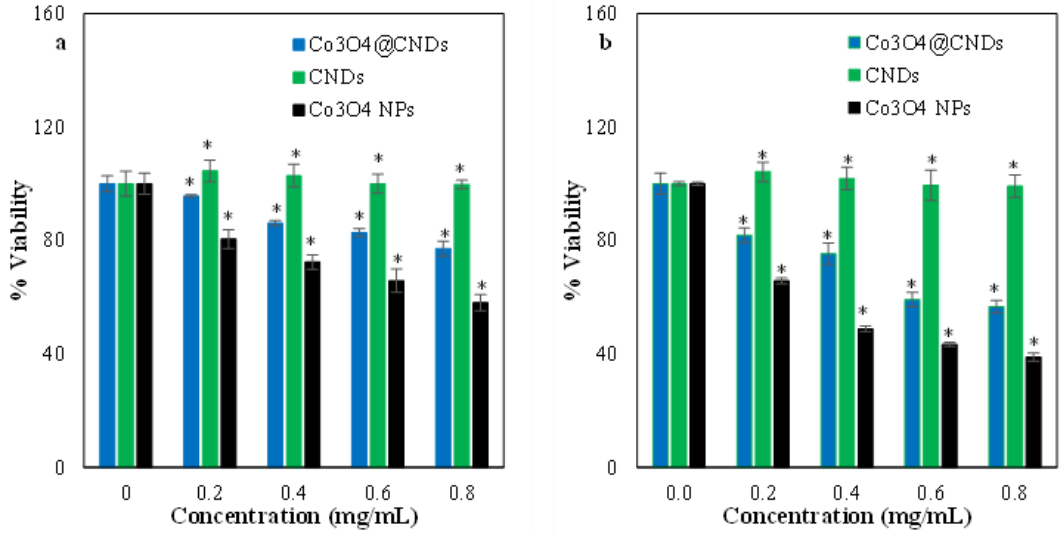

The percentage viability of Co_3O_4@CND hybrid NPs, CNDs, and Co_3O_4 NPs was assessed and compared with the AB assay for two cells, EAhy926 and A549. The AB assay measurements (**Figure. 18a,b**) revealed that the EAhy926 viability was around 77.1%, and that

of the A549 cells was around 56.6% at 0.8 mg/mL. The results suggested that at increasing concentrations of Co_3O_4@CND hybrid NPs, they possessed more cytotoxicity in the cancer cells than in the normal human cells. Also, Co_3O_4@CND hybrid NPs were more biocompatible than Co_3O_4 NPs but less than CNDs, in EAhy926 cells. This result ensured that the carbon shell prevented the direct toxicity of Co_3O_4 NPs. However, we observed some toxicity of these Co_3O_4@CND hybrid NPs at higher concentrations than the CNDs, which might be because of the toxic Co_3O_4 NPs inside them. Moreover, in A549 cancer cells, the CNDs were not toxic to them, but the Co_3O_4 NPs showed some extent of toxicity at higher concentrations. Due to this reason, in comparison with the CNDs, Co_3O_4@CND hybrid NPs were more cytotoxic to the cancer cells at higher concentrations. These observations revealed that the Co_3O_4@CND hybrid NPs might be used as an anticancer agent, suggesting they have more therapeutic efficacy than CNDs. However, they were still toxic to normal human cells at the same concentrations, which needs to be considered. Also, additional tests such as cellular uptake and ROS measurements helped us to better understand these viability results and correlated with our data analysis. Based on these results, to make the Co_3O_4@CND hybrid NPs more biocompatible and cancer-specific simultaneously and to improve the targeting of the A549 cells, some ligands such as FA-BSA, Hep, Trf, and PEGylated silica with or without DOX were attached to these NPs through different synthesis approaches from the literature.

Selective cancer cell targeting of ligand and DOX conjugated Co_3O_4@CND hybrid NPs using viability studies

After characterizing and understanding the properties of the conjugated NPs, the percentage viability of FA-BSA-Co_3O_4@CND-DOX, Co_3O_4@CND-Hep-DOX, Co_3O_4@CND-

Rhod, and Co_3O_4@CND-Trf-DOX were evaluated with the AB assay in both cell types, EAhy926 (**Figure. S4.11a-d**) and A549 (**Figure. S4.12a-d**), and compared with FA, DOX, FA-BSA-Co_3O_4@CNDs, Co_3O_4@CND-Hep, Hep, Co_3O_4@CND-Trf, Trf, Co_3O_4@CNDs, and DOX. At 0.4 mg/mL concentration, AB assay measurements revealed that the EAhy926 cell viability was 83.05% for FA-BSA-Co_3O_4@CNDs, and 66.83% for FA-BSA-Co_3O_4@CNDs-DOX, whereas for A549 cells are 62.01% for FA-BSA-Co_3O_4@CNDs, and 58.76% for FA-BSA-Co_3O_4@CNDs-DOX. The AB assay measurements revealed that the EAhy926 cell viability at 0.4 mg/mL was 80.21% for Hep-Co_3O_4@CNDs, and 41.62% for Hep-Co_3O_4@CNDs-DOX and that of the A549 cells was 83.12% for Hep-Co_3O_4@CNDs, and 42.66% for Hep-Co_3O_4@CNDs-DOX. The EAhy926 cell percentage viability was 80.21% for Hep-Co_3O_4@CNDs, and 41.62% for Hep-Co_3O_4@CNDs-DOX and that of the A549 cells was 83.12% for Hep-Co_3O_4@CNDs, and 42.66% for Hep-Co_3O_4@CNDs-DOX. The EAhy926 cell percentage viability was 78.15% for Co_3O_4@CNDs-Rhod and that of the A549 cells was 66.54% for Co_3O_4@CNDs-Rhod. The EAhy926 cell percentage viability was 68.18% for Co_3O_4@CNDs-Trf, and 82.86% for Co_3O_4@CNDs-Trf-DOX and that of the A549 cells was 64.93% for Co_3O_4@CNDs-Trf, and 51.19% for Co_3O_4@CNDs-Trf-DOX.

The AB cell viability measurement results showed that at increasing concentrations of FA-BSA-Co_3O_4@CND-DOX NPs, more cytotoxicity in the cancer cells (**Figure. S4.12a)** than in the EAhy926 cells (**Figure. S4.11a)** was observed. Moreover, in A549 cancer cells, the FA-BSA-Co_3O_4@CND-DOX were not much toxic to them, but in the EAhy926 cells, the viability decreased faster with the increase in the concentrations, which might be partly disadvantageous. Compared with Co_3O_4@CNDs, the same variations in viability were observed for FA-BSA-Co_3O_4@CND-DOX conjugates in the EAhy926 and A549 cells. FA has excellent biocompatibility but is not

anticancerous itself, as it serves widely as a better carrier for anticancer drugs [86]. Free DOX showed significant toxicity in both cell types, particularly in the EAhy926 type, instead of being cancer-specific only. This ligand FA-BSA, combined with Co_3O_4@CND NPs, was toxic to normal human cells at higher concentrations. Due to this reason, the FA-BSA might not be an effective ligand for the Co_3O_4@CNDs to target A549 cells. The mechanism of the anticancer activity was predicted to be that FA ligands conjugated on Co_3O_4@CND-DOX target excessive FA receptors on the surface of A549 cancer cells with high affinity [232]. However, other ligands were also tried by optimizing to see which receptors are overexpressed on A549 cancer cells specifically. In **Figure. S4.11b and S4.12b,** Hep-NHS was safe for EAhy926 and A549 cells in their native form and when combined with Co_3O_4@CNDs. At increasing concentrations of Hep-Co_3O_4@CND-DOX NPs, they possessed more cytotoxicity in EAhy926 cells than in A549 cells from the results. Moreover, in A549 cancer cells, the Hep-Co_3O_4@CNDs were not toxic to them, but in the EAhy926 cells, with the increase in the concentrations, they started to die at a faster rate with increasing concentrations. The anticancer efficacy was not improved by modifying with Hep-NHS but improved after modifying with DOX. The mechanism of the anticancer activity might be predicted that the Hep ligands target the overexpressed CD44 and heparin-binding growth factor receptors on the surface of the A549 cells, which plays a significant role in metastasis formation and cell adhesion [233]. More importantly, Co_3O_4@CNDs–Hep-DOX also prohibited cancer cell proliferation significantly, and the anticancer effect was higher than that of Co_3O_4@CNDs. However, the Co_3O_4@CNDs-Hep-DOX conjugates significantly affected the normal human cells too. This ligand Hep and DOX combined with Co_3O_4@CND NPs was more cytotoxic to the normal human cells at higher concentrations than the A549 cells. Due to this adverse effect, the Hep might not be an effective ligand for the Co_3O_4@CNDs to target A549 cells, though it was

toxic to them. The cell viability results (in **Figure. S4.11c and S4.12c**) showed that at increasing concentrations of Co_3O_4@CND-Rhod, they possessed more cytotoxicity in the A549 cells than in the EAhy926 cells. Compared with Co_3O_4@CNDs, where the cell viability at a concentration of 0.4 mg/mL, the viability of EAhy926 and A549 cells was 65.02% and 76.31%, the Co_3O_4@CNDs-Rhod were more biocompatible and anticancerous to A549 cells. Due to this reason, the PEG-SiO_2(Rhod) might be considered an effective ligand for the Co_3O_4@CNDs to target A549 cells but comparing them with the FA-BSA-Co_3O_4@CNDs-DOX, the anticancerous effect was relatively less. The anticancer mechanism of these conjugates was expected that these ligands might be transported, internalized, and uptake by the cancer cells through energy-dependent endocytosis and phagocytosis [206]. In addition, these ligands might target the folate receptors that are overexpressed on the surface of cancer cells due to the PEG and SiO_2 functionalization on the Co_3O_4@CNDs [234]. **Figure. S4.11d and S4.12d** showed that at increasing concentrations of Co_3O_4@CND-Trf-DOX, they possessed more cytotoxicity in the A549 than in the EAhy926 cells. Moreover, in A549 cancer cells, the Co_3O_4@CND-Trf-DOX were not toxic to them, but in the EAhy926 cells, with the increase in the concentrations, the viability decreased faster. In comparison with Co_3O_4@CNDs, the same variations were observed for these Co_3O_4@CND-Trf-DOX conjugates in both the EAhy926 and A549 cells. This ligand Trf and DOX combined with Co_3O_4@CND NPs were more cytotoxic to the cancer cells at higher concentrations, and Trf was safe to normal human cells, whereas DOX was not according to the results. Due to this reason, the Trf is proven to be an effective ligand for the Co_3O_4@CNDs to target A549 cells. The efficacy of Trf-loaded Co_3O_4@CNDs NPs was improved by modification with DOX. Trf-Co_3O_4@CNDs-DOX resulted in a decrease in efficacy values (51.16%), compared with Trf (59.63%), Trf-Co_3O_4@CNDs (64.03%), and Co_3O_4@CNDs (65.02%) after 24-h incubation with A549 cells,

respectively, **at the concentration of 0.4 mg/mL.** The mechanism of anticancer activity of this ligand-based targeting was evident from the literature that this complex might target the specific overexpressed Trf and Trf1 receptors on the surface of A549 cancer cells resulting in endocytosis [209], [210], [227], [228].

Discussion

The biological properties such as cell viability, anticancer, bioimaging, and antioxidant studies of the Co_3O_4@CND hybrid NPs were performed and compared with their counterparts. The bioimaging results showed that the Co_3O_4@CND hybrid NPs were better than the CNDs, which confirmed them to be an efficient diagnostic tool. Cancer cell specificity was based on different ligands through the cell viability test, and the effects of ligands are compared. Though the cell viability and the anticancer studies were not much efficient compared to the CNDs for their biocompatibility, it was improved through the successful modification with different ligands. This research work, where different ligands were synthesized and compared, was mainly done to target the A549 lung cancer cells specifically with the help of ligands. Hence, after synthesizing the hybrid NPs with different ligands, their cell viability was compared in both the normal and the cancer cells. The above cell viability comparison results (**Figure. 19**) showed that the Rhod and Trf-DOX conjugated Co_3O_4@CND hybrid NPs were more specifically targeting ligands for A549 cancer cells and less toxic to EAhy926 normal cells.

A detailed explanation for **Figure. 19** was elaborated with a comparison table in **Table. S4.2** for a clearer understanding of the anticancer effects of all the conjugated ligands with Co_3O_4@CND hybrid NPs. Trf-Dox, Co_3O_4@CNDs-Rhod, and FA-BSA-DOX conjugation with Co_3O_4@CND hybrid NPs are better-targeting conjugates for A549 cells than the Hep-DOX. Among all the conjugates, the Co_3O_4@CND hybrid NPs-Trf-DOX complex showed cell viability

of 51.2% at 0.4 mg/mL, whereas Co_3O_4@CND hybrid NPs-FA-BSA-DOX showed cell viability of 58.76% at 0.4 mg/mL for A549 cells. Hence these ligands are considered the best and safest conjugations that make the Co_3O_4@CND hybrid NPs more anticancerous, decrease the toxicity to EAhy926 cells, and are more specific and targeted.

Figure 19. Percentage viability in EAhy926 (Solid filled) and A549 cells (Pattern filled) for the Co_3O_4@CND hybrid NPs with different conjugations

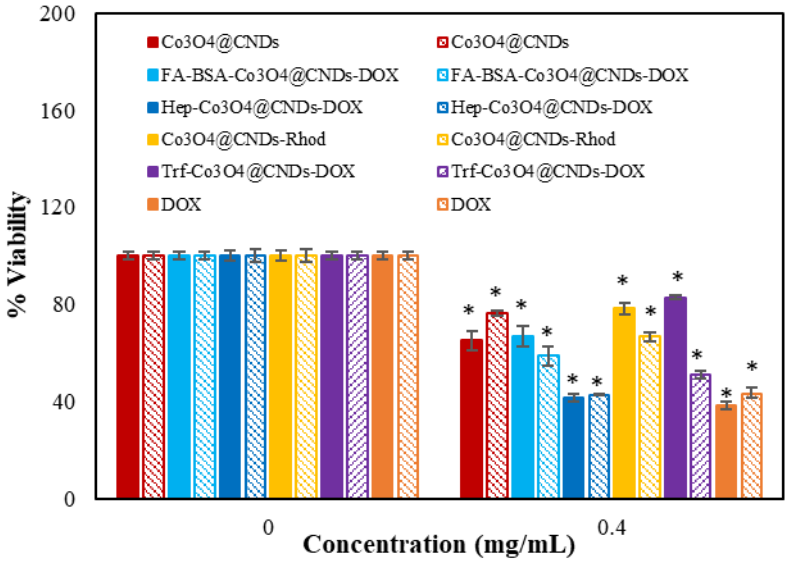

Proposed Anticancer Mechanism

A mechanism of anticancer activity of the Co_3O_4@CND hybrid NPs with ligands and drugs loaded onto them was proposed and described in **Figure. 20.** We proposed that the ligands FA-BSA, Heparin, PVP-PEG-SiO2-Rhod, and Trf and the anticancer drug DOX target the receptors such as folate, FGFR, Trf1, alpha 5, and beta 3 ($\alpha_v\beta_3$) integrin, hepatocyte GFR (HGFR), G-protein coupled, CXCR4, EGFR, and CD44, respectively in the A549 lung cancer cells, as mentioned in the literature [203], [205], [235]–[238].

Figure 20. Proposed Anticancer Mechanism for the ligand and DOX conjugated Co_3O_4@CND hybrid NPs

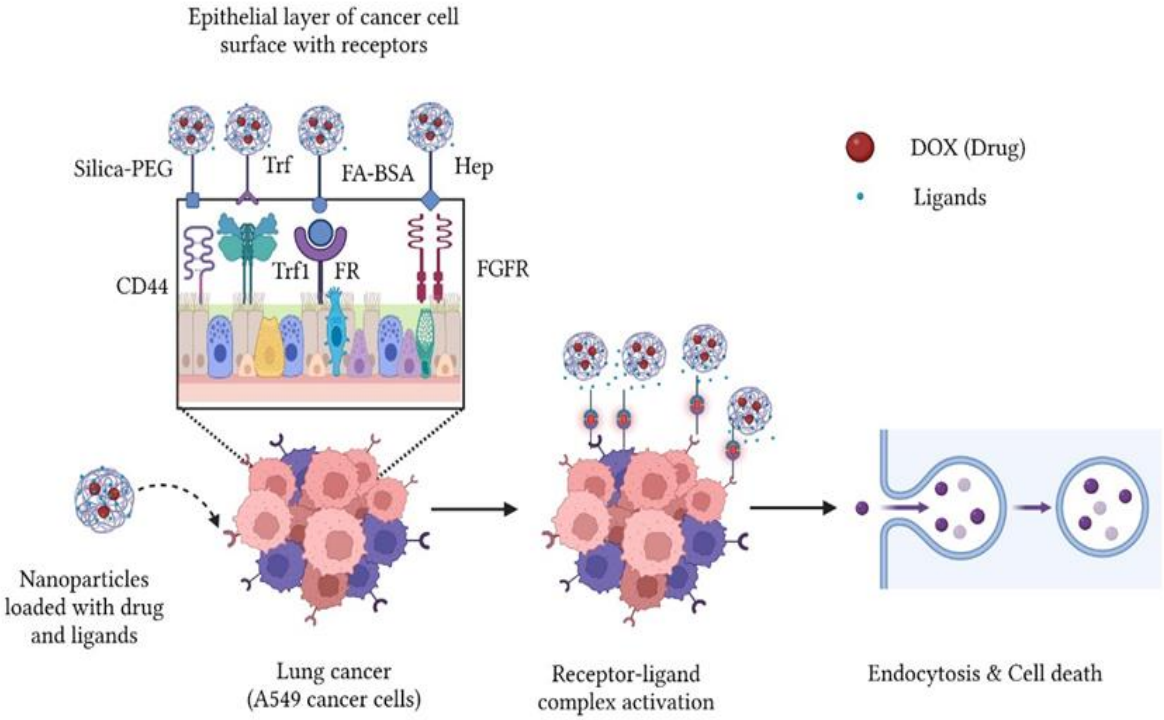

The anticancer mechanism was expected due to the active targeting of the ligands through receptor activation. The active targeting of A549 cancer cells was achieved through the proper receptor-ligand complex activation for the delivery of NPs combined with the anticancer drug DOX. Once the receptors on the A549 cancer cell surface are activated, the NPs and drugs are released inside the cells through the endocytosis mechanism, which might be likely clathrin, lipid-raft, or caveolae-mediated or pinocytosis, inducing lysosomal degradation, which further leads to apoptosis and cell death [187], [235], [238]. The Co_3O_4@CND hybrid NPs with Trf and DOX were more specific and targeted without affecting the normal cells indicating that the A549 cancer cells specifically targeting Trf1 and CD44 receptors, respectively, to which the ligands

bind, releasing the NPs and thus enhancing the anticancer activity. Also, the ligand Trf was more biocompatible than the other ligands used, which is an added advantage for delivering the NPs, according to our discussions.

Conclusion

Co_3O_4@CND hybrid NPs were studied in this research for their advanced multifunctional applications, such as anticancer, bioimaging, and antioxidant, and as a drug delivery vehicle. This study suggested that the Co_3O_4@CND hybrid NPs possessed excellent anticancer and antioxidant activity on their own and could serve as an excellent imaging probe due to their brighter fluorescence compared to the CNDs. Also, advanced active targeting strategies were utilized with this novel Co_3O_4@CND hybrid NPs for loading anticancer drug (DOX) for enhanced anticancer activity, along with increasing the specificity to target A549 cancer cells using specific ligands. The anticancer activity was tested for each ligand and compared in the EAhy926 and A549 cancer cells. By comparing four types of ligands based on different anticancer mechanisms, we finally inferred that the Trf-DOX conjugate with Co_3O_4@CND hybrid NPs possessed an excellent improved anticancer activity with enhanced biocompatibility. Further future cell studies such as confocal and flow cytometry could be performed to prove and study their penetration mechanism in cells.

CHAPTER V: CONCLUSION

In chapter II, I studied the factors affecting the photocatalytic dye degradation efficiency, such as the dye's charge, dye concentration, and wavelength of the light source (UV and Visible)

at varying time intervals by fixing the Co_3O_4@CNDs, with catalyst dosage as constant value and discussed their respective kinetics and scavenging properties, and finally proposed a mechanism associated with the degradation. This Co_3O_4@CNDs with a core-shell morphology possessed a more uniform, well-defined morphology and was proven to be a UV and visible light-responsive photocatalyst with better degradation kinetics, a well-defined charge-transfer mechanism, and reusability, thus satisfying the ideal requirements of a photocatalyst. The comparison studies in chapter II showed that the UV-light-based degradation rate kinetics was more than the visible with faster degradation kinetics at a shorter time duration within 40 minutes, whereas, with an extended time of up to 75 minutes, the visible light degradation percentage efficiency was greater compared to the UV for both cationic and anionic dyes. Also, the Co_3O_4@CNDs showed better degradation kinetics and efficiency compared to their counterparts, such as Co_3O_4 NPs and CNDs, due to the heterogeneous interface, which accelerated the generation of electron-hole pairs more rapidly. Further studies could be carried out with these Co_3O_4@CNDs to increase their efficiency with better light power sources to degrade any types of dyes.

Chapter III demonstrated electrochemical applications of these Co_3O_4@CNDs such as capacitance calculation studies by cyclic voltammetry. The findings showed that when Co_3O_4@CNDs were combined with binders and activated carbons, their capacitance improved. But still satisfactory or larger energy storage capacity was not achieved with Co_3O_4@CNDs. In future studies, further modifications in their structure by combining them with one, two, or three-dimensional support materials might provide a better use of these Co_3O_4@CNDs hybrid NPs in the electrochemical research areas.

In Chapter IV, an attempt to improve the targeting efficiency specific to lung cancer cells was also done by modifying these Co_3O_4@CNDs hybrid NPs with the help of different ligands,

such as folic acid, heparin, silica, and transferrin and their anticancer efficacy was compared for specific targeting of the A549 lung cancer cells with improved biocompatibility. Several ligand modifications with the core-shell modifications were synthesized, characterized, and compared for their anticancer-specific targeting in this chapter. A clearer understanding of the ligand-receptor mechanism was achieved, and a mechanism was proposed for the transferrin-Co_3O_4@CNDs-DOX which demonstrated the best anti-cancer efficacy, specifically to A549 cells. Also, the enhanced optical properties of the Co_3O_4@CNDs were studied in detail and their bioimaging characteristics were demonstrated by comparing them with the CNDs. The results suggested that the Co_3O_4@CNDs reach the mitochondrial and nuclear regions of both normal and cancer cells through their enhanced fluorescence.

The overall conclusions of this research suggested the investigation of Co_3O_4@CNDs core-shell hybrid NPs in photocatalytic dye degradation, anticancer and bioimaging, and electrochemical studies, and to get a comprehensive understanding of their mechanism from their physicochemical properties associated for the particular applications. To this end, these exciting dissertation findings presented a better understanding and technical strategies for using the hybrid NPs for a variety of application studies as photocatalysts, bioimaging, anticancer agents, and electrocatalysts/energy storage in electrochemistry. Future studies might further be required to optimize these Co_3O_4@CNDs core-shell hybrid NPs for photocatalytic and electrochemical studies by introducing a support material to improve their properties. For commercialization and long-term applications, continuous research studies had to be performed to explore advanced science and technologies using hybrid nanomaterials. The anticancer and imaging efficacy specific to the lung cancer cells using the Co_3O_4@CNDs core-shell hybrid NPs might be very

useful to the emerging world needs for cancer therapy and diagnostics and could serve the community needs with its enhanced efficacy.

REFERENCES

[1] M. A. Macchione, C. Biglione, and M. Strumia, ‘Design, Synthesis and Architectures of Hybrid Nanomaterials for Therapy and Diagnosis Applications’, *Polymers (Basel)*, vol. 10, no. 5, May 2018, doi: 10.3390/POLYM10050527.

[2] A. S. de Dios and M. E. Díaz-García, ‘Multifunctional nanoparticles: Analytical prospects’, *Anal Chim Acta*, vol. 666, no. 1–2, pp. 1–22, May 2010, doi: 10.1016/J.ACA.2010.03.038.

[3] M. J. Sailor and J. H. Park, ‘Hybrid Nanoparticles for Detection and Treatment of Cancer’, *Adv Mater*, vol. 24, no. 28, p. 3779, Jul. 2012, doi: 10.1002/ADMA.201200653.

[4] D. Ma, ‘Hybrid Nanoparticles: An Introduction’, *Noble Metal-Metal Oxide Hybrid Nanoparticles: Fundamentals and Applications*, pp. 3–6, Jan. 2019, doi: 10.1016/B978-0-12-814134-2.00001-2.

[5] R. Vargas-Bernal and R. Vargas-Bernal, ‘Introductory Chapter: Hybrid Nanomaterials’, *Hybrid Nanomaterials - Flexible Electronics Materials*, Jun. 2020, doi: 10.5772/INTECHOPEN.92012.

[6] N. Mishra and N. Mishra, ‘Metal–Semiconductor Hybrid Nano-Heterostructures for Photocatalysis Application’, *Semiconductor Photocatalysis - Materials, Mechanisms and Applications*, Aug. 2016, doi: 10.5772/62636.

[7] M. S. Saveleva *et al.*, ‘Hierarchy of hybrid materials-the place of inorganics-in-organics in it, their composition and applications’, *Front Chem*, vol. 7, no. APR, p. 179, Apr. 2019, doi: 10.3389/FCHEM.2019.00179/BIBTEX.

[8] M. Khatami, H. Q. Alijani, M. S. Nejad, and R. S. Varma, ‘Core@shell Nanoparticles: Greener Synthesis Using Natural Plant Products’, *Applied Sciences 2018, Vol. 8, Page 411*, vol. 8, no. 3, p. 411, Mar. 2018, doi: 10.3390/APP8030411.

[9] T. A. Saleh, ‘Hybrid materials: fundamentals and classifications’, *Polymer Hybrid Materials and Nanocomposites*, pp. 147–176, Jan. 2021, doi: 10.1016/B978-0-12-813294-4.00001-7.

[10] S. Zhang, C. I. Pelligra, X. Feng, and C. O. Osuji, ‘Directed Assembly of Hybrid Nanomaterials and Nanocomposites’, *Advanced Materials*, vol. 30, no. 18, p. 1705794, May 2018, doi: 10.1002/ADMA.201705794.

[11] A. Subhan, K. P. Choudhury, N. Neogi, A. Castellanos-Gomez, and S. Baskoutas, ‘Advances with Molecular Nanomaterials in Industrial Manufacturing Applications’, *Nanomanufacturing 2021, Vol. 1, Pages 75-97*, vol. 1, no. 2, pp. 75–97, Aug. 2021, doi: 10.3390/NANOMANUFACTURING1020008.

[12] F. M. Galogahi, Y. Zhu, H. An, and N. T. Nguyen, ‘Core-shell microparticles: Generation approaches and applications’, *Journal of Science: Advanced Materials and Devices*, vol. 5, no. 4, pp. 417–435, Dec. 2020, doi: 10.1016/J.JSAMD.2020.09.001.

[13] R. Ghosh Chaudhuri and S. Paria, ‘Core/shell nanoparticles: Classes, properties, synthesis mechanisms, characterization, and applications’, *Chem Rev*, vol. 112, no. 4, pp. 2373–2433, Apr. 2012, doi: 10.1021/CR100449N/ASSET/IMAGES/CR-2010-00449N_M017.GIF.

[14] K. S. Kumar, V. B. Kumar, and P. Paik, ‘Recent Advancement in Functional Core-Shell Nanoparticles of Polymers: Synthesis, Physical Properties, and Applications in Medical

Biotechnology', *Journal of Nanoparticles*, vol. 2013, pp. 1–24, Mar. 2013, doi: 10.1155/2013/672059.

[15] A. Jana and D. H. Gregory, 'Microwave-Assisted Synthesis of ZnO-rGO Core-Shell Nanorod Hybrids with Photo- and Electro-Catalytic Activity', *Chemistry*, vol. 26, no. 29, pp. 6703–6714, May 2020, doi: 10.1002/CHEM.202000535.

[16] A. A. Womiloju *et al.*, 'Microwave-Assisted Synthesis of Core–Shell Nanoparticles—Insights into the Growth of Different Geometries', *Particle & Particle Systems Characterization*, vol. 37, no. 7, p. 2000019, Jul. 2020, doi: 10.1002/PPSC.202000019.

[17] D. v. Pryazhnikov, O. O. Efanova, M. S. Kiseleva, and I. v. Kubrakova, 'Microwave synthesis of core–shell nanosize materials on the basis of magnetite functionalized with gold and doxorubicine', *Nanotechnol Russ*, vol. 12, no. 3–4, pp. 199–207, Mar. 2017, doi: 10.1134/S1995078017020094/METRICS.

[18] Z. Zeng *et al.*, 'A fluorescence-electrochemical study of carbon nanodots (CNDs) in bio- and photoelectronic applications and energy gap investigation', *Physical Chemistry Chemical Physics*, vol. 19, no. 30, pp. 20101–20109, Aug. 2017, doi: 10.1039/C7CP02875J.

[19] D. Nunes, A. Pimentel, R. Branquinho, E. Fortunato, and R. Martins, 'Metal Oxide-Based Photocatalytic Paper: A Green Alternative for Environmental Remediation', *Catalysts 2021, Vol. 11, Page 504*, vol. 11, no. 4, p. 504, Apr. 2021, doi: 10.3390/CATAL11040504.

[20] M. A. A. Mohd Abdah, N. H. N. Azman, S. Kulandaivalu, and Y. Sulaiman, 'Review of the use of transition-metal-oxide and conducting polymer-based fibres for high-

performance supercapacitors', *Mater Des*, vol. 186, p. 108199, Jan. 2020, doi: 10.1016/J.MATDES.2019.108199.

[21] Y. Zhang, Q. Fu, B. Song, and P. Xu, 'Regulation Strategy of Transition Metal Oxide-Based Electrocatalysts for Enhanced Oxygen Evolution Reaction', *Acc Mater Res*, vol. 3, no. 10, pp. 1088–1100, Oct. 2022, doi: 10.1021/ACCOUNTSMR.2C00161/ASSET/IMAGES/MEDIUM/MR2C00161_0008.GIF

[22] W. H. Low, P. S. Khiew, S. S. Lim, C. W. Siong, and E. R. Ezeigwe, 'Recent development of mixed transition metal oxide and graphene/mixed transition metal oxide based hybrid nanostructures for advanced supercapacitors', *J Alloys Compd*, vol. 775, pp. 1324–1356, Feb. 2019, doi: 10.1016/J.JALLCOM.2018.10.102.

[23] P. Singh, S. Mandal, and N. Chanda, 'Metal–Reduced Graphene Oxide-based Nanocomposites: Synthesis, Characterization, and Sensing Applications', *Carbon Nanostructures*, pp. 9–1, Nov. 2021, doi: 10.1063/9780735423114_009.

[24] M. Srivastava, J. Singh, T. Kuila, R. K. Layek, N. H. Kim, and J. H. Lee, 'Recent advances in graphene and its metal-oxide hybrid nanostructures for lithium-ion batteries', *Nanoscale*, vol. 7, no. 11, pp. 4820–4868, Mar. 2015, doi: 10.1039/C4NR07068B.

[25] D. Seok, Y. Jeong, K. Han, D. Y. Yoon, and H. Sohn, 'Recent Progress of Electrochemical Energy Devices: Metal Oxide–Carbon Nanocomposites as Materials for Next-Generation Chemical Storage for Renewable Energy', *Sustainability 2019, Vol. 11, Page 3694*, vol. 11, no. 13, p. 3694, Jul. 2019, doi: 10.3390/SU11133694.

[26] V. Raman *et al.*, 'Synthesis of Co3O4 nanoparticles with block and sphere morphology, and investigation into the influence of morphology on biological toxicity', *Exp Ther Med*, vol. 11, no. 2, pp. 553–560, Feb. 2016, doi: 10.3892/ETM.2015.2946/HTML.

[27] P. Zhang, T. uo Wang, X. Chang, L. Zhang, and and Jinlong Gong, ‘Synergistic Cocatalytic Effect of Carbon Nanodots and Co3O4 Nanoclusters for the Photoelectrochemical Water Oxidation on Hematite’, *Angewandte Chemie*, vol. 128, no. 19, pp. 5945–5949, May 2016, doi: 10.1002/ANGE.201600918.

[28] H. Alshaikh, A. Shawky, R. M. Mohamed, J. G. Knight, and L. S. Roselin, ‘Solution-based synthesis of Co3O4/ZnO p-n heterojunctions for rapid visible-light-driven oxidation of ciprofloxacin’, *J Mol Liq*, vol. 334, p. 116092, Jul. 2021, doi: 10.1016/J.MOLLIQ.2021.116092.

[29] S. Akshatha *et al.*, ‘Microwave assisted green synthesis of p-type Co3O4@Mesoporous carbon spheres for simultaneous degradation of dyes and photocatalytic hydrogen evolution reaction’, *Mater Sci Semicond Process*, vol. 121, p. 105432, Jan. 2021, doi: 10.1016/J.MSSP.2020.105432.

[30] S. Vijayakumar, A. Kiruthika Ponnalagi, S. Nagamuthu, and G. Muralidharan, ‘Microwave assisted synthesis of Co3O4 nanoparticles for high-performance supercapacitors’, *Electrochim Acta*, vol. 106, pp. 500–505, Sep. 2013, doi: 10.1016/J.ELECTACTA.2013.05.121.

[31] S. Iravani and R. S. Varma, ‘Sustainable synthesis of cobalt and cobalt oxide nanoparticles and their catalytic and biomedical applications’, *Green Chemistry*, vol. 22, no. 9, pp. 2643–2661, May 2020, doi: 10.1039/D0GC00885K.

[32] M. Hafeez *et al.*, ‘Green synthesis of cobalt oxide nanoparticles for potential biological applications’, *Mater Res Express*, vol. 7, no. 2, p. 025019, Feb. 2020, doi: 10.1088/2053-1591/AB70DD.

[33] L. Han, D. P. Yang, and A. Liu, ‘Leaf-templated synthesis of 3D hierarchical porous cobalt oxide nanostructure as direct electrochemical biosensing interface with enhanced electrocatalysis’, *Biosens Bioelectron*, vol. 63, pp. 145–152, Jan. 2015, doi: 10.1016/J.BIOS.2014.07.031.

[34] Z. Yin *et al.*, ‘Manipulating cobalt oxide on N-doped aligned electrospun carbon nanofibers towards instant electrochemical detection of dopamine secreted by living cells’, *Appl Surf Sci*, vol. 577, p. 151912, Mar. 2022, doi: 10.1016/J.APSUSC.2021.151912.

[35] S. Sawalha *et al.*, ‘Optical properties and photoactivity of carbon nanodots synthesized from olive solid wastes at different carbonization temperatures’, *RSC Adv*, vol. 12, no. 8, p. 4490, Feb. 2022, doi: 10.1039/D1RA09273A.

[36] J. Zhang, Y. Ma, Y. Du, H. Jiang, D. Zhou, and S. Dong, ‘Carbon nanodots/WO3 nanorods Z-scheme composites: Remarkably enhanced photocatalytic performance under broad spectrum’, *Appl Catal B*, vol. 209, pp. 253–264, Jul. 2017, doi: 10.1016/J.APCATB.2017.03.017.

[37] D. M. Arvapalli, A. T. Sheardy, K. Allado, H. Chevva, Z. Yin, and J. Wei, ‘Design of Curcumin Loaded Carbon Nanodots Delivery System: Enhanced Bioavailability, Release Kinetics, and Anticancer Activity’, *ACS Appl Bio Mater*, vol. 3, no. 12, pp. 8776–8785, Dec. 2020, doi: 10.1021/ACSABM.0C01144/SUPPL_FILE/MT0C01144_SI_001.PDF.

[38] W. Zhang, Z. Zeng, and J. Wei, ‘Electrochemical Study of DPPH Radical Scavenging for Evaluating the Antioxidant Capacity of Carbon Nanodots’, *Journal of Physical Chemistry C*, vol. 121, no. 34, pp. 18635–18642, Aug. 2017, doi: 10.1021/ACS.JPCC.7B05353/ASSET/IMAGES/LARGE/JP-2017-05353V_0007.JPEG.

[39] Z. Ji, Z. Yin, Z. Jia, and J. Wei, ‘Carbon Nanodots Derived from Urea and Citric Acid in Living Cells: Cellular Uptake and Antioxidation Effect’, *Langmuir*, vol. 36, no. 29, pp. 8632–8640, Jul. 2020, doi: 10.1021/ACS.LANGMUIR.0C01598/SUPPL_FILE/LA0C01598_SI_001.PDF.

[40] L. Wang, X. Zhang, K. Yang, L. Wang, and C. S. Lee, ‘Oxygen/nitrogen-related surface states controlled carbon nanodots with tunable full-color luminescence: Mechanism and bio-imaging’, *Carbon N Y*, vol. 160, pp. 298–306, Apr. 2020, doi: 10.1016/J.CARBON.2020.01.029.

[41] M. Mehta, M. Sharma, K. Pathania, P. K. Jena, and I. Bhushan, ‘Degradation of synthetic dyes using nanoparticles: a mini-review’, *Environmental Science and Pollution Research*, vol. 28, no. 36, pp. 49434–49446, Sep. 2021, doi: 10.1007/S11356-021-15470-5/TABLES/3.

[42] M. Nan Chong, B. Jin, C. W. Chow, and C. Saint, ‘Recent developments in photocatalytic water treatment technology: A review’, 2010, doi: 10.1016/j.watres.2010.02.039.

[43] B. Lellis, C. Z. Fávaro-Polonio, J. A. Pamphile, and J. C. Polonio, ‘Effects of textile dyes on health and the environment and bioremediation potential of living organisms’, *Biotechnology Research and Innovation*, vol. 3, no. 2, pp. 275–290, Jul. 2019, doi: 10.1016/J.BIORI.2019.09.001.

[44] B. Ohtani, ‘Photocatalysis A to Z—What we know and what we do not know in a scientific sense’, *Journal of Photochemistry and Photobiology C: Photochemistry Reviews*, vol. 11, no. 4, pp. 157–178, Dec. 2010, doi: 10.1016/J.JPHOTOCHEMREV.2011.02.001.

[45] I. Khan *et al.*, ‘Review on Methylene Blue: Its Properties, Uses, Toxicity and Photodegradation’, *Water (Basel)*, vol. 14, no. 2, p. 242, Jan. 2022, doi: 10.3390/W14020242.

[46] K. Rokesh, M. Sakar, and T.-O. Do, ‘Emerging Hybrid Nanocomposite Photocatalysts for the Degradation of Antibiotics: Insights into Their Designs and Mechanisms’, 2021, doi: 10.3390/nano11030572.

[47] A. Dey and P. R. Gogate, ‘Nanocomposite photocatalysts-based wastewater treatment’, *Handbook of Nanomaterials for Wastewater Treatment*, pp. 779–809, Jan. 2021, doi: 10.1016/B978-0-12-821496-1.00022-2.

[48] M. B. Tahir, M. Sohaib, M. Sagir, and M. Rafique, ‘Role of Nanotechnology in Photocatalysis’, *Reference Module in Materials Science and Materials Engineering*, pp. 578–589, 2020, doi: 10.1016/B978-0-12-815732-9.00006-1.

[49] K. Kannan, D. Radhika, K. K. Sadasivuni, K. R. Reddy, and A. v. Raghu, ‘Nanostructured metal oxides and its hybrids for photocatalytic and biomedical applications’, *Adv Colloid Interface Sci*, vol. 281, p. 102178, Jul. 2020, doi: 10.1016/J.CIS.2020.102178.

[50] S. S. Watson, D. Beydoun, J. A. Scott, and R. Amal, ‘The effect of preparation method on the photoactivity of crystalline titanium dioxide particles’, *Chemical Engineering Journal*, vol. 95, no. 1–3, pp. 213–220, Sep. 2003, doi: 10.1016/S1385-8947(03)00107-4.

[51] P. Ahuja, S. K. Ujjain, R. Kanojia, and P. Attri, ‘Transition Metal Oxides and Their Composites for Photocatalytic Dye Degradation’, *Journal of Composites Science 2021, Vol. 5, Page 82*, vol. 5, no. 3, p. 82, Mar. 2021, doi: 10.3390/JCS5030082.

[52] M. Farooq Warsi, N. Shaheen, M. Ilyas Sarwar, P. O. Agboola, I. Shakir, and S. Zulfiqar, ‘A comparative study on photocatalytic activities of various transition metal oxides

nanoparticles synthesized by wet chemical route', *Desalination Water Treat*, vol. 211, pp. 181–195, 2021, doi: 10.5004/dwt.2021.26463.

[53] R. He, H. Liang, C. Li, and J. Bai, 'Enhanced photocatalytic hydrogen production over Co3O4@g-C3N4 p-n junction adhering on one-dimensional carbon fiber', *Colloids Surf A Physicochem Eng Asp*, vol. 586, p. 124200, Feb. 2020, doi: 10.1016/J.COLSURFA.2019.124200.

[54] S. Sekar, V. Preethi, S. Saravanan, D. Y. Kim, and S. Lee, 'Excellent photocatalytic performances of Co3O4–AC nanocomposites for H2 production via wastewater splitting', *Chemosphere*, vol. 286, p. 131823, Jan. 2022, doi: 10.1016/J.CHEMOSPHERE.2021.131823.

[55] B. Guo, C. Li, and Z. Y. Yuan, 'Nanostructured Co3O4 Materials: Synthesis, Characterization, and Electrochemical Behaviors as Anode Reactants in Rechargeable Lithium Ion Batteries', *Journal of Physical Chemistry C*, vol. 114, no. 29, pp. 12805–12817, Jul. 2010, doi: 10.1021/JP103705Q/ASSET/IMAGES/LARGE/JP-2010-03705Q_0007.JPEG.

[56] T. Zhang *et al.*, 'Co3O4 nanoparticles anchored on nitrogen-doped reduced graphene oxide as a multifunctional catalyst for H2O2 reduction, oxygen reduction and evolution reaction', *Sci Rep*, vol. 7, Mar. 2017, doi: 10.1038/SREP43638.

[57] N. Zhang, J. Shi, S. S. Mao, and L. Guo, 'Co3O4 quantum dots: reverse micelle synthesis and visible-light-driven photocatalytic overall water splitting', *Chemical Communications*, vol. 50, no. 16, pp. 2002–2004, Jan. 2014, doi: 10.1039/C3CC48026G.

[58] S. Jamil, X. Jing, J. Wang, S. Li, J. Liu, and M. Zhang, 'The synthesis of porous Co3O4 micro cuboid structures by solvothermal approach and investigation of its gas sensing

properties and catalytic activity', *Mater Res Bull*, vol. 48, no. 11, pp. 4513–4520, Nov. 2013, doi: 10.1016/J.MATERRESBULL.2013.07.059.

[59] P. B. Koli, K. H. Kapadnis, U. G. Deshpande, and M. R. Patil, 'Fabrication and characterization of pure and modified Co3O4 nanocatalyst and their application for photocatalytic degradation of eosine blue dye: a comparative study', *J Nanostructure Chem*, vol. 8, no. 4, pp. 453–463, Dec. 2018, doi: 10.1007/S40097-018-0287-0/FIGURES/11.

[60] M. K. Uddin and U. Baig, 'Synthesis of Co3O4 nanoparticles and their performance towards methyl orange dye removal: Characterisation, adsorption and response surface methodology', *J Clean Prod*, vol. 211, pp. 1141–1153, Feb. 2019, doi: 10.1016/J.JCLEPRO.2018.11.232.

[61] J. Rosen, G. S. Hutchings, and F. Jiao, 'Synthesis, structure, and photocatalytic properties of ordered mesoporous metal-doped Co3O4', *J Catal*, vol. 310, pp. 2–9, Feb. 2014, doi: 10.1016/J.JCAT.2013.05.003.

[62] C. Ravi Dhas *et al.*, 'Visible light driven photocatalytic degradation of Rhodamine B and Direct Red using cobalt oxide nanoparticles', *Ceram Int*, vol. 41, no. 8, pp. 9301–9313, Sep. 2015, doi: 10.1016/J.CERAMINT.2015.03.238.

[63] K. M. Omer, N. N. Mohammad, S. O. Baban, and A. Q. Hassan, 'Carbon nanodots as efficient photosensitizers to enhance visible-light driven photocatalytic activity', *J Photochem Photobiol A Chem*, vol. 364, pp. 53–58, Sep. 2018, doi: 10.1016/J.JPHOTOCHEM.2018.05.041.

[64] M. Singh, D. Vaya, R. Kumar, and B. K. Das, ‘Role of EDTA capped cobalt oxide nanomaterial in photocatalytic degradation of dyes’, *Journal of the Serbian Chemical Society*, vol. 86, no. 3, pp. 327–340, 2021, doi: 10.2298/JSC200711074S.

[65] T. Warang, N. Patel, R. Fernandes, N. Bazzanella, and A. Miotello, ‘Co3O4 nanoparticles assembled coatings synthesized by different techniques for photo-degradation of methylene blue dye’, *Appl Catal B*, vol. 132–133, pp. 204–211, Mar. 2013, doi: 10.1016/J.APCATB.2012.11.040.

[66] L. M. Kustov, ‘Catalysis by Hybrid Nanomaterials’, *Molecules*, vol. 26, no. 2, Jan. 2021, doi: 10.3390/MOLECULES26020352.

[67] A. Kumar and G. Pandey, ‘A review on the factors affecting the photocatalytic degradation of hazardous materials’, *Material Science & Engineering International Journal*, vol. Volume 1, no. Issue 3, Nov. 2017, doi: 10.15406/MSEIJ.2017.01.00018.

[68] A. Ibarbia, H. J. Grande, V. Ruiz, A. Ibarbia, H. J. Grande, and V. Ruiz, ‘On the Factors behind the Photocatalytic Activity of Graphene Quantum Dots for Organic Dye Degradation’, *Particle & Particle Systems Characterization*, vol. 37, no. 5, p. 2000061, May 2020, doi: 10.1002/PPSC.202000061.

[69] L. Yang *et al.*, ‘Carbon-Based Metal-Free ORR Electrocatalysts for Fuel Cells: Past, Present, and Future’, *Advanced Materials*, vol. 31, no. 13, p. 1804799, Mar. 2019, doi: 10.1002/ADMA.201804799.

[70] J. Yu *et al.*, ‘Cobalt Oxide and Cobalt-Graphitic Carbon Core–Shell Based Catalysts with Remarkably High Oxygen Reduction Reaction Activity’, *Advanced Science*, vol. 3, no. 9, Sep. 2016, doi: 10.1002/ADVS.201600060.

[71] R. Madhu, V. Veeramani, S. M. Chen, A. Manikandan, A. Y. Lo, and Y. L. Chueh, 'Honeycomb-like Porous Carbon-Cobalt Oxide Nanocomposite for High-Performance Enzymeless Glucose Sensor and Supercapacitor Applications', *ACS Appl Mater Interfaces*, vol. 7, no. 29, pp. 15812–15820, Jul. 2015, doi: 10.1021/ACSAMI.5B04132/SUPPL_FILE/AM5B04132_SI_001.PDF.

[72] C. Hu, M. Li, J. Qiu, and Y. P. Sun, 'Design and fabrication of carbon dots for energy conversion and storage', *Chem Soc Rev*, vol. 48, no. 8, pp. 2315–2337, Apr. 2019, doi: 10.1039/C8CS00750K.

[73] K. Allado, M. Liu, A. Jayapalan, D. Arvapalli, K. Nowlin, and J. Wei, 'Binary MnO2/Co3O4metal oxides wrapped on superaligned electrospun carbon nanofibers as binder free supercapacitor electrodes', *Energy and Fuels*, vol. 35, no. 9, pp. 8396–8405, May 2021, doi: 10.1021/ACS.ENERGYFUELS.1C00556.

[74] Y. Yang, R. Zeng, Y. Xiong, F. J. Disalvo, and H. D. Abruña, 'Cobalt-Based Nitride-Core Oxide-Shell Oxygen Reduction Electrocatalysts', *J Am Chem Soc*, vol. 141, no. 49, pp. 19241–19245, Dec. 2019, doi: 10.1021/JACS.9B10809/SUPPL_FILE/JA9B10809_SI_001.PDF.

[75] Z. Zeng *et al.*, 'Magnetic Field-Enhanced 4-Electron Pathway for Well-Aligned Co3O4/Electrospun Carbon Nanofibers in the Oxygen Reduction Reaction', *ChemSusChem*, vol. 11, no. 3, pp. 580–588, Feb. 2018, doi: 10.1002/CSSC.201701947.

[76] Z. Mahdavi, H. Rezvani, and M. Keshavarz Moraveji, 'Core-shell nanoparticles used in drug delivery-microfluidics: a review', 2020, doi: 10.1039/d0ra01032d.

[77] S. Deshpande, S. Sharma, V. Koul, and N. Singh, 'Core-shell nanoparticles as an efficient, sustained, and triggered drug-delivery system', *ACS Omega*, vol. 2, no. 10, pp. 6455–

6463, Oct. 2017, doi: 10.1021/ACSOMEGA.7B01016/ASSET/IMAGES/AO-2017-010168_M002.GIF.

[78] A. Soto-Quintero, N. Guarrotxena, O. García, and I. Quijada-Garrido, 'Curcumin to Promote the Synthesis of Silver NPs and their Self-Assembly with a Thermoresponsive Polymer in Core-Shell Nanohybrids', *Scientific Reports 2019 9:1*, vol. 9, no. 1, pp. 1–14, Dec. 2019, doi: 10.1038/s41598-019-54752-4.

[79] A. Wang, C. Wang, L. Fu, W. Wong-Ng, and Y. Lan, 'Recent Advances of Graphitic Carbon Nitride-Based Structures and Applications in Catalyst, Sensing, Imaging, and LEDs', *Nano-Micro Letters 2017 9:4*, vol. 9, no. 4, pp. 1–21, Jun. 2017, doi: 10.1007/S40820-017-0148-2.

[80] Z. Ji *et al.*, 'Tuning the Functional Groups on Carbon Nanodots and Antioxidant Studies', *Molecules 2019, Vol. 24, Page 152*, vol. 24, no. 1, p. 152, Jan. 2019, doi: 10.3390/MOLECULES24010152.

[81] W. Zhang *et al.*, 'Antioxidant capacity of nitrogen and sulfur codoped carbon nanodots', *ACS Appl Nano Mater*, vol. 1, no. 6, pp. 2699–2708, Jun. 2018, doi: 10.1021/ACSANM.8B00404/SUPPL_FILE/AN8B00404_SI_001.PDF.

[82] D. M. Arvapalli, A. T. Sheardy, J. J. Bang, and J. Wei, 'Antiproliferative and ROS Regulation Activity of Photoluminescent Curcumin-Derived Nanodots', *ACS Appl Bio Mater*, vol. 4, no. 12, pp. 8477–8486, Dec. 2021, doi: 10.1021/ACSABM.1C00991/SUPPL_FILE/MT1C00991_SI_001.PDF.

[83] J. Zhou, J. Gu, C. Tian, D. Jiang, Y. Chen, and K. Xi, 'Co3O4-cored carbon dots for chemiluminescence analysis of intracellular hydrogen peroxide', *RSC Adv*, vol. 6, no. 45, pp. 39480–39483, Apr. 2016, doi: 10.1039/C6RA04029B.

[84] F. Sabir *et al.*, ‘Onco-Receptors Targeting in Lung Cancer via Application of Surface-Modified and Hybrid Nanoparticles: A Cross-Disciplinary Review’, *Processes*, vol. 9, no. 4, p. 621, Apr. 2021, doi: 10.3390/pr9040621.

[85] F. Danhier, O. Feron, and V. Préat, ‘To exploit the tumor microenvironment: Passive and active tumor targeting of nanocarriers for anti-cancer drug delivery’, *Journal of Controlled Release*, vol. 148, no. 2, pp. 135–146, Dec. 2010, doi: 10.1016/J.JCONREL.2010.08.027.

[86] G. Hu *et al.*, ‘Utilizing G2/M retention effect to enhance tumor accumulation of active targeting nanoparticles’, *Scientific Reports 2016 6:1*, vol. 6, no. 1, pp. 1–10, Jun. 2016, doi: 10.1038/srep27669.

[87] J. Wang, Y. Li, and G. Nie, ‘Multifunctional biomolecule nanostructures for cancer therapy’, *Nature Reviews Materials 2021 6:9*, vol. 6, no. 9, pp. 766–783, May 2021, doi: 10.1038/s41578-021-00315-x.

[88] I. Khan *et al.*, ‘Review on Methylene Blue: Its Properties, Uses, Toxicity and Photodegradation’, *Water 2022, Vol. 14, Page 242*, vol. 14, no. 2, p. 242, Jan. 2022, doi: 10.3390/W14020242.

[89] K. Rokesh, M. Sakar, and T. O. Do, ‘Emerging Hybrid Nanocomposite Photocatalysts for the Degradation of Antibiotics: Insights into Their Designs and Mechanisms’, *Nanomaterials*, vol. 11, no. 3, pp. 1–34, Mar. 2021, doi: 10.3390/NANO11030572.

[90] J. Cheng *et al.*, ‘Highly Efficient Removal of Methylene Blue Dye from an Aqueous Solution Using Cellulose Acetate Nanofibrous Membranes Modified by Polydopamine’, *ACS Omega*, vol. 5, no. 10, pp. 5389–5400, Mar. 2020, doi: 10.1021/acsomega.9b04425.

[91] Y. H. Chiu, T. F. M. Chang, C. Y. Chen, M. Sone, and Y. J. Hsu, ‘Mechanistic Insights into Photodegradation of Organic Dyes Using Heterostructure Photocatalysts’, *Catalysts 2019, Vol. 9, Page 430*, vol. 9, no. 5, p. 430, May 2019, doi: 10.3390/CATAL9050430.

[92] M. F. Chowdhury, S. Khandaker, F. Sarker, A. Islam, M. T. Rahman, and M. R. Awual, ‘Current treatment technologies and mechanisms for removal of indigo carmine dyes from wastewater: A review’, *J Mol Liq*, vol. 318, p. 114061, Nov. 2020, doi: 10.1016/J.MOLLIQ.2020.114061.

[93] P. Shah, A. Unnarkat, F. Patel, M. Shah, and P. Shah, ‘A comprehensive review on spinel based novel catalysts for visible light assisted dye degradation’, *Process Safety and Environmental Protection*, vol. 161, pp. 703–722, May 2022, doi: 10.1016/J.PSEP.2022.03.030.

[94] Mohan. Sakar, R. Geetha. Balakrishna, and T.-On. Do, ‘Photocatalystic systems by design : materials, mechanisms and applications’, 2021.

[95] H. A. A. Jamjoum, K. Umar, R. Adnan, M. R. Razali, and M. N. Mohamad Ibrahim, ‘Synthesis, Characterization, and Photocatalytic Activities of Graphene Oxide/metal Oxides Nanocomposites: A Review’, *Front Chem*, vol. 9, p. 789, Sep. 2021, doi: 10.3389/FCHEM.2021.752276/BIBTEX.

[96] A. Mehta *et al.*, ‘Band gap tuning and surface modification of carbon dots for sustainable environmental remediation and photocatalytic hydrogen production – A review’, *J Environ Manage*, vol. 250, p. 109486, Nov. 2019, doi: 10.1016/J.JENVMAN.2019.109486.

[97] H. peng Feng *et al.*, ‘Core-shell nanomaterials: Applications in energy storage and conversion’, *Adv Colloid Interface Sci*, vol. 267, pp. 26–46, May 2019, doi: 10.1016/J.CIS.2019.03.001.

[98] K. S. Obayomi, S. Y. Lau, M. Danquah, T. Chiong, and M. Takeo, ‘Advances in graphene oxide based nanobiocatalytic technology for wastewater treatment’, *Environ Nanotechnol Monit Manag*, vol. 17, p. 100647, May 2022, doi: 10.1016/J.ENMM.2022.100647.

[99] S. Homaeigohar, ‘The Nanosized Dye Adsorbents for Water Treatment’, 2020, doi: 10.3390/nano10020295.

[100] R. Al-Tuwirqi, A. A. Al-Ghamdi, N. A. Aal, A. Umar, and W. E. Mahmoud, ‘Facile synthesis and optical properties of Co 3 O 4 nanostructures by the microwave route’, *Superlattices Microstruct*, vol. 49, pp. 416–421, 2011, doi: 10.1016/j.spmi.2010.12.010.

[101] N. Barka, A. Assabbane, A. Nounah, and Y. A. Ichou, ‘Photocatalytic degradation of indigo carmine in aqueous solution by TiO2-coated non-woven fibres’, *J Hazard Mater*, vol. 152, no. 3, pp. 1054–1059, Apr. 2008, doi: 10.1016/J.JHAZMAT.2007.07.080.

[102] Y. Dong, K. He, L. Yin, and A. Zhang, ‘A facile route to controlled synthesis of Co3O4 nanoparticles and their environmental catalytic properties’, *Nanotechnology*, vol. 18, no. 43, Oct. 2007, doi: 10.1088/0957-4484/18/43/435602.

[103] D. M. Arvapalli, A. T. Sheardy, K. C. Alapati, and J. Wei, ‘High Quantum Yield Fluorescent Carbon Nanodots for Detection of Fe (III) Ions and Electrochemical Study of Quenching Mechanism’, 2019.

[104] R. Uma, K. Ravichandran, S. Sriram, and B. Sakthivel, ‘Cost-effective fabrication of ZnO/g-C3N4 composite thin films for enhanced photocatalytic activity against three

different dyes (MB, MG and RhB)', *Mater Chem Phys*, vol. 201, pp. 147–155, Nov. 2017, doi: 10.1016/J.MATCHEMPHYS.2017.08.015.

[105] W. J. Int Environ Res, S. Figueiredo, M. Otero, H. Liu, H. Chen, and N. Ding, 'Visible Light-Based Ag3PO4/g-C3N4@MoS2 for Highly Efficient Degradation of 2-Amino-4-acetylaminoanisole (AMA) from Printing and Dyeing Wastewater', *International Journal of Environmental Research and Public Health 2022, Vol. 19, Page 2934*, vol. 19, no. 5, p. 2934, Mar. 2022, doi: 10.3390/IJERPH19052934.

[106] Y. Hu *et al.*, 'Fluorescence and photocatalytic activity of metal-free nitrogen-doped carbon quantum dots with varying nitrogen contents', *Appl Surf Sci*, vol. 531, p. 147344, Nov. 2020, doi: 10.1016/J.APSUSC.2020.147344.

[107] K. J. Mintz *et al.*, 'A deep investigation into the structure of carbon dots', *Carbon N Y*, vol. 173, pp. 433–447, Mar. 2021, doi: 10.1016/J.CARBON.2020.11.017.

[108] H. H. Hammud *et al.*, 'Hierarchical Porous Carbon Cobalt Nanocomposites-Based Sensor for Fructose', *Chemosensors 2021, Vol. 9, Page 6*, vol. 9, no. 1, p. 6, Dec. 2020, doi: 10.3390/CHEMOSENSORS9010006.

[109] S. Akshatha *et al.*, 'Microwave assisted green synthesis of p-type Co3O4@Mesoporous carbon spheres for simultaneous degradation of dyes and photocatalytic hydrogen evolution reaction', *Mater Sci Semicond Process*, vol. 121, p. 105432, Jan. 2021, doi: 10.1016/J.MSSP.2020.105432.

[110] A. Diallo, A. C. Beye, T. B. Doyle, E. Park, and M. Maaza, 'Green synthesis of Co3O4 nanoparticles via Aspalathus linearis: Physical properties', *http://mc.manuscriptcentral.com/tgcl*, vol. 8, no. 3–4, pp. 30–36, Oct. 2015, doi: 10.1080/17518253.2015.1082646.

[111] S. J. Folkman, M. Zhou, M. Nicki, and R. G. Finke, 'Alcohol Solvent Effects in the Synthesis of Co3O4 Metal-Oxide Nanoparticles: Disproof of a Surface-Ligand Thermodynamic Effect en Route to Alternative Kinetic and Thermodynamic Explanations', *Inorg Chem*, vol. 57, no. 3, pp. 1517–1526, Feb. 2018, doi: 10.1021/ACS.INORGCHEM.7B02831/ASSET/IMAGES/IC-2017-028317_M001.GIF.

[112] Z. Zeng *et al.*, 'A fluorescence-electrochemical study of carbon nanodots (CNDs) in bio- and photoelectronic applications and energy gap investigation †', *Phys. Chem. Chem. Phys*, vol. 19, pp. 20101–20109, 2017, doi: 10.1039/c7cp02875j.

[113] K. Qi *et al.*, 'Facile and Efficient Fabrication of Bandgap Tunable Carbon Quantum Dots Derived From Anthracite and Their Photoluminescence Properties', *Frontiers in Chemistry | www.frontiersin.org*, vol. 8, p. 123, 2020, doi: 10.3389/fchem.2020.00123.

[114] R. Atchudan *et al.*, 'Concurrent synthesis of nitrogen-doped carbon dots for cell imaging and ZnO@nitrogen-doped carbon sheets for photocatalytic degradation of methylene blue', *J Photochem Photobiol A Chem*, vol. 350, pp. 75–85, Jan. 2018, doi: 10.1016/J.JPHOTOCHEM.2017.09.038.

[115] R. He, H. Liang, C. Li, and J. Bai, 'Enhanced photocatalytic hydrogen production over Co3O4@g-C3N4 p-n junction adhering on one-dimensional carbon fiber', *Colloids Surf A Physicochem Eng Asp*, vol. 586, p. 124200, Feb. 2020, doi: 10.1016/J.COLSURFA.2019.124200.

[116] Y. Zhang *et al.*, 'Biopolymer-Activated Graphitic Carbon Nitride towards a Sustainable Photocathode Material', *Scientific Reports 2013 3:1*, vol. 3, no. 1, pp. 1–5, Jul. 2013, doi: 10.1038/srep02163.

[117] P. M. Gharat, J. M. Chethodil, A. P. Srivastava, P. K. Praseetha, H. Pal, and S. Dutta Choudhury, ‘An insight into the molecular and surface state photoluminescence of carbon dots revealed through solvent-induced modulations in their excitation wavelength dependent emission properties’, *Photochemical & Photobiological Sciences*, vol. 18, no. 1, pp. 110–119, Jan. 2019, doi: 10.1039/C8PP00373D.

[118] J. Liqiang *et al.*, ‘Review of photoluminescence performance of nano-sized semiconductor materials and its relationships with photocatalytic activity’, *Solar Energy Materials and Solar Cells*, vol. 90, no. 12, pp. 1773–1787, Jul. 2006, doi: 10.1016/J.SOLMAT.2005.11.007.

[119] A. Alhebshi, E. Sharaf Aldeen, R. S. Mim, B. Tahir, and M. Tahir, ‘Recent advances in constructing heterojunctions of binary semiconductor photocatalysts for visible light responsive CO2 reduction to energy efficient fuels: A review’, *Int J Energy Res*, vol. 46, no. 5, pp. 5523–5584, Apr. 2022, doi: 10.1002/ER.7563.

[120] K. M. Reza, A. Kurny, and F. Gulshan, ‘Parameters affecting the photocatalytic degradation of dyes using TiO2: a review’, *Applied Water Science 2015 7:4*, vol. 7, no. 4, pp. 1569–1578, Dec. 2015, doi: 10.1007/S13201-015-0367-Y.

[121] S. S. Mohtar *et al.*, ‘Impact of Doping and Additive Applications on Photocatalyst Textural Properties in Removing Organic Pollutants: A Review’, *Catalysts 2021, Vol. 11, Page 1160*, vol. 11, no. 10, p. 1160, Sep. 2021, doi: 10.3390/CATAL11101160.

[122] M. B. Tahir, M. Sohaib, M. Sagir, and M. Rafique, ‘Role of Nanotechnology in Photocatalysis’, *Reference Module in Materials Science and Materials Engineering*, pp. 578–589, Jan. 2020, doi: 10.1016/B978-0-12-815732-9.00006-1.

[123] X. Wan, M. Yuan, S.-L. Tie, and S. Lan, ‘Effects of catalyst characters on the photocatalytic activity and process of NiO nanoparticles in the degradation of methylene blue’, *Appl Surf Sci*, vol. 277, pp. 40–46, 2013, doi: 10.1016/j.apsusc.2013.03.126.

[124] F. F. Zhang *et al.*, ‘Visible light-assisted photocatalytic degradation of methylene blue in water by highly chemically stable Cd-coordination polymers at room temperature’, *New Journal of Chemistry*, vol. 45, no. 42, pp. 19660–19665, Nov. 2021, doi: 10.1039/D1NJ03958J.

[125] T. Qu, X. Yao, G. Owens, L. Gao, and H. Zhang, ‘A sustainable natural clam shell derived photocatalyst for the effective adsorption and photodegradation of organic dyes’, 123AD, doi: 10.1038/s41598-022-06981-3.

[126] R. Javaid and U. Y. Qazi, ‘Catalytic Oxidation Process for the Degradation of Synthetic Dyes: An Overview’, *Int J Environ Res Public Health*, vol. 16, no. 11, Jun. 2019, doi: 10.3390/IJERPH16112066.

[127] M. F. Elkady and H. S. Hassan, ‘Photocatalytic Degradation of Malachite Green Dye from Aqueous Solution Using Environmentally Compatible Ag/ZnO Polymeric Nanofibers’, *Polymers (Basel)*, vol. 13, no. 13, Jul. 2021, doi: 10.3390/POLYM13132033.

[128] A. Alaghmandfard and K. Ghandi, ‘A Comprehensive Review of Graphitic Carbon Nitride (g-C3N4)–Metal Oxide-Based Nanocomposites: Potential for Photocatalysis and Sensing’, *Nanomaterials 2022, Vol. 12, Page 294*, vol. 12, no. 2, p. 294, Jan. 2022, doi: 10.3390/NANO12020294.

[129] A. Chithambararaj, N. S. Sanjini, A. C. Bose, and S. Velmathi, ‘Flower-like hierarchical h-MoO3: new findings of efficient visible light driven nano photocatalyst for methylene

blue degradation', *Catal Sci Technol*, vol. 3, no. 5, pp. 1405–1414, Apr. 2013, doi: 10.1039/C3CY20764A.

[130] A. Xu, X. Li, S. Ye, G. Yin, and Q. Zeng, 'Catalyzed oxidative degradation of methylene blue by in situ generated cobalt (II)-bicarbonate complexes with hydrogen peroxide', *Appl Catal B*, vol. 102, no. 1–2, pp. 37–43, Feb. 2011, doi: 10.1016/J.APCATB.2010.11.022.

[131] S. Mohamadi and M. Ghorbanali, 'Adsorption and UV-assisted photodegradation of methylene blue by CeO2-decorated graphene sponge', *https://doi.org/10.1080/01496395.2020.1728325*, vol. 56, no. 3, pp. 507–517, 2020, doi: 10.1080/01496395.2020.1728325.

[132] M. Seffen and A. Nd, 'Photocatalytic degradation of indigo carmine using [Zn-Al] LDH supported on PAN nanofibres', 2015, doi: 10.1180/claymin.2015.050.2.03.

[133] Z. Ju, J. Sun, and Y. Liu, 'Molecular Structures and Spectral Properties of Natural Indigo and Indirubin: Experimental and DFT Studies', *Molecules*, vol. 24, no. 21, Oct. 2019, doi: 10.3390/MOLECULES24213831.

[134] M. R. Abhilash, G. Akshatha, and S. Srikantaswamy, 'Photocatalytic dye degradation and biological activities of the Fe 2 O 3 /Cu 2 O nanocomposite', *RSC Adv*, vol. 9, no. 15, pp. 8557–8568, Mar. 2019, doi: 10.1039/C8RA09929D.

[135] D. He *et al.*, 'A multifunctional platform by controlling of carbon nitride in the core-shell structure: From design to construction, and catalysis applications', *Appl Catal B*, vol. 258, p. 117957, Dec. 2019, doi: 10.1016/J.APCATB.2019.117957.

[136] A. Ejsmont, A. Jankowska, and J. Goscianska, 'Insight into the Photocatalytic Activity of Cobalt-Based Metal–Organic Frameworks and Their Composites', *Catalysts 2022, Vol. 12, Page 110*, vol. 12, no. 2, p. 110, Jan. 2022, doi: 10.3390/CATAL12020110.

[137] A. B. Djurišić, Y. He, and A. M. C. Ng, ‘Visible-light photocatalysts: Prospects and challenges’, *APL Mater*, vol. 8, no. 3, p. 030903, Mar. 2020, doi: 10.1063/1.5140497.

[138] M. Nazim, A. Aslam, P. Khan, A. M. Asiri, and J. H. Kim, ‘Exploring Rapid Photocatalytic Degradation of Organic Pollutants with Porous CuO Nanosheets: Synthesis, Dye Removal, and Kinetic Studies at Room Temperature’, vol. 6, 2601, doi: 10.1021/acsomega.0c04747.

[139] N. Akram, J. Guo, W. Ma, Y. Guo, A. Hassan, and J. Wang, ‘Synergistic Catalysis of Co(OH)2/CuO for the Degradation of Organic Pollutant Under Visible Light Irradiation’, *Scientific Reports 2020 10:1*, vol. 10, no. 1, pp. 1–12, Feb. 2020, doi: 10.1038/s41598-020-59053-9.

[140] N. Kumar, S. bin Kim, S. Y. Lee, and S. J. Park, ‘Recent Advanced Supercapacitor: A Review of Storage Mechanisms, Electrode Materials, Modification, and Perspectives’, *Nanomaterials 2022, Vol. 12, Page 3708*, vol. 12, no. 20, p. 3708, Oct. 2022, doi: 10.3390/NANO12203708.

[141] N. Kumar, S. bin Kim, S. Y. Lee, and S. J. Park, ‘Recent Advanced Supercapacitor: A Review of Storage Mechanisms, Electrode Materials, Modification, and Perspectives’, *Nanomaterials*, vol. 12, no. 20, Oct. 2022, doi: 10.3390/NANO12203708.

[142] S. Bhoyate, P. K. Kahol, and R. K. Gupta, ‘Nanostructured materials for supercapacitor applications’, *SPR Nanoscience*, vol. 5, pp. 1–29, Nov. 2018, doi: 10.1039/9781788013871-00001.

[143] R. Kumar *et al.*, ‘An overview of recent progress in nanostructured carbon-based supercapacitor electrodes: From zero to bi-dimensional materials’, *Carbon N Y*, vol. 193, pp. 298–338, Jun. 2022, doi: 10.1016/J.CARBON.2022.03.023.

[144] K. C. Seetha Lakshmi *et al.*, 'Carbon-Based Materials for Supercapacitors: Recent Progress, Challenges and Barriers', *Batteries 2023, Vol. 9, Page 19*, vol. 9, no. 1, p. 19, Dec. 2022, doi: 10.3390/BATTERIES9010019.

[145] S. Zallouz, B. Réty, L. Vidal, J. M. le Meins, and C. Matei Ghimbeu, 'Co3O4Nanoparticles Embedded in Mesoporous Carbon for Supercapacitor Applications', *ACS Appl Nano Mater*, vol. 4, no. 5, pp. 5022–5037, May 2021, doi: 10.1021/ACSANM.1C00522/ASSET/IMAGES/LARGE/AN1C00522_0009.JPEG.

[146] A. M. Bryan, L. M. Santino, Y. Lu, S. Acharya, and J. M. D'Arcy, 'Conducting Polymers for Pseudocapacitive Energy Storage', *Chemistry of Materials*, vol. 28, no. 17, pp. 5989–5998, Sep. 2016, doi: 10.1021/ACS.CHEMMATER.6B01762/ASSET/IMAGES/MEDIUM/CM-2016-01762Q_0008.GIF.

[147] Z. Yu, L. Tetard, L. Zhai, and J. Thomas, 'Supercapacitor electrode materials: nanostructures from 0 to 3 dimensions', *Energy Environ Sci*, vol. 8, no. 3, pp. 702–730, Mar. 2015, doi: 10.1039/C4EE03229B.

[148] R. Wang, X. Li, Z. Nie, Y. Zhao, and H. Wang, 'Metal/Metal Oxide Nanoparticles-Composited Porous Carbon for High-Performance Supercapacitors', *J Energy Storage*, vol. 38, p. 102479, Jun. 2021, doi: 10.1016/J.EST.2021.102479.

[149] R. Madhu, V. Veeramani, S. M. Chen, A. Manikandan, A. Y. Lo, and Y. L. Chueh, 'Honeycomb-like Porous Carbon-Cobalt Oxide Nanocomposite for High-Performance Enzymeless Glucose Sensor and Supercapacitor Applications', *ACS Appl Mater Interfaces*, vol. 7, no. 29, pp. 15812–15820, Jul. 2015, doi: 10.1021/ACSAMI.5B04132/SUPPL_FILE/AM5B04132_SI_001.PDF.

[150] S. Kumar, G. Saeed, L. Zhu, K. N. Hui, N. H. Kim, and J. H. Lee, ‘0D to 3D carbon-based networks combined with pseudocapacitive electrode material for high energy density supercapacitor: A review’, *Chemical Engineering Journal*, vol. 403, p. 126352, Jan. 2021, doi: 10.1016/J.CEJ.2020.126352.

[151] T. Chen and L. Dai, ‘Carbon nanomaterials for high-performance supercapacitors’, *Materials Today*, vol. 16, no. 7–8, pp. 272–280, Jul. 2013, doi: 10.1016/J.MATTOD.2013.07.002.

[152] X. Zhou, B. Liu, Y. Chen, L. Guo, and G. Wei, ‘Carbon nanofiber-based three-dimensional nanomaterials for energy and environmental applications’, *Mater Adv*, vol. 1, no. 7, pp. 2163–2181, Oct. 2020, doi: 10.1039/D0MA00492H.

[153] J. Yu *et al.*, ‘Cobalt Oxide and Cobalt-Graphitic Carbon Core–Shell Based Catalysts with Remarkably High Oxygen Reduction Reaction Activity’, *Advanced Science*, vol. 3, no. 9, Sep. 2016, doi: 10.1002/ADVS.201600060.

[154] L. Yang *et al.*, ‘Carbon-Based Metal-Free ORR Electrocatalysts for Fuel Cells: Past, Present, and Future’, *Advanced Materials*, vol. 31, no. 13, p. 1804799, Mar. 2019, doi: 10.1002/ADMA.201804799.

[155] J. Xiao, R. Momen, and C. Liu, ‘Application of carbon quantum dots in supercapacitors: A mini review’, *Electrochem commun*, vol. 132, p. 107143, Nov. 2021, doi: 10.1016/J.ELECOM.2021.107143.

[156] A. Aboagye, Y. Liu, J. G. Ryan, J. Wei, and L. Zhang, ‘Hierarchical carbon composite nanofibrous electrode material for high-performance aqueous supercapacitors’, *Mater Chem Phys*, vol. 214, pp. 557–563, Aug. 2018, doi: 10.1016/J.MATCHEMPHYS.2018.05.009.

[157] Z. Xiao, G. Xiao, M. Shi, and Y. Zhu, ‘Homogeneously Dispersed Co9S8 Anchored on Nitrogen and Sulfur Co-Doped Carbon Derived from Soybean as Bifunctional Oxygen Electrocatalysts and Supercapacitors’, *ACS Appl Mater Interfaces*, vol. 10, no. 19, pp. 16436–16448, May 2018, doi: 10.1021/ACSAMI.8B01592/ASSET/IMAGES/LARGE/AM-2018-01592S_0008.JPEG.

[158] S. N. Faisal *et al.*, ‘Pyridinic and graphitic nitrogen-rich graphene for high-performance supercapacitors and metal-free bifunctional electrocatalysts for ORR and OER’, *RSC Adv*, vol. 7, no. 29, pp. 17950–17958, Mar. 2017, doi: 10.1039/C7RA01355H.

[159] Z. Lei, J. Zhang, and X. S. Zhao, ‘Ultrathin MnO2 nanofibers grown on graphitic carbon spheres as high-performance asymmetric supercapacitor electrodes’, *J Mater Chem*, vol. 22, no. 1, pp. 153–160, Dec. 2011, doi: 10.1039/C1JM13872C.

[160] A. Kulkarni, S. Siahrostami, A. Patel, and J. K. Nørskov, ‘Understanding Catalytic Activity Trends in the Oxygen Reduction Reaction’, *Chem Rev*, vol. 118, no. 5, pp. 2302–2312, Mar. 2018, doi: 10.1021/ACS.CHEMREV.7B00488/ASSET/IMAGES/MEDIUM/CR-2017-00488T_0009.GIF.

[161] X. Wang, Y. Feng, P. Dong, and J. Huang, ‘A Mini Review on Carbon Quantum Dots: Preparation, Properties, and Electrocatalytic Application’, *Front Chem*, vol. 7, p. 671, Oct. 2019, doi: 10.3389/FCHEM.2019.00671/BIBTEX.

[162] A. Sharma and J. Das, ‘Small molecules derived carbon dots: synthesis and applications in sensing, catalysis, imaging, and biomedicine’, *Journal of Nanobiotechnology 2019 17:1*, vol. 17, no. 1, pp. 1–24, Aug. 2019, doi: 10.1186/S12951-019-0525-8.

[163] Y. Song, S. Zhu, and B. Yang, ‘Bioimaging based on fluorescent carbon dots’, *RSC Adv*, vol. 4, no. 52, pp. 27184–27200, Jun. 2014, doi: 10.1039/C3RA47994C.

[164] X. C. Dong *et al.*, ‘3D graphene-cobalt oxide electrode for high-performance supercapacitor and enzymeless glucose detection’, *ACS Nano*, vol. 6, no. 4, pp. 3206–3213, Apr. 2012, doi: 10.1021/NN300097Q/SUPPL_FILE/NN300097Q_SI_001.PDF.

[165] Y. Li, Q. Li, H. Wang, L. Zhang, D. P. Wilkinson, and J. Zhang, ‘Recent Progresses in Oxygen Reduction Reaction Electrocatalysts for Electrochemical Energy Applications’, *Electrochemical Energy Reviews 2019 2:4*, vol. 2, no. 4, pp. 518–538, Oct. 2019, doi: 10.1007/S41918-019-00052-4.

[166] M. S. Ahmed, B. Choi, and Y. B. Kim, ‘Development of Highly Active Bifunctional Electrocatalyst Using Co3O4 on Carbon Nanotubes for Oxygen Reduction and Oxygen Evolution’, *Scientific Reports 2018 8:1*, vol. 8, no. 1, pp. 1–10, Feb. 2018, doi: 10.1038/s41598-018-20974-1.

[167] C. Song and J. Zhang, ‘Electrocatalytic oxygen reduction reaction’, *PEM Fuel Cell Electrocatalysts and Catalyst Layers: Fundamentals and Applications*, pp. 89–134, 2008, doi: 10.1007/978-1-84800-936-3_2/COVER.

[168] A. T. Sheardy, D. M. Arvapalli, and J. Wei, ‘Experimental and Time-Dependent Density Functional Theory Modeling Studies on the Optical Properties of Carbon Nanodots’, *Journal of Physical Chemistry C*, vol. 124, no. 8, pp. 4684–4692, Feb. 2020, doi: 10.1021/ACS.JPCC.9B10373/SUPPL_FILE/JP9B10373_SI_001.PDF.

[169] D. M. Arvapalli, A. T. Sheardy, K. C. Alapati, and J. Wei, ‘High Quantum Yield Fluorescent Carbon Nanodots for detection of Fe (III) Ions and Electrochemical Study of

Quenching Mechanism', *Talanta*, vol. 209, p. 120538, Mar. 2020, doi: 10.1016/J.TALANTA.2019.120538.

[170] N. K. Yetim, 'Hydrothermal synthesis of Co3O4 with different morphology: Investigation of magnetic and electrochemical properties', *J Mol Struct*, vol. 1226, p. 129414, Feb. 2021, doi: 10.1016/J.MOLSTRUC.2020.129414.

[171] K. Allado, M. Liu, A. Jayapalan, D. Arvapalli, K. Nowlin, and J. Wei, 'Binary MnO2/Co3O4metal oxides wrapped on superaligned electrospun carbon nanofibers as binder free supercapacitor electrodes', *Energy and Fuels*, vol. 35, no. 9, pp. 8396–8405, May 2021, doi: 10.1021/ACS.ENERGYFUELS.1C00556/ASSET/IMAGES/LARGE/EF1C00556_0006.JPEG.

[172] C. Liu, R. L. Sacci, R. Sahore, G. M. Veith, N. J. Dudney, and X. C. Chen, 'Polyacrylonitrile-based electrolytes: How processing and residual solvent affect ion transport and stability', *J Power Sources*, vol. 527, p. 231165, Apr. 2022, doi: 10.1016/J.JPOWSOUR.2022.231165.

[173] F. Lufrano, P. Staiti, and M. Minutoli, 'Influence of Nafion Content in Electrodes on Performance of Carbon Supercapacitors', *J Electrochem Soc*, vol. 151, no. 1, p. A64, Dec. 2004, doi: 10.1149/1.1626670/XML.

[174] M. Arunkumar and A. Paul, 'Importance of Electrode Preparation Methodologies in Supercapacitor Applications', *ACS Omega*, vol. 2, no. 11, pp. 8039–8050, Nov. 2017, doi: 10.1021/ACSOMEGA.7B01275/SUPPL_FILE/AO7B01275_SI_001.PDF.

[175] K. M. Ajay and M. N. Dinesh, ‘Influence of various Activated Carbon based Electrode Materials in the Performance of Super Capacitor’, *IOP Conf Ser Mater Sci Eng*, vol. 310, no. 1, p. 012083, Feb. 2018, doi: 10.1088/1757-899X/310/1/012083.

[176] J. Li and P. J. Burke, ‘Measurement of the combined quantum and electrochemical capacitance of a carbon nanotube’, *Nature Communications 2019 10:1*, vol. 10, no. 1, pp. 1–9, Aug. 2019, doi: 10.1038/s41467-019-11589-9.

[177] Y. Lim and S.-Y. Lee, ‘Capacitance Evaluation of Inorganic Core–Shell Nanoparticles with Different Shell Layers Using SPM-Combined Impedance Spectroscopy’, *J Electrochem Soc*, vol. 163, no. 2, pp. H9–H14, Nov. 2016, doi: 10.1149/2.0251602JES/XML.

[178] J. N. Tiwari, R. N. Tiwari, and K. S. Kim, ‘Zero-dimensional, one-dimensional, two-dimensional and three-dimensional nanostructured materials for advanced electrochemical energy devices’, *Prog Mater Sci*, vol. 57, no. 4, pp. 724–803, May 2012, doi: 10.1016/J.PMATSCI.2011.08.003.

[179] X. Li and J. Wang, ‘One-dimensional and two-dimensional synergized nanostructures for high-performing energy storage and conversion’, *InfoMat*, vol. 2, no. 1, pp. 3–32, Jan. 2020, doi: 10.1002/INF2.12040.

[180] Y. Lim and S.-Y. Lee, ‘ Capacitance Measurement of SiO 2 @BSA Core–Shell Nanoparticles Using AC Impedance Spectroscopy ’, *J Electrochem Soc*, vol. 162, no. 8, pp. G48–G53, May 2015, doi: 10.1149/2.0751508JES/XML.

[181] A. Kéri *et al.*, ‘Porosity determination of nano- and sub-micron particles by single particle inductively coupled plasma mass spectrometry’, *J Anal At Spectrom*, vol. 35, no. 6, pp. 1139–1147, Jun. 2020, doi: 10.1039/D0JA00020E.

[182] Y. Liu, H. Huang, W. Cao, B. Mao, Y. Liu, and Z. Kang, ‘Advances in carbon dots: from the perspective of traditional quantum dots’, *Mater Chem Front*, vol. 4, no. 6, pp. 1586–1613, Jun. 2020, doi: 10.1039/D0QM00090F.

[183] X. Zhang *et al.*, ‘Intracellular pH-propelled assembly of smart carbon nanodots and selective photothermal therapy for cancer cells’, *Colloids Surf B Biointerfaces*, vol. 188, p. 110724, Apr. 2020, doi: 10.1016/J.COLSURFB.2019.110724.

[184] A. Sciortino, A. Cannizzo, and F. Messina, ‘Carbon Nanodots: A Review—From the Current Understanding of the Fundamental Photophysics to the Full Control of the Optical Response’, *C 2018, Vol. 4, Page 67*, vol. 4, no. 4, p. 67, Dec. 2018, doi: 10.3390/C4040067.

[185] Q. X. Mao *et al.*, ‘Hydrophobic carbon nanodots with rapid cell penetrability and tunable photoluminescence behavior for in vitro and in vivo imaging’, *Langmuir*, vol. 32, no. 46, pp. 12221–12229, Nov. 2016, doi: 10.1021/ACS.LANGMUIR.6B03331/SUPPL_FILE/LA6B03331_SI_001.PDF.

[186] A. Kundu *et al.*, ‘Facile approach to synthesize highly fluorescent multicolor emissive carbon dots via surface functionalization for cellular imaging’, *J Colloid Interface Sci*, vol. 513, pp. 505–514, Mar. 2018, doi: 10.1016/J.JCIS.2017.10.095.

[187] Z. Ji, Z. Yin, Z. Jia, and J. Wei, ‘Carbon Nanodots Derived from Urea and Citric Acid in Living Cells: Cellular Uptake and Antioxidation Effect’, *Langmuir*, vol. 36, no. 29, pp. 8632–8640, Jul. 2020, doi: 10.1021/ACS.LANGMUIR.0C01598/ASSET/IMAGES/LARGE/LA0C01598_0007.JPEG.

[188] M. Zhang, P. Yuan, N. Zhou, Y. Su, M. Shao, and C. Chi, ‘pH-Sensitive N-doped carbon dots–heparin and doxorubicin drug delivery system: preparation and anticancer research’, *RSC Adv*, vol. 7, no. 15, pp. 9347–9356, Jan. 2017, doi: 10.1039/C6RA28345D.

[189] J. Pardo, Z. Peng, and R. M. Leblanc, ‘Cancer Targeting and Drug Delivery Using Carbon-Based Quantum Dots and Nanotubes’, *Molecules 2018, Vol. 23, Page 378*, vol. 23, no. 2, p. 378, Feb. 2018, doi: 10.3390/MOLECULES23020378.

[190] H. Tian *et al.*, ‘Enhancing the therapeutic efficacy of nanoparticles for cancer treatment using versatile targeted strategies’, *Journal of Hematology & Oncology 2022 15:1*, vol. 15, no. 1, pp. 1–40, Sep. 2022, doi: 10.1186/S13045-022-01320-5.

[191] D. M. Arvapalli, A. T. Sheardy, K. Allado, H. Chevva, Z. Yin, and J. Wei, ‘Design of Curcumin Loaded Carbon Nanodots Delivery System: Enhanced Bioavailability, Release Kinetics, and Anticancer Activity’, *ACS Appl Bio Mater*, vol. 3, no. 12, pp. 8776–8785, Dec. 2020, doi: 10.1021/ACSABM.0C01144/ASSET/IMAGES/LARGE/MT0C01144_0008.JPEG.

[192] A. Waris *et al.*, ‘Green fabrication of Co and Co3O4 nanoparticles and their biomedical applications: A review’, *Open Life Sci*, vol. 16, no. 1, p. 14, Jan. 2021, doi: 10.1515/BIOL-2021-0003.

[193] M. Hafeez *et al.*, ‘Green synthesis of cobalt oxide nanoparticles for potential biological applications’, *Mater Res Express*, vol. 7, no. 2, p. 025019, Feb. 2020, doi: 10.1088/2053-1591/AB70DD.

[194] A. T. Khalil, M. Ovais, I. Ullah, M. Ali, Z. K. Shinwari, and M. Maaza, ‘Physical properties, biological applications and biocompatibility studies on biosynthesized single phase cobalt oxide (Co3O4) nanoparticles via Sageretia thea (Osbeck.)’, *Arabian Journal*

of Chemistry, vol. 13, no. 1, pp. 606–619, Jan. 2020, doi: 10.1016/J.ARABJC.2017.07.004.

[195] R. C. Shete *et al.*, 'Review of Cobalt Oxide Nanoparticles: Green Synthesis, Biomedical Applications, and Toxicity Studies', *Journal of Chemical Reviews*, vol. 4, no. 4, pp. 331–345, Oct. 2022, doi: 10.22034/JCR.2022.342398.1172.

[196] S. Haq *et al.*, 'Green synthesis of cobalt oxide nanoparticles and the effect of annealing temperature on their physiochemical and biological properties', *Mater Res Express*, vol. 8, no. 7, p. 075009, Jul. 2021, doi: 10.1088/2053-1591/AC1187.

[197] S. Khan, A. A. Ansari, A. A. Khan, R. Ahmad, O. Al-Obaid, and W. Al-Kattan, 'In vitro evaluation of anticancer and antibacterial activities of cobalt oxide nanoparticles', *Journal of Biological Inorganic Chemistry*, vol. 20, no. 8, pp. 1319–1326, Dec. 2015, doi: 10.1007/S00775-015-1310-2/TABLES/1.

[198] K. Kannan, D. Radhika, K. K. Sadasivuni, K. R. Reddy, and A. v. Raghu, 'Nanostructured metal oxides and its hybrids for photocatalytic and biomedical applications', *Adv Colloid Interface Sci*, vol. 281, p. 102178, Jul. 2020, doi: 10.1016/J.CIS.2020.102178.

[199] R. A. Bohara, N. D. Thorat, H. M. Yadav, and S. H. Pawar, 'One-step synthesis of uniform and biocompatible amine functionalized cobalt ferrite nanoparticles: a potential carrier for biomedical applications', *New Journal of Chemistry*, vol. 38, no. 7, pp. 2979–2986, Jun. 2014, doi: 10.1039/C4NJ00344F.

[200] M. K. Yu, J. Park, and S. Jon, 'Targeting Strategies for Multifunctional Nanoparticles in Cancer Imaging and Therapy', *Theranostics*, vol. 2, no. 1, p. 3, 2012, doi: 10.7150/THNO.3463.

[201] C. O. Silva, J. O. Pinho, J. M. Lopes, A. J. Almeida, M. M. Gaspar, and C. Reis, 'Current Trends in Cancer Nanotheranostics: Metallic, Polymeric, and Lipid-Based Systems', *Pharmaceutics 2019, Vol. 11, Page 22*, vol. 11, no. 1, p. 22, Jan. 2019, doi: 10.3390/PHARMACEUTICS11010022.

[202] E. Carrasco-Esteban *et al.*, 'Current role of nanoparticles in the treatment of lung cancer', *J Clin Transl Res*, vol. 7, no. 2, p. 140, Apr. 2021, doi: 10.18053/jctres.07.202102.005.

[203] S. Tan and G. Wang, 'Lung cancer targeted therapy: Folate and transferrin dual targeted, glutathione responsive nanocarriers for the delivery of cisplatin', *Biomedicine and Pharmacotherapy*, vol. 102, pp. 55–63, Jun. 2018, doi: 10.1016/J.BIOPHA.2018.03.046.

[204] Y. Nakamura, A. Mochida, P. L. Choyke, and H. Kobayashi, 'Nano-drug delivery: Is the enhanced permeability and retention (EPR) effect sufficient for curing cancer?', *Bioconjug Chem*, vol. 27, no. 10, p. 2225, Oct. 2016, doi: 10.1021/ACS.BIOCONJCHEM.6B00437.

[205] B. Yu, H. C. Tai, W. Xue, L. J. Lee, and R. J. Lee, 'Receptor-targeted nanocarriers for therapeutic delivery to cancer', *Mol Membr Biol*, vol. 27, no. 7, p. 286, Oct. 2010, doi: 10.3109/09687688.2010.521200.

[206] J. S. Kim *et al.*, 'Cellular uptake of magnetic nanoparticle is mediated through energy-dependent endocytosis in A549 cells', *J Vet Sci*, vol. 7, no. 4, p. 321, 2006, doi: 10.4142/JVS.2006.7.4.321.

[207] P. Yuan *et al.*, 'N-Doped CDs–GP nanospheres as a drug delivery nanocarrier system with carbon dots and a fluorescent tracer', *New Journal of Chemistry*, vol. 41, no. 19, pp. 10880–10889, Sep. 2017, doi: 10.1039/C7NJ01762F.

[208] T. J. Yoon, J. S. Kim, B. G. Kim, K. N. Yu, M. H. Cho, and J. K. Lee, ‘Multifunctional Nanoparticles Possessing A “Magnetic Motor Effect” for Drug or Gene Delivery’, *Angewandte Chemie International Edition*, vol. 44, no. 7, pp. 1068–1071, Feb. 2005, doi: 10.1002/ANIE.200461910.

[209] S. Li *et al.*, ‘Transferrin conjugated nontoxic carbon dots for doxorubicin delivery to target pediatric brain tumor cells’, *Nanoscale*, vol. 8, no. 37, pp. 16662–16669, Sep. 2016, doi: 10.1039/C6NR05055G.

[210] L. Li *et al.*, ‘Targeted Delivery of Doxorubicin Using Transferrin-Conjugated Carbon Dots for Cancer Therapy’, *ACS Appl Bio Mater*, vol. 4, no. 9, pp. 7280–7289, Sep. 2021, doi: 10.1021/ACSABM.1C00811/ASSET/IMAGES/LARGE/MT1C00811_0007.JPEG.

[211] L. Lu, V. T. Duong, A. O. Shalash, M. Skwarczynski, and I. Toth, ‘Chemical Conjugation Strategies for the Development of Protein-Based Subunit Nanovaccines’, *Vaccines (Basel)*, vol. 9, no. 6, Jun. 2021, doi: 10.3390/VACCINES9060563.

[212] M. D. Sonawane and S. B. Nimse, ‘Surface Modification Chemistries of Materials Used in Diagnostic Platforms with Biomolecules’, *J Chem*, vol. 2016, 2016, doi: 10.1155/2016/9241378.

[213] S. Keleştemur, M. Altunbek, and M. Culha, ‘Influence of EDC/NHS coupling chemistry on stability and cytotoxicity of ZnO nanoparticles modified with proteins’, *Appl Surf Sci*, vol. 403, pp. 455–463, May 2017, doi: 10.1016/J.APSUSC.2017.01.235.

[214] K. Zhao *et al.*, ‘Fluorescence turn-off magnetic COF composite as a novel nanocarrier for drug loading and targeted delivery’, *Microporous and Mesoporous Materials*, vol. 311, p. 110713, Feb. 2021, doi: 10.1016/J.MICROMESO.2020.110713.

[215] A. Mewada, S. Pandey, M. Thakur, D. Jadhav, and M. Sharon, ‘Swarming carbon dots for folic acid mediated delivery of doxorubicin and biological imaging’, *J Mater Chem B*, vol. 2, no. 6, pp. 698–705, Jan. 2014, doi: 10.1039/C3TB21436B.

[216] Y. Lu, Y. Yin, B. T. Mayers, and Y. Xia, ‘Modifying the Surface Properties of Superparamagnetic Iron Oxide Nanoparticles through A Sol−Gel Approach’, *Nano Lett*, vol. 2, no. 3, pp. 183–186, Jan. 2002, doi: 10.1021/nl015681q.

[217] J. Feng, S. Chen, Y. L. Yu, and J. H. Wang, ‘Red-emission hydrophobic porphyrin structure carbon dots linked with transferrin for cell imaging’, *Talanta*, vol. 217, Sep. 2020, doi: 10.1016/J.TALANTA.2020.121014.

[218] B. Kalyanaraman *et al.*, ‘Measuring reactive oxygen and nitrogen species with fluorescent probes: challenges and limitations’, *Free Radic Biol Med*, vol. 52, no. 1, p. 1, Jan. 2012, doi: 10.1016/J.FREERADBIOMED.2011.09.030.

[219] S. Al-Nasiry, N. Geusens, M. Hanssens, C. Luyten, and R. Pijnenborg, ‘The use of Alamar Blue assay for quantitative analysis of viability, migration and invasion of choriocarcinoma cells’, doi: 10.1093/humrep/dem011.

[220] J. Jia *et al.*, ‘Facile and Efficient Fabrication of Bandgap Tunable Carbon Quantum Dots Derived From Anthracite and Their Photoluminescence Properties’, *Front Chem*, vol. 8, p. 123, Feb. 2020, doi: 10.3389/FCHEM.2020.00123/BIBTEX.

[221] F. Li, G. Yang, Z. P. Aguilar, Y. Xiong, and H. Xu, ‘Affordable and simple method for separating and detecting ovarian cancer circulating tumor cells using BSA coated magnetic nanoprobes modified with folic acid’, *Sens Actuators B Chem*, vol. 262, pp. 611–618, Jun. 2018, doi: 10.1016/J.SNB.2018.02.038.

[222] L. Chen *et al.*, ‘A redox stimuli-responsive superparamagnetic nanogel with chemically anchored DOX for enhanced anticancer efficacy and low systemic adverse effects’, *J Mater Chem B*, vol. 3, no. 46, pp. 8949–8962, Nov. 2015, doi: 10.1039/C5TB01851J.

[223] F. Qu, F. Xue, J. Liu, and J. You, ‘Preparation of carbon nanodots capped by polyethylene glycol as a multifunctional sensor for temperature and paracetamol’, *Analytical Methods*, vol. 9, no. 31, pp. 4533–4538, Aug. 2017, doi: 10.1039/C7AY01180F.

[224] R. J. Fan, Q. Sun, L. Zhang, Y. Zhang, and A. H. Lu, ‘Photoluminescent carbon dots directly derived from polyethylene glycol and their application for cellular imaging’, *Carbon N Y*, vol. 71, pp. 87–93, May 2014, doi: 10.1016/J.CARBON.2014.01.016.

[225] Y. Tian, Z. Ran, and W. Yang, ‘Carbon dot-silica composite nanoparticle: an excitation-independent fluorescence material with tunable fluorescence’, *RSC Adv*, vol. 7, no. 69, pp. 43839–43844, Sep. 2017, doi: 10.1039/C7RA07990G.

[226] J. H. Sun *et al.*, ‘Multifunctional mesoporous silica nanoparticles as efficient transporters of doxorubicin and chlorin e6 for chemo-photodynamic combinatorial cancer therapy’, *J Biomater Appl*, vol. 32, no. 9, pp. 1253–1264, Apr. 2018, doi: 10.1177/0885328218758925/ASSET/IMAGES/LARGE/10.1177_0885328218758925-FIG1.JPEG.

[227] S. Li *et al.*, ‘Crossing the blood–brain–barrier with transferrin conjugated carbon dots: A zebrafish model study’, *Colloids Surf B Biointerfaces*, vol. 145, pp. 251–256, Sep. 2016, doi: 10.1016/J.COLSURFB.2016.05.007.

[228] Y. Guo, L. Wang, P. Lv, and P. Zhang, ‘Transferrin-conjugated doxorubicin-loaded lipid-coated nanoparticles for the targeting and therapy of lung cancer’, *Oncol Lett*, vol. 9, no. 3, pp. 1065–1072, Mar. 2015, doi: 10.3892/OL.2014.2840.

[229] C. Wu, B. Bull, C. Szymanski, K. Christensen, and J. McNeill, ‘Multicolor conjugated polymer dots for biological fluorescence imaging’, *ACS Nano*, vol. 2, no. 11, pp. 2415–2423, Nov. 2008, doi: 10.1021/NN800590N/ASSET/IMAGES/LARGE/NN-2008-00590N_0004.JPEG.

[230] L. P. Fernando, P. K. Kandel, J. Yu, J. McNeill, P. C. Ackroyd, and K. A. Christensen, ‘Mechanism of Cellular Uptake of Highly Fluorescent Conjugated Polymer Nanoparticles’, *Biomacromolecules*, vol. 11, no. 10, p. 2675, Oct. 2010, doi: 10.1021/BM1007103.

[231] Z. Ji, D. M. Arvapalli, W. Zhang, Z. Yin, and J. Wei, ‘Nitrogen and sulfur co-doped carbon nanodots in living EA.hy926 and A549 cells: oxidative stress effect and mitochondria targeting’, *Journal of Materials Science 2020 55:14*, vol. 55, no. 14, pp. 6093–6104, Feb. 2020, doi: 10.1007/S10853-020-04419-7.

[232] M. Toporkiewicz, J. Meissner, L. Matusewicz, A. Czogalla, and A. F. Sikorski, ‘Toward a magic or imaginary bullet? Ligands for drug targeting to cancer cells: principles, hopes, and challenges’, *Int J Nanomedicine*, vol. 10, p. 1399, Feb. 2015, doi: 10.2147/IJN.S74514.

[233] E. H. Knelson, J. C. Nee, and G. C. Blobe, ‘Heparan sulfate signaling in cancer’, *Trends Biochem Sci*, vol. 39, no. 6, p. 277, 2014, doi: 10.1016/J.TIBS.2014.03.001.

[234] S. Zhao *et al.*, ‘In Situ Synthesis of Fluorescent Mesoporous Silica–Carbon Dot Nanohybrids Featuring Folate Receptor-Overexpressing Cancer Cell Targeting and Drug Delivery’, *Nanomicro Lett*, vol. 11, no. 1, pp. 1–13, Apr. 2019, doi: 10.1007/S40820-019-0263-3/FIGURES/6.

[235] U. Koli, A. Dey, P. Nagendra, P. v. Devarajan, R. Jain, and P. Dandekar, ‘Lung Cancer Receptors and Targeting Strategies’, *AAPS Advances in the Pharmaceutical Sciences Series*, vol. 39, pp. 229–268, 2019, doi: 10.1007/978-3-030-29168-6_8/COVER.

[236] V. Gubala, G. Giovannini, F. Kunc, M. P. Monopoli, and C. J. Moore, ‘Dye-doped silica nanoparticles: synthesis, surface chemistry and bioapplications’, *Cancer Nanotechnology 2020 11:1*, vol. 11, no. 1, pp. 1–43, Jan. 2020, doi: 10.1186/S12645-019-0056-X.

[237] S. N. Ma *et al.*, ‘The anti-cancer properties of heparin and its derivatives: a review and prospect’, *https://doi.org/10.1080/19336918.2020.1767489*, vol. 14, no. 1, pp. 118–128, Jan. 2020, doi: 10.1080/19336918.2020.1767489.

[238] T. M. Allen, ‘Ligand-targeted therapeutics in anticancer therapy’, *Nature Reviews Cancer 2002 2:10*, vol. 2, no. 10, pp. 750–763, Oct. 2002, doi: 10.1038/nrc903.

[239] N. K. Yetim, ‘Hydrothermal synthesis of Co3O4 with different morphology: Investigation of magnetic and electrochemical properties’, *undefined*, vol. 1226, Feb. 2021, doi: 10.1016/J.MOLSTRUC.2020.129414.

[240] X. Fan, Y. Xu, C. Ma, and W. He, ‘In-situ growth of Co3O4 nanoparticles based on electrospray for an acetone gas sensor’, *undefined*, vol. 854, Feb. 2021, doi: 10.1016/J.JALLCOM.2020.157234.

[241] I. Shaheen, K. S. Ahmad, C. Zequine, R. K. Gupta, A. G. Thomas, and M. A. Malik, ‘Modified sol-gel synthesis of Co3O4 nanoparticles using organic template for electrochemical energy storage’, *Energy*, vol. 218, Mar. 2021, doi: 10.1016/J.ENERGY.2020.119502.

[242] T. Ozkaya, A. Baykal, M. S. Toprak, Y. Koseoğlu, and Z. Durmuş, ‘Reflux synthesis of Co3O4 nanoparticles and its magnetic characterization’, *J Magn Magn Mater*, vol. 321, no. 14, pp. 2145–2149, Jul. 2009, doi: 10.1016/J.JMMM.2009.01.003.

[243] V. Raman *et al.*, ‘Synthesis of Co3O4 nanoparticles with block and sphere morphology, and investigation into the influence of morphology on biological toxicity’, *Exp Ther Med*, vol. 11, no. 2, pp. 553–560, Feb. 2016, doi: 10.3892/ETM.2015.2946/HTML.

[244] D. Zou, C. Xu, H. Luo, L. Wang, and T. Ying, ‘Synthesis of Co3O4 nanoparticles via an ionic liquid-assisted methodology at room temperature’, *Mater Lett*, vol. 62, no. 12–13, pp. 1976–1978, Apr. 2008, doi: 10.1016/J.MATLET.2007.10.056.

[245] Y. Zhao, X. Xu, Y. Zhao, H. Zhou, J. Li, and H. Jin, ‘Synthesis and their physicochemical behaviors of flower-like Co3O4 microspheres’, *J Alloys Compd*, vol. 654, pp. 523–528, Jan. 2016, doi: 10.1016/J.JALLCOM.2015.09.145.

[246] S. Asadizadeh, M. Amirnasr, S. Meghdadi, F. Fadaei Tirani, and K. Schenk, ‘Facile synthesis of Co 3 O 4 nanoparticles from a novel tetranuclear cobalt(III) complex. Application as efficient electrocatalyst for oxygen evolution reaction in alkaline media’, 2018, doi: 10.1016/j.ijhydene.2018.01.104.

[247] T. He, D. Chen, and X. Jiao, ‘Controlled Synthesis of Co3O4 Nanoparticles through Oriented Aggregation’, *Chemistry of Materials*, vol. 16, no. 4, pp. 737–743, Feb. 2004, doi: 10.1021/CM0303033/SUPPL_FILE/CM0303033_S.PDF.

[248] X. Wang, X. Chen, L. Gao, H. Zheng, Z. Zhang, and Y. Qian, ‘One-dimensional arrays of Co3O4 nanoparticles: Synthesis, characterization, and optical and electrochemical properties’, *Journal of Physical Chemistry B*, vol. 108, no. 42, pp. 16401–16404, Oct. 2004, doi: 10.1021/JP048016P/ASSET/IMAGES/LARGE/JP048016PF00007.JPEG.

[249] S. Kumar, A. K. Ojha, B. Ahmed, A. Kumar, J. Das, and A. Materny, ‘Tunable (violet to green) emission by high-yield graphene quantum dots and exploiting its unique properties towards sun-light-driven photocatalysis and supercapacitor electrode materials’, *Mater Today Commun*, vol. 11, pp. 76–86, Jun. 2017, doi: 10.1016/J.MTCOMM.2017.02.009.

[250] B. Ahmed, S. Kumar, A. K. Ojha, F. Hirsch, S. Riese, and I. Fischer, ‘Facile synthesis and photophysics of graphene quantum dots’, *J Photochem Photobiol A Chem*, vol. 364, pp. 671–678, Sep. 2018, doi: 10.1016/J.JPHOTOCHEM.2018.07.006.

[251] B. N. Jusuf, N. S. Sambudi, I. Isnaeni, and S. Samsuri, ‘Microwave-assisted synthesis of carbon dots from eggshell membrane ashes by using sodium hydroxide and their usage for degradation of methylene blue’, *J Environ Chem Eng*, vol. 6, no. 6, pp. 7426–7433, Dec. 2018, doi: 10.1016/J.JECE.2018.10.032.

[252] K. Akbar, E. Moretti, and A. Vomiero, ‘Carbon Dots for Photocatalytic Degradation of Aqueous Pollutants: Recent Advancements’, *Adv Opt Mater*, vol. 9, no. 17, p. 2100532, Sep. 2021, doi: 10.1002/ADOM.202100532.

[253] Z. W. Heng, W. C. Chong, Y. L. Pang, and C. H. Koo, ‘An overview of the recent advances of carbon quantum dots/metal oxides in the application of heterogeneous photocatalysis in photodegradation of pollutants towards visible-light and solar energy exploitation’, *J Environ Chem Eng*, vol. 9, no. 3, p. 105199, Jun. 2021, doi: 10.1016/J.JECE.2021.105199.

[254] Y. Cheng *et al.*, ‘Synthesis of fluorescent carbon quantum dots from aqua mesophase pitch and their photocatalytic degradation activity of organic dyes’, *J Mater Sci Technol*, vol. 35, no. 8, pp. 1515–1522, Aug. 2019, doi: 10.1016/J.JMST.2019.03.039.

[255] D. Qu *et al.*, ‘Highly luminescent S, N co-doped graphene quantum dots with broad visible absorption bands for visible light photocatalysts’, *Nanoscale*, vol. 5, no. 24, pp. 12272–12277, Nov. 2013, doi: 10.1039/C3NR04402E.

APPENDIX A: EVALUATION OF UV AND VISIBLE LIGHT RESPONSIVE COBALT OXIDE CARBON Co_3O_4@CND HYBRID NANOPARTICLES AS A PHOTOCATALYST FOR DYE DEGRADATION

Figure S2.1. Schematic of synthesis of a). Co_3O_4 NPs and b). Co_3O_4@CNDs hybrid NPs

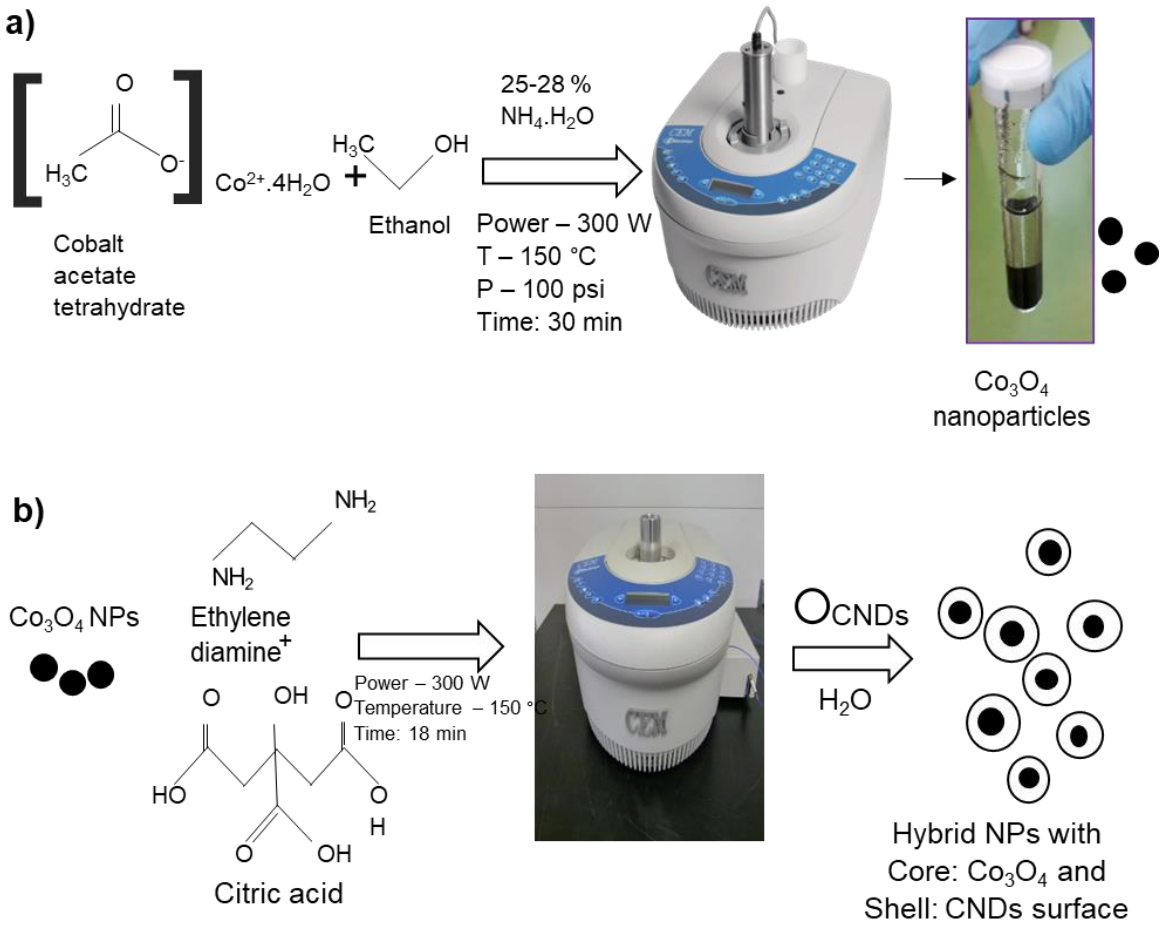

Figure S2.2. Texture of the synthesized Co_3O_4, CNDs, and Co_3O_4@CNDs hybrid NPs

Figure S2.3. TEM of CNDs

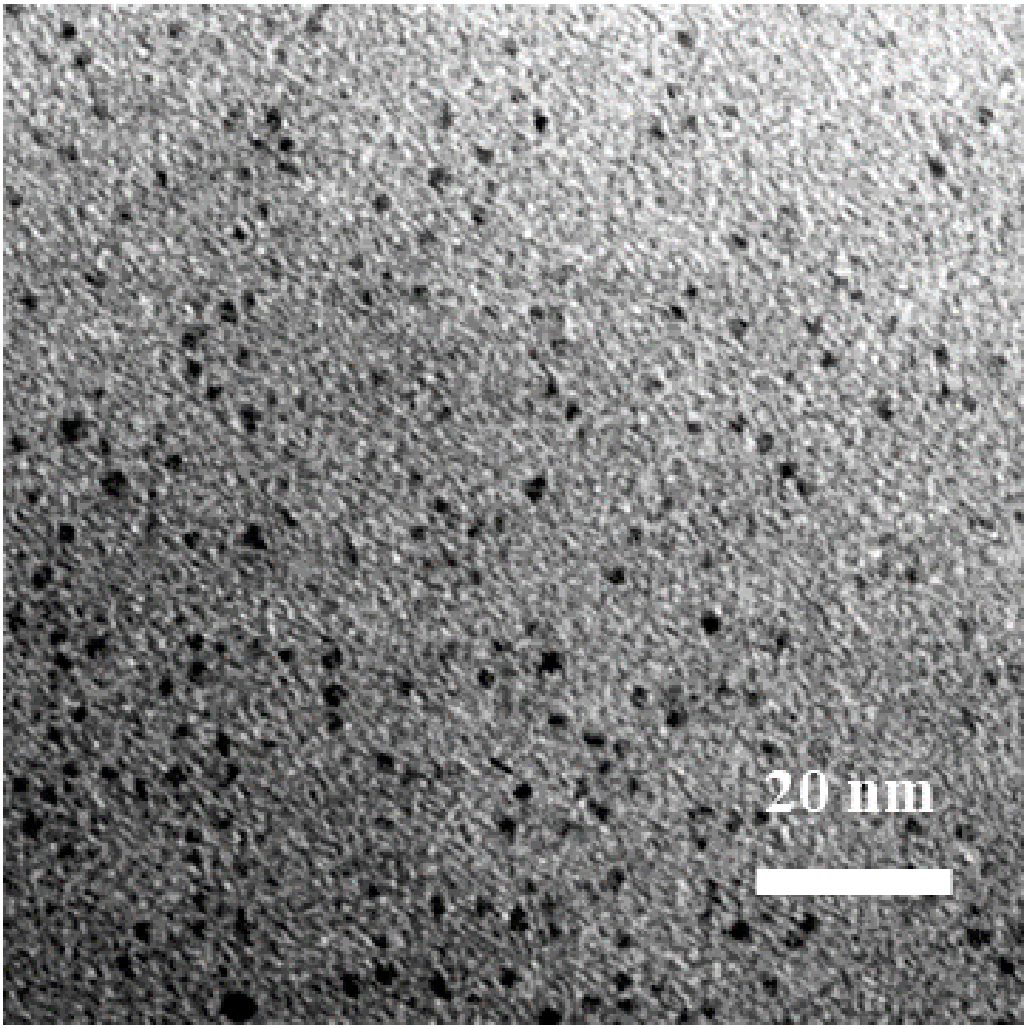

Figure S2.4. a) size distribution and b). SAED of Co_3O_4 NPs; and c). size distribution and d. SAED of Co_3O_4@CNDs hybrid NPs.

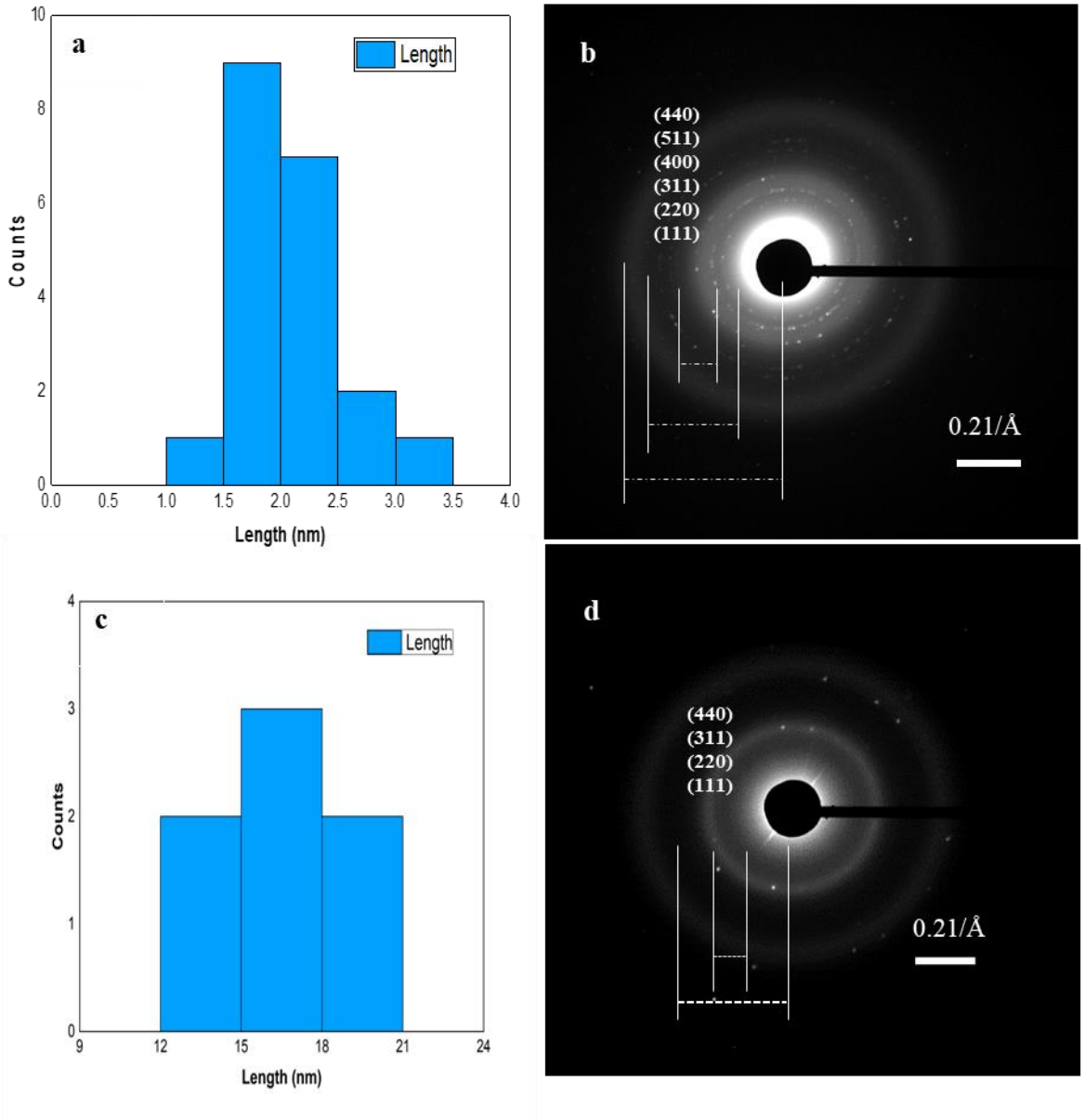

Figure S2.5. FTIR spectra of Co_3O_4 NPs, CNDs, and Co_3O_4@CNDs hybrid NPs

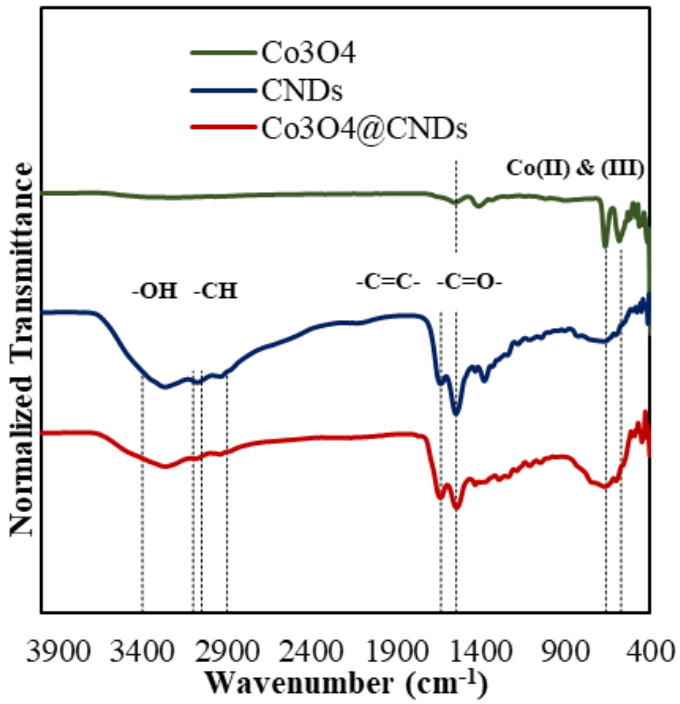

Figure S2.6. Raman spectra of Co_3O_4 NPs, CNDs, and Co_3O_4@CNDs hybrid NPs

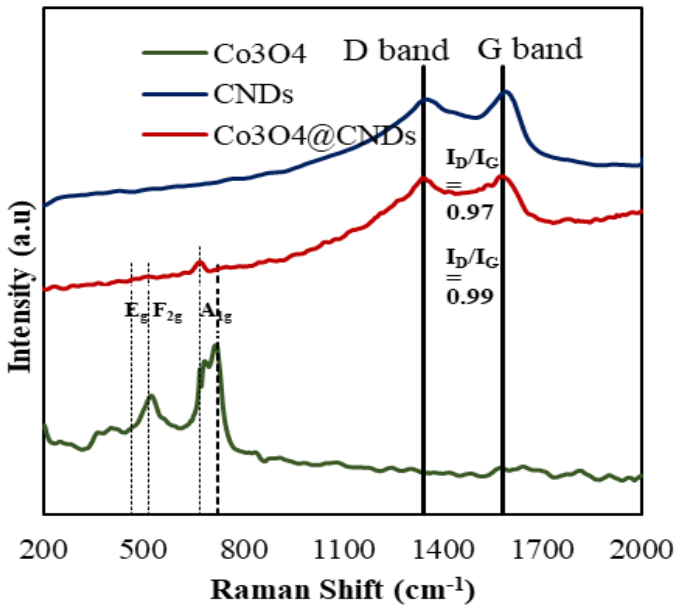

Figure S2.7. Convoluted full XPS spectra of Co_3O_4 NPs, CNDs, and Co_3O_4@CNDs hybrid NPs.

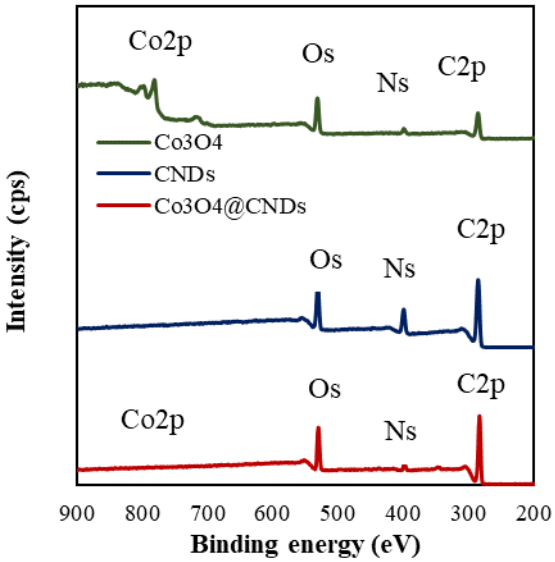

Figure S2.8. HRXPS of Co_3O_4 NPs of a. C 1s, b. O 1s, and c. Co 2p

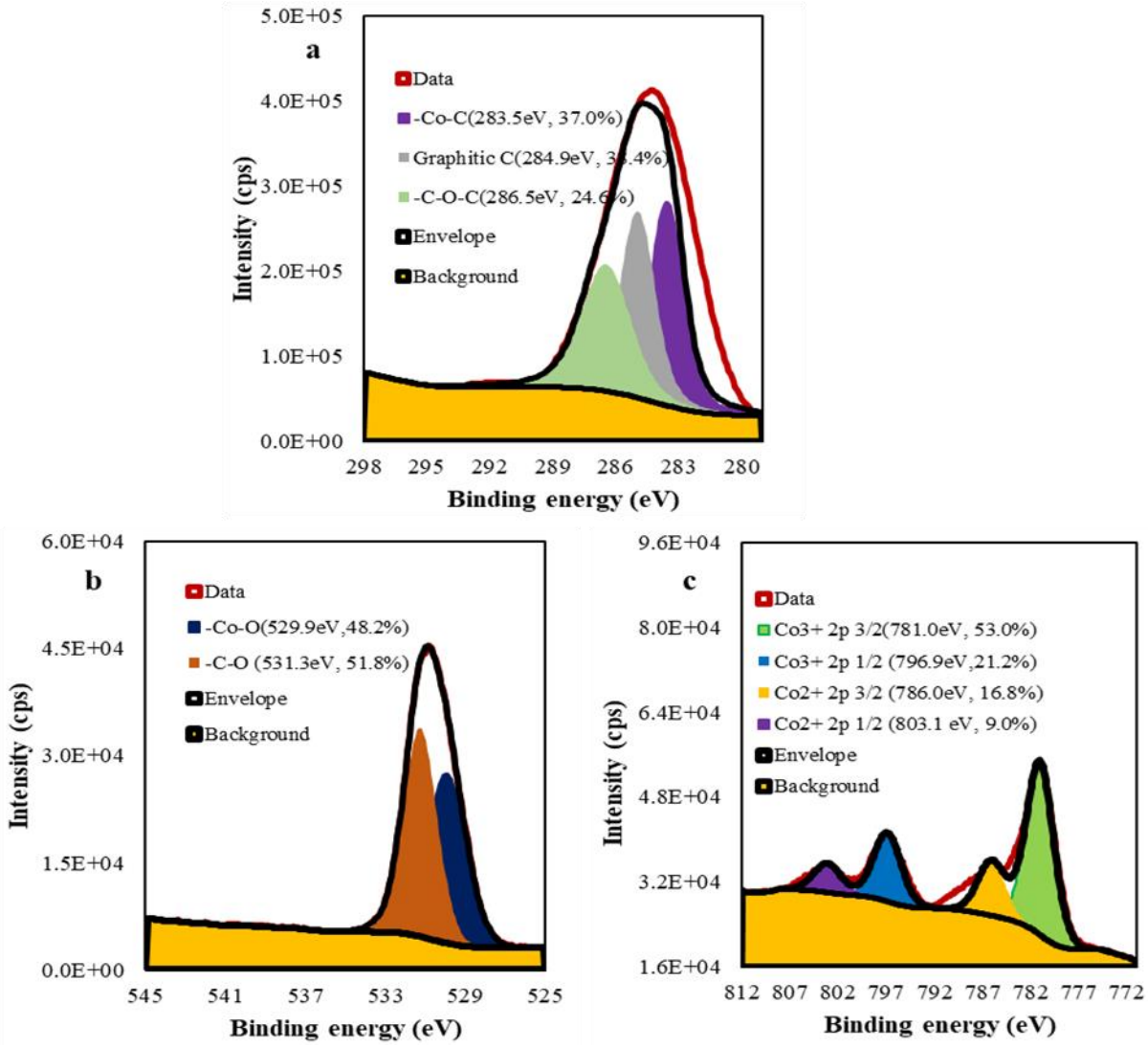

Figure S2.9. Zeta potential for Co_3O_4, CNDs, and Co_3O_4@CNDs hybrid NPs

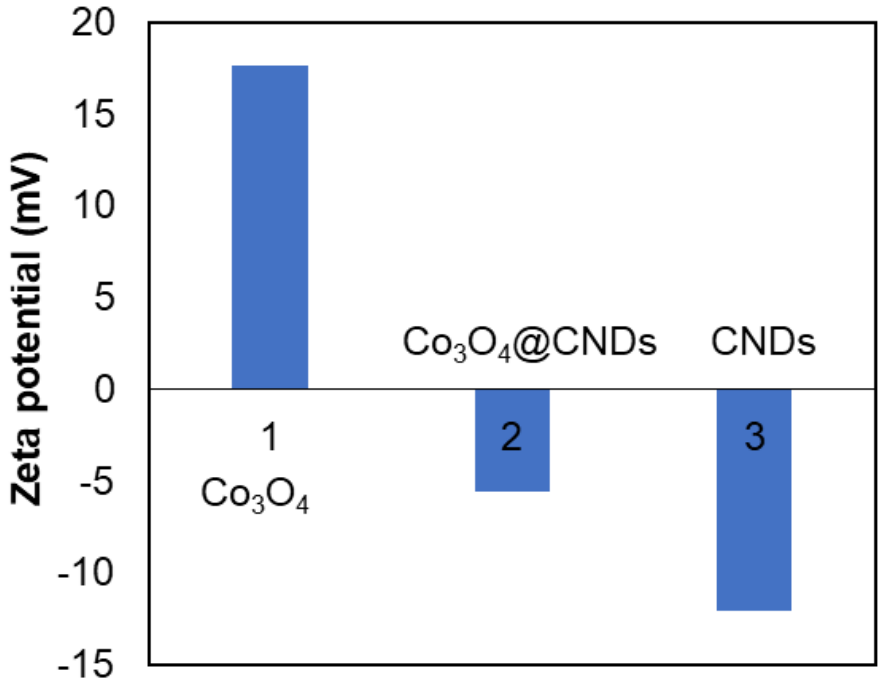

Figure S2.10. UV-Visible absorbance study of 1mg/mL of a. Co_3O_4@CNDs, b. CNDs, and c. Co_3O_4 NPs with 20 mg L^{-1} MB dye degradation in the presence of visible light for up to 120 minutes

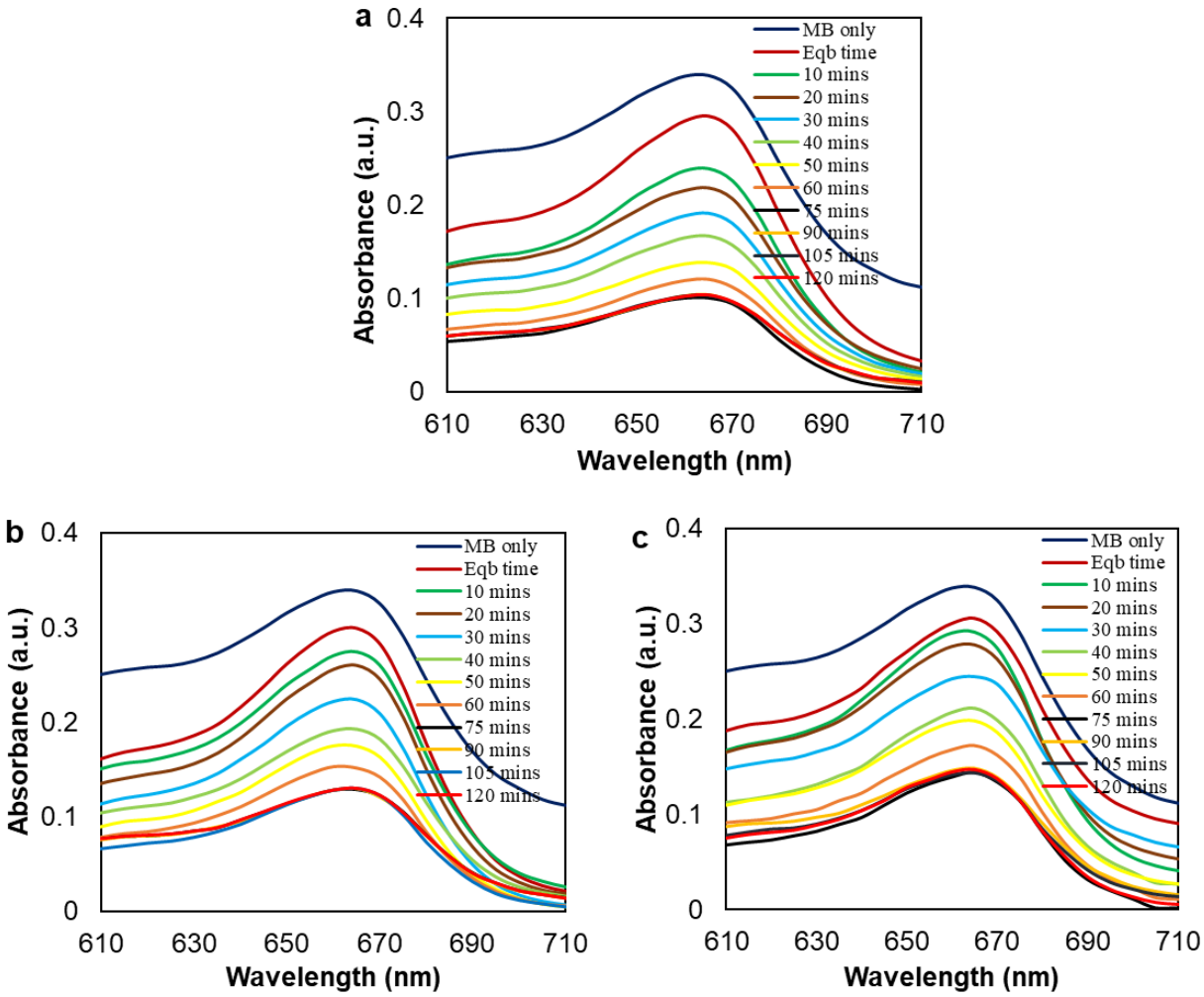

Figure S2.11. UV-Visible absorbance study of 1mg/mL of a. Co_3O_4@CNDs, b. CNDs, and c. Co_3O_4 NPs with 50 mg L^{-1} MB dye degradation in the presence of visible light for up to 120 minutes

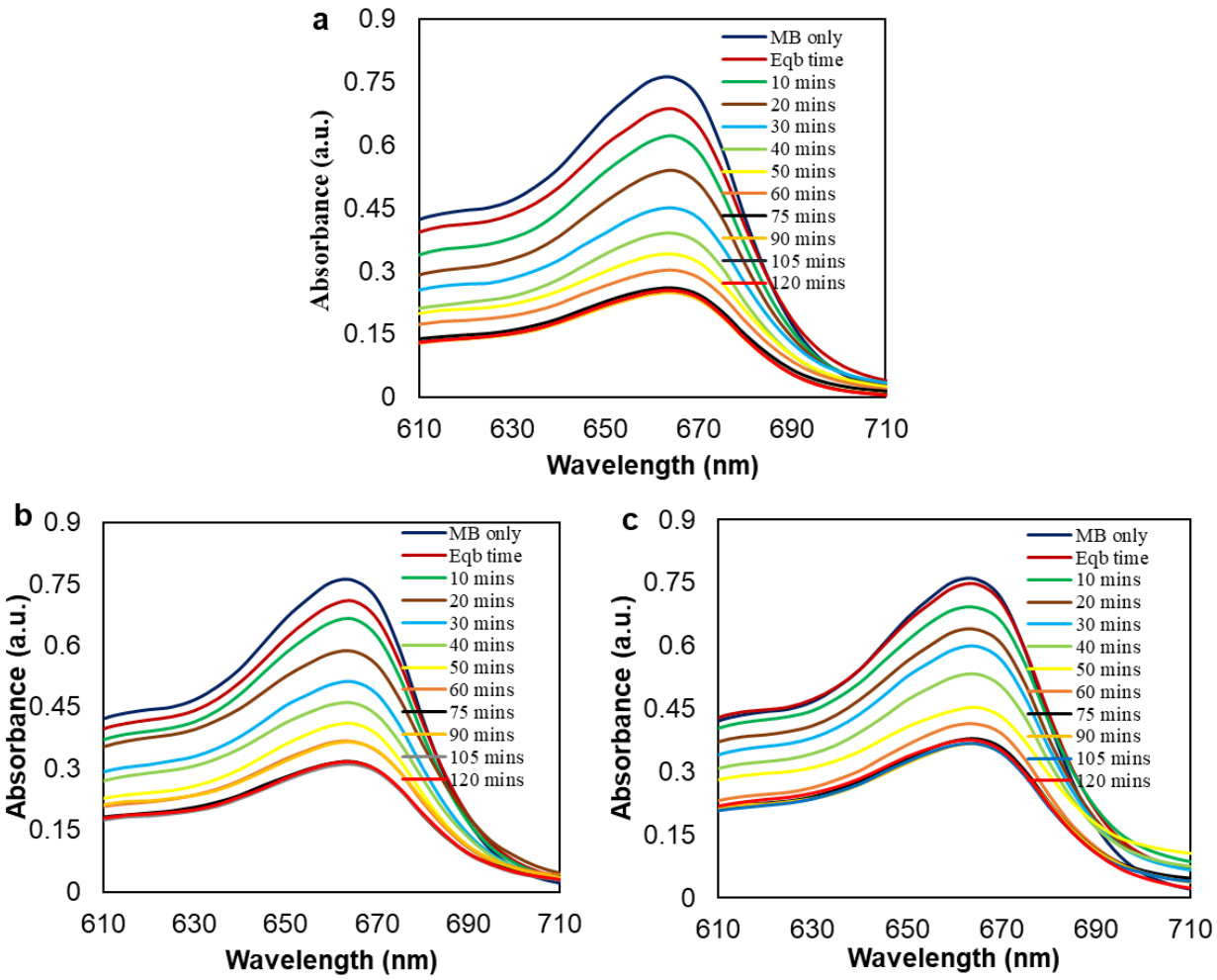

Figure S2.12. UV-Visible absorbance study of 1mg/mL of a. Co_3O_4@CNDs, b. CNDs, and c. Co_3O_4 NPs with 20 mg L^{-1} MB dye degradation in the presence of UV light for up to 60 minutes

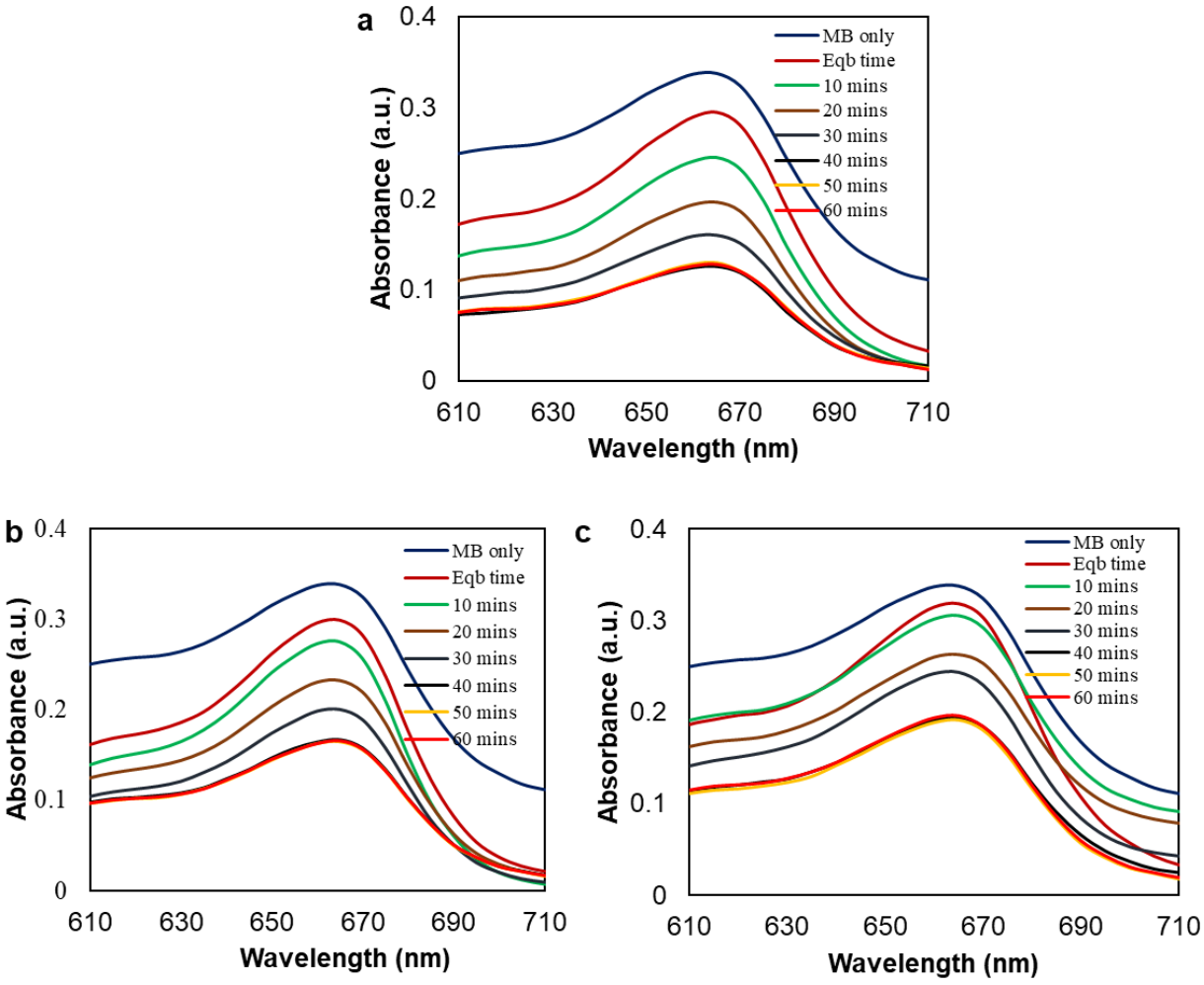

Figure S2.13. UV-Visible absorbance study of 1mg/mL of a. Co_3O_4@CNDs, b. CNDs, and c. Co_3O_4 NPs with 50 mg L^{-1} MB dye degradation in the presence of UV light for up to 60 minutes

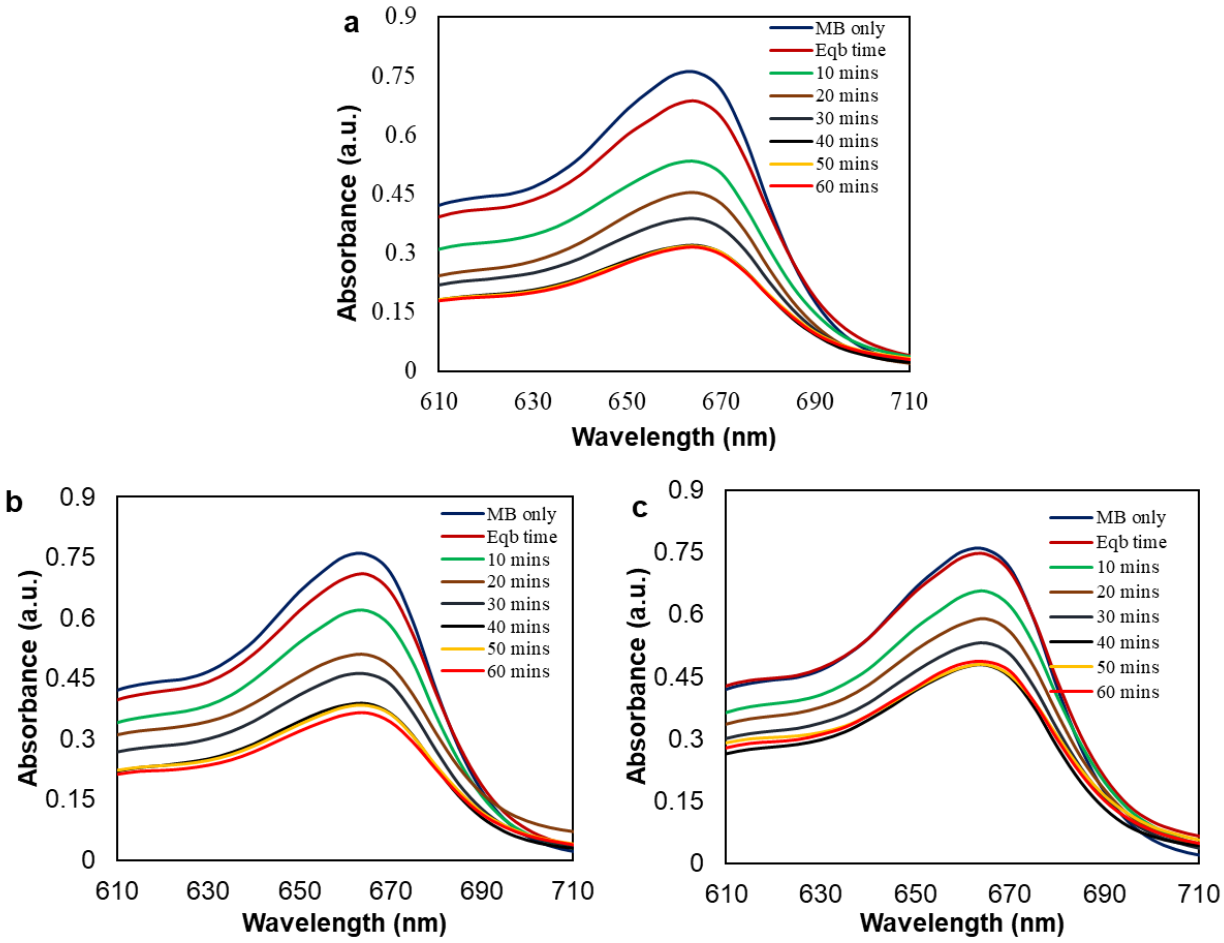

Figure S2.14. UV-Visible absorbance study of 1mg/mL of a. Co_3O_4@CNDs, b. CNDs, and c. Co_3O_4 NPs with 20 mg L^{-1} IC dye degradation in the presence of visible light for up to 120 minutes

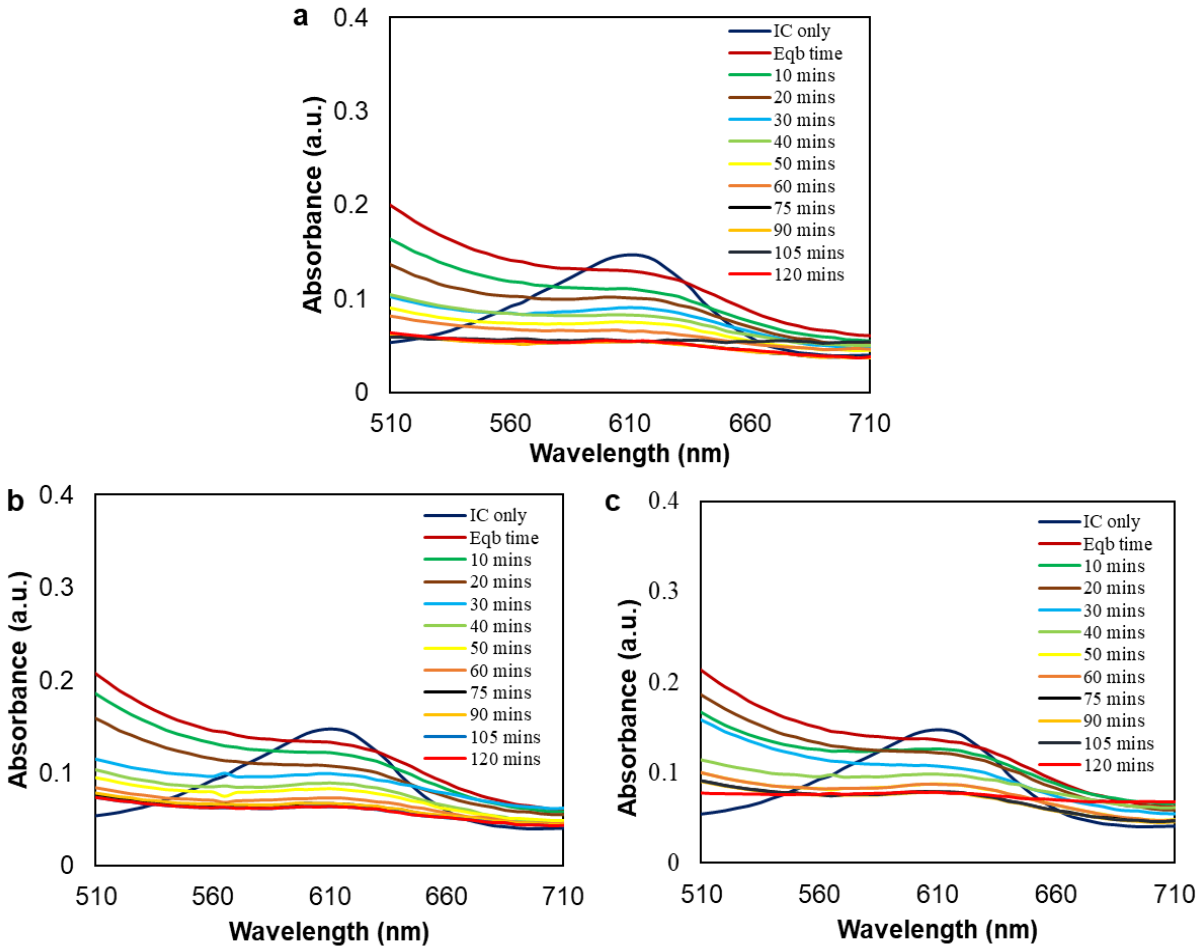

Figure S.2.15. UV-Visible absorbance study of 1mg/mL of a. Co_3O_4@CNDs, b. CNDs, and c. Co_3O_4 NPs with 50 mg L^{-1} IC dye degradation in the presence of visible light for up to 120 minutes

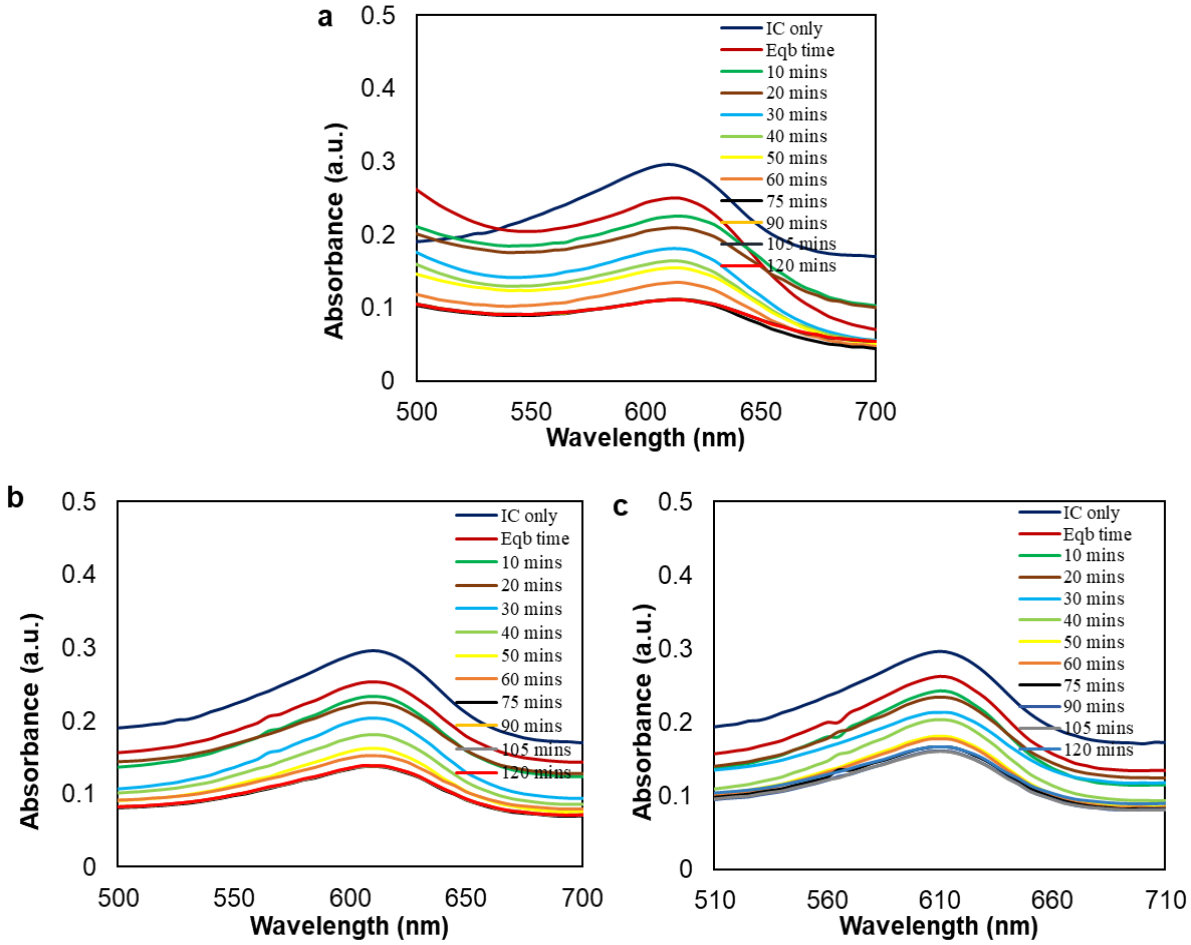

Figure S2.16. UV-Visible absorbance study of 1mg/mL of a. Co_3O_4@CNDs, b. CNDs, and c. Co_3O_4 NPs with 20 mg L^{-1} IC dye degradation in the presence of UV light for up to 60 minutes

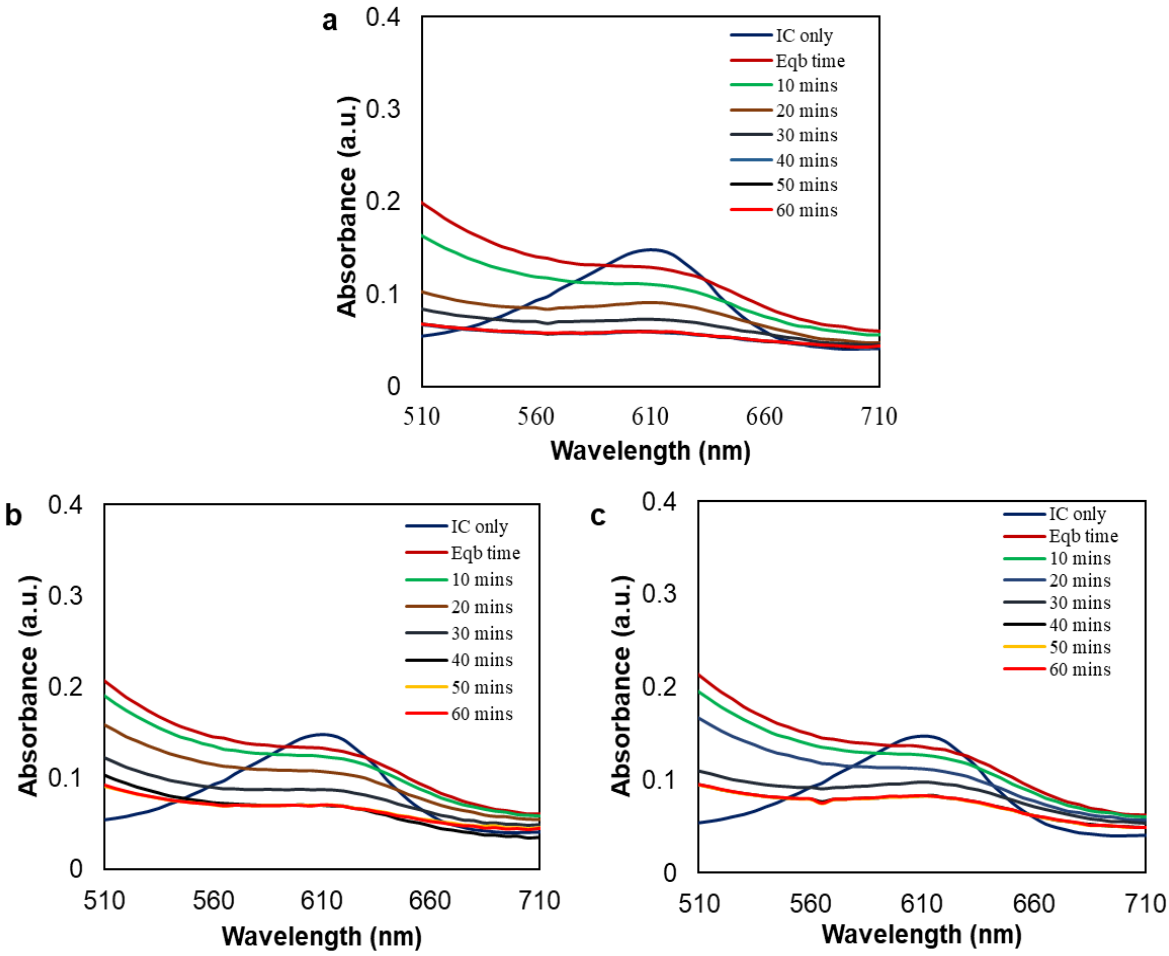

Figure S2.17. UV-Visible absorbance study of 1mg/mL of a. Co_3O_4@CNDs, b. CNDs, and c. Co_3O_4 NPs with 50 mg L^{-1} IC dye degradation in the presence of UV light for up to 60 minutes

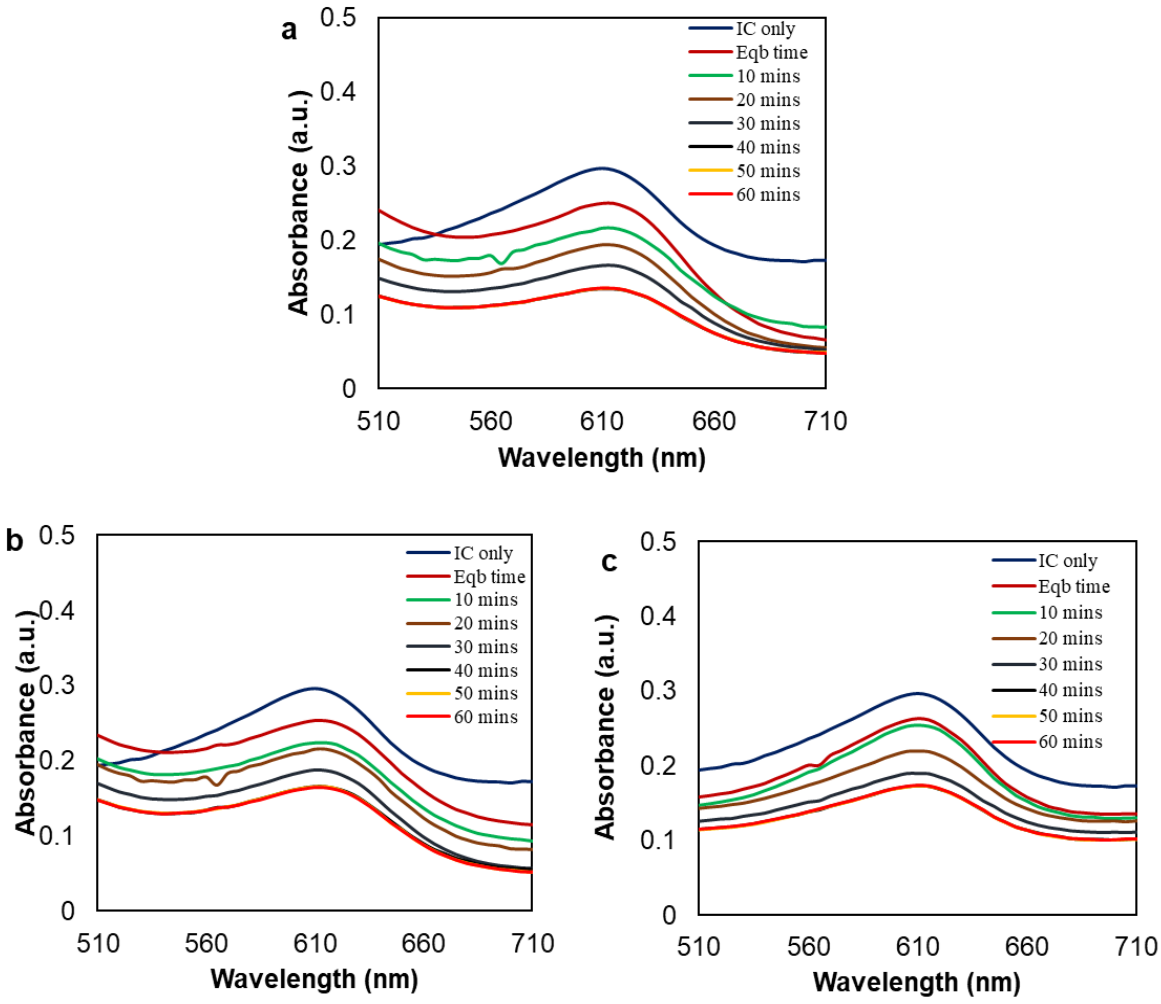

Figure S2.18. C_t/C_0 vs. time plots of 1mg/mL of Co_3O_4@CNDs, CNDs, and Co_3O_4 NPs with 50 mg L^{-1} a. MB and b. IC dye degradation in visible light, c. MB and d. IC in the presence of UV light

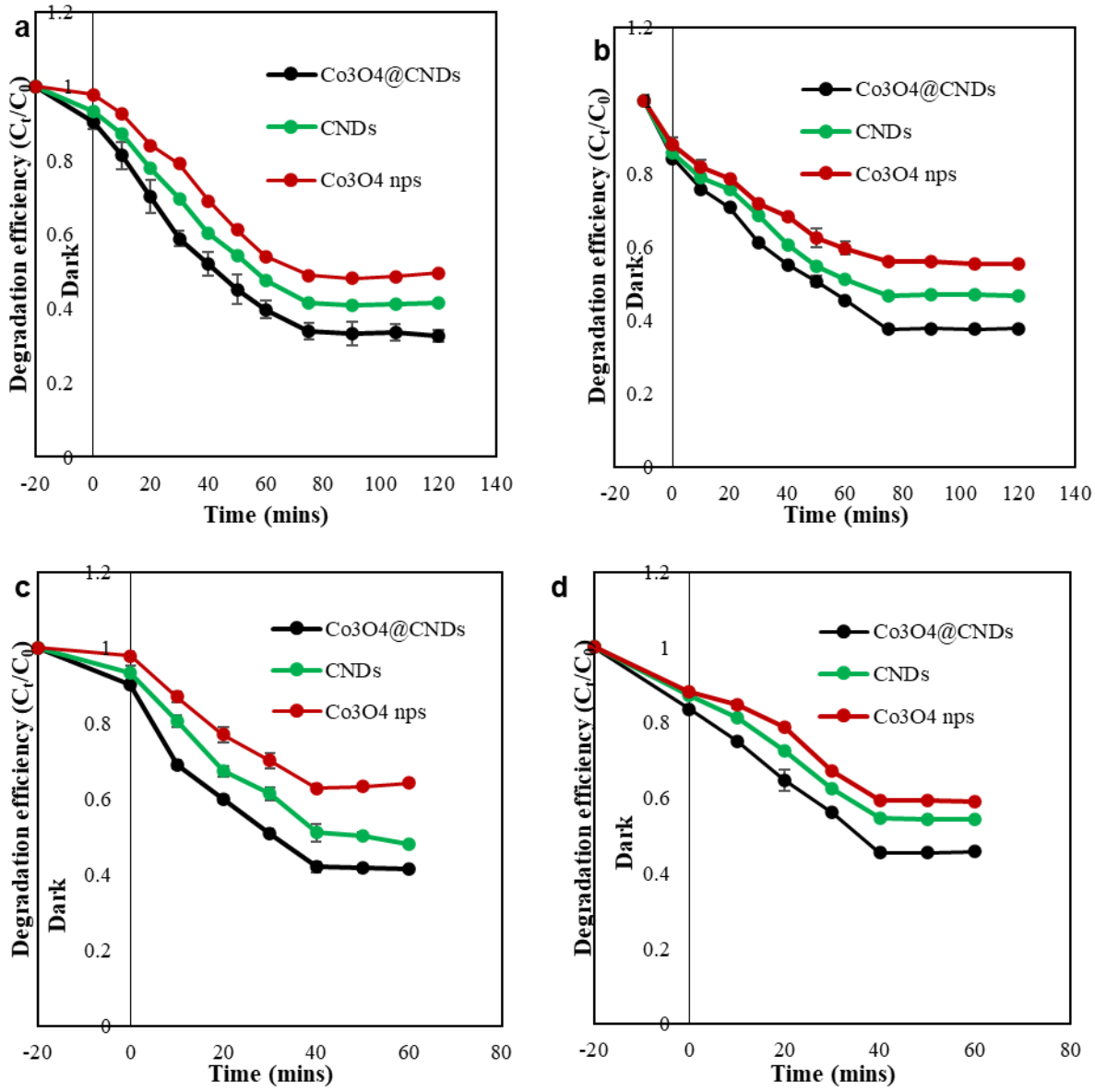

Figure S2.19. ln(C_0/C_t) vs. time plots of 1mg/mL of Co_3O_4@CNDs, CNDs, and Co_3O_4 NPs with 50 mgL^{-1} a. MB and b. IC dye degradation in visible light, c. MB and d. IC in the presence of UV light

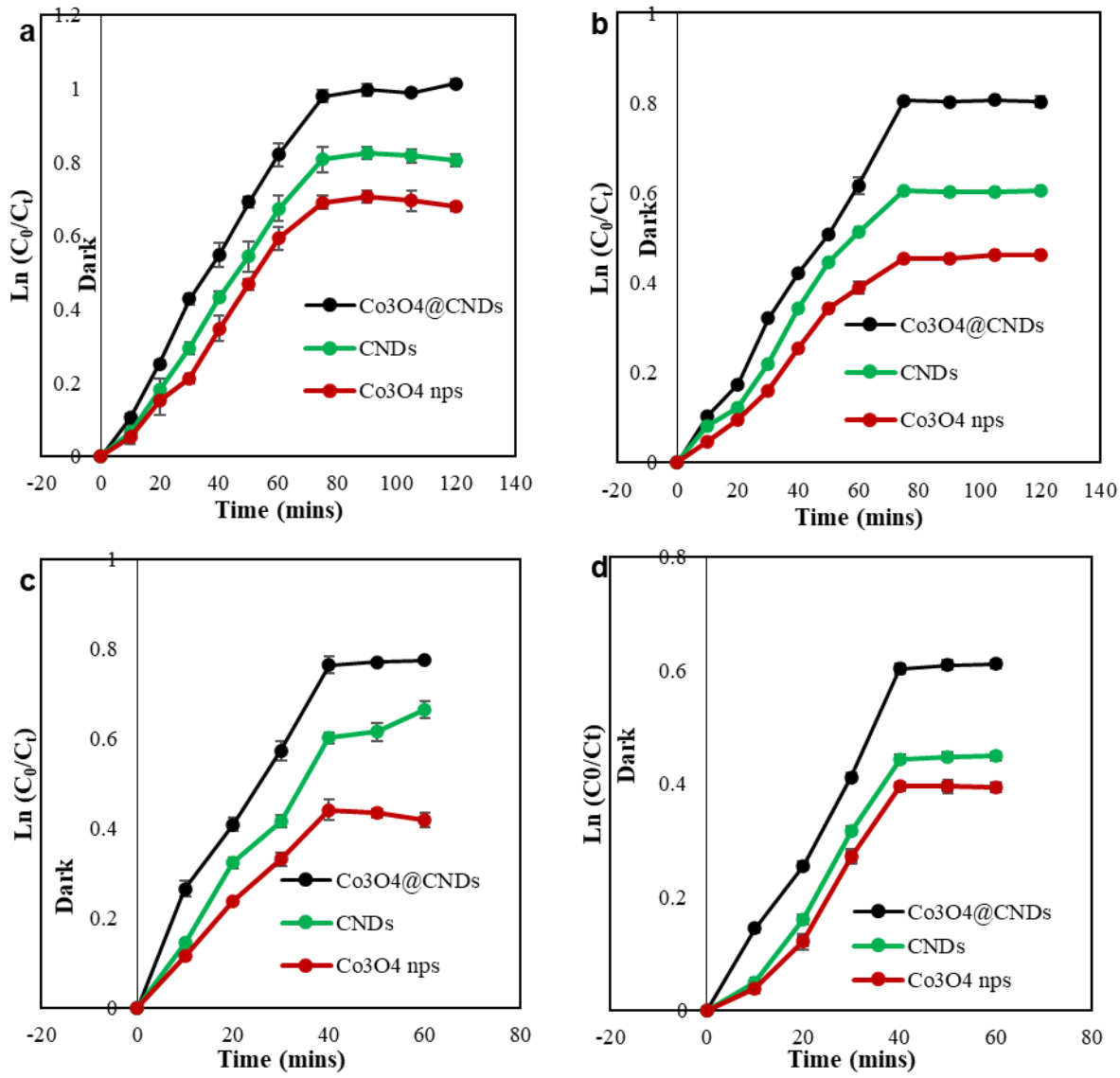

Figure S2.20. UV Visible absorbance spectra of 1mg/mL of a. Co_3O_4@CNDs, b. CNDs, and c. Co_3O_4 NPs with 20 mg L^{-1} MB dye degradation in the dark and their respective d. C_t/C_0 vs. time plots of 1mg/mL of Co_3O_4@CNDs, CNDs, and Co_3O_4 NPs with 20 mg L^{-1} MB

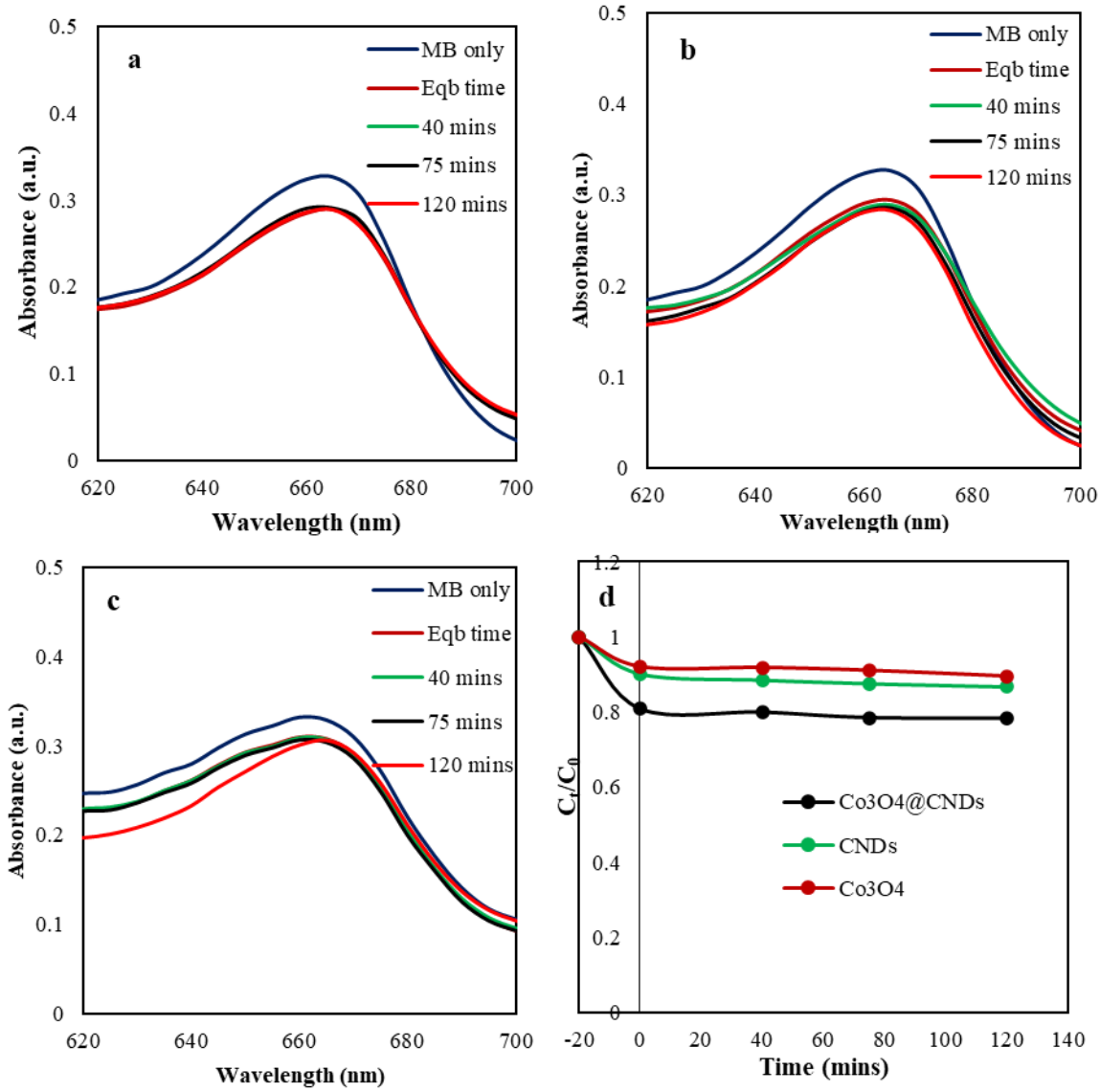

Figure S2.21. UV Visible absorbance spectra of 1mg/mL of a. Co_3O_4@CNDs, b. CNDs, and c. Co_3O_4 NPs with 50 mg L^{-1} MB dye degradation in the dark and their respective d. C_t/C_0 vs. time plots of 1mg/mL of Co_3O_4@CNDs, CNDs, and Co_3O_4 NPs with 50 mg L^{-1} MB

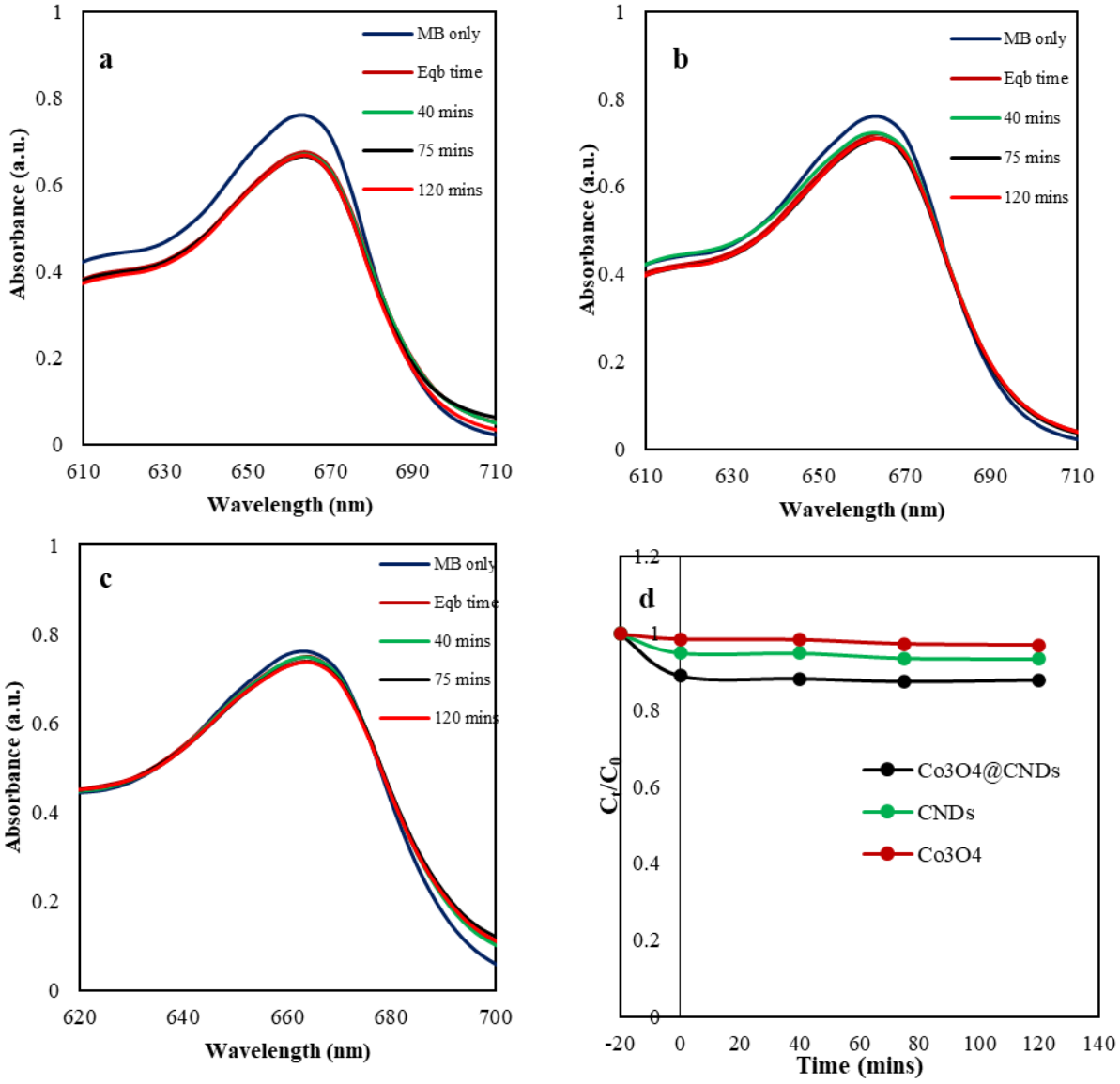

Figure S2.22. UV Visible absorbance spectra of 1mg/mL of a. Co_3O_4@CNDs, b. CNDs, and c. Co_3O_4 NPs with 20 mg L^{-1} IC dye degradation in the dark and their respective d. C_t/C_0 vs. time plots of 1mg/mL of Co_3O_4@CNDs, CNDs, and Co_3O_4 NPs with 20 mg L^{-1} IC

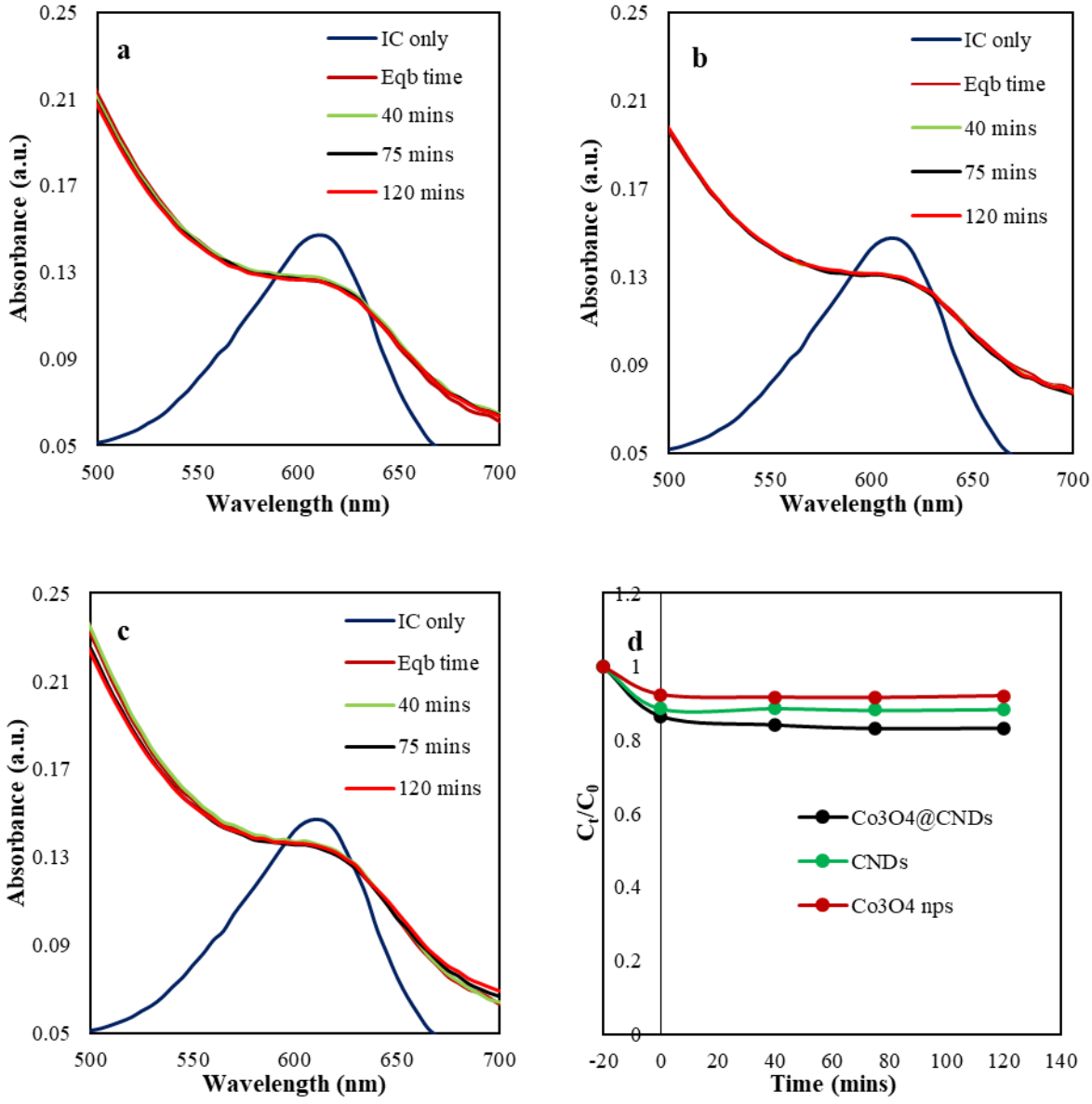

Figure S2.23. UV Visible absorbance spectra of 1mg/mL of a. Co_3O_4@CNDs, b. CNDs, and c. Co_3O_4 NPs with 50 mg L^{-1} IC dye degradation in the dark and their respective d. C_t/C_0 vs. time plots of 1mg/mL of Co_3O_4@CNDs, CNDs, and Co_3O_4 NPs with 50 mg L^{-1} IC

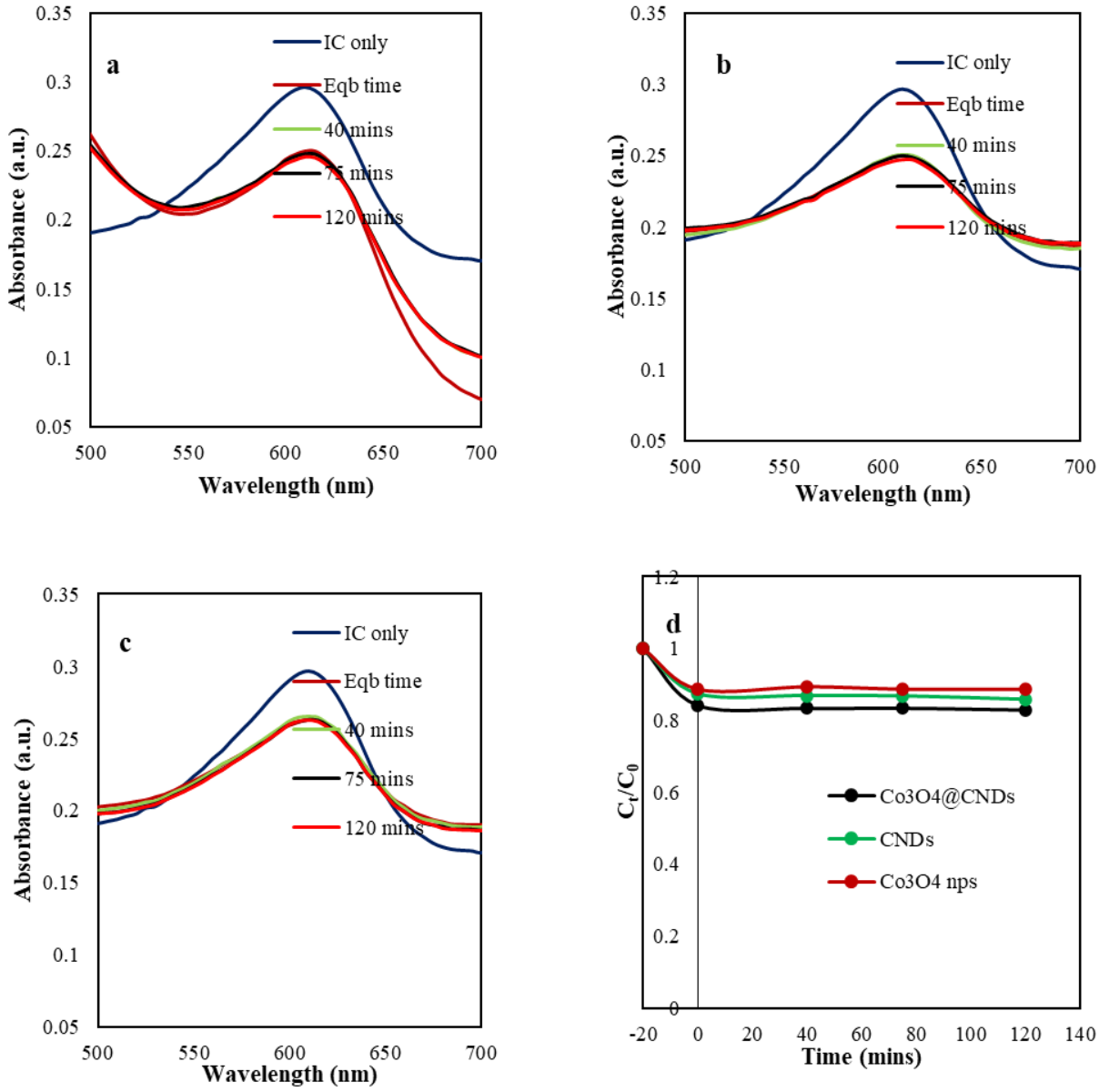

Figure S2.24. UV Visible absorbance spectra of IC dye degradation without any NPs a. 20 mg L^{-1} b. 50 mg L^{-1}; C_t/C_0 vs. time plots compared to c. 20 and d. 50 mg L^{-1} MB dye degradation without any NPs and with Co_3O_4@CNDs in dark and light

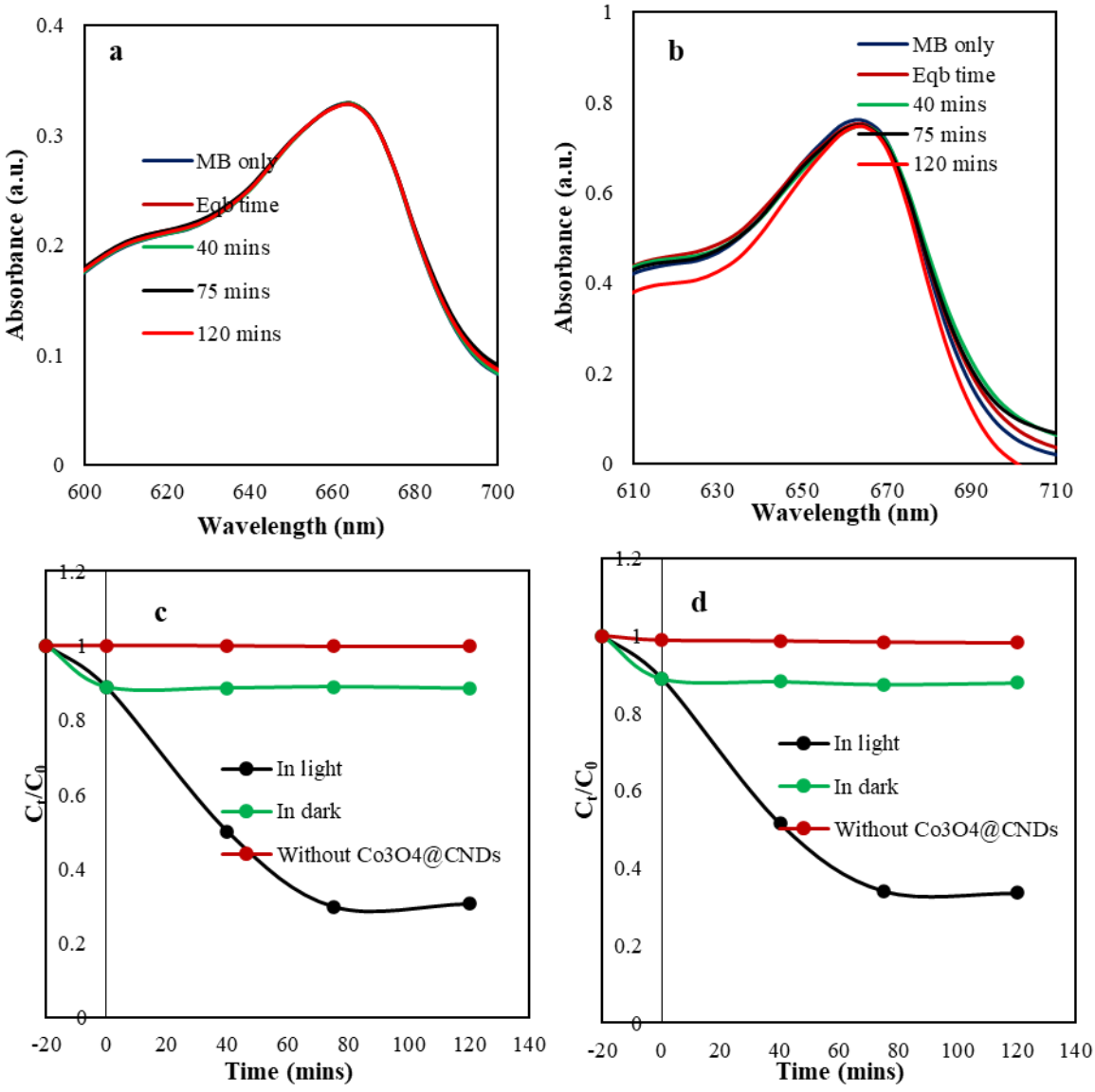

Figure S2.25. UV Visible absorbance spectra of IC dye degradation without any NPs a. 20 mg L^{-1}; b. 50 mg L^{-1}; C_t/C_0 vs. time plots compared to c. 20 and d. 50 mg L^{-1} MB dye degradation without any NPs and with Co_3O_4@CNDs in dark and light

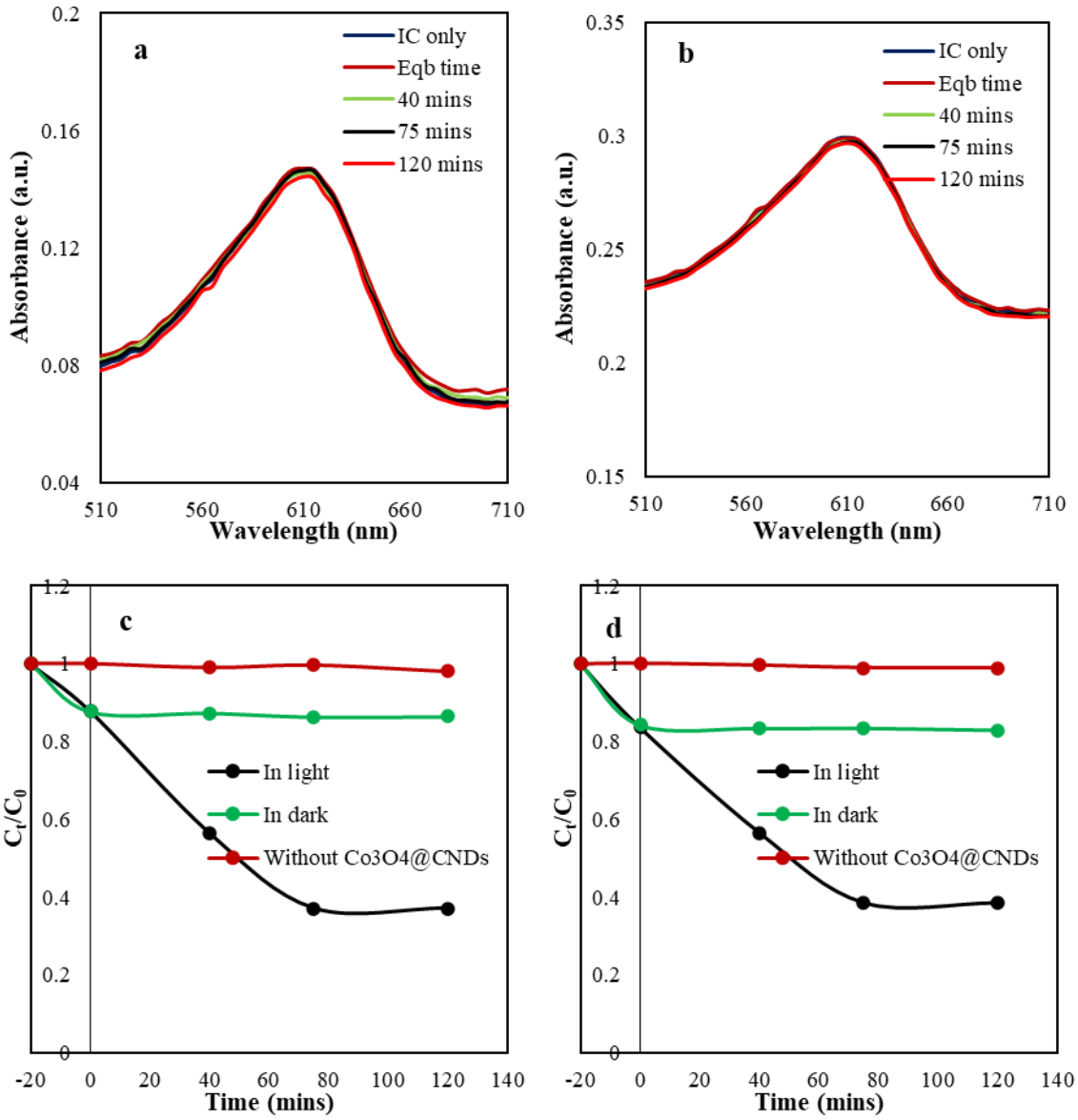

Figure S2.26. ln(C_0/C_t) vs. time plots of 1mg/mL of Co_3O_4@CNDs NPs with 20 mg L^{-1} MB dye degradation in the presence of visible light for up to 75 minutes and UV light for up to 40 minutes

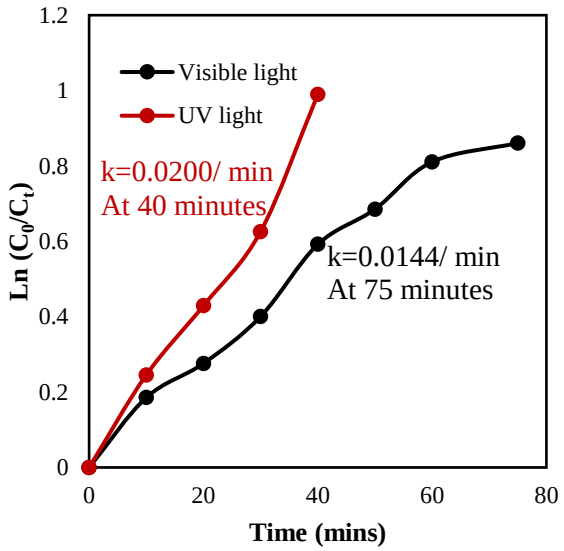

Figure S2.27. C_t/C_0 vs. time plots with the role of scavengers in the mechanism of the Co_3O_4@CNDs based MB dye degradation in the presence of visible light (a) & (b), and UV light (c) & (d)

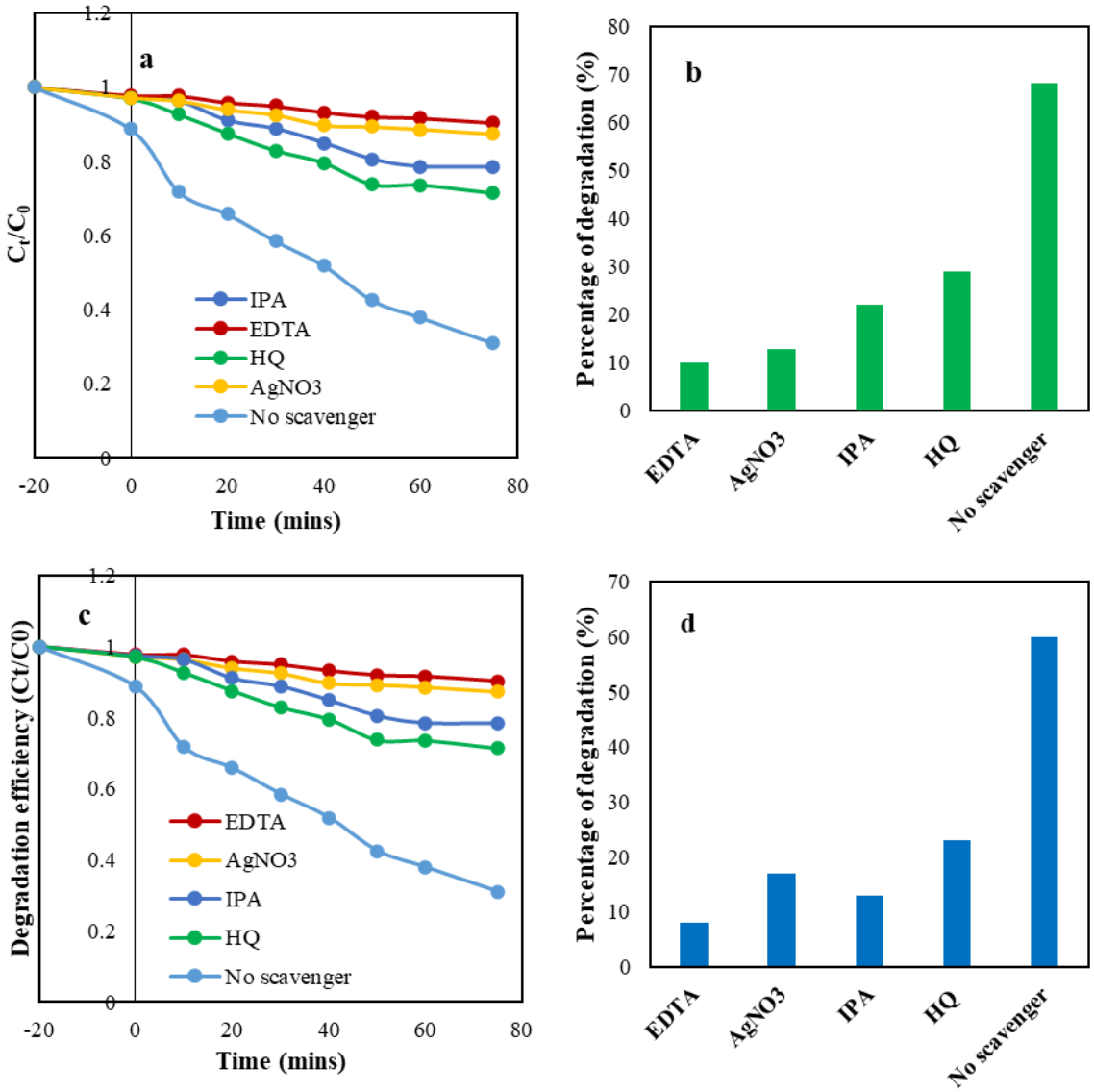

Figure S2.28. a. C_t/C_0 vs. time and b. degradation percentage at 75 minutes after the visible light radiation of the Co_3O_4@CNDs in the MB dye degradation for 3 cycles; c. C_t/C_0 vs. time and d. degradation percentage at 75 minutes after the visible light radiation of the Co_3O_4@CNDs in the MB dye degradation for 3 cycles

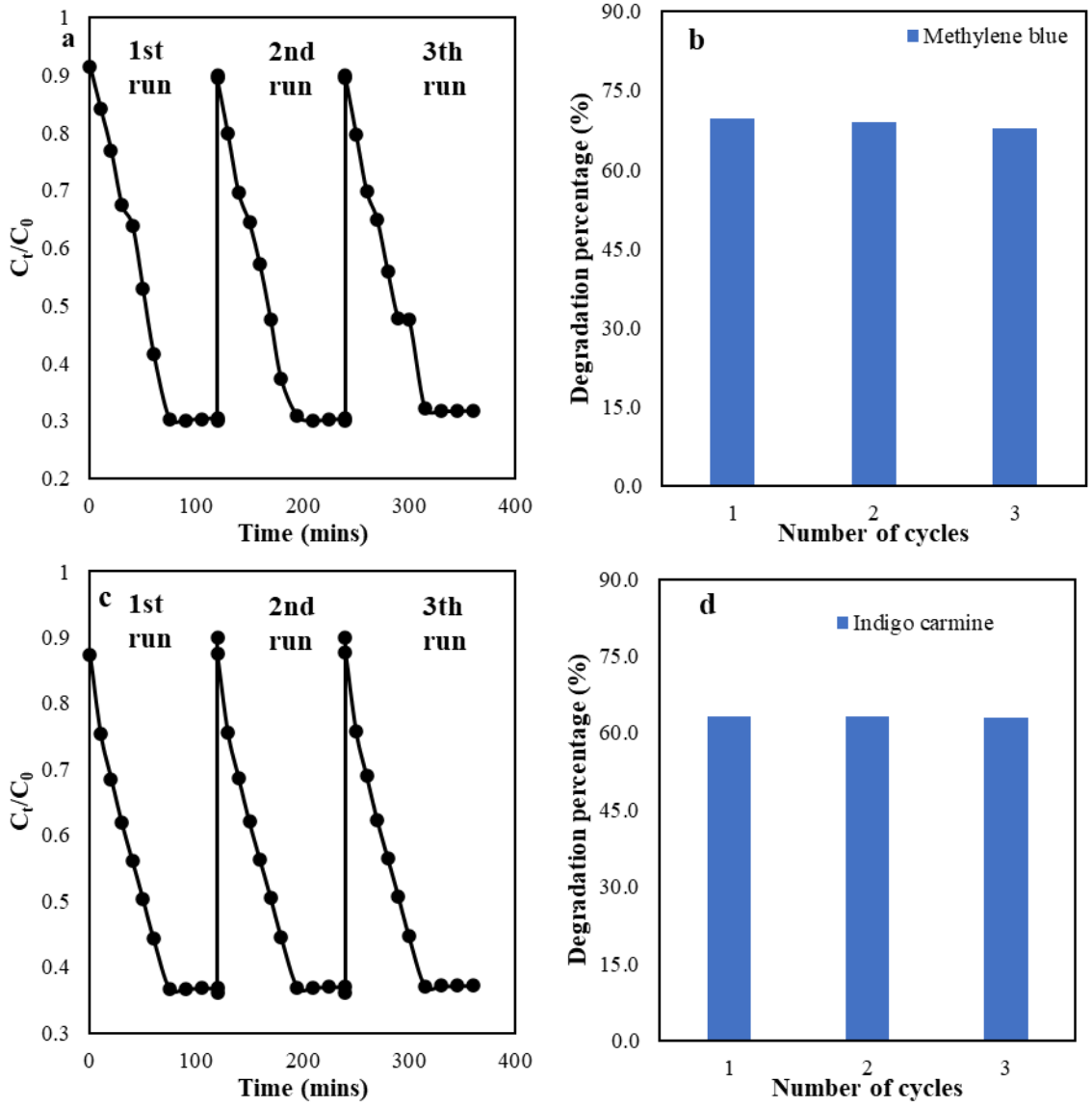

Figure S2.29. XPS of the Co_3O_4@CNDs in the a). MB and b). IC dye degradation after 3 cycles

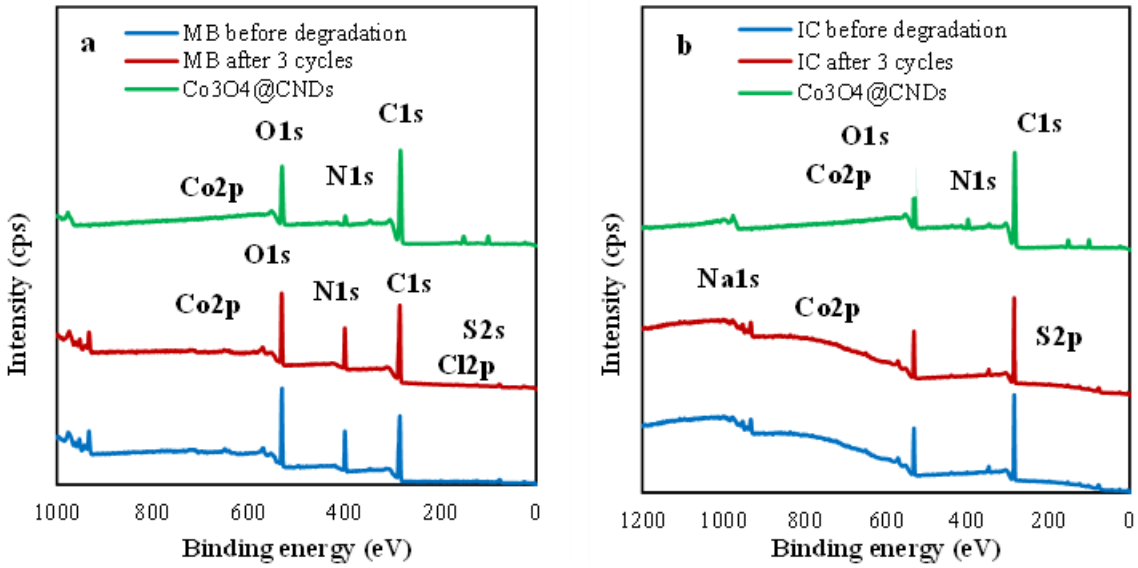

Table S2.1. Comparison of different synthesis parameters for Co_3O_4 NPs and their size.

Author	Stoichiometry and Morphology	Method	Reaction time	Reaction Temperature (°C)	Size (nm)
Yetim et al.[239]	Co_3O_4 nanospheres	Hydrothermal	4 hours	150	700
Fan et al.[240]	Co_3O_4 porous film with a spinel structure	In situ, electrospray	4 – 4.5 hours	150	28.6
Shaheen et al.[241]	Co_3O_4 NPs	Sol-gel method	24 hours	90	17
Ozkaya et al. [242]	Co_3O_4 NPs	Reflux condenser	4 hours	100	28
Raman et al.[243]	Co_3O_4 NPs with block and sphere morphology	Agitation	6 hours	Room temperature with organic agents	40-60
Zou et al.[244]	Co_3O_4 particles quasi-spherical	Solution oxidation	6 hours	Room temperature with ionic liquid	10-50 nm
Zhao et al.[245]	Co_3O_4 3D flower-like microstructure	One-pot reaction	3 hours	180	5 µm

Jamil et al.[58]	Porous cuboids Co_3O_4	Solvothermal route	10 hours	220	400-500 nm
Uddin et al.[60]	Co_3O_4 NPs	Simple precipitation	72 hours	100	10-20 nm
Asadizadeh et al.[246]	Co_3O_4 NPs	Thermal decomposition	2 hours	600	~30 nm
Vijayakumar et al.[30]	Co_3O_4 NPs	Microwave-assisted precipitation	5 minutes	Power at 240W	14 nm
He et al.[247]	Co_3O_4 NPs	Thermal decomposition	4 hours	180	40-nm aggregates
Wang et al.[248]	Co_3O_4 NPs	Solvothermal method	12 hours	120	50 nm
Dong et al.[102]	Co_3O_4 NPs	Solvothermal method	3 hours	150	3.5 nm
This work	Co_3O_4 NPs	Microwave method	30 minutes	150	3±1 nm

Table S2.2. XRD comparison for 2Ɵ and planes of Co_3O_4, CNDs, and Co_3O_4@CNDs hybrid NPs.

Co_3O_4	**2Ɵ**	20.5	23	31.6	37	40	43.6	56	59.6	65.4
	Planes	(111)	(002)	(220)	(311)	(222)	(400)	(422)	(333)	(440)
CNDs	**2Ɵ**	23								
	Planes	(002)								
Co_3O_4@CNDs hybrid NPs	**2Ɵ**	20.5	23	31.6	40	43.6				
	Planes	(111)	(002)	(220)	(222)	(400)				

Table S2.3. Detailed Elemental compositions comparison of the constituents present in Co_3O_4, CNDs, and Co_3O_4@CNDs hybrid NPs from XPS data.

Particles	C				N				O			Co			
	-C-C	-C=O	-C-O-C-	-Co-C-					-C-O-	-C=O-	-Co-O-	Co3+ 2p 3/2	Co3+ 2p 1/2	Co2+ 2p 3/2	Co2+ 2p 1/2
Hybrid nanoparticles	75.22%				4.83%				19.22%			0.73%			
	64.87		12.45	22.68								41.91	21.55	21.35	15.19
CNDs	63.26%				19.25%				17.5%						
	33.68	32.89	33.43												
Co_3O_4 nanoparticles	15.33%								63.26%			21.41%			
	38		26	36					38.89		61.11	53.01	16.83	21.15	9.01

Table S2.4. 'k' values of 1mg/mL of Co_3O_4@CNDs, CNDs, and Co_3O_4 NPs with 20 and 50 mg L^{-1} MB dye degradation in the presence of visible and UV light.

Light Source	20 mg L^{-1} MB			50 mg L^{-1} MB		
	Co_3O_4@CNDs	CNDs	Co_3O_4	Co_3O_4@CNDs	CNDs	Co_3O_4
Visible at 75 mins	1.39±0.05×10^{-2} /min	1.16±0.02×10^{-2} /min	0.98±0.02×10^{-2} /min	1.3±0.02×10^{-2} /min	1.08±0.05×10^{-2} /min	0.9±0.02×10^{-2} /min
UV at 40 mins	1.95±0.05×10^{-2} /min	1.58±0.02×10^{-2} /min	1.28±0.04×10^{-2} /min	1.89±0.05×10^{-2} /min	1.55±0.03×10^{-2} /min	1.1±0.06×10^{-2} /min

Table S2.5. 'k' values of 1mg/mL of Co_3O_4@CNDs, CNDs, and Co_3O_4 NPs with 20 and 50 mg L^{-1} IC dye degradation in the presence of visible and UV light

Light Source	20 mg L^{-1} IC			50 mg L^{-1} IC		
	Co_3O_4@CNDs	CNDs	Co_3O_4	Co_3O_4@CNDs	CNDs	Co_3O_4
Visible at 75 mins	$1.15\pm0.01\times10^{-2}$ /min	$0.93\pm0.01\times10^{-2}$ /min	$0.72\pm0.01\times10^{-2}$ /min	$1.03\pm0.02\times10^{-2}$ /min	$0.84\pm0.002\times10^{-2}$ /min	$0.63\pm0.003\times10^{-2}$ /min
UV at 40 mins	$1.92\pm0.04\times10^{-2}$ /min	$1.47\pm0.02\times10^{-2}$ /min	$1.21\pm0.01\times10^{-2}$ /min	$1.52\pm0.002\times10^{-2}$ /min	$1.17\pm0.004\times10^{-2}$ /min	$0.98\pm0.03\times10^{-2}$ /min

Table S2.6. Comparison study with other Co_3O_4-based or carbon-based photocatalysts

Catalysts	Pollutant/ Dye	Source of light	Degradation efficiency and time	References
GQDs	MB	Sunlight	45%, 100 min	[249]
GQDs	RhG	Sunlight	80%, 80 min	[250]
C-dots	MB	Sunlight	43%/10 h	[251], [252]
N-CQDs From coal tar	MB IC	Natural light	23% in 4h (5mL,15 mg L^{-1}) 56% in 4h (5mL, 30 mg L^{-1})	[253], [254]
N-GQDs/TiO_2	RhB	Visible	60%/100 min	[255]
GQDS	RhB	Visible	55%,360 min	[68]
Co_3O_4 NPs	MB	UV–Vis	56.40%, 80 min	[52]

Co_3O_4@CNDs	MB IC	Visible light and UV light Visible UV	72%, 75 mins ($20\ mg\ L^{-1}$) 67%, 40 mins ($20\ mg\ L^{-1}$) 63%, 75 mins 59%, 40 mins	This work

Calculations of band edges for Co_3O_4 and CNDs

The conduction band (CB) and valence band (VB) edge can be calculated through equations (1) and (2)

$$E_{CB} = \chi - E_e - 0.5E_g \quad (1) \qquad E_{VB} = E_{CB} + E_g \quad (2)$$

Where E_{VB} and E_{CB} are the Valence and Conduction band potentials, respectively. Moreover, E_e is the energy of free electrons vs. hydrogen (4.5 eV), and χ is the electronegativity of the semiconductor, and it was calculated by the following equation:

$$\chi = [x(A)^a x(B)^b x(C)^c]^{1/(a+b+c)} \quad (3)$$

in which a, b, and c are the number of atoms in the semiconductor compounds.

In case of Co_3O_4, the χ calculation for Co_3O_4 as follows:

The electronegativity for each element is Co: 4.3 eV, O: 7.54 eV (Data of all elements in website: http://www.knowledgedoor.com/2/elements_handbook/pearson_absolute_electronegativity.htmL

$\chi\ Co_3O_4 = (4.3^3 \times 7.54^4)^{1/7} = 5.927$ eV

$E_{CB1} = 5.927 - 4.5 - (0.5 \times 1.57) = 0.642$ eV

$E_{VB1} = 0.642 + 1.57 = 2.212$ eV

$E_{CB2} = 5.927 – 4.5– (0.5×1.77) = 0.542$ eV

$E_{VB2} = 0.542 + 1.77 = 2.312$ eV

In the case of CNDs, the χ calculation for N-CNDs $_{is}$ as follows:

The molecular formula for CNDs is $C_{36}H_{58}N_6O_{11}$, as mentioned by Zeng et al.[112]

The electronegativity for each element is C: 2.55 eV, H: 2.2 eV, N: 3.04 eV, O: 7.54 eV

χ CNDs ($C_{36}H_{58}N_6O_{11}$) = $(2.55^{36}×2.2^{58}x3.04^{6}×7.54^{11})^{1/(36+58+6+11)}$ = 2.65 eV

$E_{CB} = 2.65 – 4.5– (0.5×2.9) = -3.3$ eV

$E_{VB} = -3.3 + 2.9 = -0.4$ eV

APPENDIX B: MULTIFUNCTIONAL CORE-SHELL COBALT OXIDE @ CARBON NANODOT HYBRID CONJUGATES FOR IMAGING AND TARGETING A549 CELLS

Figure S4.1. A photograph of synthesized NPs in vials under UV light

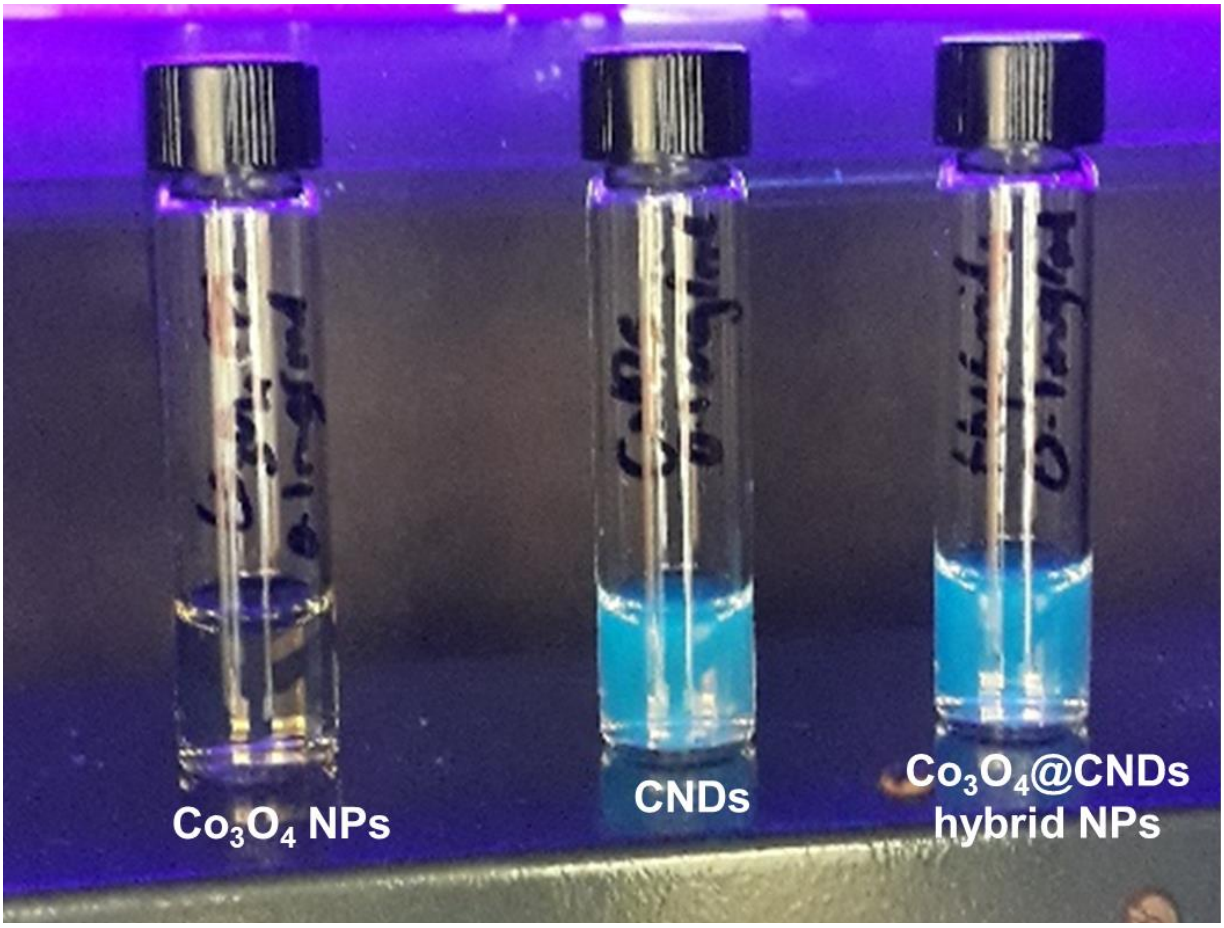

Figure S4.2. FTIR of a. FA-BSA-Co_3O_4@CND-DOX, b. Hep-Co_3O_4@CND-DOX, c. Co_3O_4@CND-Rhod, and d. Co_3O_4@CND-Trf-DOX hybrids

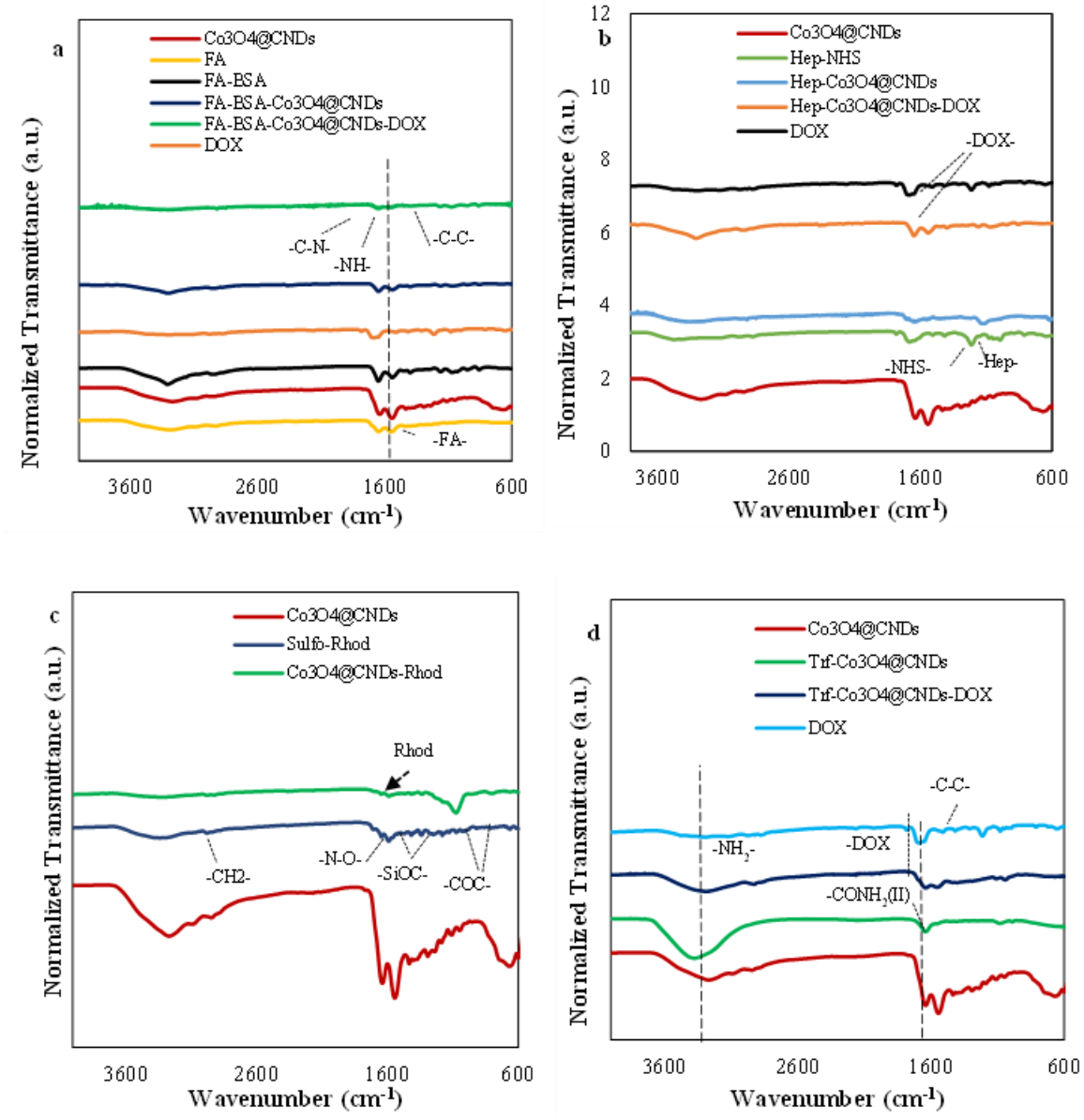

Figure S4.3. UV-Visible Spectroscopic data of a. FA-BSA-Co_3O_4@CND-DOX, b. Hep-Co_3O_4@CND-DOX, c. Co_3O_4@CND-Rhod, and d. Co_3O_4@CND-Trf-DOX hybrids

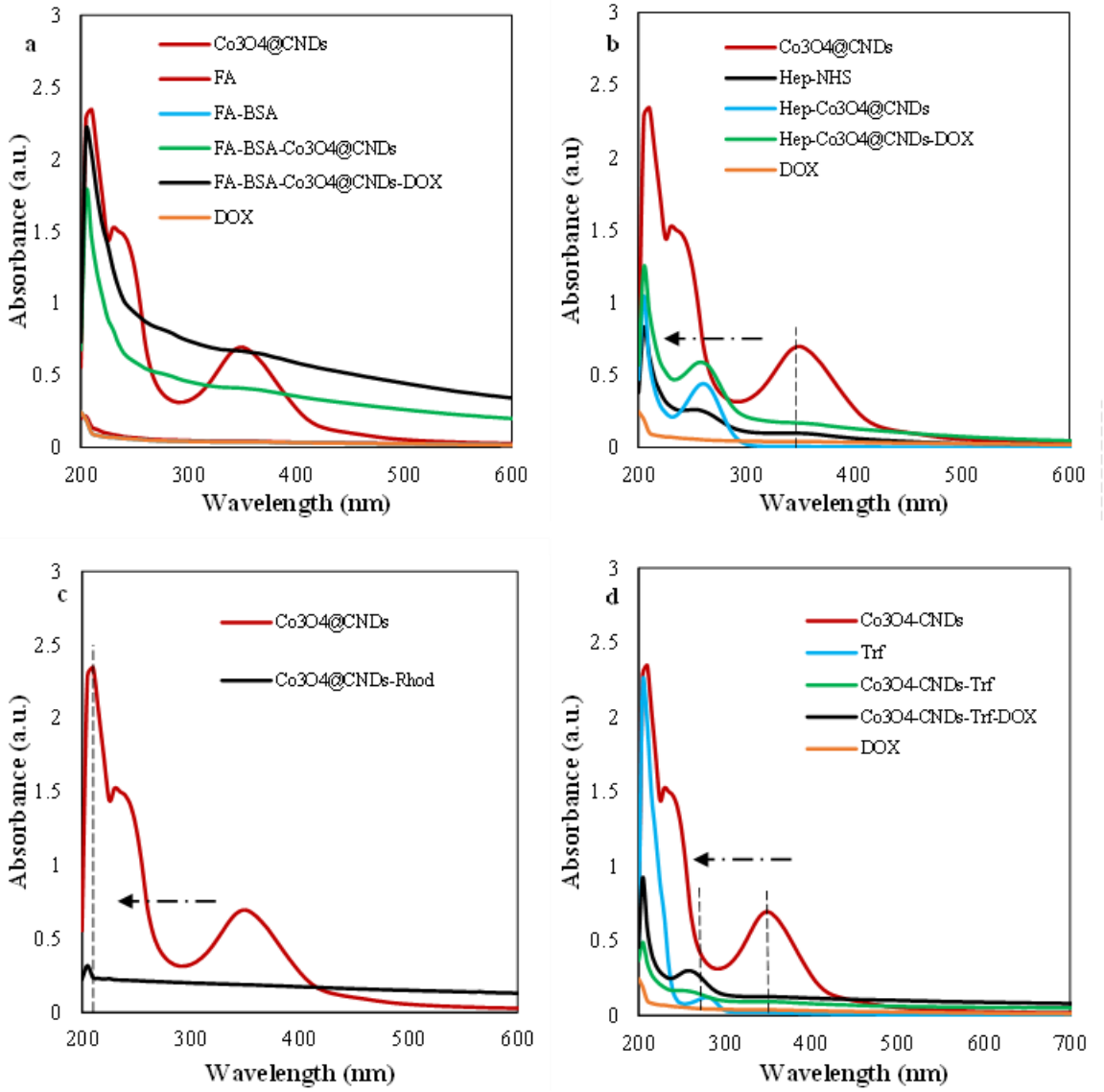

Figure S4.4. PL Spectroscopic data of a. FA-BSA-Co_3O_4@CND-DOX, b. Hep-Co_3O_4@CND-DOX, c. Co_3O_4@CND-Rhod, and d. Co_3O_4@CND-Trf-DOX hybrids

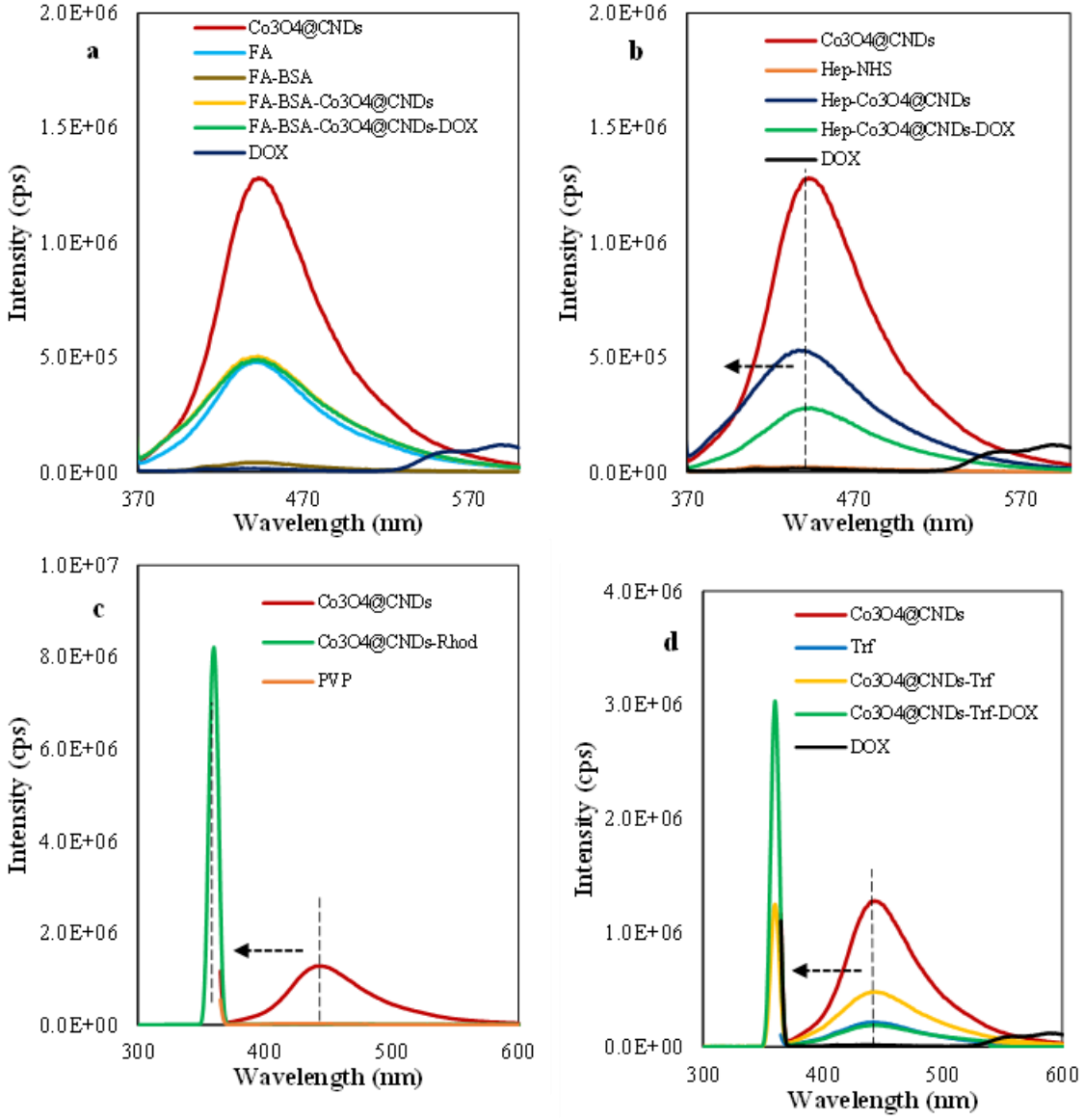

Figure S4.5. Excitation dependency emission spectra of a. CNDs, b. Co_3O_4@CND hybrid NPs, c. FA-BSA-Co_3O_4@CND-DOX, d. Hep-Co_3O_4@CND-DOX, and e. Co_3O_4@CND-Trf-DOX hybrids

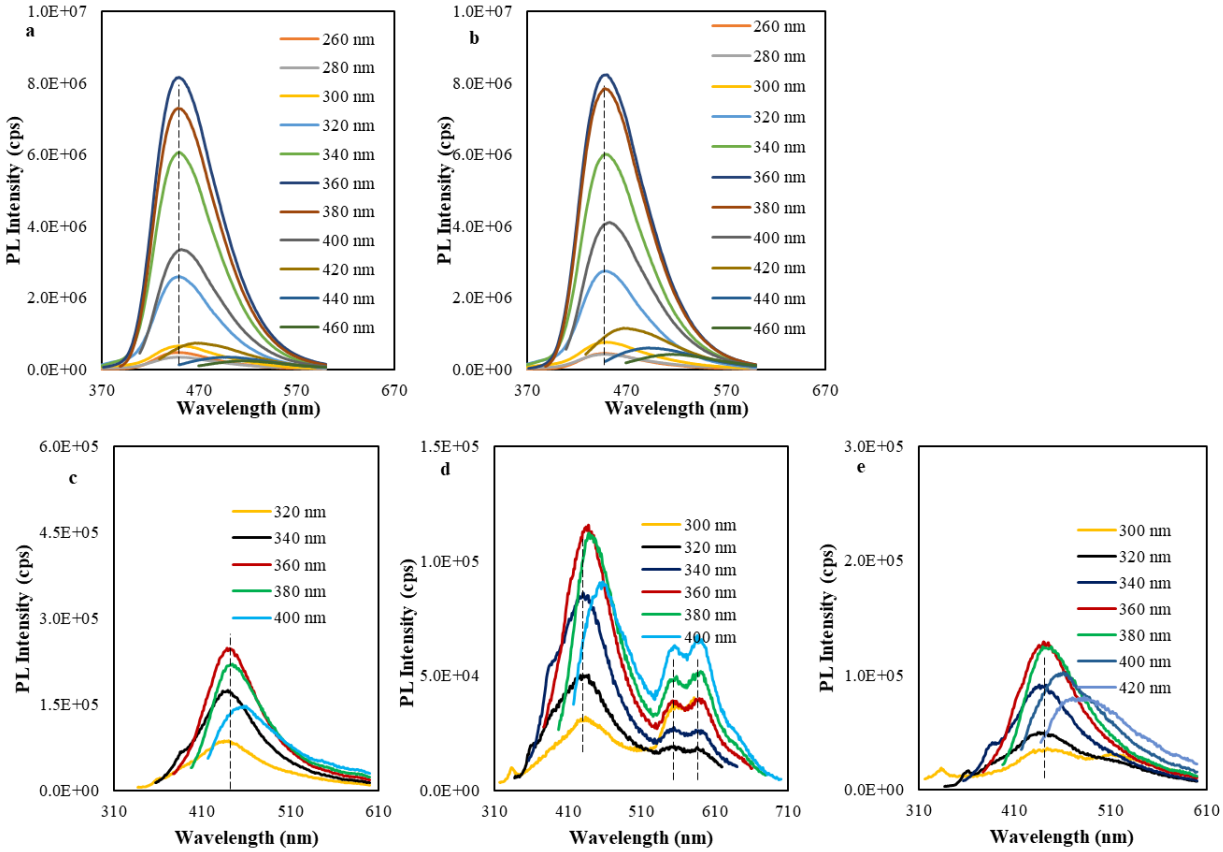

Figure S4.6. Zeta Potential data of a. FA-BSA-Co_3O_4@CND-DOX, b. Hep-Co_3O_4@CND-DOX, c. Co_3O_4@CND-Rhod, and d. Co_3O_4@CND-Trf-DOX hybrids

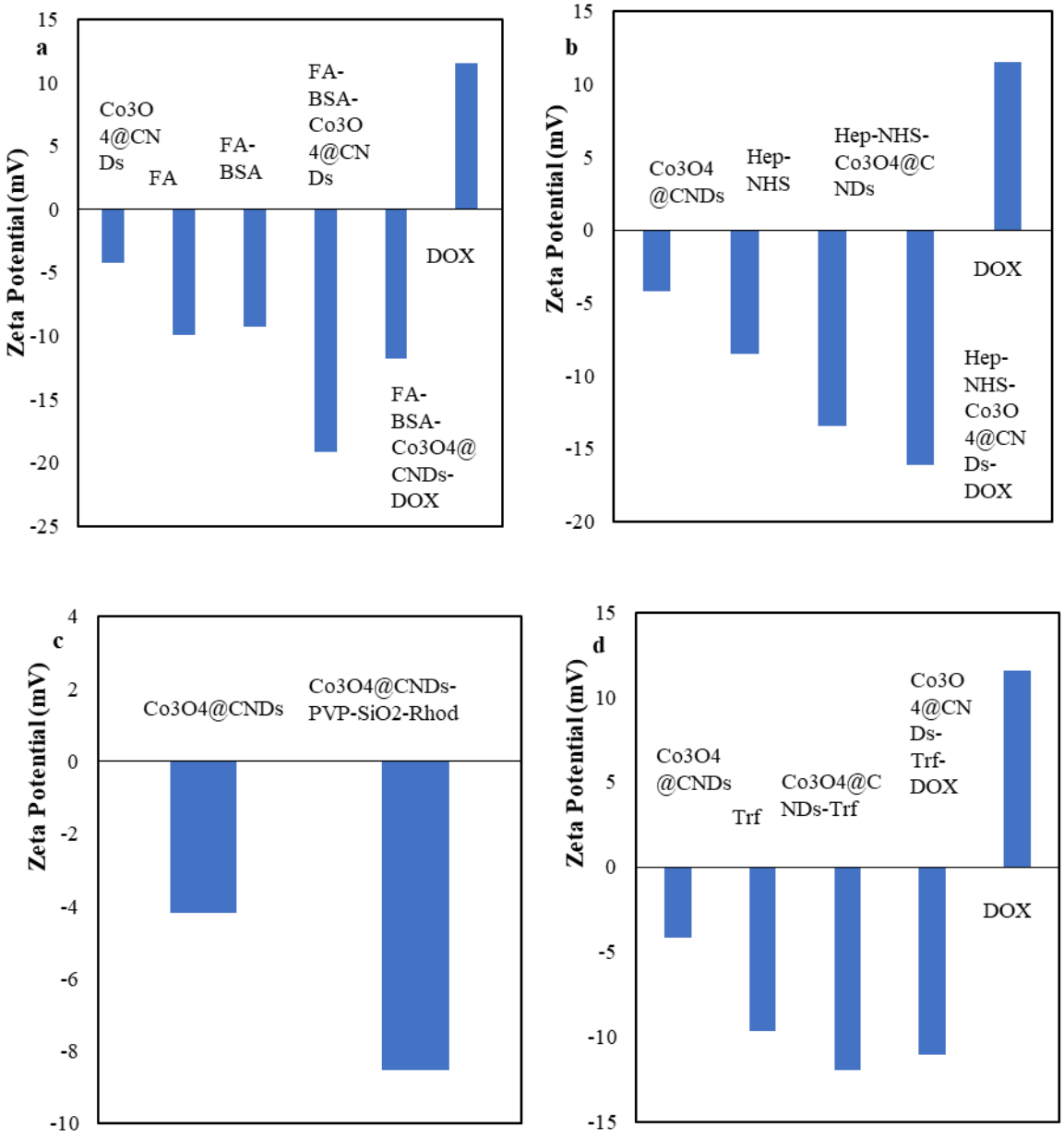

Figure S4.7. Cellular uptake of Co_3O_4@CND hybrid NPs with an increase in concentrations in EAhy926 cells at 63X magnification

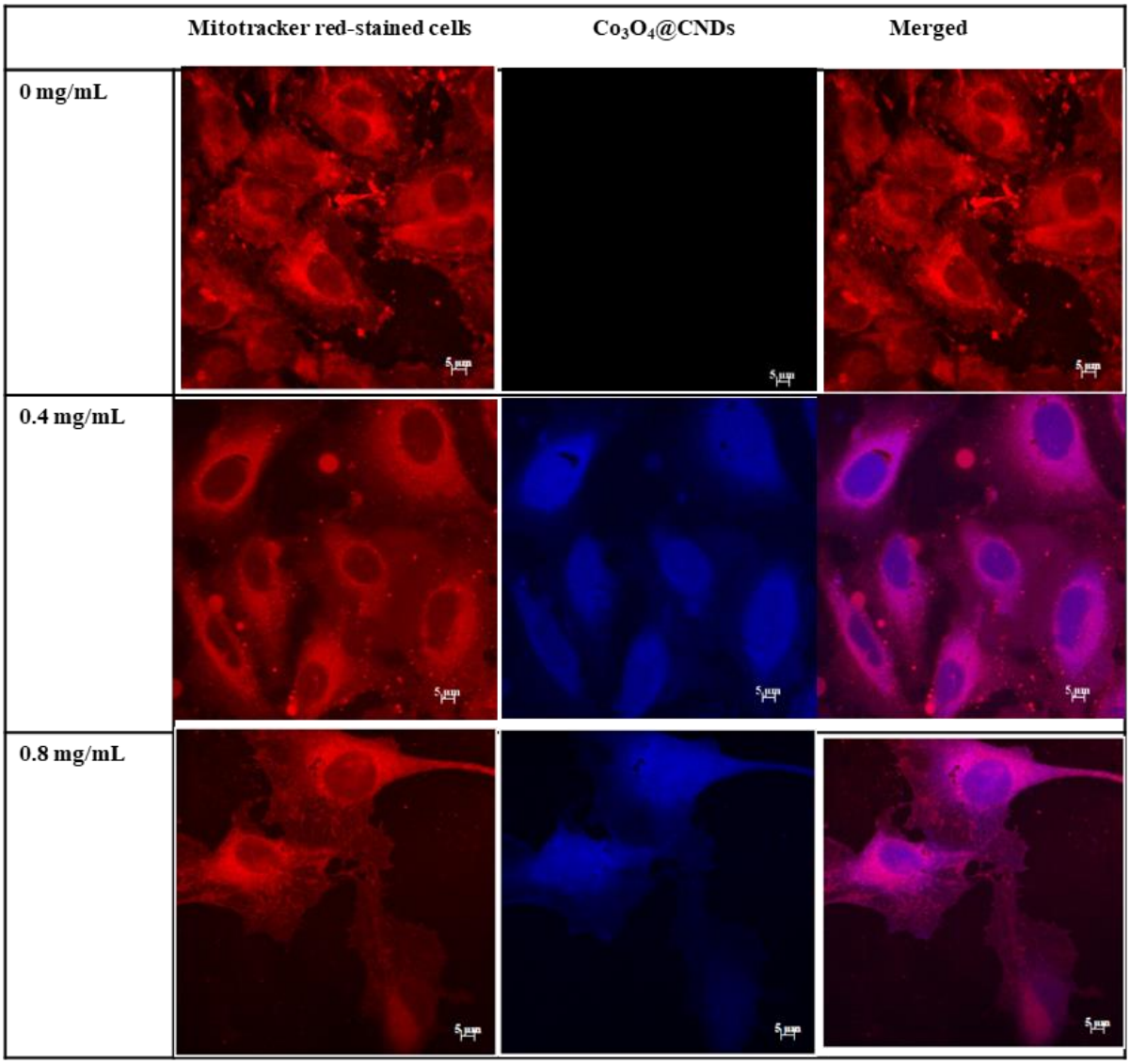

Figure S4.8. Cellular uptake of Co_3O_4@CND hybrid NPs with an increase in concentrations in A549 cells at 63X magnification

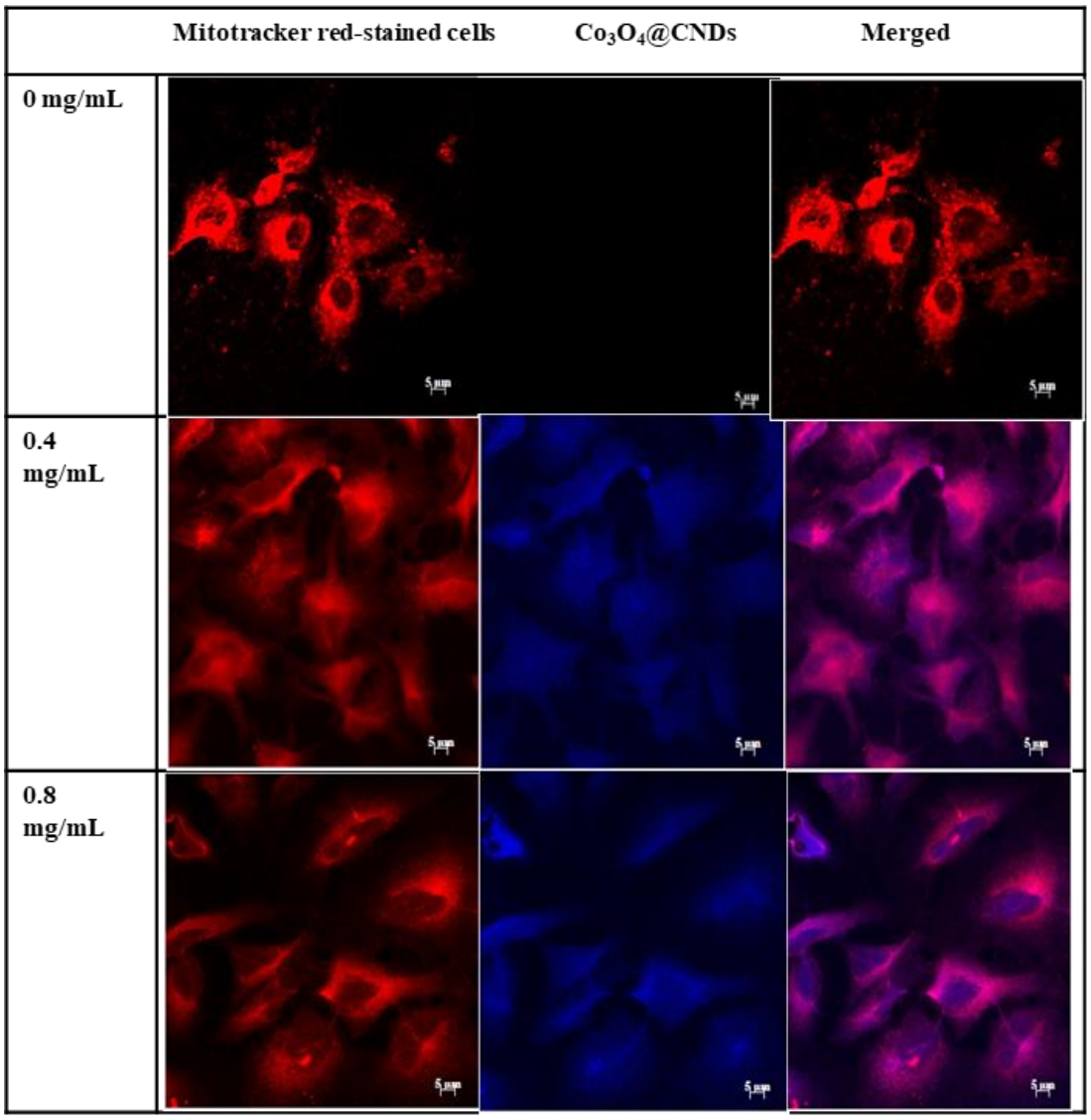

Figure S4.9. Sub-cellular localization of CNDs in EAhy926 and A549 cells at 100X magnification

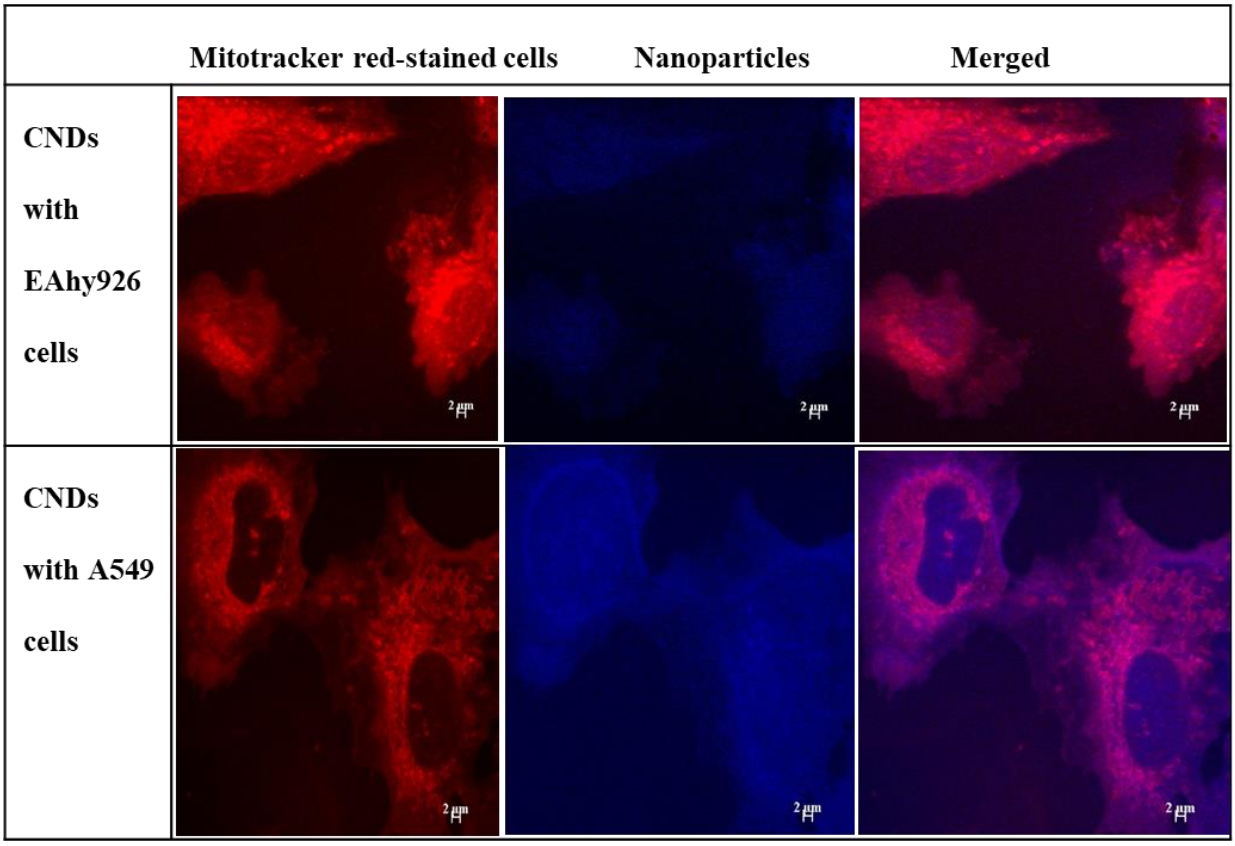

Figure S4.10. DCFH-DA comparison plots of Co_3O_4@CND hybrid NPs in both cell types

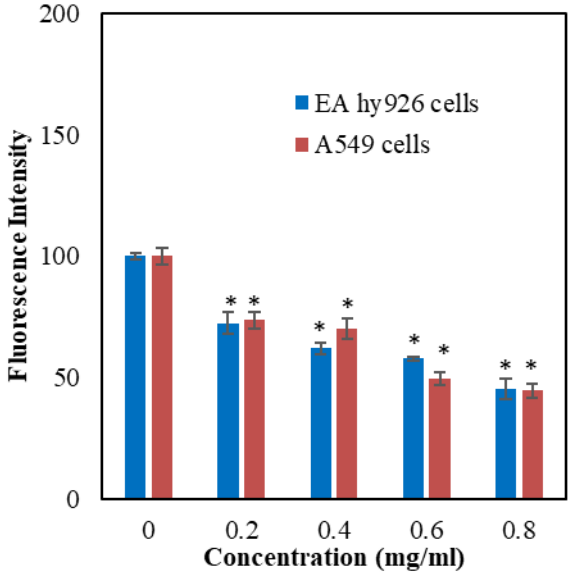

Figure S4.11. Percentage viability plots of EAhy926 cells with a. FA-BSA-Co_3O_4@CND-DOX, b. Hep-Co_3O_4@CND-DOX, c. Co_3O_4@CND-Rhod, and d. Co_3O_4@CND-Trf-DOX hybrids

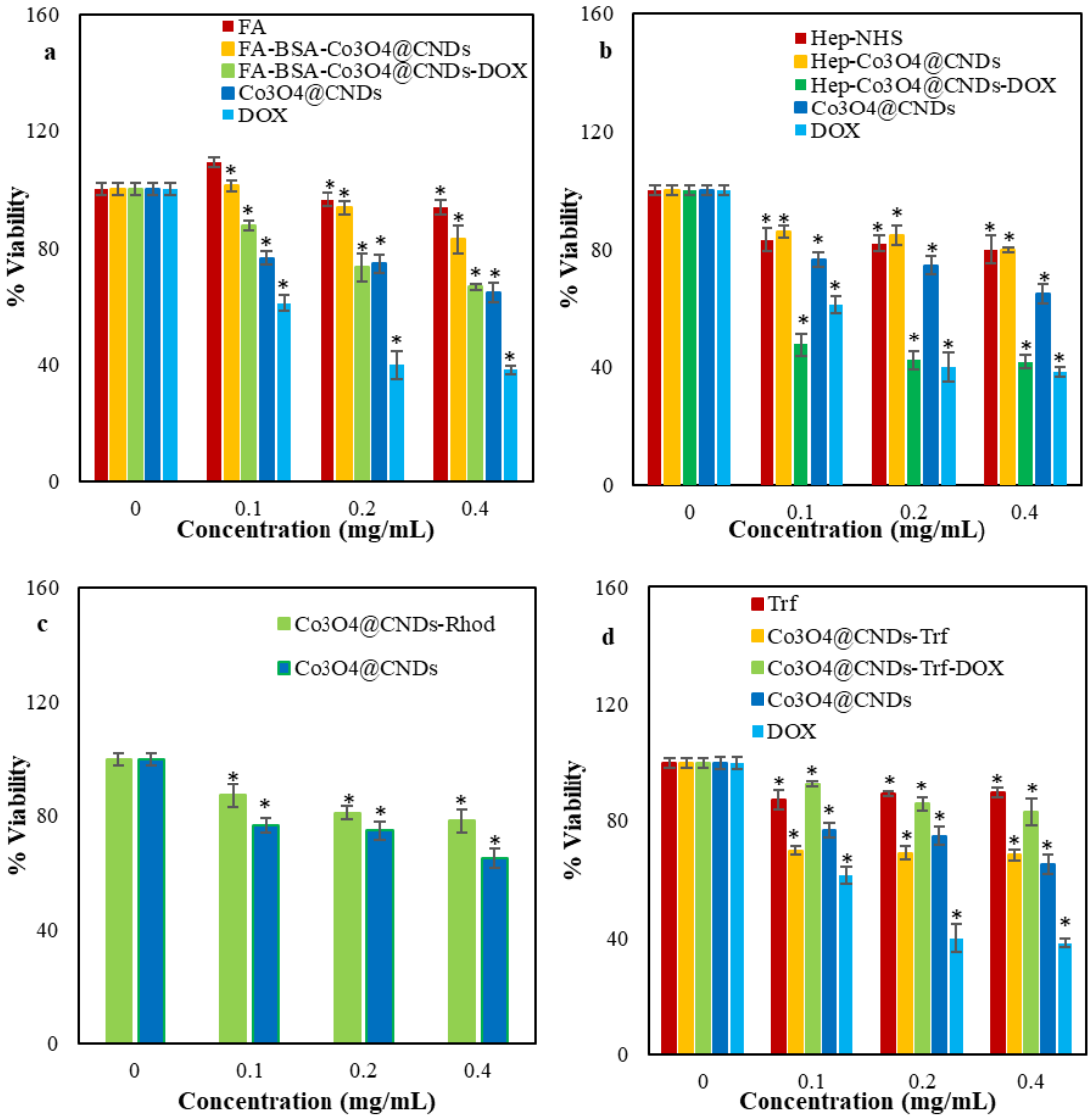

Figure S4.12. Percentage viability plots of A549 cells with a. FA-BSA-Co_3O_4@CND-DOX, b. Hep-Co_3O_4@CND-DOX, c. Co_3O_4@CND-Rhod, and d. Co_3O_4@CND-Trf-DOX hybrids.

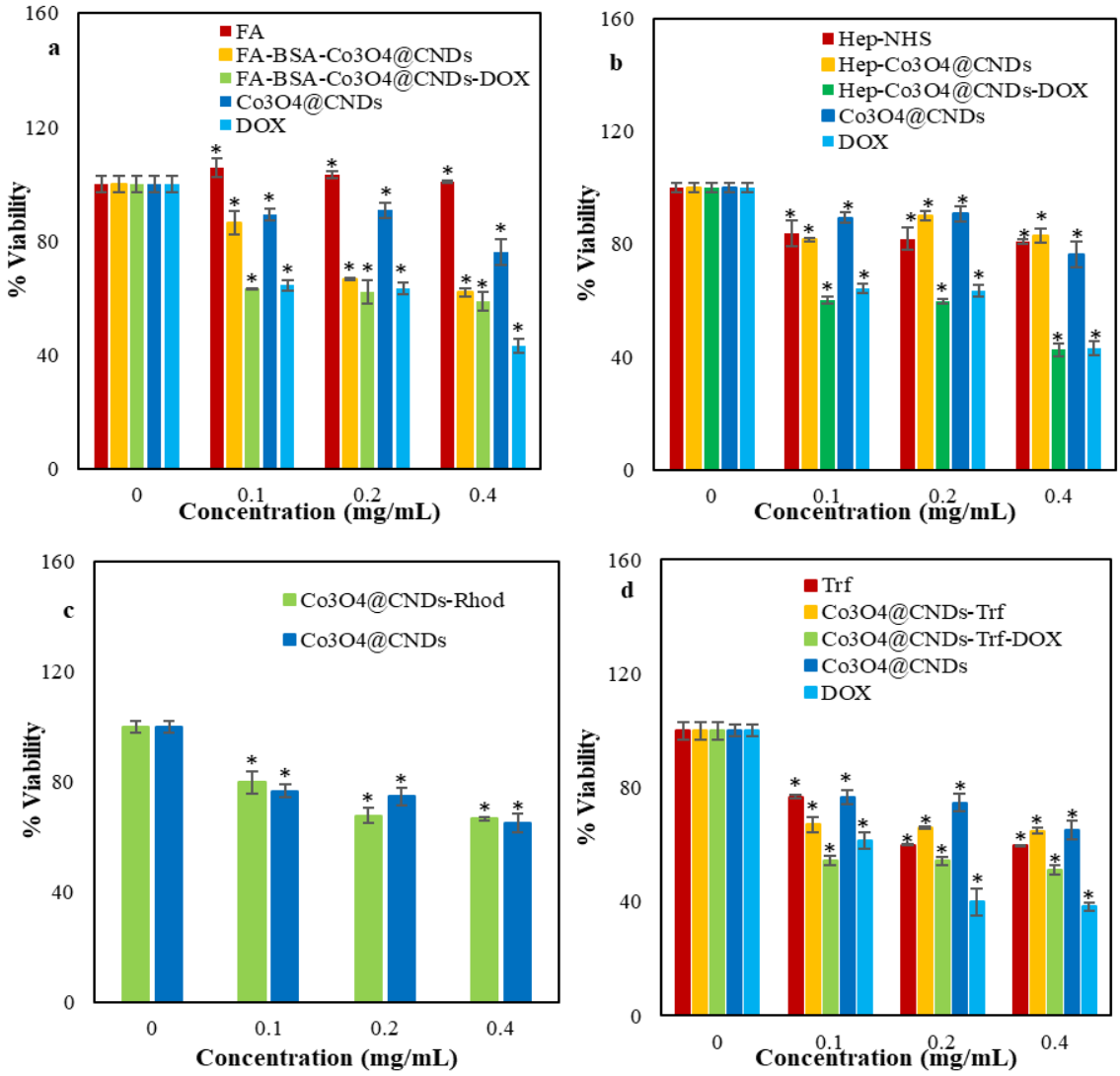

Table S4.1. Zeta potential of all the conjugated particles

Samples	Zeta Potential
Co_3O_4@CNDs	-4.19±0.11 mV
FA	-9.81±0.43 mV
FA-BSA	-9.30±0.36 mV
FA-BSA-Co_3O_4@CNDs	-19.13±1.23 mV
FA-BSA-Co_3O_4@CNDs-DOX	-11.8±0.8 mV
Hep-NHS	-8.52±0.24 mV
Hep-NHS-Co_3O_4@CNDs	-13.47±0.27 mV
Hep-NHS-Co_3O_4@CNDs-DOX	-16.1±0.9 mV
Co_3O_4@CNDs-Rhod	-8.52±0.24 mV
Trf	-9.63±0.29 mV
Co_3O_4@CND-Trf	-11.97±0.53 mV
Co_3O_4@CND-Trf-DOX	-11.03±0.73 mV
DOX	11.53±0.77 mV

Table S4.2. Comparison analysis of the percentage viability in EAhy926 and A549 cells for the Co_3O_4@CND hybrid NPs with different conjugations

Conjugated targeting ligands with Co_3O_4@CND hybrid NPs	Pros	Cons
FA-BSA-DOX	More cancer specific Viability at 0.4 mg/mL: 58.76%	At 0.4 mg/mL concentration, viability: 66.83%
Hep-DOX	Viability for A549 cells at 0.4 mg/mL: 42.66%	Not much safe to EA hy926 cells; toxic at 0.4 mg/ml concentration, viability: 41.61% and at 0.1 mg/mL
Rhod	Viability for EAhy926 cells at 0.4 mg/mL: 78.15% Viability for A549 cells at 0.4 mg/mL: 66.54%	
Trf-DOX	Viability for EAhy926 cells at 0.4 mg/mL: 82.86% Viability for A549 cells at 0.4 mg/mL: 51.19%	
Co_3O_4@CND hybrid NPs only – no conjugation		Viability for EAhy926 cells at 0.4 mg/mL: 65.02% Viability for A549 cells at 0.4 mg/mL: 76.31%
DOX only - no conjugation		Viability for EAhy926 cells at 0.4 mg/mL: 38.25% Viability for A549 cells at 0.4 mg/mL: 43.16%